Mehrdaad Ghorashi

Statics and Rotational Dynamics of Composite Beams

Springer

Statics and Rotational Dynamics of Composite Beams

Mehrdaad Ghorashi

Statics and Rotational Dynamics of Composite Beams

Springer

Mehrdaad Ghorashi
University of Southern Maine
Gorham, ME
USA

ISBN 978-3-319-14958-5 ISBN 978-3-319-14959-2 (eBook)
DOI 10.1007/978-3-319-14959-2

Library of Congress Control Number: 2015960409

Printed on acid-free paper

This Springer imprint is published by SpringerNature
The registered company is Springer International Publishing AG Switzerland

To the memory of my beloved mother,
Touraandokht Khoshravaan,
and
my dear brother, Mahdaad

Preface

A helicopter, with its capability of vertical take-off and landing, is a crucial means of aerial transportation. In fire-fighting rescue operations and missions for helping survivors of an earthquake or an avalanche, helicopters have played vital roles. The expansion of the domain of the application of helicopters, however, faces a few serious constraints; among them is the relatively poor ride quality due to severe vibration and noise. Vibration can reduce the fatigue life of structural components and hence increase the operating costs. Furthermore, environmental consequences of noise and vibration have limited the range of application and the velocity of helicopters. That is why reducing noise and vibration is a major goal in the design of helicopters.

Smart materials are good candidates for providing a way to control noise and vibrations in helicopters. Embedded strain sensing and actuation in active structures can be used to reduce blade vibration, minimize blade vortex interaction, decrease noise, and improve stability and response characteristics of the helicopter (Traugott et al. 2005).

Reliable and economically viable design of structures and machine elements is impossible without the use of accurate and efficient methods of structural analysis. Such methods should be capable of analyzing real-world problems that involve different types of materials. While isotropic materials behave identically when loaded in different directions, anisotropic materials are direction-dependent. Fiber-reinforced composites are among the latter type of materials and by proper orientation of fibers with respect to the direction of loading, they can provide higher values of strength-to-weight ratio compared to conventional isotropic materials.

Materials may also be classified as passive or active. The usual characteristic of active materials is that they deform in response to electrical stimuli. The conversion of electrical input to mechanical output corresponds to the actuator mode of operation and the resulting deformation is used as mechanical excitation. Conversely, active materials may generate electrical signals when they are subjected to mechanical loading and deformation. This is the sensor mode of operation. By embedding such sensors and actuators in structures such as helicopter rotor blades, the two modes of operation (i.e., sensing and actuating) are combined. A control strategy then uses the sensor output, processes it, and provides necessary input to the actuators in order to minimize harmful effects such as noise and vibration.

In the linear range of response, small deformations are linearly related to the imposed loads on a structure; so, doubling a load results in doubling deformation. However, beyond a certain level of deformation, the linear relationship between loading and deformation ends and transforms to a geometrically nonlinear relation. In this nonlinear region, the superposition principle is no longer valid. Therefore, many of the conventional methods that are used for solving differential equations, such as splitting the general solution of a non-homogeneous equation into a homogeneous (natural or transient) and a particular (forced or steady-state) part, are no longer applicable. Solving such problems requires the use of alternative methods such as the perturbation methods.

Various methods have been used for analyzing the mechanical behavior of structures. Among them, the finite element method (FEM) has been successful in solving problems with complicated geometry and without the need to accept many simplifying assumptions. Application of the FEM, however, requires modeling of the whole structure and calculation of large stiffness and inertia matrices.

An alternative solution technique is the variational asymptotic method (VAM). This method splits the solution of the three-dimensional (3-D) problem into two major parts. The first is a two-dimensional (2-D) analysis that develops the cross-sectional stiffness and inertia matrices as well as the warping functions. These results can then be used in a 3-D simulation of structures without the need to repeat the 2-D analysis. The second is a geometrically nonlinear one-dimensional (1-D) analysis of the beam-like structure along its longitudinal direction. Combining these two solutions provides the complete 3-D response of the structure. Since VAM eliminates the need to recalculate the cross-sectional properties, it is a more efficient solution method compared to the 3-D FEM.

Using VAM and the corresponding cross-sectional and 1-D solutions, this book covers the elastic response of isotropic and composite beams and rotor blades in geometrically linear and nonlinear statics, as well as nonlinear dynamics situations. The effects of aerodynamic loading, damping, and embedded actuators are also discussed.

This book is intended as a thorough study of nonlinear elasticity of slender beams and is targeted to researchers, graduate students, and practicing engineers in the fields of structural dynamics, aerospace structures, and mechanical engineering. It broadens readers' understanding of the nonlinear static and dynamic response of composite beams, required in many applications such as helicopter rotor blades and wind turbines, through comprehensive and step-by-step analysis. It provides graduated analyses of phenomena beginning with the fundamental (static, linear, isotropic, passive, and clamped) progressing through the complex (dynamic, nonlinear, composite, with actuators, and articulated), and it models both clamped and hinged rotating beams and blades as well as analyzing beams and blades with embedded active fiber composites.

The presented static solution can be used independently or to provide the initial conditions that are needed for performing a dynamic analysis. The considered dynamic problems include the analysis of accelerating clamped (hingeless) and articulated (hinged) rotating blades. Independent numerical solutions for the transient and the steady-state responses are presented, and as a verification, it is illustrated that the transient solution converges to the steady-state solution obtained by the shooting method. Other key topics include calculating the effect of perturbing the steady-state solution, coupled nonlinear flap-lag dynamics of a rotating articulated blade with hinge offset and aerodynamic damping, and static and nonlinear dynamic responses of composite beams with embedded piezocomposite actuators. The results obtained in each section are verified or justified.

The book starts with an introduction in Chap. 1, which is then followed in Chap. 2 by a review of the VAM and the equations of motion. These equations apply to beams made of arbitrary materials and cross sections. In the rest of the book, the equations of motion are used for solving a set of progressively complex problems involving the dynamics of rotating blades.

Chapter 3 is dedicated to the linear static analysis of isotropic and composite beams, and it is followed by Chap. 4 that presents the nonlinear static analysis of such structures. In Chap. 4, foreshortening which is an inherently nonlinear phenomenon is used for the verification of the results.

Chapter 5 is on the transient nonlinear dynamics of a clamped (hingeless) blade that rotates at variable speed. The rotor blade starts its motion from rest and after an acceleration interval converges to a steady-state condition. In order to solve this problem, an explicit (direct) integration algorithm is developed that utilizes the finite difference and the perturbation methods. A computer program that uses this algorithm solves the transient form of the nonlinear differential equations of motion and provides the elasto-dynamic response of the rotating composite blade. Using this method, the steady-state behavior can also be obtained. However, it is only possible after the whole transient response of the blade is calculated.

In Chap. 6, an alternative method for obtaining the steady-state behavior of a rotating blade is presented. This method does not require calculating the transient response in advance. Instead, it solves a boundary value problem that is based on the steady-state form of the nonlinear differential equations of a beam. This problem is then converted to a series of initial value problems which are solved by iterating an implicit (indirect) integration method. In each iteration, the estimations for the unknown initial conditions are improved by the use of the Newton–Raphson algorithm and the shooting method. The solution is repeated and its convergence is checked at every step. When a convergence criterion is satisfied, the correct solution of the boundary value problem and the steady-state response of the blade are obtained. The calculated response includes the steady-state values of forces, moments, velocities, and angular velocities along the blade. These results compare very well with the solution obtained in Chap. 5 as the transient solution discussed in Chap. 5 converges to the steady-state solution of Chap. 6. Having calculated the steady-state response, the effect of imposing input perturbations on the blade (when it is already in its steady-state condition) is analyzed. Small perturbations are considered; therefore, the solution is valid only near the steady-state response.

The rotating blades considered in Chaps. 5 and 6 are all clamped (hingeless). In Chap. 7, the dynamics of rotating articulated (hinged) blades, both rigid and elastic, is discussed. It starts with an introduction on the extended Euler equations of motion and continues by using these equations to calculate the coupled nonlinear flap-lag rigid body dynamics of articulated blades. The rigid body dynamics at the root of the blade is used to provide the boundary conditions for the case of the elastic rotating articulated blade. These boundary conditions together with the solution method developed in Chap. 5 are implemented to calculate the nonlinear dynamic response of an accelerating articulated blade. The solution is shown to be in good agreement with approximate formulas for the axial force and with the implemented boundary conditions.

Embedded actuators are used in rotating blades to control their shape in order to reduce noise and vibrations or to gain other satisfactory performance such as higher lift forces. In Chap. 8, the effect of inclusion of embedded piezocomposite actuators in a composite beam structure is analyzed. Both geometrically nonlinear static and dynamic cases are considered and the response sensitivity to the performance of actuators oriented at various directions along the blade is evaluated. Specifically, the steady-state force and moment components generated in the rotating blade are calculated. Such results can be used to control the elasto-dynamic response of rotating blades.

This book is based on my second Ph.D. thesis in mechanical engineering that I worked on in Carleton University in Ottawa. However, in this book, I also use a few solution techniques that I had developed in my earlier research for my first Ph.D. in mechanical engineering in Sharif University of Technology in Tehran. That research dealt with the dynamics of structures subjected to moving loads.

There have been a number of people that have contributed to this book in one way or another. First, I sincerely thank Professor Fred Nitzsche, for introducing Professor Hodges' fascinating book, Hodges (2006), to me. This is clearly the best resource for understanding the VAM. Also during the research that led to this book, I have had the privilege of receiving plenty of valuable hints and suggestions from Professors Dewey H. Hodges of Georgia Institute of Technology, Wenbin Yu of Purdue University, Carlos E.S. Cesnik of University of Michigan, and Rafael Palacios of Imperial College for which I am grateful. The constructive comments received from four anonymous reviewers of an earlier draft of this book are also thankfully appreciated.

I also gratefully acknowledge the Alexander Graham Bell Canada Graduate Scholarship Award (CGS) by the Natural Science and Engineering Research Council of Canada (NSERC), the J.Y. and E.W. Wong Research Award in Mechanical/Aerospace Engineering, and the Research Assistantship Award for carrying out my Ph.D. research that ultimately led to this publication.

Last, but not least, I appreciate the love and support that I have received from my wife Marjaneh, my daughter Mehrnaz, and my son Ali during all the years that I have been working on this book and the corresponding research.

Mehrdaad Ghorashi, Ph.D., P.E.

References

Traugott, J. P., Patil, M. J., & Holzapfel, F. (2005). Nonlinear dynamics and control of integrally actuated helicopter blades. In *Proceedings of the 46th AIAA/ASME/ASCE/ AHS/ASC Structures, Structural Dynamics and Materials Conference*, 18–21 April, 2005, Austin, Texas. Paper No: AIAA 2005-2271.

Hodges, D. H. (2006). *Nonlinear composite beam theory*. New York: AIAA.

Contents

Nomenclature

A	Cross-sectional area of the undeformed beam in the x_2–x_3 plane
B	Deformed reference frame (B_1 is perpendicular to the plane of deformed cross section of the beam and other two base vectors on this plane)
b	Undeformed reference frame (b_1 is perpendicular to the plane of undeformed cross section of the beam and other two base vectors on this plane)
C	Finite rotation tensor
D	Material matrix (Chap. 2)
D	Vector of electric displacements (Chap. 8)
d_{ijk}	Piezoelectric moduli in tensor form (i, j, k = 1, 2, 3)
E_i	Electric field (Chap. 8)
E_i	Moduli of elasticity (i = 1, 2, 3)
e	Hinge offset ratio (offset as a fraction of the rotor radius, R)
e_{ijk}	Permutation symbol (i, j, k = 1, 2, 3)
e_1	$\begin{bmatrix} 1 & 0 & 0 \end{bmatrix}^T$
F_i	Elements of the column matrix of internal forces (i = 1, 2, 3)
f	Applied forces vector per unit length
G_{ij}	Shear moduli (i, j = 1, 2, 3)
g	Determinant of the metric tensor in curvilinear coordinates (Chap. 2)
g	Current boundary value at the tip (Chap. 6)
H	Sectional angular momenta vector
i_2, i_3	Cross-sectional mass moment of inertia
i_{23}	Cross-sectional product of inertia
K	Deformed beam curvature vector $= k + \kappa$
k	Undeformed beam curvature vector
L	Length of the beam
L	Lift force per unit length (Chap. 7)
M_i	Elements of the column matrix of internal moments (i = 1, 2, 3)
m	Applied moments vector per unit length

N	Number of nodes
P	Sectional linear momenta vector
R	Rotor radius
S	Cross-sectional stiffness matrix
$S(x_2, x_3)$	Matrix of the FEM shape functions
t	Time
U	Strain energy per unit length
u_i	Displacement field in the b_i ($i = 1, 2, 3$) reference frame
V	Vector of nodal warping displacements (Chap. 2)
V	Velocity vector field in the B_i ($i = 1, 2, 3$) reference frame
v	Velocity field in the b_i ($i = 1, 2, 3$) reference frame
w_i	Warping displacement components ($i = 1, 2, 3$)
x_i	Global system of coordinates ($i = 1, 2, 3$)
x_1	Axis along the beam
x_2, x_3	Cross-sectional axes
$\bar{x}_2$ and $\bar{x}_3$	Offsets from the reference line of the cross-sectional mass center (coordinates of the cross-sectional centroid with respect to the shear center of the cross section)
x_G	Spanwise position of the mass center
α	Magnitude of the rotation used in the Rodrigues parameters (Chap. 2)
α	Assumed initial conditions at the root (Chap. 6)
β	Boundary conditions at the tip (Chap. 6)
β	Flap angle (Chap. 7)
Γ	Strain tensor $= \lfloor \Gamma_{11} \quad 2\Gamma_{12} \quad 2\Gamma_{13} \quad \Gamma_{22} \quad 2\Gamma_{23} \quad \Gamma_{33} \rfloor^T$
γ	$\lfloor \gamma_{11} \quad 2\gamma_{12} \quad 2\gamma_{13} \rfloor^T$ (Chap. 2)
γ	Lock number (Chap. 7)
$\bar{\gamma}_{11}$	Extension of the reference line (the bar indicates that transversal shear deformation has been neglected: $\bar{\gamma}_{12} = \bar{\gamma}_{13} = 0$)
Δ	3 × 3 identity matrix
$\delta\bar{q}$	Virtual displacement vector (the bar indicates that it need not be the variation of a functional)
$\delta\bar{\psi}$	Virtual rotation vector (the bar indicates that it need not be the variation of a functional)
$\bar{\varepsilon}$	Generalized strain in the classical theory $= \lfloor \bar{\gamma}_{11} \quad \bar{\kappa}_1 \quad \bar{\kappa}_2 \quad \bar{\kappa}_3 \rfloor^T$ (the bar indicates that transversal shear deformation has been neglected: $\bar{\gamma}_{12} = \bar{\gamma}_{13} = 0$)
ε^{Γ}	Matrix of dielectric permittivity at constant strain
Θ	Rodrigues parameters $= \lfloor \theta_1 \quad \theta_2 \quad \theta_3 \rfloor^T$; $\theta_i = 2e_i \tan\left(\alpha/2\right)$
κ_1	Elastic twist
κ_i	Elastic bending curvatures ($i = 2, 3$)
μ	Mass per unit length
ν_{ij}	Poisson's ratios ($i, j = 1, 2, 3$)
ρ	Mass density
σ_{ij}	Stress tensor components $= \lfloor \sigma_{11} \quad \sigma_{12} \quad \sigma_{13} \quad \sigma_{22} \quad \sigma_{23} \quad \sigma_{33} \rfloor^T$

ψ	Kernel matrix
Ω	Angular velocity vector in the B_i (i = 1, 2, 3) reference frame
ω	Angular velocity vector in the b_i (i = 1, 2, 3) reference frame
ξ	Lead-lag angle
$\left(\overset{\smile}{\bullet}\right)$	Perturbations in space
$\left(\overset{\frown}{\bullet}\right)$	Perturbations in time
$(\bullet)'$	$\frac{\partial(\bullet)}{\partial x_1}$ = derivative w.r.t. the axis along the undeformed reference line
$(\dot{\bullet})$	Derivative w.r.t. time, t
$(\delta\bar{\bullet})$	The bar indicates that it need not be the variation of a functional
$(\tilde{\bullet})_{ij}$	$-e_{ijk}(\bullet)_k$: The cross product operator (transformation from a vector to its dual skew-symmetric matrix) For two vectors a and b, $\tilde{a}b = \underbrace{\begin{bmatrix} 0 & -a_3 & a_2 \\ a_3 & 0 & -a_1 \\ -a_2 & a_1 & 0 \end{bmatrix}}_{\tilde{a}} \begin{Bmatrix} b_1 \\ b_2 \\ b_3 \end{Bmatrix} = a \times b$
$\langle\bullet\rangle$	$\int\limits_A (\bullet)\mathrm{d}x_2\mathrm{d}x_3$
$\langle\langle\bullet\rangle\rangle$	$\left\langle(\bullet)\sqrt{g}\right\rangle = \int\limits_A (\bullet)\sqrt{g}\mathrm{d}x_2\mathrm{d}x_3,\ \sqrt{g} = 1 - x_2k_3 - x_3k_2$

Chapter 1
Introduction

1.1 Preliminary Remarks

The analysis of structures that have one dimension much larger than the other two can be done by modeling them as beams. A beam model, also called a one-dimensional (1-D) model, provides the advantage of simplicity of analysis and faster solution. Such a modeling is widely used in applications like helicopter rotor blades and wind turbine blades. However, one should always assure that the simpler 1-D model is able to provide a satisfactory picture of the truly three-dimensional (3-D) real-life problem.

In many engineering applications where isotropic materials are used and the member under consideration has simple geometry and undergoes small deformations, a classical beam theory can be used to provide an adequate solution for the 3-D problem. However, there are severe limitations for the use of classical beam theories in today's engineering applications.

The first limitation is the replacement of isotropic materials by composite materials in many applications including helicopter rotor blades. A major reason for the growing use of composites as the materials of choice is that they provide much higher strength-to-weight ratios compared to isotropic materials. The second limitation is that structural members in many engineering applications have complex geometry that includes initial curvature.

The third limitation is due to the small deformations assumption that is a major simplifying assumption in classical beam theories. The main impact of this assumption is that all formulations become linear, and therefore, one may use the superposition principle for solving problems. However, many lightweight and thin-walled structural members undergo large deflections (even though at small strain) when subjected to service loads. An example is the aeroelastic analysis of high-altitude, long-endurance (HALE) aircraft that features high aspect ratio flexible wings that requires the analysis of structural geometrical nonlinearities and dynamic stall (Jian and Jinwu 2009). As a result, the nonlinear behavior of such

M. Ghorashi, *Statics and Rotational Dynamics of Composite Beams*,
DOI 10.1007/978-3-319-14959-2_1

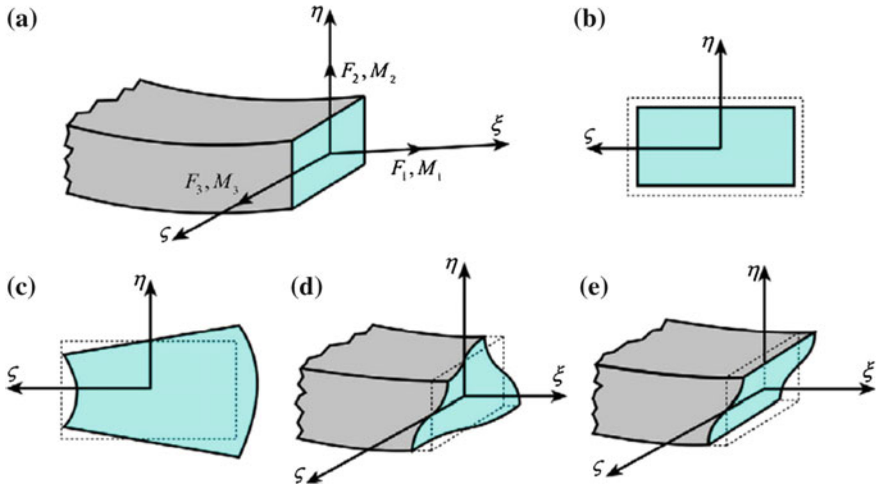

Fig. 1.1 Cross-sectional warpings: (**a**) six stress resultants, (**b**) extension-induced in-plane warping (due to F_1), (**c**) bending-induced warping (due to M_2), (**d**) torsion-induced out-of-plane warping (due to M_1), and (**e**) shear-induced out-of-plane warping (due to F_2) (Pai 2014), © Elsevier Ltd., reprinted with permission

structures cannot be ignored and nonlinear theories that can handle large deformations should be used. Furthermore, geometrical nonlinearity is not the only type of nonlinearity, and the material behavior or the existence of friction between contacting surfaces of objects can also result in nonlinear formulations. A major difficulty in analyzing nonlinear problems is that the superposition principle, which is widely used for solving linear problems, is not applicable to nonlinear ones.

In order to understand the fourth limitation of classical beam theories, the concept of warping should be reviewed. Figure 1.1a illustrates the application of three force and three moment components (collectively named, stress resultants) to the free end of a beam with rectangular cross section. Other parts of Fig. 1.1 show the warping of this cross section, when the beam is free to warp (it has no warping restraint), as a result of the application of each stress resultant.

Warping restraint is another source of nonlinearity and departure from classical beam theories. Twisting a member with warping restraint requires increasingly more torque than what is needed in the simple linear torsion theory. So, the relation between torque and twist angle, even in the elastic region, is not linear. The reason for this phenomenon is that warping restraint restricts the flow of the material (Park and Yang 2007).

In Fig. 1.2, the effect of warping restraint on the clamped end of a cantilever beam subjected to torsion is shown. It is seen that, as predicted by the Vlasov's theory, a bimoment (or moment couple) is generated at the clamped end to prevent the warping shown in Fig. 1.1d from happening. Variations of such moments along the length of the beam would be possible only if self-balanced shear forces are

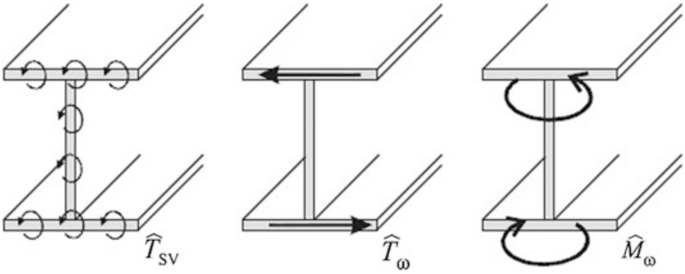

Fig. 1.2 From *left* to *right*—illustration of Saint-Venant's torque, restrained warping-induced torque and bimoment on an I-beam (Kollár and Pluzsik 2012), © SAGE Publications, reprinted with permission

developed in flanges. Such force couples in turn generate a restrained warping-induced torque that is added to the Saint-Venant's torque to provide the total torque.

In-plane and out-of-plane warpings are much smaller than the global displacements. However, these warpings offer extra degrees of freedom for cross-sectional deformation and hence significantly affect stiffness values. In linear extension, torsion, and bending solutions for isotropic beams, one commonly applies Saint-Venant's principle. Saint-Venant's principle implies that stresses at a point far from the loaded cross section depend only on the magnitude of the applied load and are independent of the load distribution pattern over the loaded cross section.

Deformations at points away from a loaded section subject to nonzero stress resultants are called central solutions, Saint-Venant's solutions or particular solutions. Saint-Venant's principle also implies that a set of distributed loads having zero resultant forces and moments (i.e., a set of self-balanced loads) produces a strain field that is negligible at points far away from the loading end. For highly anisotropic and heterogeneous materials, however, such a self-balanced distributed load can result in nonzero strain fields with long decay lengths, which are called boundary solutions, extremity solutions, eigensolutions, or transitional solutions (Pai 2014). The warping restraint effect is due to the contribution of such boundary solutions, and they are needed in the analysis of composite beams.

The fourth limitation of classical beam theories is that they use ad hoc assumptions about the displacement field and usually ignore warping displacements or their couplings. The most accurate and powerful of the ad hoc methods appears to be Jung et al. (2002). While ad hoc assumptions are not valid in general, they work well for problems with simple geometry and for homogeneous and isotropic materials. Conventional beam models rely on ad hoc assumptions on displacement or stress fields. An example is the Saint-Venant's torsion theory which assumes that the cross section of a beam remains rigid in its own plane as it twists (i.e., warping is possible only along the longitudinal axis of the beam). Ad hoc assumptions, however, may not provide acceptable results for problems with more complex geometry and for non-homogeneous and composite materials. In those cases, ad hoc assumptions are not valid and effects like in-plane and out-of-plane components of warping displacement as well as the bending-twist and extension-twist couplings should be taken into consideration.

In the analysis of helicopter blades which are made of composites (for weight saving and enhanced fatigue life) ad hoc assumptions do not provide satisfactory results. In fact, even though warping is small, it has effects that cannot be ignored. While one may ignore its influence on the inertial and applied load terms, due to its magnitude, the strain field depends on the gradient of the warping displacement, which is not necessarily small. Ad hoc assumptions are neither necessary nor correct in any sense (Hodges 2006).

Helicopter rotor blades have initial twist, and since they are laterally flexible, they usually operate in the nonlinear range. Therefore, a beam theory that is suitable for composite rotor blade analysis is required to include geometrical nonlinearities and initial twist. The beam can undergo small strain, while it experiences large deformations and rotations. The theory must accurately analyze global deformation problems, such as static deflection, buckling, natural frequencies, mode shapes, dynamic stability, and aeroelastic stability (when augmented by a suitable aerodynamic theory); it must accurately recover 3-D stresses. In addition, it should reduce to the usual elementary theory when applied to prismatic, isotropic beams (Yu et al. 2012).

In the past three decades, research has been focused on the analysis of anisotropic composite beams using the variational asymptotic method (VAM). VAM, as a powerful method for solving composite thin-walled beam problems, was first introduced in Berdichevsky (1981). VAM solves problems that can be formulated as minimization of a functional (e.g., finding the stationary points for the energy functional) and have an inherently small dimension (e.g., beams, plates, and shells). The solution has the common advantage of asymptotic methods of being mathematically well grounded with no ad hoc assumptions about displacement or stress fields. Interestingly, there are no theoretical restrictions on the geometry of the cross section or on the materials of the problems for which VAM can be applied. It is especially proper for realistic modeling of initially curved and twisted anisotropic beams (like rotor blades) (Hodges 2006).

Figure 1.3 illustrates the beam analysis procedure by VAM. It can be seen how VAM splits the three-dimensional (3-D) geometrically nonlinear elasticity analysis of active composite rotating blades into two major parts. The first part is a (usually) linear two-dimensional (2-D) analysis to determine the cross-sectional stiffness and mass matrices as well as the warping functions. These results can then be used in 3-D simulation of structures without the need to repeat the 2-D analysis.

The second part is a geometrically nonlinear one-dimensional (1-D) beam model, which utilizes the stiffness and mass matrices in order to solve the nonlinear intrinsic equations of motion of a beam. These equations are not tied to a specific choice of displacement or rotation variables. Combining these two solutions provides the complete 3-D response of the structure. Since VAM eliminates the need to recalculate the cross-sectional properties, it is a more efficient solution method compared to the 3-D finite element method (FEM).

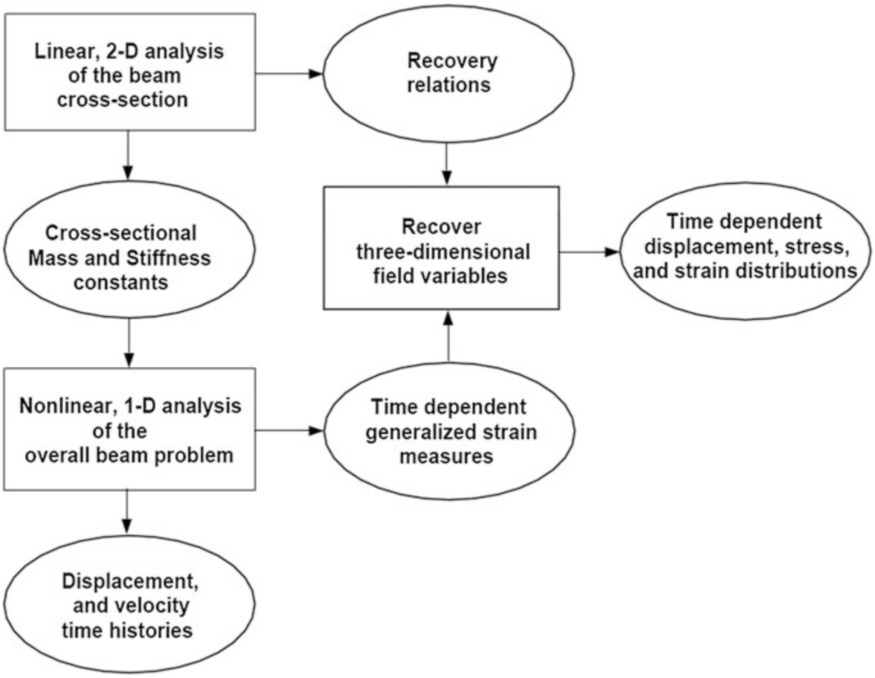

Fig. 1.3 Beam analysis procedure by VAM (Bauchau and Hodges 1999), © Kluwer Academic Publishers, reprinted with permission

This beam theory addresses the following three aspects: a cross-sectional analysis leading to a stiffness matrix that is input into the 1-D analysis, the 1-D analysis itself, and the formulae or procedure to recover stress, strain, and 3-D displacements (Rajagopal and Hodges 2012).

The cross-sectional analysis requires details of the cross-sectional geometry, elastic constants of materials, and material densities. It is solved by minimizing strain energy with respect to warping. The asymptotic analysis yields asymptotically exact results for section constants for beams with thin-walled geometries.

For certain cases like isotropic beams with relatively simple cross-sectional geometry or thin-walled beams made of laminated composite materials, the 2-D analysis could be performed analytically and the stiffness matrices be calculated in closed form. These matrices depend on the cross-sectional geometry, material properties, and the initial twist and bending curvature distributions along the beam.

For complex cross sections, a 2-D FEM computer program named the *variational asymptotic beam sectional* analysis program (VABS) can be used to implement the VAM cross-sectional analysis. Professor D.H. Hodges initiated the research project that gave birth to VABS when he was first introduced to VAM by Professor V.L. Berdichevsky at Georgia Tech in 1989 (Hodges 2006). Professor C.E.S. Cesnik is the author of the original version of VABS in Fortran 77, which appeared in 1992.

He continued his work on VABS for piezoelectric materials at MIT and later at University of Michigan. The original version of VABS was a research code, but later research led to its transition to a production analysis tool for practicing engineers (Palacios 2005). In Chen et al. (2010), a comprehensive set of test problems have been presented and solved using VABS and a few other methods including analytical methods. VABS has been shown to be an effective tool in the analysis of complex elasto-dynamic problems like the analysis of the behavior of helicopter rotor blades.

The mentioned beam modeling has been used for analyzing beams and rotating blades with and without embedded actuators. The reason is that modeling initially twisted and curved active rotor blades using 3-D FEM is computationally demanding and it is not suitable for preliminary design or for control purposes. Beam modeling is suitable since a helicopter rotor blade is a slender structural member and it can be modeled as a thin-walled composite beam. Such a model for helicopter rotor blades is an efficient alternative (Hopkins and Ormiston 2003). Beam modeling of these structures is simpler and is expected to yield sufficiently accurate results. This dimensional reduction transforms the 3-D rotating structure into a 1-D nonlinear rotating composite blade, which utilizes the cross-sectional properties obtained by a 2-D analysis done by VABS.

The objective of this book is to analyze the geometrically nonlinear elasto-static and elasto-dynamic responses of hingeless or articulated composite beams with or without embedded actuators, and with or without the effects of aerodynamic loading or damping. After considering a few static problems, a scenario is studied in which the blade is accelerated from rest and its speed of rotation gradually converges to a steady-state value. Both the transient and the steady-state solutions are calculated. Results of the cross-sectional analysis are obtained by VABS, and the solution of the nonlinear intrinsic equations of the beam is performed using finite differences, perturbations, and the shooting method. To verify the results, they are compared with those of the perturbed steady-state method.

The mentioned topics are mainly based on the contents of Ghorashi and Nitzsche (2008), Ghorashi (2009), Ghorashi and Nitzsche (2009), and Ghorashi (2012) and are covered in the following order:

1. Linear and nonlinear elasto-statics of passive isotropic or composite beams. Such static solutions provide initial conditions for performing the corresponding dynamic analyses.
2. Nonlinear dynamics of passive clamped rotating composite blades (transient and steady-state) accelerating from rest.
3. Analyzing the effects of perturbations on the response of rotating blades that are already at their steady-state condition and comparing the results with those of the accelerating blade analysis.
4. Generalizing the formulation of the nonlinear dynamics of rigid articulated rotating blades by considering the nonlinearly coupled flap and lag motions, hinge offset, and aerodynamic loads.
5. Combining the developed elastic model of the beam and the rigid body dynamics model in order to formulate the hinge boundary condition of an accelerating elastic articulated blade.

6. Linear and nonlinear statics and stress analysis of composite beams with embedded piezocomposite actuators.
7. Nonlinear dynamics of rotating composite blades with embedded piezocomposite actuators and analyzing the sensitivity of the response of such blades to excitations received from actuators located at various directions.

1.2 Literature Review

A comprehensive monograph on the subject of nonlinear behavior of composite beams is Hodges (2006). In this reference, the reasons why VAM is the optimal solution method and the advantages of using the 1-D intrinsic equations of beams have been discussed. It also includes a detailed review of the literature. The major topics, which are not covered in that reference, are the application of embedded actuators in beams and rotating blades and the way one can analyze complex boundary conditions. In what follows, a summary of other significant contributions to the subject is listed.

Danielson and Hodges (1987) and Atilgan and Hodges (1991) are among the earliest studies on the subject. They include the nonlinear beam kinematics that is valid for non-homogeneous, anisotropic beams undergoing large global rotation, small local rotation, and small strain.

A review of various boundary conditions imposed on helicopter blades can be found in Rosen et al. (1991). In this reference, many combinations of boundary conditions at the root of the blades, including those with springs and dampers, are discussed. The formulation is applicable to both linear and nonlinear problems, but it is valid only for isotropic materials.

In Berdichevsky et al. (1992), VAM is applied to the cross-sectional analysis of thin-walled closed anisotropic beams and results in a closed-form solution for the 4×4 stiffness matrices. The nonlinear 1-D intrinsic equations of a beam are used in Shang and Hodges (1995) in order to perform the stability analysis of a hingeless composite rotor blade in hover. The stability equations are obtained by imposing small time-dependent perturbations to the steady-state solutions and substituting the summation into the intrinsic equations of motion. Due to sparse coefficient matrices, the method is computationally efficient and has low memory requirements. The obtained numerical results are compared with available experimental data extracted from Sharpe (1986).

A revised and extended version of Shang and Hodges (1995) is Shang et al. (1999) in which it is shown that composite blades with appropriately chosen values of initial twist and curvature can exhibit significantly improved stability characteristics while simultaneously reducing steady-state loads. It is also shown that blades with positive pitch–flap coupling have increased stability margin and reduced structural load.

In Hodges et al. (1996), VAM is used in order to analyze initially curved and twisted composite beams. The resulting nonlinear equations are solved numerically for both the nonlinear static deformation and the linearized free vibration about the static equilibrium position. The results are compared with the available exact solutions for isotropic beams and the published experimental data for rotating isotropic and composite beams with swept tips, which are presented in Epps and Chandra (1996).

In Trabucho and Viãno (1996) and Buannic and Cartraud (2000, 2001), the formal asymptotic method (FAM) has been presented. This method was later generalized in Kim et al. (2008), and its results were compared with VAM. The results of the two methods have been shown to be close (Kim et al. 2008).

VABS was first introduced in Cesnik and Hodges (1997) where it has been applied to perform the cross-sectional analysis of composite box and I-beams with initial twist and curvature. It has been used for the computation of cross-sectional properties like stiffness matrix, principal axes, neutral axes, area centroid, mass centroid, and mass matrix.

At present, there are mainly two versions of VABS in use. A comparison of the capabilities of these two versions can be found in Ghorashi and Nitzsche (2007) and in Roy and Yu (2009a). One of these codes has been developed at Georgia Tech and University of Utah and is simply named VABS. Professor Wenbin Yu who is presently at Purdue University is maintaining it. The results of this code have been validated in Yu et al. (2002). In this reference, the VABS results for elliptical, channel, and triangular prism bars, as well as box and I-beams, are compared with other methods. It is shown how the classical solution loses its validity in the nonlinear range of behavior of composite members. Furthermore, it has been demonstrated that although VABS is restricted to beam applications, it provides a level of accuracy, which is comparable to that of standard 3-D FEM codes but with fewer computing and processing requirements. In Yu and Hodges (2004), the results of VABS are compared with those of 3-D elasticity. Identical results were reported for beams with elliptical and rectangular cross sections. Therefore, VABS can be used to avoid difficulties in dealing with 3-D elastic problems while providing results that are coincident with the exact solutions.

The other version is the University of Michigan version (UM/VABS) that has been released and maintained by Professor Carlos E.S. Cesnik. The success of the VAM as confirmed by 3-D elasticity FEM solutions and experimental results has led researchers to extend its application to smart beams with embedded active materials like active/macro fiber composites (AFC/MFC) (Cesnik and Palacios 2003; Palacios and Cesnik 2005, 2008). This extension has been included in UM/VABS and more recently in VABS (Roy et al. 2007). UM/VABS is used to analyze a beam with embedded actuators and to determine its sectional properties such as stiffness and mass matrices, the chordwise locations of the center of gravity, and the shear center. It can also provide the actuation forces, moments, and deformations induced by smart materials.

Recently, a third version of VABS, named YF/VABS, has been introduced and explained in Friedmann et al. (2009). It is based on coupling VAM and the work presented in Yuan and Friedmann (1995, 1998). The model has been validated by comparing the fundamental rotating natural frequencies, aeroelastic stability characteristics in hover, and vibratory hub loads in forward flight with other composite rotor blade analyses.

In Cesnik and Shin (1998), an asymptotic formulation for analyzing multi-cell composite helicopter rotor blades with integral anisotropic active plies is presented. It discusses both the cross-sectional and the 1-D analyses. The theory is applied to a two-cell thin-walled box beam as well as a single-cell airfoil-shaped cross section (NACA 0012). In Cesnik and Ortega-Morales (1999), the VAM's 2-D analysis is applied to include the effect of an embedded active element in the structure. An extended version of the same paper is Cesnik and Ortega-Morales (2001). In this paper, stiffness and actuation constants for an active box beam, an active NACA 0012 blade, Mach-scaled CH47-D active blade section, and the active twist rotor (ATR) prototype blade are calculated.

In Cesnik and Shin (2001a, b), piezocomposite actuators are added to the model and an asymptotic closed-form solution of the actuation force using Berdichevsky et al. (1992) method is presented. But since in Berdichevsky et al. (1992), the shell bending strains are neglected, incorrect stiffness constants for certain cross sections are reported in Cesnik and Shin (2001a, b) that also affected the active material modeling. This flaw is discussed in Volovoi and Hodges (2000, 2002) and Volovoi et al. (2001). In these references, an asymptotically correct theory for thin-walled beams is developed. It is demonstrated how neglecting the shell bending strains can lead to an overprediction of the torsional stiffness for certain cross sections by almost 100 %. It is also shown that contrary to a widespread belief during twisting *a cross section of a composite beam is not rigid in its own plane*.

In Roy et al. (2007), a classical model with piezoelectric materials is developed and the results are compared with UM/VABS and a 3-D FEM solution performed in ANSYS. As a continuation to that research, in Roy (2007) and Roy and Yu (2009a, b), a generalized Timoshenko model for a composite rod with embedded or attached piezoelectric materials is developed. The results of this electromechanical analysis are compared with those of the ANSYS's 3-D solution, and excellent agreement is reported.

The VABS programs can calculate 2-D asymptotically correct solutions for slender beams with embedded actuators and calculate sectional properties for solid, open, closed, and multi-cell thin-walled cross sections. The beams can be initially curved and twisted, been made of arbitrary material (isotropic or composite), and have no constraint on their cross-sectional geometry. Trapeze effect and embedded actuators can also be included in the analysis. Trapeze effect is a geometrically nonlinear phenomenon, and it deals with the variations of the torsional rigidity and the torsional natural frequency of rotor blades due to changes in their rotational speed that alter the axial force. Using VABS, the classical, generalized Timoshenko (for analyzing shear deformation) and generalized Vlasov (for analyzing thin-walled open-section beams) studies have been performed.

Traugott et al. (2005) presents the use of VAM and the nonlinear 1-D analysis in order to obtain the response of an active articulated rotor blade. The cross-sectional model with embedded actuators used in Traugott et al. (2005) is based on the model developed in Patil and Johnson (2005). The rigid body modes of the articulated blade are analyzed, and a multi-input and multi-output (MIMO) controller based on full-state optimal control and optimal state estimation is presented with the aim of enhancing the damping characteristics of the weakly damped system. No detail about the way the articulated blades and their boundary conditions are modeled is given.

The complex, unsteady aerodynamic environment near rotor blades in forward flight causes poor ride quality, high levels of vibration and noise, and low fatigue life of structural components. Higher harmonic control (HHC) and individual blade control (IBC) have been proposed to tackle these problems and to improve helicopter performance. The HHC is accomplished by manipulating a conventional swashplate to enable blade pitch control at a higher multiple frequency than integer multiple frequencies of the rotor rotational frequency (Molusis et al. 1983; Wood et al. 1985; Shaw et al. 1989). The IBC installs a feathering actuator in each blade rather than modulating the swashplate and permits blade pitch control at arbitrary frequencies (Ham 1987; Jacklin et al. 1995).

Figures 1.4 and 1.5 illustrate the NASA/Army/MIT ATR discussed in Shin et al. (2008). In this project, integral blade twist actuation to achieve helicopter vibration reduction has been implemented and a Mach-scaled fully active rotor system has been tested in a wind tunnel. Shin et al. (2008) presents a general framework for active rotor blade modeling. It includes 2-D cross-sectional, 1-D beam, and laminate stress recovery analyses. This blade structural model has then been combined with an aerodynamics model, and the resulting aeroelastic system has been solved in the frequency domain. The Comprehensive Analytical Model of Rotorcraft Aerodynamics and Dynamics (CAMRAD II) rotorcraft analysis software developed

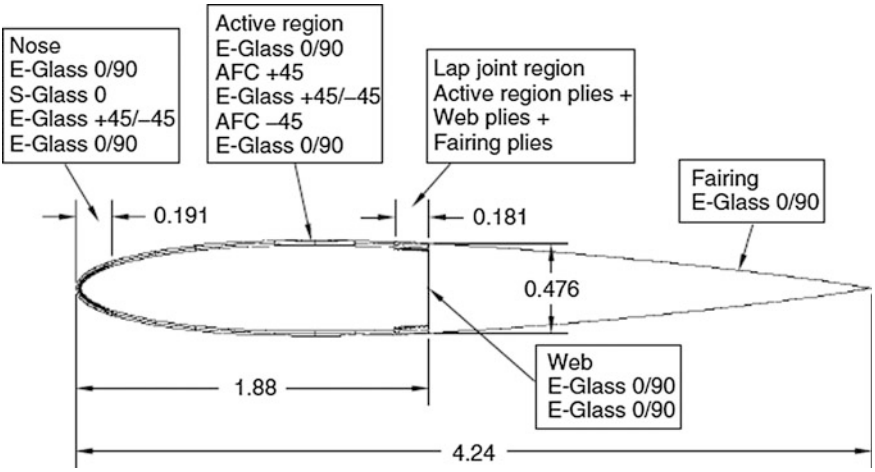

Fig. 1.4 Schematic diagram of the ATR blade section design. Dimensions are in inches (Shin et al. 2008), © SAGE Publications, reprinted with permission

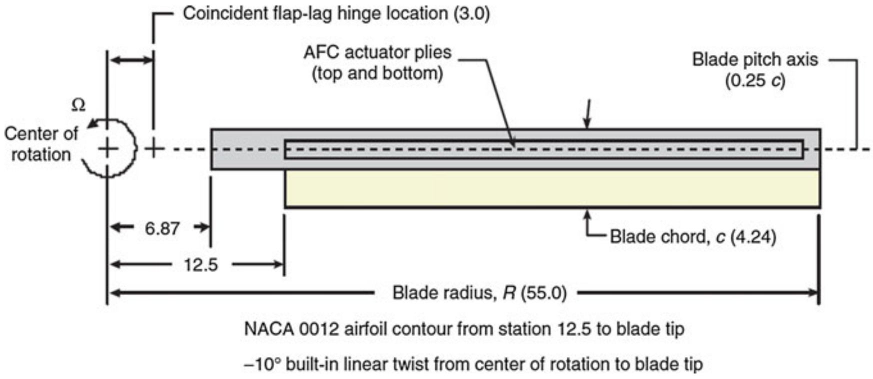

Fig. 1.5 ATR aeroelastically scaled model blade geometry. Dimensions are in inches (Shin et al. 2008), © SAGE Publications, reprinted with permission

by Dr. Wayne Johnson of Johnson Aeronautics has been used for preliminary study of the ATR concept in forward flight.

In ATR, a blade is integrally twisted by direct strain actuation which is accomplished by distributing embedded piezoelectric AFC along its span to twist it directly (Bent 1997). The AFC laminae are embedded in the blade structure at alternating ±45° orientation angles to maximize the twist actuation capabilities of the active plies. With an even number of AFC plies, it is also possible to keep the passive structure of the rotor blade elastically uncoupled. This enables actuation of blade torsional motion without applying either bending or axial actuation. In a modified version of ATR discussed in Park and Kim (2008) to alleviate the need of applying high voltages in the order of 4000 V peak to peak, as needed for the AFC actuators, MFC actuators introduced in Wilkie et al. (2000) have been used.

There are three comprehensive analysis tools for rotorcraft. The first is CAMRAD II, the second is the finite element-based multi-body dynamics code for the comprehensive modeling of flexible multi-body systems (DYMORE) that has been developed by *DYMORE Solutions*, and the third is the Rotorcraft Comprehensive Analysis System (RCAS). All three codes can take output from VABS as input and they all use the geometrically exact 1-D beam models.

DYMORE is used in Park et al. (2010) in order to investigate the whirl flutter stability. It has various multi-body element libraries of rigid/elastic joints as well as rigid bodies and elastic bodies such as beams, plates, and shells. The location, orientation, and connections of these multi-body elements should be specified to construct a complete DYMORE model. This powerful multi-body modeling capability allows for highly realistic modeling of rotorcrafts.

In Roy and Yu (2009a), the results of the generalized Timoshenko model with embedded or attached piezoelectric materials have been compared with those of UM/VABS. It has been observed that the two solutions deviate in cases that the percentage of the piezoelectric material is significant compared to the base non-piezoelectric material. The authors state that such deviation is due to stronger electromechanical coupling that can be handled by the fully coupled approach presented by them.

For the analysis of smart beams with piezoelectric sensors/actuators, two types of finite elements are presented in Neto et al. (2009). One is an ad hoc smart beam element (ADSBE), and the other is the variational asymptotic smart beam element (VASBE). The mathematical formulation of ADSBE uses a first-order displacement field and a piecewise, linear, through-the-thickness electric potential. For VASBE, the formulation allows decoupling of the original 3-D problem of the smart structure into a 1-D beam analysis and a 2-D coupled cross-sectional analysis. It has been observed that the VASBE model provides results that are closer to the ones published in the literature.

An asymptotically correct analysis of passive anisotropic thin-walled open cross section beamlike structures using VAM has been extended to include MFCs (Khouli et al. 2010). The developed linear 2-D cross-sectional theory is validated by comparing its results with those of UM/VABS. A thin-walled open cross section (TWOCS) model is used in the analysis for which the classic Vlasov theory is applicable. This theory, as explained in Gjelsvik (1981), relies on ad hoc kinematic assumptions that are based on engineering intuition and therefore lack in rigor. In this theory, strain measures of stretch, $\bar{\gamma}_{11}$, twist, κ_1, and mutual orthogonal bendings, κ_2 and κ_3, and the derivative of the twist strain measure, κ_1', are used.

In the context of the VAM, thin-walled slender beams have two inherent small parameters. The first is the slenderness ratio *a*/*L*, which is the ratio of the characteristic dimension of the cross section to the wavelength of the deformation mode. The second is the thinness ratio *h*/*a,* which is the ratio of the characteristic thickness of the wall to the characteristic dimension of the cross section. The existence of the inverse of the latter parameter in the asymptotically correct elastic displacement field has rigorously confirmed the importance of the Vlasov solution for TWOCS slender beams (Volovoi et al. 1999; Hodges and Volovoi 2000). The advantage of having two inherently small parameters, as in the thin-walled slender beam problem, is the possibility of arriving at an analytical closed-form solution for the asymptotically correct stiffness constants (Hodges and Volovoi 2000).

In Chakravarty (2010), SectionBuilder, an FEM-based tool for the analysis and design of composite rotor blade cross sections, has been introduced. The tool can create cross sections with parametric shapes and arbitrary configurations. It has the ability to generate single- and multi-cell cross sections with arbitrary layups.

The process of using advanced analytical tools for the design and analysis of composite rotor blade cross sections has been presented in Chakravarty (2010). In this process, the rotor blade cross-sectional geometry is defined in a CAD tool, CATIA, where the cross section is defined by areas with specified laminate material properties, and the areas are bounded by reference curves that define material orientation. This geometry is then exported to ANSYS and is used to create the analysis mesh and identify reference edges for all areas. Custom macros and a special-purpose C language code have been used to construct free meshes within each area. The results along with material properties are exported in the form of a

VABS input file. VABS is then run, and finally, ANSYS is used for postprocessing and visualization: Custom macros create a two-dimensional stress field in a cross-sectional layer (single element thick) to enable the user to visualize stress and strain over the cross section (Chakravarty 2010).

Recently, the range of problems for which VAM is used has considerably expanded. For example, this method has been applied for solving steady-state thermoelastic problems in composite beam structures (Wang and Yu 2011, 2013). In Lee and Yu (2011), modeling of composite beams with spanwise heterogeneity has been presented. In addition, the nonlinear normal modes of oscillations of beams have been derived from intrinsic equations (Palacios 2011).

In Freno and Cizmas (2011), the order of the nonlinear terms retained in the analysis is extended to the third order. Additionally, comparisons are made between the results of linear, quadratic, and cubic beam models. The authors mention that their beam model accurately calculates natural frequencies and linear and nonlinear responses. They conclude by saying that their results agree favorably with those obtained through FEM, while taking less time.

In Chakravarty (2011), the analyses of composite beam cross sections using VABS are compared with the corresponding boundary element method (BEM) solutions. While in VABS, meshing of the entire cross section is required, in BEM only a mesh of the boundary is needed. By using BEM, first the solution is obtained on the boundary, and then, it is calculated inside the domain. While VABS matrices are sparse and symmetric, the BEM matrices are fully populated and non-symmetric. The integrals to be calculated in the BEM are generally more difficult to evaluate, and some contain integrands that might be singular. The paper concludes by stating that VABS is a less computationally expensive method than BEM.

In Patil and Altoff (2011), a few models including a nonlinear steady-state solution, a linear dynamic perturbation solution about the calculated nonlinear steady state, and a nonlinear dynamic solution are presented.

Analysis of a tiltrotor (also called proprotor) aircraft has been presented in Park et al. (2011). A tiltrotor aircraft is a highly attractive and versatile vehicle since it has the capability of vertical take-off/landing and high-speed flight. The vehicle consists of three operation modes: helicopter mode, transition mode, and the airplane mode. The tiltrotor blade can function as a blade in the helicopter mode and as a propeller in the airplane mode. The difference in the inflows and rotor speeds between the helicopter and airplane operation modes requires that the tiltrotor has a low built-in twist for the helicopter mode but a high built-in twist for the airplane mode in order to have a good performance characteristic. Because of the conflicting requirements, in conventional design, the built-in twist often is determined from a compromise between the two built-in twist angles. Therefore, this conventional design is unable to guarantee the best performance in either operation mode.

One way for solving this problem is to take advantage of the anisotropic nature of fiber-reinforced composite materials. When a composite blade is elastically tailored in an appropriate manner, the extension and torsion behaviors may be coupled. In this way, the change of centrifugal forces due to different rotor speeds between the two operation modes is used to vary the built-in twist distribution

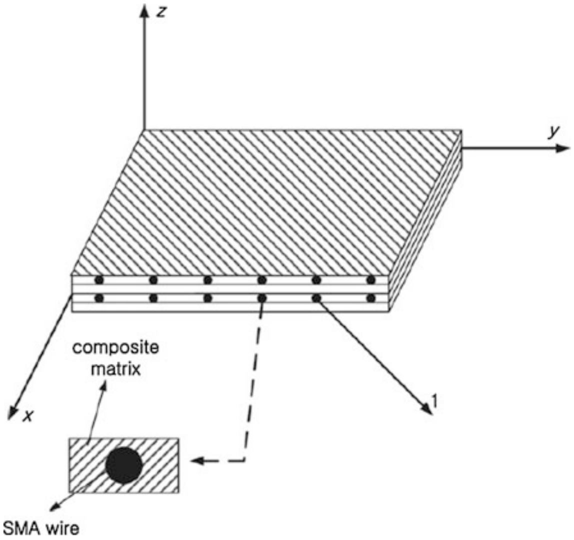

Fig. 1.6 SMA hybrid composite (SMAHC) (Park et al. 2011), © Elsevier Ltd., reprinted with permission

(Nixon 1988; Soykasap 1999; Ozbay et al. 2005). However, since this approach is based on a passive change, it is difficult to achieve the necessary build-in twist angles under different flight conditions. To overcome this drawback, in Prahlad and Chopra (2001), a variable-twist tiltrotor is obtained by the introduction of shape memory alloy (SMA) wires in the blade structure. Since SMA can produce large strain at low actuator frequency, it is mostly suitable for structural shape control rather than vibration and noise control.

Figures 1.6 and 1.7 show an SMA hybrid composite (SMAHC), which consists of SMA wires, embedded in a composite matrix. In Park et al. (2011), the SMAHC has been used as actuator for built-in twist control of a variable-twist tiltrotor. The optimal design framework consists of the following numerical tools: UM/VABS, an automated mesh generator described in Brown (2003), the nonlinear flexible multi-body dynamics analysis code, DYMORE, which has simple aerodynamic models and can be used to calculate the rotating frequencies of the tiltrotor blade, a MATLAB-based 3-D strain analysis module to investigate the structural integrity of the blade, and a gradient-based constrained nonlinear optimizer provided by MATLAB’s optimization tool box (using the ‘fmincon’ command). In Park et al. (2011), all of these tools are explained and integrated using MATLAB. This optimization framework is an extension of Park and Shin (2007), where the twist performance of an ATR has been maximized using MFCs.

A geometrically exact beam theory (GEBT) and a general-purpose tool for nonlinear analysis of slender composite structures are developed in Yu and Blair (2012). Coupled with VABS, GEBT can analyze geometrically nonlinear slender structures having any cross sections and made of arbitrary materials. GEBT has been used for analyzing rotating blades and to perform steady-state response and eigenvalue analyses. It can be downloaded from the Web site AnalySwift.com.

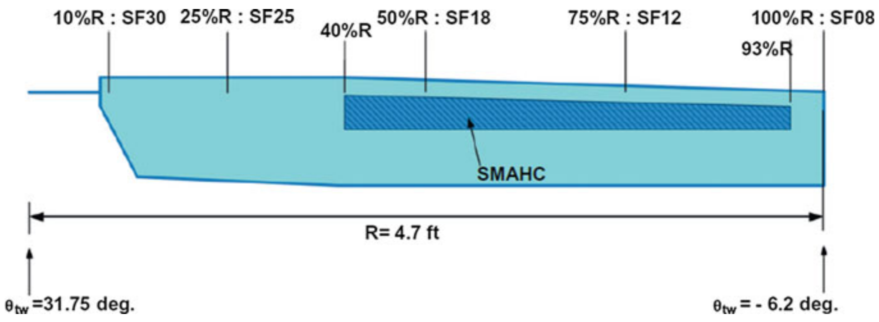

Fig. 1.7 Planform configuration of the variable-twist tiltrotor using SMAHC (Park et al. 2011), © Elsevier Ltd., reprinted with permission

In the VAM approach, as mentioned in Kollár and Pluzsik (2012), the 1-D displacement field is perturbed by an unknown 3-D warping field, *w*. Minimizing the total strain energy of the cross section provides the warping function. Then, an anisotropic beam theory that takes the effects of torsional warping shear deformation into consideration is developed. It is shown that the outcome of this theory is compatible with ANSYS, but the VABS results are far since VABS does not consider the restrained warping-induced shear deformations in calculations. The authors present a new method to determine stiffnesses of anisotropic beams without assuming kinematical relationships. The applied theory contains the restrained torsional warping (Vlasov theory), the in-plane shear deformations (Timoshenko theory), and the torsional warping shear deformations.

In Rajagopal et al. (2012), VAM is used to develop a beam theory for planar deformation of isotropic strips with initial in-plane curvature. Comparison shows that variation of cross-sectional stiffness versus initial curvature obtained from VABS 3.3 is in error. Corrections embodied in the newer edition, VABS 3.4, capture the correct behavior.

A beam theory for analyzing the in-plane deformation of an initially curved laminated strip beam has been proposed in Rajagopal and Hodges (2012). The validity of this theory is limited to laminates whose in-plane and out-of-plane deformations are decoupled (i.e., vanishing of matrix *B* in the classical lamination plate theory). This is most common in the case of symmetric layup configurations. This work serves as a validation tool for VABS and provides analytical expressions for the stiffness matrix and stress–strain recovery, a rarity for composite structures.

In Yu et al. (2012), recent updates to VABS are introduced. The first update is a modification of the warping constraints and torsional deformation. The second one incorporates applied loads into the cross-sectional analysis. Finally, the third update improves the energy transformation into generalized Timoshenko form. Examples are presented to demonstrate that the updated energy transformation may yield significantly different stiffness predictions from previous versions of VABS and to show that the updated version is more accurate.

A geometrically nonlinear cross-sectional analysis of certain composite beam-based four-bar mechanisms is presented in Pollayi and Harursampath (2012). The component bars of the mechanisms are made of fiber-reinforced laminates. They could, in general, be pretwisted and/or possess initial curvature, either by design or by defect. The only restriction in the analysis is that the strains within each elastic body (beam) remain small.

Another extension to the analysis of a four-bar mechanism is presented in Pollayi et al. (2013) where the component laminate load-carrying capacity, i.e., the load that causes the failure of individual layers and the component laminate as a whole, is evaluated. Calculation of the load-carrying capacity is performed by the use of the Tsai–Wu–Hahn failure criterion for various layups.

A helicopter rotor or the rotor system of a wind turbine operates in a highly dynamic and unsteady environment leading to severe vibratory loads present in the system. Repeated exposure to this loading condition can induce damage in the composite rotor blades. Pollayi and Yu (2014) deal with the first damage mode (i.e., matrix micro-cracking) in helicopter rotor or wind turbine blades and explain how this phenomenon affects the overall cross-sectional stiffness.

The 1-D and 3-D methods for modeling helicopter rotor blade structural dynamics are presented in Truong et al. (2013), and the accuracy of the 1-D structural models is evaluated. Natural frequencies are calculated at various rotor angular velocities and for a large variety of blades ranging from simple isotropic beams to realistic composite blades. The 1-D beam analysis is conducted using RCAS with 2-D cross-sectional properties calculated from VABS and 3-D FEM results obtained using MSC/Marc. When there is no coupling between modes of different nature (e.g., flap and torsion) and the blade length is greater than ten times the chord, very good agreement between the 1-D and the 3-D predictions for the first eight modes of a large variety of blades is observed. With the presence of flap–torsion coupling between the modes due to the composite material layup, the two approaches provide different values for the torsion-dominated and the flap-dominated modes.

Modern rotor blades have begun to depart from the simple straight planform by incorporating tip sweep and taper (Truong et al. 2013). The aim of such a deviation from the classical rectangular shape has been to reduce the noise generated by blades as demonstrated in the ‘ERATO’ blade (Prieur and Splettstoesser 1999; Truong 2005). The blade has been developed jointly by DLR (German Aerospace Center) and ONERA (Office National d’Etudes et de Recherches Aérospatiale). EUROCOPTER and ONERA created the ‘Blue Edge’ blade for the same purpose (Rauch et al. 2011).

The US Army Aero Flight Dynamics Directive (AFDD) and the French ONERA conducted research to investigate the differences between a 1-D beam model approach and a 3-D FEM approach (Truong et al. 2013). The objective of this effort was to better understand the accuracy of current rotor blade structural modeling and identify the level of sophistication required to model modern rotor blades, i.e., to determine when the use of 3-D methodology will be necessary. In this paper, authors summarize the key results obtained in Truong et al. (2010) and Yeo et al.

(2010) on the comparison of using 1-D and 3-D methods to analyze blades with rectangular planform shape and with various lengths.

While, for decades, there have been many investigations on nonlinear effects in the helicopter society, it is a relatively new focus area in the wind turbine society. However, since wind turbine blades are getting larger and more flexible, higher nonlinear behavior of wind turbines is expected. The nonlinear behavior of wind turbine blades is considered in Kim et al. (2013).

Effects of multiple engine placement on aeroelastic trim and flutter characteristics of a backswept flying wing resembling the HORTEN IV are investigated in Mardanpour et al. (2014), using the code Nonlinear Aeroelastic Trim And Stability of HALE Aircraft (NATASHA). NATASHA is based on the geometrically exact formulation of the composite beam theory of Hodges (2006) and the finite state inflow aerodynamic model of Peters et al. (1995). The governing equations for structural model are geometrically exact, fully intrinsic, and capable of analyzing the dynamical behavior of a general, non-uniform, twisted, curved, and anisotropic beam undergoing large deformations. The partial differential equations' dependence on the axial direction coordinate is approximated by central differences, as presented in Patil and Hodges (2006). The resulting nonlinear ordinary differential equations are linearized about a static equilibrium state. The equilibrium state is governed by nonlinear algebraic equations, which NATASHA solves to obtain the steady-state trim solution using the Newton–Raphson algorithm (Patil and Hodges 2006). This system of nonlinear aeroelastic equations, when linearized about the resulting trim state, leads to a standard eigenvalue problem that NATASHA uses to analyze the stability of the structure. NATASHA is also capable of time-marching the nonlinear aeroelastic system of equations using a schedule of the flight controls, which may be obtained from sequential trim solutions.

Finally, a few solutions for the 1-D intrinsic equations of a beam are presented in Shang and Hodges (1995), Cesnik and Shin (1998), and Cesnik et al. (2001). These solutions operate in two steps. The first is to calculate the steady-state response. Then, in the second step, the steady-state solution is perturbed and motion about the obtained steady-state position is calculated by solving the perturbed steady-state equations for small perturbations of the dependent variables. This perturbed steady-state solution is, of course, valid in the vicinity of the steady-state response. An alternative solution is to calculate the whole dynamics of the rotating blade, including its start from static equilibrium, acceleration to full speed, and even experiencing some perturbations afterward, as will be explained in Chaps. 5 and 6.

References

Atilgan, A. R., & Hodges, D. H. (1991). A unified nonlinear analysis for non-homogeneous, anisotropic beams with closed cross-sections. *AIAA Journal, 29*, 1990–1999.

Bauchau, O. A., & Hodges, D. H. (1999). Analysis of nonlinear multibody systems with elastic couplings. *Multibody System Dynamics, 3*, 163–188.

Bent, A. A. (1997). *Active fiber composites for structural actuation*. Ph.D. Thesis, Department of Aeronautics and Astronautics, Massachusetts Institute of Technology.

Berdichevsky, V. L. (1981). On the energy of an elastic rod. *Prikladnaya Matematika i Mekhanika, 45*, 518–529.

Berdichevsky, V. L., Armanios, E. A., & Badir, A. M. (1992). Theory of anisotropic thin-walled closed cross-section beams. *Composite Engineering, 2*, 411–432.

Brown, E. L. (2003). *Integrated strain actuation in aircraft with highly flexible composite wings*. Ph.D. Thesis, Department of Aeronautics and Astronautics, Massachusetts Institute of Technology.

Buannic, N., & Cartraud, P. (2000). Higher-order asymptotic model for a heterogeneous beam, including corrections due to end effects. In *Proceedings of the 41st AIAA/ASME/ASCE/AHS/ASC Structures, Structural Dynamics, and Material Conference and Exhibit*, Atlanta, GA, USA. Paper No.: AIAA-2000-1495.

Buannic, N., & Cartraud, P. (2001). Higher-order effective modeling of periodic heterogeneous beams. I. Asymptotic expansion method. *International Journal of Solids and Structures, 38*, 7139–7161.

Cesnik, C. E. S., & Hodges, D. H. (1997). VABS: A new concept for composite rotor blade cross-sectional modeling. *Journal of the American Helicopter Society*, pp. 27–38.

Cesnik, C. E. S., & Ortega-Morales, M. (1999). Active composite beam cross-sectional modeling—stiffness and active force constraints. In *Proceedings of the 40th AIAA/ASCE/AHS/ASC Structures, Structural Dynamics, and Materials Conference*, 12–15 April, 1999, St. Louis, Missouri. Paper No.: AIAA-99-1548.

Cesnik, C. E. S., & Ortega-Morales, M. (2001). Active beam cross-sectional modeling. *Journal of Intelligent Material Systems and Structures, 12*, 483–496.

Cesnik, C. E. S., & Palacios, R. (2003). Modeling piezocomposite actuators embedded in slender structures. In *Proceedings of the 44th AIAA/ASME/ASCE/AHS Structures, Structural Dynamics, and Materials Conference*, 7–10 April, 2003, Norfolk, Virginia. Paper No.: AIAA 2003-1803.

Cesnik, C. E. S., & Shin, S.J. (1998). Structural analysis for designing rotor blades with integral actuators. In *Proceedings of the 39th AIAA/ASME/ASCE/ASC Structures, Structural Dynamics, and Materials Conference*, 20–23 April, 1998, Long Beach, CA. Paper No.: AIAA-98-2107.

Cesnik, C. E. S., & Shin, S. J. (2001a). On the modeling of integrally actuated helicopter blades. *International Journal of Solids and Structures, 38*, 1765–1789.

Cesnik, C. E. S., & Shin, S. J. (2001b). On the twist performance of a multiple-cell active helicopter blade. *Smart Materials and Structures, 10*, 53–61.

Cesnik, C. E. S., Shin, S. J., & Wilbur, M. L. (2001). Dynamic response of active twist rotor blades. *Smart Materials and Structures, 10*, 62–76.

Chakravarty, U. K. (2010). SectionBuilder: An innovative finite element tool for analysis and design of composite rotor blade cross-sections. *Composite Structures, 92*, 284–294.

Chakravarty, U. K. (2011). On the modeling of composite beam cross-sections. *Composites: Part B*, *42*, 982–991.

Chen, H., Yu, W., & Capellaro, M. (2010). A critical assessment of computer tools for calculating composite wind turbine blade properties. *Wind Energy, 13*, 497–516.

Danielson, D. A., & Hodges, D. H. (1987). Nonlinear beam kinematics by decomposition of the rotation tensor. *Journal of Applied Mechanics, 54*, 258–262.

Epps, J. J., & Chandra, R. (1996). The natural frequencies of rotating composite beams with tip sweep. *Journal of the American Helicopter Society, 41*, 29–36.

Freno, B. A., & Cizmas, P. G. A. (2011). A computationally efficient non-linear beam model. *International Journal of Non-Linear Mechanics, 46*, 854–869.

Friedmann, P. P., Glaz, B., & Palacios, R. (2009). A moderate deflection composite helicopter rotor blade model with an improved cross-sectional analysis. *International Journal of Solids and Structures, 46*, 2186–2200.

Ghorashi, M. (2009). *Dynamics of elastic nonlinear rotating composite beams with embedded actuators.* Ph.D. Thesis, Mechanical and Aerospace Engineering Department, Carleton University.

Ghorashi, M. (2012). Nonlinear analysis of the dynamics of articulated composite rotor blades. *Nonlinear Dynamics*, *67*, 227–249.

Ghorashi, M., & Nitzsche, F. (2007). Comparison of the variational asymptotic beam sectional analysis methods applied to composite beams. In *Proceedings of the 18th International Conference of Adaptive Structures and Technologies*, Ottawa, Canada, 3–5 October, 2007.

Ghorashi, M., & Nitzsche, F. (2008). Steady-state nonlinear dynamic response of a composite rotor blade using implicit integration of intrinsic equations of a beam. *International Review of Aerospace Engineering*, *1*, 225–233.

Ghorashi, M., & Nitzsche, F. (2009). Nonlinear dynamic response of an accelerating composite rotor blade using perturbations. *Journal of Mechanics of Materials and Structures*, *4*, 693–718.

Gjelsvik, A. (1981). *The Theory of Thin-Walled Bars*. New York: John Wiley & Sons.

Ham, N. D. (1987). Helicopter individual-blade-control research at MIT 1977-1985. *Vertica, 11*, 109–122.

Hodges, D. H. (2006). *Nonlinear composite beam theory*. New York: AIAA.

Hodges, D. H., Shang, X., & Cesnik, C. E. S. (1996). Finite element solution of nonlinear intrinsic equations for curved composite beams. *Journal of the American Helicopter Society*, pp. 313–321.

Hodges, D. H., & Volovoi, V. V. (2000). Theory of anisotropic thin-walled beams. *Journal of Applied Mechanics, 67*, 453–459.

Hopkins, A. S., & Ormiston, R. A. (2003). An examination of selected problems in rotor blade structural mechanics and dynamics. In *Proceedings of the American Helicopter Society 59th Annual Forum,* Phoenix, Arizona.

Jacklin, S. A., Blaas, A., Teves, D., & Kube, R. (1995). Reduction of helicopter BVI noise, vibration and power consumption through individual blade control. In *Proceedings of the American Helicopter Society 51st Annual Forum*, Fort Worth, TX.

Jian, Z., & Jinwu, X. (2009). Nonlinear aeroelastic response of high-aspect-ratio flexible wings. *Chinese Journal of Aeronautics, 22*, 355–363.

Jung, S. N., Nagaraj, V. T., & Chopra, I. (2002). Refined structural model for thin-and thick-walled composite rotor blades. *AIAA Journal, 40*, 105–116.

Khouli, F., Griffiths, J., Afagh, F. F., & Langlois, R. G. (2010). Actuation of slender thin-wall anisotropic open cross-section beams based on asymptotically correct Vlasov theory. *Journal of Intelligent Material Systems and Structures, 21*, 529–540.

Kim, J.-S., Cho, M., & Smith, E. C. (2008). An asymptotic analysis of composite beams with kinematically corrected end effects. *International Journal of Solids and Structures, 45*, 1954–1977.

Kim, T., Hansen, A. M., & Branner, K. (2013). Development of an anisotropic beam finite element for composite wind turbine blades in multibody system. *Renewable Energy, 59*, 172–183.

Kollár, L. P., & Pluzsik, A. (2012). Bending and torsion of composite beams (torsional-warping shear deformation theory). *Journal of Reinforced Plastics and Composites, 31*, 441–480.

Lee, C.-Y., & Yu, W. (2011). Variational asymptotic modeling of composite beams with spanwise heterogeneity. *Computers and Structures, 89*, 1503–1511.

Mardanpour, P., Richards, P. W., Nabipour, O., & Hodges, D. H. (2014). Effect of multiple engine placement on aeroelastic trim and stability of flying wing aircraft. *Journal of Fluids and Structures, 44*, 67–86.

Molusis, J. A., Hammond, C. E., & Cline, J. H. (1983). A unified approach to the optimal design of adaptive and gain scheduled controllers to achieve minimum helicopter rotor vibration. *Journal of the American Helicopter Society, 28*, 9–18.

Neto, M. A., Yu, W., & Roy, S. (2009). Two finite elements for general composite beams with piezoelectric actuators and sensors. *Finite Elements in Analysis and Design, 45*, 295–304.

Nixon, M. W. (1988). *Improvements to Tilt Rotor Performance through Passive Blade Twist Control.* NASA TM-100583.

Ozbay, S., Bauchau, O. A., Dancila, D. S., & Armanios, E. A. (2005) Extension-twist coupling optimization in composite rotor blades. In *Proceedings of the 46th AIAA/ASCE/AHS/ASC Structures, Structural Dynamics and Materials Conference*, Austin, TX.

Pai, P. F. (2014). High-fidelity sectional analysis of warping functions, stiffness values and wave properties of beams. *Engineering Structures, 67*, 77–95.

Palacios, R. (2005). *Asymptotic models of integrally-strained slender structures for high-fidelity nonlinear aeroelastic analysis*. Ph.D. Thesis, University of Michigan.

Palacios, R. (2011). Nonlinear normal modes in an intrinsic theory of anisotropic beams. *Journal of Sound and Vibration, 330*, 1772–1792.

Palacios, R., & Cesnik, C. E. S. (2005). Cross-sectional analysis of non-homogeneous anisotropic active slender structures. *AIAA Journal, 43*, 2624–2638.

Palacios, R., & Cesnik, C. E. S. (2008). On the one-dimensional modeling of camber bending deformations in active anisotropic slender structures. *International Journal of Solids and Structures, 45*, 2097–2116.

Park, J.-S., Jung, S.N., Lee, M.-K., & Kim, J. M. (2010). Design optimization framework for tiltrotor composite wings considering whirl flutter stability. *Composites: Part B*, *41*, 257–267.

Park, J.-S., & Kim, J.-H. (2008). Design and aeroelastic analysis of active twist rotor blades incorporating single crystal macro fiber composite actuators. *Composites: Part B*, *39*, 1011–1025.

Park, J.-S., Kim, S.-H., & Jung, S. N. (2011). Optimal design of a variable-twist proprotor incorporating shape memory alloy hybrid composites. *Composite Structures, 93*, 2288–2298.

Park, J.-S., & Shin, S. J. (2007). Preliminary design optimization on active twist rotor blades incorporating single crystal macro fiber composites. In *Proceedings of the American Helicopter Society 63rd Annual Forum*, Virginia Beach, VA.

Park, Y.-B., & Yang, D.-Y. (2007). Analysis of torsional deformation by rigid-plastic finite element method using recurrent boundary conditions. *Journal of Materials Processing Technology, 182*, 303–311.

Patil, M. J., & Althoff, M. (2011). Energy-consistent, Galerkin approach for the nonlinear dynamics of beams using intrinsic equations. *Journal of Vibration and Control, 17*, 1748–1758.

Patil, M. J., & Hodges, D. H. (2006). Flight dynamics of highly flexible wings. *Journal of Aircraft*, *43*, 1790–1799.

Patil, M. J., & Johnson, E. R. (2005). Cross-sectional analysis of anisotropic, thin-walled, closed-section beams with embedded strain actuation. In *Proceedings of the 46th AIAA/ASME/ASCE/AHS/ASC Structures, Structural Dynamics & Materials Conference*, 18–21 April, 2005, Austin, Texas. Paper No.: AIAA 2005-2037.

Peters, D. A., Karunamoorthy, S., & Cao, W.-M. (1995). Finite state induced flow models: part 1: Two dimensional thin airfoil. *Journal of Aircraft, 32*, 313–322.

Pollayi, H., & Harursampath, D. (2012). Geometrically non-linear dynamics of composite four-bar mechanisms. *International Journal of Non-Linear Mechanics, 47*, 837–850.

Pollayi, H., Harursampath, D., & Yu, W. (2013). Evaluation of strength of component-laminates in strip-based mechanisms. *Composite Structures, 100*, 1–16.

Pollayi, H., & Yu, W. (2014). Modeling matrix cracking in composite rotor blades within VABS framework. *Composite Structures, 110*, 62–76.

Prahlad, H., Chopra, I. (2001). Design of a variable twist tiltrotor blade using shape memory alloy actuators. In *Proceedings of SPIE__The International Society for Optical Engineering*.

Prieur, J., & Splettstoesser, W. R. (1999). An ONERA-DLR cooperative programme on aeroacoustic rotor optimization. In *Proceedings of the 25th European Rotorcraft Forum*, Rome, Italy, 14–16 September, 1999.

Rajagopal, A., & Hodges, D. H. (2012). Analytical beam theory for the in-plane deformation of a composite strip with in-plane curvature. *Composite Structures, 94*, 3793–3798.

Rajagopal, A., Hodges, D. H., & Yu, W. (2012). Asymptotic beam theory for planar deformation of initially curved isotropic strips. *Thin-Walled Structures, 50*, 106–115.

Rauch, P., Gervais, M., Cranga, P., Baud, A., Hirsch, J.-F., Walter, A., & Beaumier, P. (2011). Blue edge: The design, development and testing of a new blade concept. In *Proceedings of the American Helicopter Society 67th Annual Forum*, Virginia Beach, VA, 3–5 May, 2011.

Rosen, A., Loewy, R. G., & Mathew, M. B. (1991). Unified treatment for dealing with auxiliary conditions in blade dynamics. *AIAA Journal, 29*(6), 968–976.

Roy, S. (2007). *A variational asymptotic methodology of smart slender structure modeling*. Ph.D. Thesis, Mechanical and Aerospace Engineering. Utah State University.

Roy, S., & Yu, W. (2009a). A coupled Timoshenko model for smart slender structures. *International Journal of Solids and Structures, 46*, 2547–2555.

Roy, S., & Yu, W. (2009b). Dimensional reduction of a piezoelectric composite rod. *European Journal of Mechanics A/Solids*, *28*, 368–376.

Roy, S., Yu, W., & Han, D. (2007). An asymptotically correct classical model for smart beams. *International Journal of Solids and Structures, 44*, 8424–8439.

Shang, X., & Hodges, D. H. (1995). Aeroelastic stability of composite rotor blades in hover. In *Proceedings of the 36th Structures, Structural Dynamics and Materials Conference*, New Orleans. Paper No: AIAA-95-1453-CP.

Shang, X., Hodges, D. H., & Peters, D. A. (1999). Aeroelastic stability of composite hingeless rotors in hover with finite-state unsteady aerodynamics. *Journal of the American Helicopter Society*, pp. 206–221.

Sharpe, D. L. (1986). An experimental investigation of the flap-lag-torsion aeroelastic stability of a small-scale hingeless helicopter rotor in hover. NASA, TP-2546.

Shaw, J., Albion, N., Hanker, E. J., & Teal, R. S. (1989). Higher harmonic control: wind tunnel demonstration of a fully effective vibratory hub force suppression. *Journal of the American Helicopter Society, 31*, 14–25.

Shin, S. J., Cesnik, C. E. S., Wilkie, W. K., & Wilbur, M. L. (2008). Design and manufacturing of a model-scale active twist rotor prototype blade. *Journal of Intelligent Material Systems and Structures, 19*, 1443–1456.

Soykasap, O. (1999). *Aeroelastic optimization of a composite tilt rotor*. Ph.D. Thesis, School of Aerospace Engineering, Georgia Institute of Technology.

Trabucho, L., & Viãno, J. M. (1996). Mathematical modeling of rods. In P. G. Ciarlet & J. L. Lions (Eds.), *Handbook of Numerical Analysis* (Vol. 4). Amsterdam: North-Holland.

Traugott, J. P., Patil, M. J., & Holzapfel, F. (2005). Nonlinear dynamics and control of integrally actuated helicopter blades. In *Proceedings of the 46th AIAA/ASME/ASCE/ AHS/ASC Structures, Structural Dynamics and Materials Conference*, 18–21 April, 2005, Austin, Texas. Paper No: AIAA 2005-2271.

Truong, V. K. (2005). Dynamics studies of the ERATO blade, based on finite element analysis. In *Proceedings of the 31st European Rotorcraft Forum*, Florence, Italy, 13–15 September, 2005.

Truong, V. K., Yeo, H., & Ormiston, R. A. (2010). Investigation of finite element approaches for rotor blade structural dynamics. In *Proceedings of the 36th European Rotorcraft Forum*, Paris, France, 7–9 September, 2010.

Truong, V. K., Yeo, H., & Ormiston, R. A. (2013). Structural dynamics modeling of rectangular rotor blades. *Aerospace Science and Technology, 30*, 293–305.

Volovoi, V. V., & Hodges, D. H. (2002). Single- and multi-celled composite thin-walled beams. *AIAA Journal, 40*, 960–965.

Volovoi, V. V., Hodges, D. H., Berdichevsky, V. L., & Sutyrin, V. G. (1999). Asymptotic theory for static behavior of elastic anisotropic I-beams. *International Journal of Solids and Structures, 36*, 1017–1043.

Volovoi, V. V., Hodges, D. H., Cesnik, C. E. S., & Popescu, B. (2001). Assessment of beam modeling methods for rotor blade application. *Mathematical and Computer Modeling, 33*, 1099–1112.

Wang, Q., & Yu, W. (2011). Variational-asymptotic modeling of the thermoelastic behavior of composite beams. *Composite Structures, 93*, 2330–2339.

Wang, Q., & Yu, W. (2013). A refined model for thermoelastic analysis of initially curved and twisted composites beams. *Engineering Structures, 48*, 233–244.

Wilkie, W. K., Bryant, R. G., High, J. W., Fox, R.L., Hellbaum, R.F., & Jalink, A., Jr. (2000). Low-cost piezocomposite actuator for structural control applications. In *Proceedings of SPIE 7th Annual International Symposium on Smart Structures and Materials*.

Wood, E. R., Powers, R. W., Cline, J. H., & Hammond, C. E. (1985). On the developing and flight testing a higher harmonic control system. *Journal of the American Helicopter Society, 30*, 3–20.

Yeo, H., Truong, V. K., & Ormiston, R. A. (2010). Assessment of 1-D versus 3-D methods for modeling rotor blade structural dynamics. In *Proceedings of the 51st AIAA/ASME/ASCE/AHS/ASC Structures, Structural Dynamics, and Materials Conference*, Orlando, FL. 12–15 April, 2010.

Yu, W., & Blair, M. (2012). GEBT: A general-purpose nonlinear analysis tool for composite beams. *Composite Structures, 94*, 2677–2689.

Yu, W., & Hodges, D. H. (2004). Elasticity solutions versus asymptotic sectional analysis of homogeneous, isotropic, prismatic beams. *Journal of Applied Mechanics, 71*, 15–23.

Yu, W., Hodges, D. H., & Ho, J. C. (2012). Variational asymptotic beam sectional analysis—an updated version. *International Journal of Engineering Science, 59*, 40–64.

Yu, W., Volovoi, V. V., Hodges, D. H., & Hong, X. (2002). Validation of the variational asymptotic beam sectional analysis. *AIAA Journal, 40*, 2105–2112.

Yuan, K.A., & Friedmann, P. P. (1995). *Aeroelasticity and Structural Optimization of Composite Helicopter Rotor Blades with Swept Tips.* NASA CR 4665.

Yuan, K. A., & Friedmann, P. P. (1998). Structural optimization for vibratory loads reduction of composite helicopter rotor blades with advanced geometry tips. *Journal of the American Helicopter Society, 43*, 246–256.

Chapter 2
Review of the Variational Asymptotic Method and the Intrinsic Equations of a Beam

2.1 Introduction

Helicopter rotor blades can be adequately modeled as thin-walled composite beams, which are laterally flexible and, as such, usually operate in the nonlinear range. To solve such problems, one method is to use conventional beam models that rely on ad hoc assumptions on displacement or stress fields. An example of such models is the Saint-Venant's theory of torsion, which assumes that a beam remains rigid in its cross section as it twists. While this assumption works fine in the linear range of behavior for isotropic prismatic beams, it results in serious error when it is extended to composite beams. Therefore, to get acceptable results, one should use alternative solution methods.

A very promising alternative that is mentioned in Chap. 1 is VAM. It is a powerful method for solving problems of composite thin-walled beams and is free from ad hoc assumptions. The applicability of VAM in elasticity is because the elasticity problem can be stated as obtaining the stationary points of the energy functional. VAM simplifies the procedure for finding these stationary points of the energy functional when this functional depends on one or more inherently small parameters. It is therefore the right tool for building accurate models for dimensionally reducible structures (e.g., beams, plates and shells), Hodges (2006). VAM has both the merits of variational methods (viz., systematic and easily implementable numerically) and asymptotic methods (viz., without ad hoc assumptions), Roy and Yu (2009).

VAM splits the 3-D geometrically nonlinear elasticity problem into a 2-D analysis and a nonlinear 1-D analysis along the beam. The 2-D analysis is aimed at determining the cross-sectional stiffness and inertia matrices as well as the warping functions. It requires details of the cross-sectional geometry, elastic properties of materials and material densities and can be performed by VABS. The results of this analysis are used in all further 3-D analyses without the need to repeat such a 2-D analysis over again.

M. Ghorashi, *Statics and Rotational Dynamics of Composite Beams*,
DOI 10.1007/978-3-319-14959-2_2

The necessary conditions for achieving a linear cross-sectional analysis from the starting point of the geometrically nonlinear 3-D elasticity include small strain, linearly elastic material, and the smallness of a relative to l and R ($a \ll 1$). Here, a is a typical cross-sectional dimension, l is the wavelength of deformation along the beam axis, and R is the characteristic radius of initial curvature and twist (Hodges 2006).

The solution of the 1-D problem is obtained by utilizing the outcome of the 2-D cross-sectional analysis and by solving the nonlinear intrinsic differential equations of motion of the beam. Combining these two solutions provides the complete 3-D structural solution by recovering the 3-D stress, strain, and displacement fields.

2.2 Classification of Beams

2.2.1 Class T Beams

These are thin-walled beams with open cross sections, as seen in Fig. 2.1. If the wall thickness is h and the main characteristic length within the cross-sectional plane is a, then $a \gg h$. For class T beams, the torsional stiffness of the beam is considerably less than either of the two bending stiffnesses, and hence, the beam is torsionally soft. Such open section beams can be analyzed using the generalized Vlasov model.

2.2.2 Class S Beams

Figure 2.2 illustrates two examples of class S beams. These are strip-like beams that are soft in torsion, and soft in bending in one direction. Therefore, one bending stiffness is significantly larger than the other one and the torsional stiffness. Examples include high-aspect-ratio wings and helicopter blades.

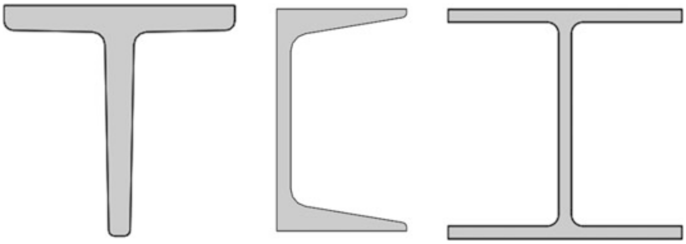

Fig. 2.1 Example cross sections of class T beams

Fig. 2.2 Example cross sections of class S beams

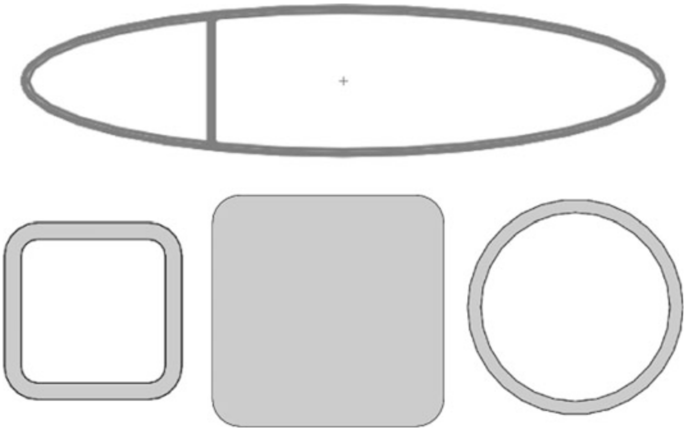

Fig. 2.3 Example cross sections of class R beams

2.2.3 *Class R Beams*

These are called regular beams. They are not class T or class S beams and may have solid or hollow sections that are closed (or closed cell) and are thin-walled. A few examples of class R beams can be seen in Fig. 2.3.

2.3 Cross-Sectional Modeling Using VAM

Accurate determination of the cross-sectional elastic constants of composite beams requires the presence of two distinct characteristics, Hodges (2006):

1. The theory behind the cross-sectional analysis must allow for elastic coupling in the 3-D material constants.
2. All six components of strain and stress and all possible components of displacement must be allowed, both in and out of the cross-sectional plane.

As seen in Fig. 2.4, two Cartesian coordinate systems are set up: the b-frame of the undeformed beam and the B-frame of the deformed beam. The origin of the undeformed system is usually put at the shear center (elastic center) of the cross section so that shear forces do not produce any twisting moments. Shear center of a cross section is a point in the cross section at which a shear force induces no twist.

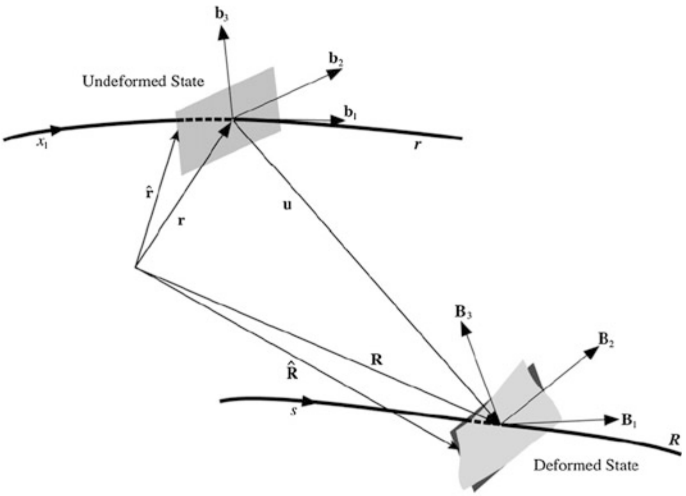

Fig. 2.4 Frames and reference lines of the beam model, Wang and Yu (2013), © Elsevier Ltd., reprinted with permission

In an isotropic beam, the shear center is the same as the center of twist. This is the point about which the cross section rotates under a pure twisting moment.

In addition, the tension center is the point in the cross section at which an axial force induces no bending (i.e., the centroid; the spanwise locus of centroids is called tension axis). Since in a cross section, the shear center, the center of gravity, and the centroid of the section are not necessarily identical, their spanwise counterparts, i.e., the elastic axis, the center of gravity axis, and the tension axis are not necessarily coincident either.

The unit vector b_1 of the undeformed b-frame is tangential to the undeformed reference line; b_2 and b_3 define the plane of the undeformed reference cross section. The origin of the deformed B-frame is the origin of the b-frame translated by the displacement components u_i. The unit vector B_1 is orthogonal to the non-warped but translated and rotated reference cross section. Note that B_1 is not necessarily tangential to the deformed reference line because the displaced cross section does not have to be orthogonal to the new reference line (i.e., Euler–Bernoulli approximation is not made; shear deformation is not neglected), Traugott et al. (2005).

Since the behavior of an elastic body is completely determined by its energy function, one may write the 3-D strain energy function, minimize it subjected to the warping constraints and then solve for the warping displacements to create an asymptotically correct 1-D energy function. In this way, by reproducing the 3-D energy in terms of 1-D quantities, a beam theory is derived. This dimensional reduction cannot be carried out exactly; however, VAM can find the 1-D energy that approximates the 3-D energy as closely as possible.

The strain energy of the cross section (per unit length) of the beam can be expressed as

$$U = \frac{1}{2}\langle\langle \varGamma^T D \varGamma \rangle\rangle \tag{2.1}$$

where $\varGamma$ is the 3-D strain vector,

$$\varGamma = \lfloor \varGamma_{11} \quad 2\varGamma_{12} \quad 2\varGamma_{13} \quad \varGamma_{22} \quad 2\varGamma_{23} \quad \varGamma_{33} \rfloor^T \tag{2.2}$$

and

$$\langle\langle \bullet \rangle\rangle = \langle (\bullet) g \rangle = \int_A (\bullet)\sqrt{g}\mathrm{d}x_2\mathrm{d}x_3, \quad \langle \bullet \rangle = \int_A (\bullet)\mathrm{d}x_2\mathrm{d}x_3 \tag{2.3}$$

$$\sqrt{g} = 1 - x_2k_3 - x_3k_2 \tag{2.4}$$

A is the cross-sectional plane of the undeformed beam (the reference cross section), D is the 6 × 6 symmetric material matrix in the local Cartesian system and g is the determinant of the metric tensor for the undeformed state.

Equation (2.1) for strain energy density implies a stress–strain law of the form

$$\sigma = D\varGamma \tag{2.5}$$

where the 3-D stress and strain components are elements of the following vectors

$$\begin{aligned} \sigma &= \lfloor \sigma_{11} \quad \sigma_{12} \quad \sigma_{13} \quad \sigma_{22} \quad \sigma_{23} \quad \sigma_{33} \rfloor^{\mathrm{T}} \\ \varGamma &= \lfloor \varGamma_{11} \quad 2\varGamma_{12} \quad 2\varGamma_{13} \quad \varGamma_{22} \quad 2\varGamma_{23} \quad \varGamma_{33} \rfloor^{\mathrm{T}} \end{aligned} \tag{2.6}$$

The basic 2-D analysis problem is to minimize the strain energy functional U subject to four no rigid body motion conditions for the warping functions $w_i = w_i(x_1, x_2, x_3)$. The explicit form of these conditions of no rigid body translation and rotation are (Hodges 2006),

$$\langle w_i \rangle = 0;\ i = 1, 2, 3, \quad \langle x_2w_3 - x_3w_2 \rangle = 0 \tag{2.7}$$

These conditions guarantee the uniqueness of the definition of the warping field and are equivalent to removing the rigid body motion components (i.e., three translations and the in-plane rotation) of the warping field. The warping field is the solution to the mentioned minimization problem. Using matrices and the concept of orthogonality, Eq. (2.7) can be expressed as the orthogonality of the warping function w to the kernel matrix ψ constraint,

$$\langle w^{\mathrm{T}}\psi \rangle = 0 \tag{2.8}$$

where

$$w = \begin{Bmatrix} w_1 \\ w_2 \\ w_3 \end{Bmatrix} \quad \psi = \begin{bmatrix} 1 & 0 & 0 & 0 \\ 0 & 1 & 0 & -x_3 \\ 0 & 0 & 1 & x_2 \end{bmatrix} \tag{2.9}$$

In order to solve the mentioned minimization problem and find the stationary value of the strain energy per unit length, U, given in Eq. (2.1) subjected to constraints (2.8), the warping vector is assumed as

$$w(x_1, x_2, x_3) = \underbrace{S(x_2, x_3)}_{\text{FEM Shape Functions}} \cdot \overbrace{V(x_1)}^{\text{Nodal Warping}} \tag{2.10}$$

where $S(x_2, x_3)$ represents the matrix of the FEM shape functions on the beam cross section and V is a column matrix of the nodal values of the warping displacement along the longitudinal axis of the beam. The use of shape functions reduces the 3-D problem (i.e., calculating w) to a 1-D problem (i.e., calculating V). So, now the strain energy per unit length, U, should be minimized with respect to V. Minimization of strain energy subjected to the orthogonality constraint (2.8) is obtained by using the method of Lagrangian multipliers. By ignoring the shear deformations, one obtains the classic approximation of the strain energy for anisotropic materials as follows (Hodges 2006):

$$2U_0 = \begin{Bmatrix} \bar{\gamma}_{11} \\ \bar{\kappa}_1 \\ \bar{\kappa}_2 \\ \bar{\kappa}_3 \end{Bmatrix}^{\mathrm{T}} \begin{bmatrix} \overline{S}_{11} & \overline{S}_{12} & \overline{S}_{13} & \overline{S}_{14} \\ \overline{S}_{12} & \overline{S}_{22} & \overline{S}_{23} & \overline{S}_{24} \\ \overline{S}_{13} & \overline{S}_{23} & \overline{S}_{33} & \overline{S}_{34} \\ \overline{S}_{14} & \overline{S}_{24} & \overline{S}_{34} & \overline{S}_{44} \end{bmatrix} \begin{Bmatrix} \bar{\gamma}_{11} \\ \bar{\kappa}_1 \\ \bar{\kappa}_2 \\ \bar{\kappa}_3 \end{Bmatrix} \tag{2.11}$$

In this quadratic form, the stiffness constants $\overline{S}_{ij}$ depend on the initial twist and curvature as well as on the geometry and material composition of the cross section. This 4 × 4 model is sufficiently accurate for the analysis of long-wavelength static or low-frequency dynamic behavior of slender initially curved and twisted composite beams (Hodges et al. 1992). Using the classic stiffness matrix S,

$$S = \begin{bmatrix} \overline{S}_{11} & \overline{S}_{12} & \overline{S}_{13} & \overline{S}_{14} \\ \overline{S}_{12} & \overline{S}_{22} & \overline{S}_{23} & \overline{S}_{24} \\ \overline{S}_{13} & \overline{S}_{23} & \overline{S}_{33} & \overline{S}_{34} \\ \overline{S}_{14} & \overline{S}_{24} & \overline{S}_{34} & \overline{S}_{44} \end{bmatrix} \tag{2.12}$$

and for small strain, the 1-D constitutive law would be linear and expressible as

$$\begin{Bmatrix} F_1 \\ M_1 \\ M_2 \\ M_3 \end{Bmatrix} = \begin{bmatrix} \overline{S}_{11} & \overline{S}_{12} & \overline{S}_{13} & \overline{S}_{14} \\ \overline{S}_{12} & \overline{S}_{22} & \overline{S}_{23} & \overline{S}_{24} \\ \overline{S}_{13} & \overline{S}_{23} & \overline{S}_{33} & \overline{S}_{34} \\ \overline{S}_{14} & \overline{S}_{24} & \overline{S}_{34} & \overline{S}_{44} \end{bmatrix} \begin{Bmatrix} \overline{\gamma}_{11} \\ \overline{\kappa}_1 \\ \overline{\kappa}_2 \\ \overline{\kappa}_3 \end{Bmatrix} \tag{2.13}$$

For homogeneous prismatic beams made of isotropic materials, the expression for classical strain energy per unit length is

$$2U_0 = \begin{Bmatrix} \overline{\gamma}_{11} \\ \overline{\kappa}_1 \\ \overline{\kappa}_2 \\ \overline{\kappa}_3 \end{Bmatrix}^{\mathrm{T}} \begin{bmatrix} \mathrm{EA} & 0 & 0 & 0 \\ 0 & \mathrm{GJ} & 0 & 0 \\ 0 & 0 & \mathrm{EI}_2 & 0 \\ 0 & 0 & 0 & \mathrm{EI}_3 \end{bmatrix} \begin{Bmatrix} \overline{\gamma}_{11} \\ \overline{\kappa}_1 \\ \overline{\kappa}_2 \\ \overline{\kappa}_3 \end{Bmatrix} \tag{2.14}$$

where the classical stiffness matrix is

$$S = \begin{bmatrix} \mathrm{EA} & 0 & 0 & 0 \\ 0 & \mathrm{GJ} & 0 & 0 \\ 0 & 0 & \mathrm{EI}_2 & 0 \\ 0 & 0 & 0 & \mathrm{EI}_3 \end{bmatrix} \tag{2.15}$$

Here, EA is the extensional stiffness, GJ is the Saint-Venant's torsional stiffness, EI_α is the bending stiffness about x_α ($\alpha = 2, 3$), E is the Young's modulus, G is the shear modulus, and the cross-sectional axes x_α are the principal axes of inertia originating at the centroid. Furthermore, $\overline{\gamma}_{11}$ is the extension of the reference line, $\overline{\kappa}_1$ is the elastic twist, and the elastic bending curvatures are denoted by $\overline{\kappa}_2$ and $\overline{\kappa}_3$. The zeros on the off-diagonal elements of the stiffness matrix are indications of the decoupled behavior of the structure in different directions. If one computes the results at the centroid (i.e., the origin of the reference frame is transferred to the centroid), the existence of off-diagonal elements in the stiffness matrix is impossible. In fact, for any homogeneous isotropic section, a 4 × 4 description, and the reference at the centroid, there is no coupling between extension and bending (Palacios 2008).

For thick beams or for beams in high-frequency vibrations, shear deformation cannot be ignored. So, the classic model should be replaced with the generalized Timoshenko model:

$$2U = \begin{Bmatrix} \gamma_{11} \\ 2\gamma_{12} \\ 2\gamma_{13} \\ \kappa_1 \\ \kappa_2 \\ \kappa_3 \end{Bmatrix}^{\mathrm{T}} \begin{bmatrix} S_{11} & S_{12} & S_{13} & S_{14} & S_{15} & S_{16} \\ S_{12} & S_{22} & S_{23} & S_{24} & S_{25} & S_{26} \\ S_{13} & S_{23} & S_{33} & S_{34} & S_{35} & S_{36} \\ S_{14} & S_{24} & S_{34} & S_{44} & S_{45} & S_{46} \\ S_{15} & S_{25} & S_{35} & S_{45} & S_{55} & S_{56} \\ S_{16} & S_{26} & S_{36} & S_{46} & S_{56} & S_{66} \end{bmatrix} \begin{Bmatrix} \gamma_{11} \\ 2\gamma_{12} \\ 2\gamma_{13} \\ \kappa_1 \\ \kappa_2 \\ \kappa_3 \end{Bmatrix} \tag{2.16}$$

or

$$2U = \begin{Bmatrix} \gamma \\ \kappa \end{Bmatrix}^{\mathrm{T}} \begin{bmatrix} A & B \\ B^{\mathrm{T}} & D \end{bmatrix} \begin{Bmatrix} \gamma \\ \kappa \end{Bmatrix} \tag{2.17}$$

Therefore, the 1-D constitutive law in generalized Timoshenko model is

$$\begin{Bmatrix} F_1 \\ F_2 \\ F_3 \\ M_1 \\ M_2 \\ M_3 \end{Bmatrix} = \begin{bmatrix} S_{11} & S_{12} & S_{13} & S_{14} & S_{15} & S_{16} \\ S_{12} & S_{22} & S_{23} & S_{24} & S_{25} & S_{26} \\ S_{13} & S_{23} & S_{33} & S_{34} & S_{35} & S_{36} \\ S_{14} & S_{24} & S_{34} & S_{44} & S_{45} & S_{46} \\ S_{15} & S_{25} & S_{35} & S_{45} & S_{55} & S_{56} \\ S_{16} & S_{26} & S_{36} & S_{46} & S_{56} & S_{66} \end{bmatrix} \begin{Bmatrix} \gamma_{11} \\ 2\gamma_{12} \\ 2\gamma_{13} \\ \kappa_1 \\ \kappa_2 \\ \kappa_3 \end{Bmatrix} \tag{2.18}$$

or

$$\begin{Bmatrix} F \\ M \end{Bmatrix} = \begin{bmatrix} A & B \\ B^{\mathrm{T}} & D \end{bmatrix} \begin{Bmatrix} \gamma \\ \kappa \end{Bmatrix} \tag{2.19}$$

Alternatively,

$$\begin{Bmatrix} \gamma \\ \kappa \end{Bmatrix} = \begin{bmatrix} R & Z \\ Z^{\mathrm{T}} & T \end{bmatrix} \begin{Bmatrix} F \\ M \end{Bmatrix} \tag{2.20}$$

As it is mentioned in Chap. 1, the linear cross-sectional analysis of the VAM is performed by VABS. In order to run VABS, a 2-D meshed model of the cross section is constructed by a CAD or FEM software. It can then be transformed into an input file for VABS. To model initially twisted and curved beams, three real numbers for the twist, k_1, and the bending curvatures, k_2 and k_3, should be provided in the input file. Also layup parameters such as the layup angle should be provided. Finally, material properties including Young's moduli, E_i, shear moduli, G_{ij}, Poisson's ratios, υ_{ij}, and mass density, ρ, should be given.

After performing the solution, the results include scalar quantities such as the mass center, the principal axes of inertia, the centroid, and the neutral axes. Matrix results include the cross-sectional 6 × 6 mass (three translation and three rotations) and the 4 × 4 cross-sectional stiffness matrix of the classical model (extension, torsion, and two bending). There are also the 6 × 6 cross-sectional stiffness matrix of the generalized Timoshenko model (extension, two shears, torsion, and two bendings), and the 5 × 5 cross-sectional stiffness matrix of the generalized Vlasov model (extension, torsion, two bendings, and the derivative of torsion).

To obtain the generalized Vlasov model, first, the generalized Timoshenko model that works best at high frequencies is constructed and the position of the shear center is determined. Then, VABS moves the origin of the coordinate system to the shear center and repeats the calculations to obtain a generalized Vlasov model. This model is useful for analyzing thin-walled beams with open sections.

The cross-sectional modeling of smart composite beams has also been successfully performed (with distributed actuators embedded within the composite structure) using UM/VABS.

2.4 General Formulation of the 1-D Analysis

Having used the VAM logic and obtained the 2-D cross-sectional properties by VABS, a 1-D analysis along the longitudinal axis of the beam is now in order. The combination of the previously mentioned 2-D solution and the solution of the 1-D problem provide a complete 3-D picture of the mechanical quantities of interest along and across the beam. The 1-D analysis utilizes the intrinsic equations of motion, the intrinsic kinematical equations, the momentum–velocity equations, and the constitutive equations of the material of the beam. It utilizes the results of the cross-sectional analysis in order to calculate the generalized stress and strain resultants as well as the 1-D displacements. It should be noted that the intrinsic equations are not tied to a specific choice of displacement or rotation variables. Furthermore, there is only one set of intrinsic equations; all other correct and variationally consistent sets of beam equations are linear combinations of the correct intrinsic set of equations.

2.4.1 Intrinsic Equations of Motion

The internal force and moment vectors F and M are partial derivatives of the strain energy of the cross section (per unit length), U,

$$F = \left(\frac{\partial U}{\partial \gamma}\right)^{\mathrm{T}}, \quad M = \left(\frac{\partial U}{\partial \kappa}\right)^{T} \tag{2.21}$$

Similarly, the generalized sectional linear and angular momenta P and H are conjugate to motion variables by derivatives of the kinetic energy function,

$$P = \left(\frac{\partial K.E.}{\partial V}\right)^{\mathrm{T}}, \quad H = \left(\frac{\partial K.E.}{\partial \Omega}\right)^{\mathrm{T}} \tag{2.22}$$

Now, recalling Hamilton's principle,

$$\int_{t_1}^{t_2} \int_{0}^{L} \left\{\delta(K.E. - U) + \overline{\delta W}\right\} \mathrm{d}x_1 \mathrm{d}t = \overline{\delta A} \tag{2.23}$$

for the case of generalized Timoshenko beam without active elements, one obtains, Hodges (2006)

$$\begin{aligned}
&\int_{t_1}^{t_2}\int_0^L \Big\{\delta\bar{q}^{\mathrm{T}}\left(F' + \tilde{K}F + f - \dot{P} - \widetilde{\Omega}P\right) + \delta\bar{\psi}^{\mathrm{T}}\big[M' + \tilde{K}M + (\tilde{e}_1 + \tilde{\gamma})F \\
&\qquad + m - \dot{H} - \widetilde{\Omega}H - \tilde{V}P\big]\Big\}\mathrm{d}x_1\mathrm{d}t \\
&= \int_0^L \left[\delta\bar{q}^T\left(\hat{P} - P\right) + \delta\bar{\psi}^{\mathrm{T}}\left(\hat{H} - H\right)\right]\Big|_{t_1}^{t_2}\mathrm{d}x_1 - \int_{t_1}^{t_2}\left[\delta\bar{q}^{\mathrm{T}}\left(\hat{F} - F\right) + \delta\bar{\psi}^{\mathrm{T}}\left(\hat{M} - M\right)\right]\Big|_0^L\mathrm{d}t
\end{aligned} \tag{2.24}$$

where the tilde notation has been used to express a cross product of two vectors in a concise matrix representation:

$$\tilde{K}F = \begin{bmatrix} 0 & -K_3 & K_2 \\ K_3 & 0 & -K_1 \\ -K_2 & K_1 & 0 \end{bmatrix}\begin{bmatrix} F_1 \\ F_2 \\ F_3 \end{bmatrix} = \begin{bmatrix} K_2F_3 - K_3F_2 \\ K_3F_1 - K_1F_3 \\ K_1F_2 - K_2F_1 \end{bmatrix} = \vec{K} \times \vec{F} \tag{2.25}$$

The corresponding Euler–Lagrange equations are

$$F' + \tilde{K}F + f = \dot{P} + \tilde{\Omega}P \tag{2.26}$$

$$M' + \tilde{K}M + (\tilde{e}_1 + \tilde{\gamma})F + m = \dot{H} + \tilde{\Omega}H + \tilde{V}P \tag{2.27}$$

Equations (2.26) and (2.27) are called the nonlinear intrinsic equations of motion of a beam. Here, F and M are column vectors of internal forces and moments, respectively. The first element of F is the axial force and the second and third elements are the shear forces, expressed in the deformed beam basis, B. Similarly, the first element of M is the twisting moment and its second and third elements are the bending moments, again in the deformed beam frame, B. The scalar form of the intrinsic equations of motion is

$$F_1' + K_2F_3 - K_3F_2 + f_1 = \dot{P}_1 + \Omega_2P_3 - \Omega_3P_2 \tag{2.28}$$

$$F_2' + K_3F_1 - K_1F_3 + f_2 = \dot{P}_2 + \Omega_3P_1 - \Omega_1P_3 \tag{2.29}$$

$$F_3' + K_1F_2 - K_2F_1 + f_3 = \dot{P}_3 + \Omega_1P_2 - \Omega_2P_1 \tag{2.30}$$

and

$$\begin{aligned} & M_1' + K_2 M_3 - K_3 M_2 + 2\gamma_{12} F_3 - 2\gamma_{13} F_2 + m_1 \\ & \quad = \dot{H}_1 + \Omega_2 H_3 - \Omega_3 H_2 + V_2 P_3 - V_3 P_2 \end{aligned} \tag{2.31}$$

$$\begin{aligned} & M_2' + K_3 M_1 - K_1 M_3 + 2\gamma_{13} F_1 - (1 + \gamma_{11}) F_3 + m_2 \\ & \quad = \dot{H}_2 + \Omega_3 H_1 - \Omega_1 H_3 + V_3 P_1 - V_1 P_3 \end{aligned} \tag{2.32}$$

$$\begin{aligned} & M_3' + K_1 M_2 - K_2 M_1 + (1 + \gamma_{11}) F_2 - 2\gamma_{12} F_1 + m_3 \\ & \quad = \dot{H}_3 + \Omega_1 H_2 - \Omega_2 H_1 + V_1 P_2 - V_2 P_1 \end{aligned} \tag{2.33}$$

These equations are the geometrically exact equations for the dynamics of a beam in an absolute frame of reference, A. They resemble Euler's dynamical equations, and their symmetric form enables one to write them in a compact matrix form.

For the special case of static behavior, Eqs. (2.26) and (2.27) reduce to those of Reissner (1973). In fact, by setting the left-hand side of these equations equal to zero, a generalized Euler–Kirchhoff–Clebsch theory is obtained. This static theory, when specialized for isotropic materials, is often called the elastica theory, Hodges (2006).

By ignoring the shear deformation components in Eqs. (2.26) and (2.27) and renaming $\kappa = \bar{\kappa}$ and $\gamma = \bar{\gamma}_{11} e_1$, the equations of motion for the classical theory of beams are obtained as (Hodges 2006)

$$F' + \tilde{K} F + f = \dot{P} + \tilde{\Omega} P \tag{2.34}$$

$$M' + \tilde{K} M + (1 + \bar{\gamma}_{11}) \tilde{e}_1 F + m = \dot{H} + \tilde{\Omega} H + \tilde{V} P \tag{2.35}$$

where the total curvature and twist of the blade are the summation of their built-in values and the added curvature and twist as a result of elastic deformation (i.e., the summation of the initial and the elastic curvatures),

$$K = k + \kappa \tag{2.36}$$

The boundary conditions are another output of the application of the Hamilton's principle in which either force or moment can be specified or calculated at the two ends of the beam.

2.4.2 *Intrinsic Kinematical Equations*

The nonlinear intrinsic kinematical equations of a beam that should be solved together with the equations of motion are (Hodges 2006)

$$V' + \tilde{K}V + (\tilde{e}_1 + \tilde{\gamma})\Omega = \dot{\gamma} \tag{2.37}$$

$$\Omega' + \tilde{K}\Omega = \dot{\kappa} \tag{2.38}$$

The corresponding scalar equations are

$$V_1' + K_2V_3 - K_3V_2 + 2\gamma_{12}\Omega_3 - 2\gamma_{13}\Omega_2 = \dot{\gamma}_{11} \tag{2.39}$$

$$V_2' + K_3V_1 - K_1V_3 - (1 + \gamma_{11})\Omega_3 + 2\gamma_{13}\Omega_1 = 2\dot{\gamma}_{12} \tag{2.40}$$

$$V_3' + K_1V_2 - K_2V_1 + (1 + \gamma_{11})\Omega_2 - 2\gamma_{12}\Omega_1 = 2\dot{\gamma}_{13} \tag{2.41}$$

$$\Omega_1' + K_2\Omega_3 - K_3\Omega_2 = \dot{\kappa}_1 \tag{2.42}$$

$$\Omega_2' + K_3\Omega_1 - K_1\Omega_3 = \dot{\kappa}_2 \tag{2.43}$$

$$\Omega_3' + K_1\Omega_2 - K_2\Omega_1 = \dot{\kappa}_3 \tag{2.44}$$

2.4.3 *Momentum–Velocity Equations*

The four nonlinear intrinsic vector equations mentioned so far, i.e., Equations (2.26), (2.27), (2.37), and (2.38), are nonlinear partial differential equations. The momentum–velocity equations, however, are a set of linear algebraic equations,

$$\begin{Bmatrix} P \\ H \end{Bmatrix} = \begin{bmatrix} \mu\Delta & -\mu\tilde{\bar{\xi}} \\ \mu\tilde{\bar{\xi}} & i \end{bmatrix} \begin{Bmatrix} V \\ \Omega \end{Bmatrix} \tag{2.45}$$

where

$$\xi = \begin{Bmatrix} 0 \\ x_2 \\ x_3 \end{Bmatrix}, \quad \bar{\xi} = \begin{Bmatrix} 0 \\ \bar{x}_2 \\ \bar{x}_3 \end{Bmatrix}, \quad \tilde{\bar{\xi}} = \begin{bmatrix} 0 & -\bar{x}_3 & \bar{x}_2 \\ \bar{x}_3 & 0 & 0 \\ -\bar{x}_2 & 0 & 0 \end{bmatrix} \tag{2.46}$$

The expanded form of Eq. (2.45) is

$$\begin{Bmatrix} P_1 \\ P_2 \\ P_3 \\ H_1 \\ H_2 \\ H_3 \end{Bmatrix} = \begin{bmatrix} \mu & 0 & 0 & 0 & \mu\bar{x}_3 & -\mu\bar{x}_2 \\ 0 & \mu & 0 & -\mu\bar{x}_3 & 0 & 0 \\ 0 & 0 & \mu & \mu\bar{x}_2 & 0 & 0 \\ 0 & -\mu\bar{x}_3 & \mu\bar{x}_2 & i_2 + i_3 & 0 & 0 \\ \mu\bar{x}_3 & 0 & 0 & 0 & i_2 & i_{23} \\ -\mu\bar{x}_2 & 0 & 0 & 0 & i_{23} & i_3 \end{bmatrix} \begin{Bmatrix} V_1 \\ V_2 \\ V_3 \\ \Omega_1 \\ \Omega_2 \\ \Omega_3 \end{Bmatrix} \tag{2.47}$$

where the quantities with a bar refer to the location of the centroid with respect to the shear center of the cross section. Also,

$$i = \langle\langle \rho\left(\xi^T\xi\Delta - \xi\xi^T\right)\rangle\rangle = \begin{bmatrix} i_2 + i_3 & 0 & 0 \\ 0 & i_2 & i_{23} \\ 0 & i_{23} & i_3 \end{bmatrix} \tag{2.48}$$

where

$$i_2 = \rho\int\limits_A x_3^2 \mathrm{d}x_2\mathrm{d}x_3, \quad i_3 = \rho\int\limits_A x_2^2 \mathrm{d}x_2\mathrm{d}x_3, \quad i_{23} = -\rho\int\limits_A x_2x_3\mathrm{d}x_2\mathrm{d}x_3 \tag{2.49}$$

are the cross-sectional mass moments and the product of inertia measured with respect to the shear center. Finally, using Eq. (2.3),

$$\mu = \langle\langle\rho\rangle\rangle = \left\langle\rho\sqrt{g}\right\rangle \rightarrow \quad \mu = \int\limits_A \left(\rho\sqrt{g}\right)\mathrm{d}x_2\mathrm{d}x_3 \tag{2.50}$$

Substitution of Eq. (2.4) in (2.50) gives

$$\mu = \int\limits_A \rho(1 - x_2k_3 - x_3k_2)\mathrm{d}x_2\mathrm{d}x_3 \tag{2.51}$$

If the initial curvature k is zero Eq. (2.51) simply reduces to

$$\mu = \int\limits_A \rho\mathrm{d}x_2\mathrm{d}x_3 \tag{2.52}$$

which for a homogeneous section results in the following familiar expression for mass per unit length,

$$\mu = \rho A \tag{2.53}$$

Now recalling Eqs. (2.45) and (2.46), since the reference frame has been put at the shear center, the location of the centroid which is shown by bar coordinates would be the position of the centroid with respect to the shear center of the section. If the centroid is close enough to the shear center, the formulation simplifies. Since then,

$$\bar{x}_2 = \bar{x}_3 = 0 \tag{2.54}$$

Therefore using Eq. (2.46),

$$\bar{\xi} = 0, \quad \tilde{\bar{\xi}} = 0 \tag{2.55}$$

Consequently, when the centroid and shear center of the cross section coincide, all off-diagonal (coupling) terms of Eq. (2.45) will vanish except for the ones that are due to the polar moment of inertia.

2.4.4 Constitutive Equations

The 2-D analysis mentioned before provides the warping functions required for the recovery of 3-D stress and strain, as well as the stiffness (or its inverse, i.e., flexibility) matrix used in the following constitutive equations:

$$\begin{Bmatrix} F \\ M \end{Bmatrix} = \underbrace{\begin{bmatrix} A & B \\ B^{\mathrm{T}} & D \end{bmatrix}}_{S} \begin{Bmatrix} \gamma \\ \kappa \end{Bmatrix}, \quad \begin{Bmatrix} \gamma \\ \kappa \end{Bmatrix} = \underbrace{\begin{bmatrix} R & Z \\ Z^{T} & T \end{bmatrix}}_{S^{-1}} \begin{Bmatrix} F \\ M \end{Bmatrix} \tag{2.56}$$

or in the scalar form,

$$\begin{Bmatrix} \gamma_{11} \\ 2\gamma_{12} \\ 2\gamma_{13} \\ \kappa_1 \\ \kappa_2 \\ \kappa_3 \end{Bmatrix} = \begin{bmatrix} R_{11} & R_{12} & R_{13} & Z_{11} & Z_{12} & Z_{13} \\ R_{21} & R_{22} & R_{23} & Z_{21} & Z_{22} & Z_{23} \\ R_{31} & R_{32} & R_{33} & Z_{31} & Z_{32} & Z_{33} \\ Z_{11} & Z_{21} & Z_{31} & T_{11} & T_{12} & T_{13} \\ Z_{12} & Z_{22} & Z_{32} & T_{21} & T_{22} & T_{23} \\ Z_{13} & Z_{23} & Z_{33} & T_{31} & T_{32} & T_{33} \end{bmatrix} \begin{Bmatrix} F_1 \\ F_2 \\ F_3 \\ M_1 \\ M_2 \\ M_3 \end{Bmatrix}$$

Such a linear structural law is valid only for small local strains which can, however, result in large global deformations as they occur in helicopter blades (Traugott et al. 2005).

In the general nonlinear elasto-dynamic case, Eqs. (2.26), (2.27), (2.36), (2.37), (2.38), (2.45), and (2.56) form a system of four nonlinear vector partial differential equations and five linear algebraic vector equations for a total of nine unknown vectors: F, M, V, Ω, P, H, γ, κ, and K, at every point along the beam and at every instant of time. These unknown vectors correspond to 27 scalar variables. Here, F and M are the internal force and moment (generalized forces), P and H are the linear and angular momentum (generalized momenta), V and Ω are the linear and angular velocity (generalized velocities), γ and κ are the beam strains and curvatures (generalized strains), and f and m are the applied external forces and moments per unit length. All quantities refer to the B-frame of the deformed cross section.

Solution of these equations requires the application of initial and boundary conditions. The boundary conditions are another output of the application of the

Hamilton's principle in which either force or moment can be specified or found at the two ends of the beam. The intrinsic equations of motion are not a stand-alone set of equations, and in general, they should be solved together with kinematical equations, constitutive relations, as well as the initial and boundary conditions. Having solved this system of equations for the mentioned unknowns, other variables of interest can be easily calculated.

2.4.5 Strain–Displacement Equations

The generalized strain–displacement equations are (Hodges 2006)

$$\gamma = C(e_1 + u' + \tilde{k}u) - e_1 \tag{2.57}$$

$$\tilde{\kappa} = -C'C^{\mathrm{T}} + C\tilde{k}C^{\mathrm{T}} - \tilde{k} \tag{2.58}$$

2.4.6 Velocity–Displacement Equations

The generalized velocity–displacement equations are

$$V = C(v + \dot{u} + \tilde{\omega}u) \tag{2.59}$$

$$\tilde{\Omega} = -\dot{C}C^{\mathrm{T}} + C\tilde{\omega}C^{\mathrm{T}} \tag{2.60}$$

where V and Ω are measured in the deformed frame, and v and ω are measured in the undeformed frame.

2.4.7 Rodrigues Parameters

One may define a rotation by four parameters: three direction cosine values e_i which define the unit vector $\vec{e} = e_i b_i$ in the direction of the axis of rotation, together with α which is the angle of rotation about this axis. Based on this logic, the Rodrigues parameters $\theta = \begin{bmatrix} \theta_1 & \theta_2 & \theta_3 \end{bmatrix}^T$ are defined as,

$$\theta_i = 2e_i \tan(\alpha/2) \tag{2.61}$$

Also, the rotation matrix is

$$C = \frac{\left[1 - (1/4)\theta^{\mathrm{T}}\theta\right]\Delta - \tilde{\theta} + (1/2)\theta\theta^{\mathrm{T}}}{1 + (1/4)\theta^{\mathrm{T}}\theta} \tag{2.62}$$

The associated curvature is related to the Rodrigues parameters in the following way:

$$\kappa = \left(\frac{\Delta - \frac{1}{2}\tilde{\theta}}{1 + \frac{1}{4}\theta^{\mathrm{T}}\theta}\right)\theta' + Ck - k \tag{2.63}$$

Finally, Ω, the column matrix of angular velocity components in the deformed system, *B*, can be related to the angular velocity vector, *ω*, in the undeformed system, *b*, using the Rodrigues parameters

$$\Omega = \left(\frac{\Delta - \frac{1}{2}\tilde{\theta}}{1 + \frac{1}{4}\theta^{T}\theta}\right)\dot{\theta} + C\omega \tag{2.64}$$

Having calculated γ and κ as a part of the solution of the system of equations mentioned before, Eq. (2.63) can now be solved for θ, [notice that C itself depends on θ as is seen in Eq. (2.62)]. Finally, Eq. (2.57) is solved for *u,* which is the displacement vector on the beam reference line.

2.5 Recovery Relations and Their Application in Stress Analysis

The suitability of a design can be evaluated using localized quantities like the 3-D stress and strain components. Nevertheless, the 1-D beam analysis only provides the global behavior of composite beams. Such a global outcome cannot replace a detailed 3-D analysis. In order to recover the complete 3-D components, the 1-D and the 2-D results should be combined properly.

Therefore, the next step is to calculate the 3-D strain and 3-D stress components. This step is usually referred to as recovering the 3-D response and in which the recovery relations are used. They include expressions for 3-D displacements, as well as strain and stress components in terms of the 1-D beam quantities and the local cross-sectional coordinates.

Referring to Fig. 2.4, one may express the position of a particle in the deformed configuration, i.e., $R(x_1, x_2, x_3)$, in terms of its position vector r in the undeformed beam,

$$R(x_1, x_2, x_3) = \left(r + \underbrace{u}_{\text{from } 1-\text{D}}\right) + \left(x_2 \underbrace{B_2}_{\text{from C got in } 1-\text{D}} + x_3 B_3\right) + \underbrace{w_i}_{\text{from } 2-\text{D}} B_i \tag{2.65}$$

Having obtained the displacement of the reference line, u, from the 1-D analysis and the warping functions of the cross section, w_{i}, from the 2-D analysis, the geometry of the deformed beam is now fully known. The 3-D strain components can be written as (Hodges 2006)

$$\Gamma = \lfloor \Gamma_{11} \quad 2\Gamma_{12} \quad 2\Gamma_{13} \quad \Gamma_{22} \quad 2\Gamma_{23} \quad \Gamma_{33} \rfloor^T \tag{2.66}$$

$$\begin{aligned} &\Gamma = \Gamma(w, w', \bar{\varepsilon}) \\ &\Gamma = \Gamma_a \underbrace{w}_{2-\text{D}} + \Gamma_\varepsilon \underbrace{\bar{\varepsilon}}_{1-\text{D}} + \underbrace{\Gamma_R w}_{\text{initial curvature } 2-\text{D}} + \Gamma_l w' \end{aligned} \tag{2.67}$$

where the 1-D generalized strain is

$$\bar{\varepsilon} = \begin{Bmatrix} \bar{\gamma}_{11} \\ \bar{\kappa}_1 \\ \bar{\kappa}_2 \\ \bar{\kappa}_3 \end{Bmatrix} \tag{2.68}$$

and the operators are, for warping,

$$\Gamma_a = \begin{bmatrix} 0 & 0 & 0 \\ \frac{\partial}{\partial x_2} & 0 & 0 \\ \frac{\partial}{\partial x_3} & 0 & 0 \\ 0 & \frac{\partial}{\partial x_2} & 0 \\ 0 & \frac{\partial}{\partial x_3} & \frac{\partial}{\partial x_2} \\ 0 & 0 & \frac{\partial}{\partial x_3} \end{bmatrix} \tag{2.69}$$

for the 1-D strain,

$$\Gamma_\varepsilon = \frac{1}{\sqrt{g}} \begin{bmatrix} 1 & 0 & x_3 & -x_2 \\ 0 & -x_3 & 0 & 0 \\ 0 & x_2 & 0 & 0 \\ 0 & 0 & 0 & 0 \\ 0 & 0 & 0 & 0 \\ 0 & 0 & 0 & 0 \end{bmatrix} \tag{2.70}$$

for the initial curvature and twist,

$$\Gamma_R = \frac{1}{\sqrt{g}} \begin{bmatrix} \tilde{k} + \Delta k_1 \left(x_3 \frac{\partial}{\partial x_2} - x_2 \frac{\partial}{\partial x_3} \right) \\ O_3 \end{bmatrix} \tag{2.71}$$

and finally for the warping derivative,

$$\Gamma_l = \frac{1}{\sqrt{g}} \begin{bmatrix} \Delta \\ O_3 \end{bmatrix} \tag{2.72}$$

Once strain components are calculated, stresses can be computed by the use of the Hooke's law,

$$\sigma = D\Gamma \tag{2.73}$$

To sum up, in a typical problem first using the VAM logic and VABS, the cross-sectional properties are calculated. Then, the 1-D analysis is performed along the span of the beam that utilizes the intrinsic equations of motion, the intrinsic kinematical equations, the constitutive equations of the material of the beam, and the momentum–velocity equations. Finally, the results are combined as shown above to provide the 3-D stress and strain distributions.

2.6 Finite Difference Formulation in Time and Space

In order to solve the system of nonlinear partial differential Eqs. (2.34), (2.35), (2.37), and (2.38) numerically, or to calculate the steady-state solution of this system, the finite difference method (FDM) and the shooting method will be used in the following chapters. In this section, a few equations that will be used later are presented.

Figure 2.5 illustrates a beam that has been discretized by N nodes along its span. The corresponding finite difference space–time grid presentation has been depicted

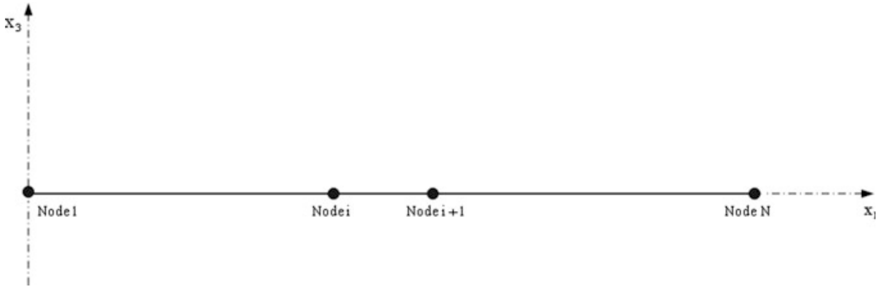

Fig. 2.5 Nodes along the blade and the coordinate system of the undeformed blade

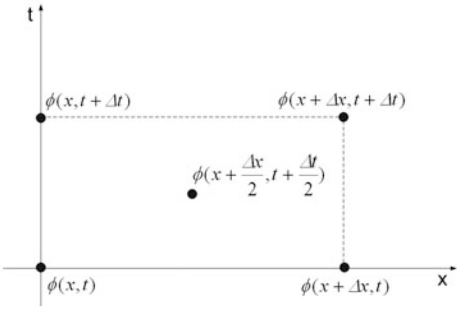

Fig. 2.6 The space–time grid for the numerical solution of a partial differential equation

in Fig. 2.6. Consider the value of a generic variable, $\phi(x,t)$, at position x and time t. In order to simplify the notation, the following convention is used to express this value:

$$\phi_i = \phi(x,t) \tag{2.74}$$

where the subscript i is the beam node number corresponding to position x. At points neighboring (x, t) on the space–time grid shown in Fig. 2.6, the same variable can be expressed as

$$\phi_{i+1} = \phi(x+\Delta x,t), \quad \phi_i^+ = \phi(x,t+\Delta t), \quad \phi_{i+1}^+ = \phi(x+\Delta x,t+\Delta t) \tag{2.75}$$

where the superscript '+' refers to the values at the next time step and i + 1 is the next spatial node (right-hand side of i). Using Taylor series expansion and a forward and a backward difference in space, one obtains, respectively,

$$\phi\left(x+\frac{\Delta x}{2},t+\frac{\Delta t}{2}\right) = \phi\left(x,t+\frac{\Delta t}{2}\right) + \phi'\left(x,t+\frac{\Delta t}{2}\right)\frac{\Delta x}{2} \tag{2.76}$$

$$\phi\left(x+\frac{\Delta x}{2},t+\frac{\Delta t}{2}\right) = \phi\left(x+\Delta x,t+\frac{\Delta t}{2}\right) - \phi'\left(x+\Delta x,t+\frac{\Delta t}{2}\right)\frac{\Delta x}{2} \tag{2.77}$$

Adding Eqs. (2.76) and (2.77) gives

$$\begin{aligned}2\phi\left(x+\frac{\Delta x}{2},t+\frac{\Delta t}{2}\right) &= \phi\left(x,t+\frac{\Delta t}{2}\right) + \phi\left(x+\Delta x,t+\frac{\Delta t}{2}\right)\\ &\quad + \left[\phi'\left(x,t+\frac{\Delta t}{2}\right) - \phi'\left(x+\Delta x,t+\frac{\Delta t}{2}\right)\right]\frac{\Delta x}{2}\end{aligned} \tag{2.78}$$

Now, considering forward and backward differences in time,

$$\phi\left(x, t+\frac{\Delta t}{2}\right) = \phi(x,t) + \dot{\phi}(x,t)\frac{\Delta t}{2} \tag{2.79}$$

$$\phi\left(x, t+\frac{\Delta t}{2}\right) = \phi(x,t+\Delta t) - \dot{\phi}(x,t+\Delta t)\frac{\Delta t}{2} \tag{2.80}$$

Adding Eqs. (2.79) and (2.80) gives,

$$2\phi\left(x, t+\frac{\Delta t}{2}\right) = \phi(x,t+\Delta t) + \phi(x,t) + \left[\dot{\phi}(x,t) - \dot{\phi}(x,t+\Delta t)\right]\frac{\Delta t}{2} \tag{2.81}$$

Similarly, using forward and backward differences in time,

$$\phi\left(x+\Delta x, t+\frac{\Delta t}{2}\right) = \phi(x+\Delta x,t) + \dot{\phi}(x+\Delta x,t)\frac{\Delta t}{2} \tag{2.82}$$

$$\phi\left(x+\Delta x, t+\frac{\Delta t}{2}\right) = \phi(x+\Delta x,t+\Delta t) - \dot{\phi}(x+\Delta x,t+\Delta t)\frac{\Delta t}{2} \tag{2.83}$$

Adding Eqs. (2.82) and (2.83) results in

$$\begin{aligned} 2\phi\left(x+\Delta x, t+\frac{\Delta t}{2}\right) &= \phi(x+\Delta x,t+\Delta t) + \phi(x+\Delta x,t) \\ &\quad + \left[\dot{\phi}(x+\Delta x,t) - \dot{\phi}(x+\Delta x,t+\Delta t)\right]\frac{\Delta t}{2} \end{aligned} \tag{2.84}$$

Substitution of Eqs. (2.81) and (2.84) into Eq. (2.78) gives

$$\begin{aligned} 2\phi\left(x+\frac{\Delta x}{2}, t+\frac{\Delta t}{2}\right) &= \frac{1}{2}[\phi(x,t) + \phi(x,t+\Delta t) + \phi(x+\Delta x,t) + \phi(x+\Delta x,t+\Delta t)] \\ &\quad + \left[\dot{\phi}(x,t) - \dot{\phi}(x,t+\Delta t)\right]\frac{\Delta t}{4} \\ &\quad + \left[\dot{\phi}(x+\Delta x,t) - \dot{\phi}(x+\Delta x,t+\Delta t)\right]\frac{\Delta t}{4} \\ &\quad + \left[\phi'\left(x,t+\frac{\Delta t}{2}\right) - \phi'\left(x+\Delta x,t+\frac{\Delta t}{2}\right)\right]\frac{\Delta x}{2} \end{aligned} \tag{2.85}$$

Taylor series expansions in time and in space can be used in Eq. (2.85) to give the generic function value at the center of the space–time grid,

$$\begin{aligned}\phi\left(x+\frac{\Delta x}{2},t+\frac{\Delta t}{2}\right) &= \frac{1}{4}[\phi(x,t)+\phi(x,t+\Delta t)+\phi(x+\Delta x,t)+\phi(x+\Delta x,t+\Delta t)] \\ &\quad -\ddot{\phi}(x,t)\frac{(\Delta t)^2}{8}-\ddot{\phi}(x+\Delta x,t)\frac{(\Delta t)^2}{8}-\phi''\left(x,t+\frac{\Delta t}{2}\right)\frac{(\Delta x)^2}{4}\end{aligned} \tag{2.86}$$

Using the notation given in Eq. (2.75), and by ignoring the higher order terms, Eq. (2.86) reduces to

$$\phi\left(x+\frac{\Delta x}{2},t+\frac{\Delta t}{2}\right)=\frac{1}{4}\left(\phi_{i+1}^{+}+\phi_i^{+}+\phi_{i+1}+\phi_i\right)+O\left(\Delta x^2,\Delta t^2\right) \tag{2.87}$$

According to Eq. (2.87), the function value at the center of a space–time grid may well be approximated by the average of its values at the neighboring grid nodes. Now, for the partial derivatives at the center point, using Taylor series expansion,

$$\phi\left(x+\Delta x,t+\frac{\Delta t}{2}\right)=\phi\left(x+\frac{\Delta x}{2},t+\frac{\Delta t}{2}\right)+\phi'\left(x+\frac{\Delta x}{2},t+\frac{\Delta t}{2}\right)\frac{\Delta x}{2}+O(\Delta x)^2 \tag{2.88}$$

$$\phi\left(x,t+\frac{\Delta t}{2}\right)=\phi\left(x+\frac{\Delta x}{2},t+\frac{\Delta t}{2}\right)-\phi'\left(x+\frac{\Delta x}{2},t+\frac{\Delta t}{2}\right)\frac{\Delta x}{2}+O(\Delta x)^2 \tag{2.89}$$

Subtracting Eq. (2.89) from Eq. (2.88) gives

$$\phi'\left(x+\frac{\Delta x}{2},t+\frac{\Delta t}{2}\right)\Delta x=\phi\left(x+\Delta x,t+\frac{\Delta t}{2}\right)-\phi\left(x,t+\frac{\Delta t}{2}\right)+O(\Delta x)^2 \tag{2.90}$$

Similarly,

$$\phi(x+\Delta x,t)=\phi\left(x+\Delta x,t+\frac{\Delta t}{2}\right)-\dot{\phi}\left(x+\Delta x,t+\frac{\Delta t}{2}\right)\frac{\Delta t}{2}+O(\Delta t)^2 \tag{2.91}$$

$$\phi(x+\Delta x,t+\Delta t)=\phi\left(x+\Delta x,t+\frac{\Delta t}{2}\right)+\dot{\phi}\left(x+\Delta x,t+\frac{\Delta t}{2}\right)\frac{\Delta t}{2}+O(\Delta t)^2 \tag{2.92}$$

Adding Eqs. (2.91) and (2.92) gives

$$2\phi\left(x+\Delta x, t+\frac{\Delta t}{2}\right) = \phi(x+\Delta x, t+\Delta t) + \phi(x+\Delta x, t) + O(\Delta t)^2 \tag{2.93}$$

Similarly,

$$\phi(x,t) = \phi\left(x, t+\frac{\Delta t}{2}\right) - \dot{\phi}\left(x, t+\frac{\Delta t}{2}\right)\frac{\Delta t}{2} + O(\Delta t)^2 \tag{2.94}$$

$$\phi(x, t+\Delta t) = \phi\left(x, t+\frac{\Delta t}{2}\right) + \dot{\phi}\left(x, t+\frac{\Delta t}{2}\right)\frac{\Delta t}{2} + O(\Delta t)^2 \tag{2.95}$$

Which result in

$$2\phi\left(x, t+\frac{\Delta t}{2}\right) = \phi(x,t) + \phi(x, t+\Delta t) + O(\Delta t)^2 \tag{2.96}$$

Substitution of Eqs. (2.93) and (2.96) into Eq. (2.90) gives

$$\begin{aligned}\phi'\left(x+\frac{\Delta x}{2}, t+\frac{\Delta t}{2}\right)\Delta x = \frac{1}{2}[&\phi(x+\Delta x, t+\Delta t) + \phi(x+\Delta x, t) - \phi(x,t) \\ &-\phi(x, t+\Delta t)] + O\left[(\Delta x)^2, (\Delta t)^2\right]\end{aligned} \tag{2.97}$$

Using Eq. (2.97) and the notation introduced in Eq. (2.75), the generic form of the derivative with respect to x_1 becomes

$$\phi'\left(x+\frac{\Delta x}{2}, t+\frac{\Delta t}{2}\right) = \frac{1}{2\Delta x}\left(\phi_{i+1}^{+} - \phi_i^{+} + \phi_{i+1} - \phi_i\right) + O\left(\Delta x^2, \Delta t^2\right) \tag{2.98}$$

For the generic form of the time derivative, one may start with

$$\phi\left(x+\frac{\Delta x}{2}, t+\Delta t\right) = \phi\left(x+\frac{\Delta x}{2}, t+\frac{\Delta t}{2}\right) + \dot{\phi}\left(x+\frac{\Delta x}{2}, t+\frac{\Delta t}{2}\right)\frac{\Delta t}{2} + O(\Delta t)^2 \tag{2.99}$$

$$\phi\left(x+\frac{\Delta x}{2}, t\right) = \phi\left(x+\frac{\Delta x}{2}, t+\frac{\Delta t}{2}\right) - \dot{\phi}\left(x+\frac{\Delta x}{2}, t+\frac{\Delta t}{2}\right)\frac{\Delta t}{2} + O(\Delta t)^2 \tag{2.100}$$

Subtracting Eq. (2.100) from Eq. (2.99) gives

$$\dot{\phi}\left(x+\frac{\Delta x}{2},t+\frac{\Delta t}{2}\right)\Delta t=\phi\left(x+\frac{\Delta x}{2},t+\Delta t\right)-\phi\left(x+\frac{\Delta x}{2},t\right)+O(\Delta t)^2 \tag{2.101}$$

Now,

$$\phi(x,t+\Delta t)=\phi\left(x+\frac{\Delta x}{2},t+\Delta t\right)-\phi'\left(x+\frac{\Delta x}{2},t+\Delta t\right)\frac{\Delta x}{2}+O(\Delta x)^2 \tag{2.102}$$

$$\phi(x+\Delta x,t+\Delta t)=\phi\left(x+\frac{\Delta x}{2},t+\Delta t\right)+\phi'\left(x+\frac{\Delta x}{2},t+\Delta t\right)\frac{\Delta x}{2}+O(\Delta x)^2 \tag{2.103}$$

Adding Eqs. (2.102) and (2.103) gives

$$2\phi\left(x+\frac{\Delta x}{2},t+\Delta t\right)=\phi(x+\Delta x,t+\Delta t)+\phi(x,t+\Delta t)+O(\Delta x)^2 \tag{2.104}$$

Similarly,

$$\phi(x,t)=\phi\left(x+\frac{\Delta x}{2},t\right)-\phi'\left(x+\frac{\Delta x}{2},t\right)\frac{\Delta x}{2}+O(\Delta x)^2 \tag{2.105}$$

$$\phi(x+\Delta x,t)=\phi\left(x+\frac{\Delta x}{2},t\right)+\phi'\left(x+\frac{\Delta x}{2},t\right)\frac{\Delta x}{2}+O(\Delta x)^2 \tag{2.106}$$

Adding Eqs. (2.105) and (2.106) results in

$$2\phi\left(x+\frac{\Delta x}{2},t\right)=\phi(x,t)+\phi(x+\Delta x,t)+O(\Delta x)^2 \tag{2.107}$$

Substitution of Eqs. (2.104) and (2.107) into Eq. (2.101) gives

$$\begin{aligned}\dot{\phi}\left(x+\frac{\Delta x}{2},t+\frac{\Delta t}{2}\right)\Delta t=&\frac{1}{2}[\phi(x+\Delta x,t+\Delta t)+\phi(x,t+\Delta t)-\phi(x,t)\\&-\phi(x+\Delta x,t)]+O\left[(\Delta x)^2,(\Delta t)^2\right]\end{aligned} \tag{2.108}$$

Finally, using Eq. (2.75) and Eq. (2.108), one obtains

$$\dot{\phi}\left(x+\frac{\Delta x}{2},t+\frac{\Delta t}{2}\right)=\frac{1}{2\Delta t}\left(\phi_{i+1}^{+}-\phi_{i+1}+\phi_{i}^{+}-\phi_{i}\right)+O\left(\Delta x^{2},\Delta t^{2}\right) \quad (2.109)$$

Therefore, the set of difference equations for a 1-D dynamic problem would be

$$\phi\left(x+\frac{\Delta x}{2},t+\frac{\Delta t}{2}\right)=\frac{1}{4}\left(\phi_{i+1}^{+}+\phi_{i}^{+}+\phi_{i+1}+\phi_{i}\right)+O\left(\Delta x^{2},\Delta t^{2}\right) \quad (2.87)$$

$$\phi'\left(x+\frac{\Delta x}{2},t+\frac{\Delta t}{2}\right)=\frac{1}{2\Delta x}\left(\phi_{i+1}^{+}-\phi_{i}^{+}+\phi_{i+1}-\phi_{i}\right)+O\left(\Delta x^{2},\Delta t^{2}\right) \quad (2.98)$$

$$\dot{\phi}\left(x+\frac{\Delta x}{2},t+\frac{\Delta t}{2}\right)=\frac{1}{2\Delta t}\left(\phi_{i+1}^{+}-\phi_{i+1}+\phi_{i}^{+}-\phi_{i}\right)+O\left(\Delta x^{2},\Delta t^{2}\right) \quad (2.109)$$

The quantities at the left-hand side of Eqs. (2.87), (2.98), and (2.109) are the elemental ones and are expressed in terms of the nodal values. Equations (2.87), (2.98), and (2.109) provide the second-order approximate finite difference expressions for a variable and its derivatives with respect to time and space. They were used in Ghorashi (1994) and in Esmailzadeh and Ghorashi (1997) to solve a moving load problem. In this research, by properly defining the initial and boundary conditions, these equations will be used to convert the discussed system of nonlinear partial differential equations into a set of linear algebraic difference equations.

References

Esmailzadeh, E., & Ghorashi, M. (1997). Vibration analysis of a Timoshenko beam subjected to a traveling mass. *Journal of Sound and Vibration, 199*(4), 615–628.

Ghorashi, M. (1994). *Dynamic and vibratory analysis of beams under dynamic loads induced by traveling masses and vehicles*. Ph.D. Thesis, Mechanical Engineering Department, Sharif University of Technology.

Hodges, D. H. (2006). *Nonlinear composite beam theory*. New York: AIAA.

Hodges, D. H., Atilgan, A. R., Cesnik, C. E. S., & Fulton, M. V. (1992). On a simplified strain energy function for geometrically nonlinear behavior of anisotropic beams. *Composites Engineering, 2*, 513–526.

Palacios, R. (2008). *Personal Communications*.

Reissner, E. (1973). On one-dimensional large-displacement finite-strain beam theory. *Studies in Applied Mathematics, LII*, 87–95.

Roy, S., & Yu, W. (2009). Dimensional reduction of a piezoelectric composite rod. *European Journal of Mechanics A/Solids, 28*, 368–376.

Traugott, J. P., Patil, M. J., & Holzapfel, F. (2005). Nonlinear dynamics and control of integrally actuated helicopter blades. In *Proceedings of the 46th AIAA/ASME/ASCE/AHS/ASC Structures, Structural Dynamics & Materials Conference*, April 18–21, 2005, Austin, Texas. Paper No: AIAA 2005-2271.

Wang, Q., & Yu, W. (2013). A refined model for thermoelastic analysis of initially curved and twisted composites beams. *Engineering Structures, 48*, 233–244.

Chapter 3
Linear Static Analysis of Composite Beams

3.1 Introduction

In Chap. 2, the set of governing equations for the nonlinear analysis of the elasto-dynamic response of a beam were reviewed. It was shown that this analysis requires the solution of a system of four nonlinear partial differential equations together with five linear vector equations for nine variables. As an especial case, in this chapter, the finite difference method (FDM) is used for calculating the linear static response of a beam. In this way, the performance of the mentioned formulation for analyzing a linear static beam problem is illustrated.

3.2 Linear Static Solution Using Finite Difference Method

Recalling the nonlinear intrinsic equations of motion of a composite beam with initial curvature and twist, i.e.,

$$F' + \widetilde{K}F + f = \dot{P} + \widetilde{\Omega}P \tag{2.26}$$

$$M' + \widetilde{K}M + (\widetilde{e}_1 + \widetilde{\gamma})F + m = \dot{H} + \widetilde{\Omega}H + \widetilde{V}P \tag{2.27}$$

and setting all of the linear and angular momentum terms equal to zero, the following equations for the nonlinear static case are obtained:

$$F' + \widetilde{K}F + f = 0 \tag{3.1}$$

$$M' + \widetilde{K}M + (\widetilde{e}_1 + \widetilde{\gamma})F + m = 0 \tag{3.2}$$

M. Ghorashi, *Statics and Rotational Dynamics of Composite Beams*,
DOI 10.1007/978-3-319-14959-2_3

Next, considering a situation where all terms that are products of two dependent variables (and hence are nonlinear) are small, the set of linear static equations are obtained as follows:

$$F' + \widetilde{k}F + f = 0 \tag{3.3}$$

$$M' + \widetilde{k}M + \widetilde{e}_1 F + m = 0 \tag{3.4}$$

On the other hand, recalling Eqs. (2.74) and (2.75), since in the special case of a static problem, variables do not change in time, at every spatial node *i*,

$$\phi_{i+1}^{+} = \phi_{i+1}, \quad \phi_{i}^{+} = \phi_{i} \tag{3.5}$$

Therefore, the static version of Eqs. (2.87) and (2.98) becomes the following:

$$\phi\left(x + \frac{\Delta x}{2}\right) = \frac{1}{2}\left(\phi_{i+1} + \phi_i\right) + O\left(\Delta x^2\right) \tag{3.6}$$

$$\phi'\left(x + \frac{\Delta x}{2}\right) = \frac{1}{\Delta x}\left(\phi_{i+1} - \phi_i\right) + O\left(\Delta x^2\right) \tag{3.7}$$

Now recall the strain–displacement equations,

$$\gamma = C(e_1 + u' + \widetilde{k}u) - e_1 \tag{2.57}$$

$$\kappa = \left(\frac{\Delta - \frac{1}{2}\widetilde{\theta}}{1 + \frac{1}{4}\theta^T\theta}\right)\theta' + Ck - k \tag{2.63}$$

together with

$$C = \frac{\left[1 - (1/4)\theta^T\theta\right]\Delta - \widetilde{\theta} + (1/2)\theta\theta^T}{1 + (1/4)\theta^T\theta} \tag{2.62}$$

Equation (2.62) can be linearized as follows:

$$C = \Delta - \widetilde{\theta} \tag{3.8}$$

Substituting Eq. (3.8) into Eq. (2.57) and linearizing the outcome gives the following:

$$\gamma = u' + \widetilde{k}u - \widetilde{\theta}e_1 \tag{3.9}$$

But, for any two 3 × 1 column vectors *Y* and *Z*,

$$\widetilde{Y}Z = -\widetilde{Z}Y \tag{3.10}$$

Therefore, Eq. (3.9) reduces to the following:

$$\gamma = u' + \widetilde{k}u + \widetilde{e}_1\theta \tag{3.11}$$

Similarly, the linearized form of Eq. (2.63) is:

$$\kappa = \theta' + Ck - k \tag{3.12}$$

Substitution of Eq. (3.8) into (3.12) gives the following:

$$\kappa = \theta' - \widetilde{\theta}k \tag{3.13}$$

Now, using Eq. (3.10), Eq. (3.13) changes to:

$$\kappa = \theta' + \widetilde{k}\theta \tag{3.14}$$

Since the vector of undeformed (initial) curvature and twist, *k*, is assumed to be known, Eq. (3.14) is linear. For a beam with zero initial curvature and twist, Eqs. (3.11) and (3.14) result in the following:

$$\gamma = u' + \widetilde{e}_1\theta \tag{3.15}$$

$$\kappa = \theta' \tag{3.16}$$

Now, recall the constitutive equation,

$$\begin{Bmatrix} \gamma \\ \kappa \end{Bmatrix} = \begin{bmatrix} R & Z \\ Z^T & T \end{bmatrix} \begin{Bmatrix} F \\ M \end{Bmatrix} \tag{2.56}$$

Substitution for γ and κ from Eq. (2.56) into the kinematical equations (3.15) and (3.16) gives the following:

$$RF + ZM = u' + \widetilde{e}_1\theta, \quad Z^TF + TM = \theta' \tag{3.17}$$

or

$$u' = -\widetilde{e}_1\theta + RF + ZM, \quad \theta' = Z^TF + TM \tag{3.18}$$

Equations (3.3), (3.4), and (3.18) form a set of four first-order vector (i.e., twelve scalar) differential equations for four vector variables. Once the boundary conditions at the two ends of the beam are specified, this boundary value problem can be solved for the four vector variables. Assuming zero distributed load (f = 0 and

$m = 0$) and zero initial twist and curvature, Eqs. (3.3) and (3.4) reduce to the following:

$$F' = 0, \quad M' = -\widetilde{e}_1 F \tag{3.19}$$

The finite difference equations (3.6) and (3.7) can now be used to convert the set of first-order differential equations (3.19) into the set of difference equations:

$$F_{i+1} = F_i \tag{3.20}$$

$$\frac{1}{\Delta x}(M_{i+1} - M_i) = -\widetilde{e}_1 \frac{1}{2}(F_{i+1} + F_i) \tag{3.21}$$

or

$$M_{i+1} + \frac{1}{2}\Delta x \widetilde{e}_1 F_{i+1} = M_i - \frac{1}{2}\Delta x \widetilde{e}_1 F_i \tag{3.22}$$

Similarly, the equivalent difference equations for Eq. (3.18) are as follows:

$$\frac{1}{\Delta x}(u_{i+1} - u_i) = -\widetilde{e}_1 \frac{1}{2}(\theta_{i+1} + \theta_i) + R\frac{1}{2}(F_{i+1} + F_i) + Z\frac{1}{2}(M_{i+1} + M_i) \tag{3.23}$$

$$\frac{1}{\Delta x}(\theta_{i+1} - \theta_i) = Z^T \frac{1}{2}(F_{i+1} + F_i) + T\frac{1}{2}(M_{i+1} + M_i) \tag{3.24}$$

or

$$\begin{aligned} &u_{i+1} + \frac{1}{2}\Delta x \widetilde{e}_1 \theta_{i+1} - \frac{1}{2}\Delta x R F_{i+1} \\ &\quad - \frac{1}{2}\Delta x Z M_{i+1} = u_i - \frac{1}{2}\Delta x \widetilde{e}_1 \theta_i + \frac{1}{2}\Delta x R F_i + \frac{1}{2}\Delta x Z M_i \end{aligned} \tag{3.25}$$

$$\theta_{i+1} - \frac{1}{2}\Delta x Z^T F_{i+1} - \frac{1}{2}\Delta x T M_{i+1} = \theta_i + \frac{1}{2}\Delta x Z^T F_i + \frac{1}{2}\Delta x T M_i \tag{3.26}$$

Equations (3.20), (3.22), (3.25), and (3.26) can be written in the following matrix form:

$$\begin{aligned} &\begin{bmatrix} I_{3\times3} & 0_{3\times3} & 0_{3\times3} & 0_{3\times3} \\ 0.5\Delta x \widetilde{e}_1 & I_{3\times3} & 0_{3\times3} & 0_{3\times3} \\ -0.5\Delta x R & -0.5\Delta x Z & I_{3\times3} & 0.5\Delta x \widetilde{e}_1 \\ -0.5\Delta x Z^T & -0.5\Delta x T & 0_{3\times3} & I_{3\times3} \end{bmatrix} \begin{Bmatrix} F_{i+1} \\ M_{i+1} \\ u_{i+1} \\ \theta_{i+1} \end{Bmatrix} \\ &= \begin{bmatrix} I_{3\times3} & 0_{3\times3} & 0_{3\times3} & 0_{3\times3} \\ -0.5\Delta x \widetilde{e}_1 & I_{3\times3} & 0_{3\times3} & 0_{3\times3} \\ 0.5\Delta x R & 0.5\Delta x Z & I_{3\times3} & -0.5\Delta x \widetilde{e}_1 \\ 0.5\Delta x Z^T & 0.5\Delta x T & 0_{3\times3} & I_{3\times3} \end{bmatrix} \begin{Bmatrix} F_i \\ M_i \\ u_i \\ \theta_i \end{Bmatrix} \end{aligned} \tag{3.27}$$

or

$$B_i q_{i+1} = A_i q_i \tag{3.28}$$

where

$$B_i = \begin{bmatrix} I_{3\times3} & 0_{3\times3} & 0_{3\times3} & 0_{3\times3} \\ 0.5\Delta x\widetilde{e}_1 & I_{3\times3} & 0_{3\times3} & 0_{3\times3} \\ -0.5\Delta xR & -0.5\Delta xZ & I_{3\times3} & 0.5\Delta x\widetilde{e}_1 \\ -0.5\Delta xZ^T & -0.5\Delta xT & 0_{3\times3} & I_{3\times3} \end{bmatrix}, \quad q_{i+1} = \begin{Bmatrix} F_{i+1} \\ M_{i+1} \\ u_{i+1} \\ \theta_{i+1} \end{Bmatrix} \tag{3.29}$$

$$A_i = \begin{bmatrix} I_{3\times3} & 0_{3\times3} & 0_{3\times3} & 0_{3\times3} \\ -0.5\Delta x\widetilde{e}_1 & I_{3\times3} & 0_{3\times3} & 0_{3\times3} \\ 0.5\Delta xR & 0.5\Delta xZ & I_{3\times3} & -0.5\Delta x\widetilde{e}_1 \\ 0.5\Delta xZ^T & 0.5\Delta xT & 0_{3\times3} & I_{3\times3} \end{bmatrix}, \quad q_i = \begin{Bmatrix} F_i \\ M_i \\ u_i \\ \theta_i \end{Bmatrix} \tag{3.30}$$

There are eight unknown scalars in the four algebraic equations (3.27). To obtain the unique solution of the problem, one needs to implement the boundary conditions by relating q_1 to q_{N} (N is the number of spatial nodes). To this end, and by using Eq. (3.28), one obtains the following:

$$q_i = \underbrace{A_i^{-1}B_i}_{a_i} q_{i+1} \tag{3.31}$$

So, one can now relate q_1 to q_2, q_2 to q_3, and so on. Therefore, finally q_1 would be related to q_N as follows:

$$q_1 = (a_1 a_2 \ldots a_{N-1}) q_N \tag{3.32}$$

One may define the following:

$$H_{N-1} = a_1 a_2 \ldots a_{N-1} \tag{3.33}$$

where

$$H_i = H_{i-1} a_i \tag{3.34}$$

In order to complete the solution, the boundary conditions of the problem should be implemented. Consider the cantilever beam shown in Fig. 2.5 where node 1 is fixed and node N is free. In this case, the displacements at $i = 1$ would be zero and the forces and moments at $i = N$ would be either known from the applied loading or just zero because of the free end condition. Thus, using the boundary conditions, half of the variables at these two nodes are already known and Eq. (3.32) relating q_1 and q_{N} gives the following:

$$\begin{Bmatrix} F_1 \\ M_1 \\ 0 \\ 0 \end{Bmatrix} = \underbrace{\begin{bmatrix} h_{11} & h_{12} & h_{13} & h_{14} \\ h_{21} & h_{22} & h_{23} & h_{24} \\ h_{31} & h_{32} & h_{33} & h_{34} \\ h_{41} & h_{42} & h_{43} & h_{44} \end{bmatrix}}_{H_{N-1}} \begin{Bmatrix} F_N \\ M_N \\ u_N \\ \theta_N \end{Bmatrix} \tag{3.35}$$

Equation (3.35) has four unknown scalars and four scalar equations. Using the last two rows of Eq. (3.35),

$$\begin{Bmatrix} 0 \\ 0 \end{Bmatrix} = \begin{bmatrix} h_{31} & h_{32} \\ h_{41} & h_{42} \end{bmatrix} \begin{Bmatrix} F_N \\ M_N \end{Bmatrix} + \begin{bmatrix} h_{33} & h_{34} \\ h_{43} & h_{44} \end{bmatrix} \begin{Bmatrix} u_N \\ \theta_N \end{Bmatrix} \tag{3.36}$$

from which the unknown displacements at the free end (node N) of the beam are as follows:

$$\begin{Bmatrix} u_N \\ \theta_N \end{Bmatrix} = -\begin{bmatrix} h_{33} & h_{34} \\ h_{43} & h_{44} \end{bmatrix}^{-1} \begin{bmatrix} h_{31} & h_{32} \\ h_{41} & h_{42} \end{bmatrix} \begin{Bmatrix} F_N \\ M_N \end{Bmatrix} \tag{3.37}$$

Substituting Eq. (3.37) into (3.35) results in the unknown forces and moments at node 1,

$$\begin{Bmatrix} F_1 \\ M_1 \end{Bmatrix} = \begin{bmatrix} h_{11} & h_{12} & h_{13} & h_{14} \\ h_{21} & h_{22} & h_{23} & h_{24} \end{bmatrix} \begin{Bmatrix} F_N \\ M_N \\ u_N \\ \theta_N \end{Bmatrix} \tag{3.38}$$

Having obtained the unknowns at boundary nodes 1 and N, one may use Eq. (3.28) to get the solution at all intermediate nodes by solving a system of four equations with four unknowns.

3.3 Case Study: Isotropic Rectangular Solid Model

Figure 3.1 illustrates a prismatic member having a solid rectangular section. To provide a numerical example, it is assumed that the beam has been made of a hypothetical homogeneous and isotropic material for which,

$$\begin{aligned} &E = 17,920\ \text{GPa}, \quad \upsilon = 0.3 \\ &A = 0.02\,\text{m}^2, \quad \rho = 1770\,\text{kg/m}^3 \end{aligned} \tag{3.39}$$

The origin of the coordinate system is located at the shear center of the cross section which in this case is identical to the centroid of the section. The following concentrated force and concentrated moment are applied at the tip of the beam:

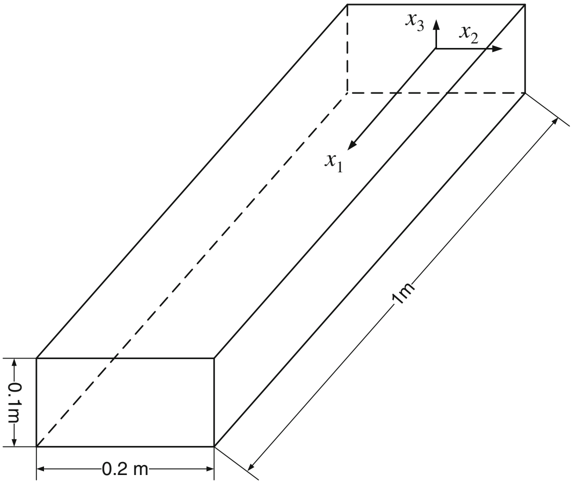

Fig. 3.1 The geometry of the beam and the coordinate system

$$F_1 = 10,000\,\mathrm{N}, \quad M_2 = 1000\,\mathrm{N.m} \tag{3.40}$$

It should be emphasized that the subscripts in Eq. (3.40) refer to the directions at which the mentioned forces and moments act, not to the node numbers. In this problem, the matrix of the cross-sectional mass moments of inertia, introduced in Eq. (2.48), can be calculated as follows:

$$i = \begin{bmatrix} 8.333 & 0 & 0 \\ 0 & 1.6667 & 0 \\ 0 & 0 & 6.6667 \end{bmatrix} \times 10^{-5} \times 1770\ \mathrm{kg.m} \tag{3.41}$$

The sectional stiffness matrix has been computed by VABS:

$$S = \begin{bmatrix} 0.358\times10^{12} & 0 & 0 & 0 & 0 & 0 \\ 0 & 0.1373\times10^{12} & 0 & 0 & 0 & 0 \\ 0 & 0 & 0.1074\times10^{12} & 0 & 0 & 0 \\ 0 & 0 & 0 & 0.354\times10^{9} & 0 & 0 \\ 0 & 0 & 0 & 0 & 0.298\times10^{9} & 0 \\ 0 & 0 & 0 & 0 & 0 & 0.119\times10^{10} \end{bmatrix} \tag{3.42}$$

Now, recalling Eq. (2.56),

$$S^{-1} = \begin{bmatrix} R & Z \\ Z^T & T \end{bmatrix} \tag{3.43}$$

where matrices R, T, and Z can be calculated by inverting Eq. (3.42). The results are as follows:

$$R = \begin{bmatrix} 2.793 & 0 & 0 \\ 0 & 7.283 & 0 \\ 0 & 0 & 9.307 \end{bmatrix} \times 10^{-12} \frac{\mathrm{s}^2}{\mathrm{kg.m}},$$
$$T = \begin{bmatrix} 28.21 & 0 & 0 \\ 0 & 33.52 & 0 \\ 0 & 0 & 8.382 \end{bmatrix} \times 10^{-10} \frac{\mathrm{s}^2}{\mathrm{kg.m}^3}, \quad \mathrm{Z} = 0_{3\mathrm{x}3} \tag{3.44}$$

For the loading given in Eq. (3.40) applied at the tip of the beam, the algorithm mentioned in Sect. 3.2 provides the results that are shown in Figs. 3.2, 3.3, 3.4, and 3.5. As expected, the induced axial force shown in Fig. 3.2 is equal to the applied force and all shear forces are zero. The internal moment illustrated in Fig. 3.3 is also equal to the applied moment. This is expected because there is no transverse load that can generate any bending moment other than that of the applied moment.

The distributions of linear and angular displacements are justifiable too, and they compare very well with the corresponding analytical solutions. For example, at an arbitrary position x_1 (in meters) from the clamped end,

$$u_1 = \frac{F_1 x_1}{AE} = \frac{10,000 \times x_1}{0.02 \times 1.7926 \times 10^{13}} = 2.7892 \times 10^{-8}\, x_1 \text{ m} \tag{3.45}$$

The distribution given by Eq. (3.45) is shown in Fig. 3.4, and it compares very well with the numerical solution. For bending deformation, the analytical solution is as follows:

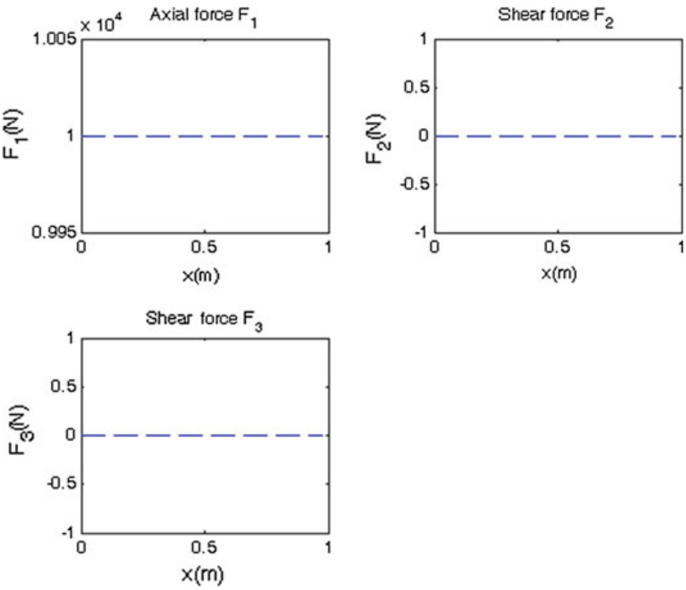

Fig. 3.2 The distribution of internal force components along the isotropic blade

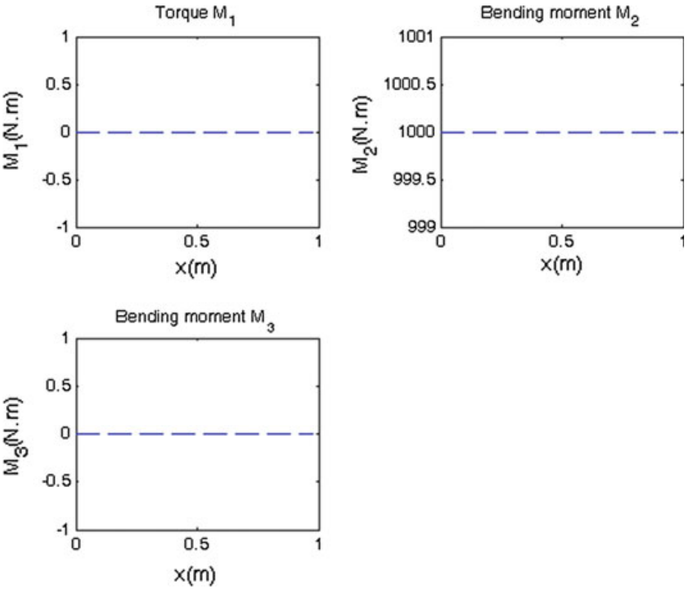

Fig. 3.3 The distribution of internal moment components along the isotropic blade

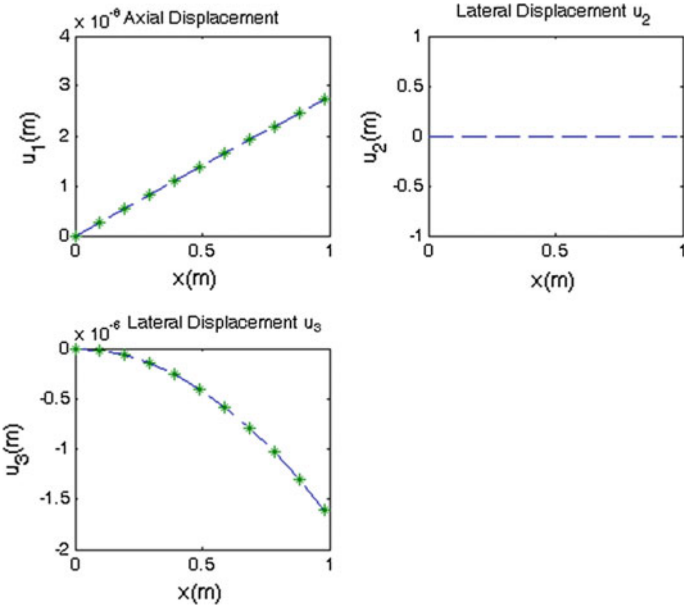

Fig. 3.4 The distribution of displacement components along the isotropic beam FDM (*dashed*) and exact solution (*asterisk*)

$$u_3 = \frac{-\frac{1}{2}M_2 x_1^2}{E(i_2/\rho)} = \frac{-\frac{1}{2}\times 1000 \times x_1^2}{1.7926\times 10^{13}\times 1.6667\times 10^{-5}} = -1.673\times 10^{-6}\times x_1^2\,\mathrm{m} \tag{3.46}$$

So, positive M_2 produces negative u_3. By combining Eqs. (3.45) and (3.46), the analytically calculated displacement field would be the following:

$$u = x_1 \times 10^{-8}\left(\begin{Bmatrix} 2.7892 \\ 0 \\ 0 \end{Bmatrix} - 100x_1\begin{Bmatrix} 0 \\ 0 \\ 1.673 \end{Bmatrix}\right) \tag{3.47}$$

Equation (3.47) has been plotted in Fig. 3.4 and is in good agreement with the displacement calculated numerically. Finally, for rotation θ_2 generated by the applied loading, the analytical solution is as follows:

$$\theta_2 = -u_3' = \frac{M_2 x_1}{E(i_2/\rho)} = \frac{1000\times x_1}{1.7926\times 10^{13}\times 1.6667\times 10^{-5}} = 3.347\times 10^{-6}\times x_1\,\mathrm{rad} \tag{3.48}$$

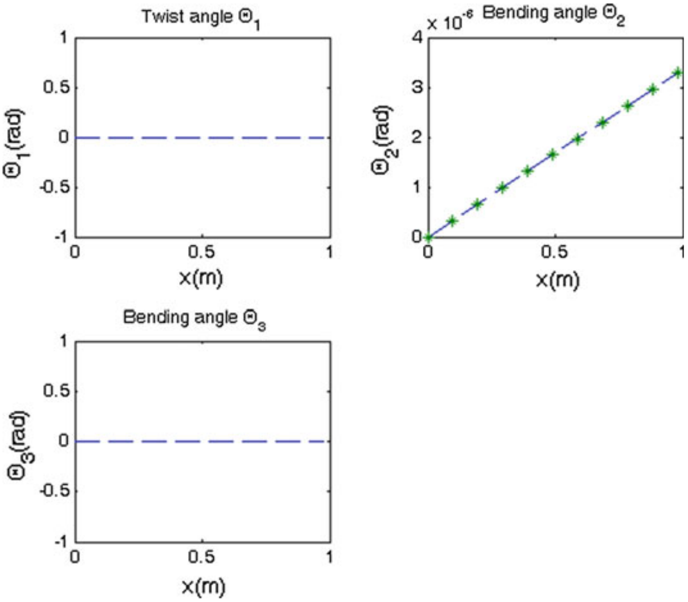

Fig. 3.5 The distribution of rotation components along the isotropic beam FDM (*dashed*) and exact solution (*asterisk*)

or

$$\theta = x_1 \times \begin{Bmatrix} 0 \\ 3.352 \\ 0 \end{Bmatrix} \times 10^{-6}\,\text{rad} \tag{3.49}$$

Equation (3.49) has been plotted in Fig. 3.5 and is in good agreement with the displacement field calculated numerically.

3.4 Case Study: Composite Box Model

Figure 3.6 illustrates a composite square box beam with constant properties along its longitudinal axis and a cross section with 2.5 cm distance between the midlines. The upper and lower sides are made of four plies of AS4/3506-1 at 45°, and the lateral sides are made of four plies of a typical anisotropic piezocomposite actuator (APA) at −45°. These ply angles are the angles of fibers with respect to the longitudinal *x*-axis as shown in Fig. 3.7. If the fibers were in the 1st and 3rd quadrants of the *x*–*y* coordinate system, the ply angle would be positive. If the fibers were in the 2nd and 4th quadrants of the *x*–*y* coordinate system, the ply angle would be negative.

Fig. 3.6 The UM/VABS model for the box beam as used in Cesnik and Palacios (2003)

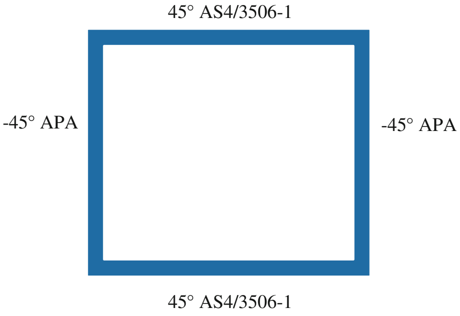

Fig. 3.7 The laminate and convention for material orientation

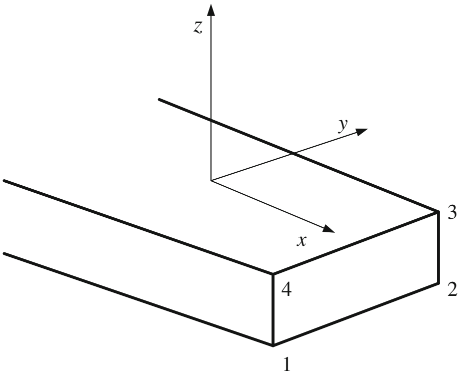

This model has been discussed in Cesnik and Palacios (2003), and the UM/VABS input file for this case has been among the examples provided with the software. It uses the CQUAD8 element that is an eight-nodded element, and it follows the numbering scheme illustrated in Fig. 3.7. In this scheme, the first two nodes (1 and 2) define the local *y*-axis, whereas nodes 2 and 3 define the local *z*-axis; and then having *y*- and *z*-axes, the cross product of *y* by *z* would give the *x*-axis. In this way, by stating the numbering sequence of the nodes, the local coordinate system would be completely defined.

The material properties of the fiber-reinforced composite material have been stated in the material coordinate system, e_i, $i = 1, 2, 3$. Direction $i = 1$ is the fiber direction, direction $i = 2$ is the transverse direction but in plane of the layer, and direction $i = 3$ is the transverse direction but out of plane of the layer. The material properties include Young's modulus in the *i* direction, E_i; Poisson's ratio in the *i*–*j* plane ν_{ij} for the material loaded in the *i* direction and its transversal deformation measured in the *j* direction; shear modulus in the *i*–*j* plane, G_{ij}; mass density, ρ; and the coefficient of thermal expansion in the *i* direction, α_i, where $i, j = 1, 2, 3$.

For this case study, some of these material properties are listed in Table 3.1. Here only the passive mechanical properties are used in the model. The active material properties will be introduced and used in Chap. 8. Furthermore, $E_3 = 0.8E_2$, $\rho = 1770\ \mathrm{kg/m^3}$ and the following equation provides the material properties that are not given.

$$E_i \nu_{ji} = E_j \nu_{ij} \quad i,j = 1,2,3 \tag{3.50}$$

In addition, the thickness of each ply is 0.127 mm and the length of the box, *L*, is 1 m.

Using UM/VABS, the 2-D cross-sectional analysis has been performed and the cross-sectional matrices of stiffness and mass moments of inertia were calculated as follows:

$$S = \begin{bmatrix} 7.977\times10^{5} & -0.9873 & -0.8575 & -1.5056\times10^{3} & -7.3017\times10^{-3} & 1.348\times10^{-3} \\ -0.9873 & 2.5482\times10^{5} & 4.6845\times10^{-3} & -3.897\times10^{-3} & 1.962\times10^{3} & 5.9626\times10^{-5} \\ -0.8575 & 4.6845\times10^{-3} & 2.296\times10^{5} & 1.0716\times10^{-2} & 9.912\times10^{-5} & -2.8055\times10^{2} \\ -1.5056\times10^{3} & -3.897\times10^{-3} & 1.0716\times10^{-2} & 86.95 & 2.1193\times10^{-4} & 1.6532\times10^{-4} \\ -7.3017\times10^{-3} & 1.962\times10^{3} & 9.912\times10^{-5} & 2.1193\times10^{-4} & 90.397 & 3.6091\times10^{-6} \\ 1.348\times10^{-3} & 5.9626\times10^{-5} & -2.8055\times10^{2} & 1.6532\times10^{-4} & 3.6091\times10^{-6} & 79.4434 \end{bmatrix} \tag{3.51}$$

Table 3.1 Material properties of the active box beam (1 = fiber direction, 2 = transverse and in plane of the layer, 3 = out of plane), Cesnik and Palacios (2003)

	E_1 (GPa)	E_2 (GPa)	G_{12} (GPa)	G_{23} (GPa)	ν_{12}	ν_{23}	d_{111} (pm/V)	d_{112} (pm/V)	*t* (mm)	Distance between electrodes (mm)
AS4/3506-1	142	9.8	6.0	4.8	0.3	0.42	_	_	0.127	_
APA	42.2	17.5	5.5	4.4	0.354	0.42	381	−160	0.127	1.143

$$i = \begin{bmatrix} 9.9555 & 0 & 0 \\ 0 & 4.9777 & 0 \\ 0 & 0 & 4.9777 \end{bmatrix} \times 10^{-9} \times 1770\ \text{kg.m} \tag{3.52}$$

Now, consider the following concentrated loading at the tip of the box beam (i.e., at the free end)

$$F_1 = 100\,\text{N}, \quad M_2 = 10\,\text{N.m} \tag{3.53}$$

where the subscripts refer to the global coordinate system shown in Fig. 3.1 (not to the node numbers or the principal material directions).

The response of the composite box beam is obtained by the method that was explained in Sect. 3.2, and the results are illustrated in Figs. 3.8, 3.9, 3.10, and 3.11. As expected, the internal axial force in Fig. 3.8 is equal to the applied force and all shear forces are zero. In Fig. 3.9, the induced moment is seen to be equal to the applied moment. This is expected as there is no transversal load that can generate moments other than that of the applied moment. The force and moment distributions in this case are similar to those of an isotropic material (shown in Figs. 3.2 and 3.3).

As to the linear and angular displacements shown in Figs. 3.10 and 3.11, because of the coupling terms in the stiffness matrix of the composite structure, u_2, θ_1, and θ_3 are no longer zero. It is in contrast with Figs. 3.4 and 3.5 for an isotropic material subjected to a similar loading in which u_2, θ_1, and θ_3 have all been calculated to be zero. The reason is because in the case of an isotropic material such coupling terms do not exist.

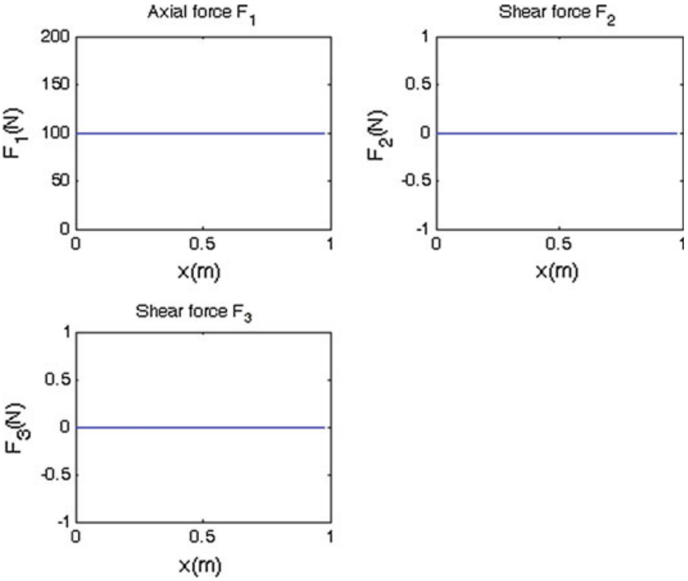

Fig. 3.8 The distribution of internal force components along the composite box beam

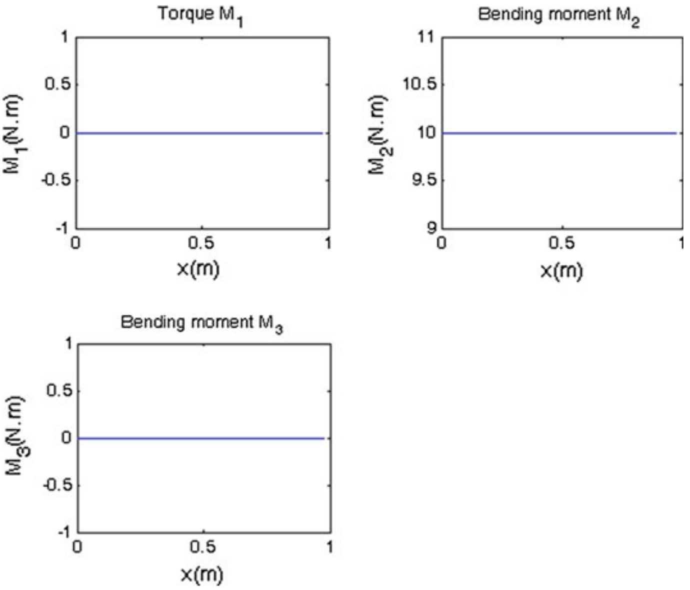

Fig. 3.9 The distribution of internal moment components along the composite box beam

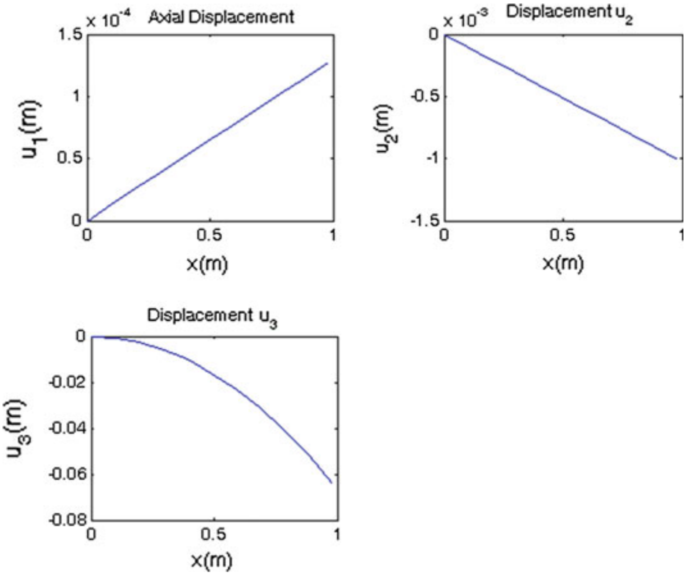

Fig. 3.10 The distribution of displacement components along the composite box beam

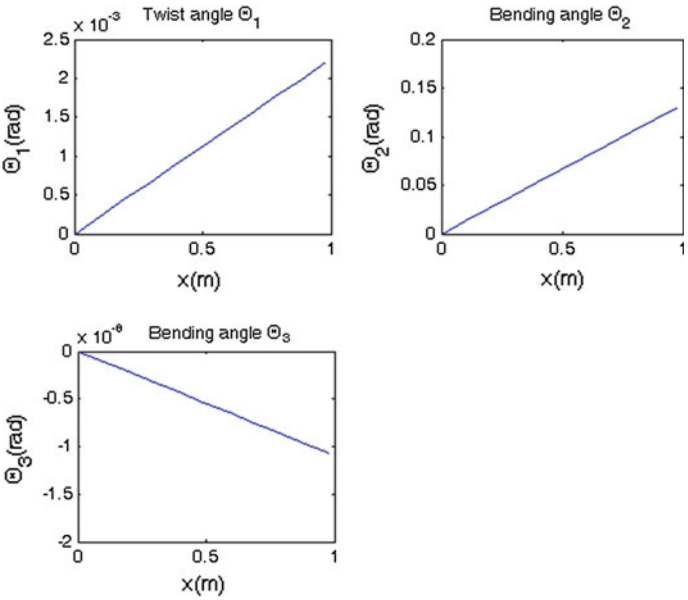

Fig. 3.11 The distribution of rotation components along the composite box beam

3.5 Calculation of 3-D Strain and 3-D Stress Using 2-D and 1-D Analyses

Having solved the 2-D cross-sectional problem by VABS and the 1-D beam problem by the method explained in Sect. 3.2, these results can now be combined to provide the generalized stress and strain values. The procedure that is necessary for performing such calculations has been discussed in Sect. 2.5, and it is implemented here for a beam made of an isotropic material.

Consider a cantilever beam that is 1 m wide and 2 m thick and is 10 m in length. The beam has been made of a hypothetical material with the following properties:

$$E = 2.6\,\text{GPa} \quad G = 1\,\text{GPa} \tag{3.54}$$

The following concentrated loads are now applied at the free end of the beam, and the aim is to apply the mentioned procedure for calculating stress and strain distributions.

$$\hat{F} = \begin{Bmatrix} 100 \\ 0 \\ 0 \end{Bmatrix} \text{N}, \quad \hat{M} = \begin{Bmatrix} 0 \\ 100 \\ 0 \end{Bmatrix} \text{N.m} \tag{3.55}$$

The load components are expressed in the global coordinate system shown in Fig. 3.1. For this linear static case, with zero distributed load ($f = 0$ and $m = 0$) and zero initial twist and curvature, Eq. (3.19) is applicable. Using the tip values of force and moment as the imposed boundary conditions, one obtains the following:

$$M = (L - x_1)\widetilde{e}_1\hat{F} + \hat{M} \tag{3.56}$$

Substituting Eq. (3.56) into (2.56) results in the following:

$$\begin{Bmatrix} \gamma \\ \kappa \end{Bmatrix} = \begin{bmatrix} R & Z \\ Z^T & T \end{bmatrix} \begin{Bmatrix} \hat{F} \\ \hat{M} + (L - x_1)\widetilde{e}_1\hat{F} \end{Bmatrix} \tag{3.57}$$

Equation (3.57) can be rewritten as follows:

$$\begin{Bmatrix} \gamma \\ \kappa \end{Bmatrix} = \begin{bmatrix} R & Z \\ Z^T & T \end{bmatrix} \begin{bmatrix} \Delta & 0 \\ (L - x_1)\widetilde{e}_1 & \Delta \end{bmatrix} \begin{Bmatrix} \hat{F} \\ \hat{M} \end{Bmatrix} \tag{3.58}$$

Now, combining Eq. (3.16) and (3.58), one obtains the following:

$$\theta' = \left[Z^T + (L - x_1)T\widetilde{e}_1\right]\hat{F} + T\hat{M} \tag{3.59}$$

Using the following boundary condition at the clamped end,

$$x_1 = 0, \quad \theta = 0 \tag{3.60}$$

Equation (3.59) may be integrated to give:

$$\theta(x_1) = \left[x_1 Z^T + (Lx_1 - 0.5x_1^2)T\widetilde{e}_1\right]\hat{F} + x_1 T\hat{M} \tag{3.61}$$

Substitution of the numerical values in Eq. (3.61) results in the following:

$$\theta = x_1 \times \begin{Bmatrix} 0 \\ 5.77 \\ 0 \end{Bmatrix} \times 10^{-8} \text{ rad} \tag{3.62}$$

This result is reasonable. First, F has no rotational effect, and secondly, M is applied about x_2. That is why it produces rotation about x_2. This rotation increases linearly with x_1 (measured from the fixed end and in meters). Having calculated the rotation vector in Eq. (3.62), one can now compute the rotation matrix C by using Eq. (2.62). This matrix, for such a lightly loaded beam, is very close to the identity matrix, as expected. The displacement vector, u, can be calculated using Eq. (3.15) which is the linearized form of Eq. (2.57).

$$\gamma = u' + \widetilde{e}_1\theta \tag{3.15}$$

Expansion of Eq. (3.57) gives the following:

$$\gamma = [R + (L - x_1)Z\widetilde{e}_1]\hat{F} + Z\hat{M} \tag{3.63}$$

Using the given numerical values in Eq. (3.63) results in the following:

$$\gamma = 10^{-8}\begin{Bmatrix} 1.92 \\ 0 \\ 0 \end{Bmatrix} \tag{3.64}$$

Substituting Eqs. (3.62) and (3.64) into Eq. (3.15) and applying the boundary condition

$$x_1 = 0, \quad u = 0 \tag{3.65}$$

gives

$$u = x_1 \times 10^{-8}\left(\begin{Bmatrix} 1.92 \\ 0 \\ 0 \end{Bmatrix} - 0.5x_1\begin{Bmatrix} 0 \\ 0 \\ 5.77 \end{Bmatrix}\right) \text{m} \tag{3.66}$$

So, the moment about x_2 has produced u_3, and for positive M_2, the corresponding u_3 is negative, as expected. Using Eq. (3.65), the displacement vector at the tip of the 10 m beam is as follows:

$$u = \begin{Bmatrix} 1.92 \times 10^{-7} \\ 0 \\ -28.85 \times 10^{-7} \end{Bmatrix} \text{m} \tag{3.67}$$

To obtain the stress distribution, one may use the calculated u, θ, and C matrices in the VABS input file. VABS then uses these data, as well as the sectional stiffness and inertia matrices and the warping functions to calculate the 3-D stress and strain matrices along the beam. The calculations are performed at the Gaussian points across the section. As an example, at a Gaussian point with x_3 = 0.887m, a stress value $\sigma_1 = -83\,\text{Pa}$ is calculated by VABS. At the same location, using the following well-known linear elasticity equation, one obtains the following:

$$\sigma_1 = -\frac{M_2 x_3}{I_2} + \frac{F_1}{A} \tag{3.68}$$

or

$$\sigma_1 = \frac{-100 \times \overbrace{0.887}^{\text{Gaussian Point}}}{(1 \times 2^3/12)} + \frac{100}{2} = -83\,\text{Pa} \tag{3.69}$$

which is identical to the VABS output.

Reference

Cesnik, C. E. S., & Palacios, R. (2003). Modeling piezocomposite actuators embedded in slender structures. In *Proceedings of the 44th AIAA/ASME/ASCE/AHS Structures, Structural Dynamics, and Materials Conference*, 7–10 April, 2003, Norfolk, Virginia. Paper No.: AIAA 2003-1803.

Chapter 4
Nonlinear Static Analysis of Composite Beams

4.1 Introduction

In Chap. 3, the linear static analysis of composite beams was carried out by using the finite difference method and by transforming a set of linear differential equations to a corresponding set of difference equations. These equations were then solved by applying the boundary conditions. A linear solution is based on equilibrium equations written with respect to the undeformed geometry. However, linearization of differential equations is not always justifiable. If the displacements are large, the nonlinear solution with equations of equilibrium written with respect to the deformed geometry should be taken into consideration. In such a case, the governing differential equations cannot be linearized without compromising the accuracy of the solution. Therefore, other methods of solution such as perturbations should be used instead.

4.2 Case Study: Solving a Nonlinear Initial Value Problem

Let us illustrate the perturbations method with an example. Consider the following nonlinear ordinary differential equation that illustrates an initial value problem,

$$\dot{x}(t) + 0.03x^2(t) = \sin(t), \quad x(0) = 0 \tag{4.1}$$

Due to the continuity of $x(t)$, for a small time increment Δt, the value of the dependent variable in the following time step, i.e., $x(t + \Delta t)$ or x^+, is only slightly away from the value of the dependent variable at the present time, $x(t)$ or x. This slight variation or perturbation is shown by $\widehat{x}$. So,

M. Ghorashi, *Statics and Rotational Dynamics of Composite Beams*,
DOI 10.1007/978-3-319-14959-2_4

$$x(t+\Delta t) - x(t) = \widehat{x} \tag{4.2}$$

or

$$x^{+} = x + \widehat{x} \tag{4.3}$$

Using Taylor series and forward differences, i.e.,

$$x(t+\Delta t) = x(t) + \dot{x}(t)\Delta t + \frac{1}{2!}\ddot{x}(\xi)(\Delta t)^2 \tag{4.4}$$

One obtains,

$$\dot{x}(t) = \frac{1}{\Delta t}[x(t+\Delta t) - x(t)] - \frac{1}{2!}\ddot{x}(\xi)\Delta t \tag{4.5}$$

or

$$\dot{x}(t) = \frac{1}{\Delta t}[x(t+\Delta t) - x(t)] + O(\Delta t) \tag{4.6}$$

A more accurate forward difference approximation is given as follows:

$$\dot{x}(t) = \frac{1}{2\Delta t}[-3x(t) + 4x(t+\Delta t) - x(t+2\Delta t)] + O(\Delta t)^2 \tag{4.7}$$

However, this one requires two initial conditions that are not available in a first-order problem given in Eq. (4.1). One may now start the solution by substituting Eq. (4.6) into (4.1) to get the following equation:

$$\frac{1}{\Delta t}[x(t+\Delta t) - x(t)] + 0.03x^2(t) = \sin(t) \tag{4.8}$$

Using Eqs. (4.2) and (4.8), the following equation for the perturbations is obtained as

$$\widehat{x} = \Delta t\left(\sin(t) - 0.03x^2\right) \tag{4.9}$$

Equations (4.3) and (4.9) result in the following perturbation solution for Eq. (4.1),

$$x^{+} = x + \Delta t\left(\sin(t) - 0.03x^2\right) \tag{4.10}$$

The solution starts at the initial condition $x(0) = 0$. Then, the repetitive use of Eq. (4.10) provides future values of the dependent variable, x, at corresponding t values.

At each iteration, the current t and x values are updated. Figure 4.1 illustrates the outcome of this procedure and the corresponding Runge–Kutta solution. The two results are undistinguishable.

Another way of solving Eq. (4.1) using perturbations is to solve it in two steps. First is to use Eq. (4.10) only once to produce a second "initial condition," Then, these two initial conditions can be used together in the more accurate Eq. (4.7) in order to continue the solution.

In general, for a continuous variable $\phi(t)$ with gradual changes if its value ϕ at an instant t is known its perturbed value ϕ^+ (after a small increment Δt of the independent variable t) would not be far from ϕ. So, the perturbed variable can be written as

$$\phi^+ = \phi + \overset{\frown}{\phi} \tag{4.11}$$

where $\overset{\frown}{\phi}$ is the small perturbation of the dependent variable ϕ.

Substitution of Eq. (4.11) into the nonlinear differential equation of interest and then ignoring higher order terms of $\overset{\frown}{\phi}$ result in a set of linear equations for the unknown perturbations $\overset{\frown}{\phi}$. These equations, using initial conditions, may then be solved for $\overset{\frown}{\phi}$. Having obtained the perturbations, they can be substituted into Eq. (4.11) in order to provide the solution of the nonlinear problem.

If ϕ is not small, linearization of nonlinear terms involving ϕ in the governing equations may not be justifiable. However, if ϕ varies slowly, then its perturbations would be small. Consequently, linearizing higher order terms containing $\overset{\frown}{\phi}$ can be done without a problem. By choosing small enough time steps, perturbations can be made as small as needed to increase the accuracy of the solution. However, too small time steps will clearly increase the solution time.

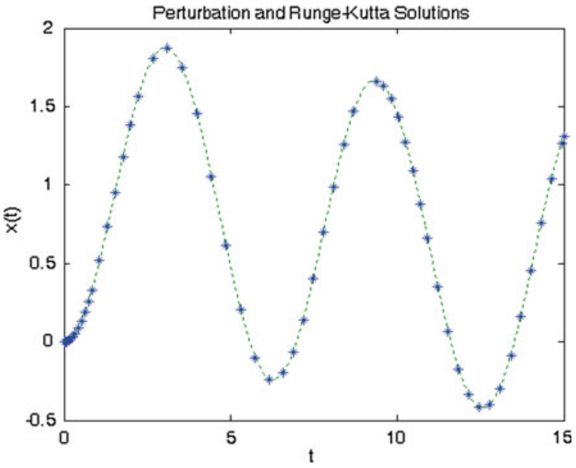

Fig. 4.1 The two solutions for Eq. (4.1): using the Runge–Kutta method (asterisks) and the perturbation method (dashes)

4.3 The Governing Nonlinear Statics Equations

The general nonlinear static intrinsic equations of a beam were discussed in Chap. 3 and are reminded here as follows:

$$F' + \tilde{K}F + f = 0 \tag{3.1}$$

$$M' + \tilde{K}M + (\tilde{e}_1 + \tilde{\gamma})F + m = 0 \tag{3.2}$$

The constitutive equations are given as

$$\begin{Bmatrix} \gamma \\ \kappa \end{Bmatrix} = \begin{bmatrix} R & Z \\ Z^T & T \end{bmatrix} \begin{Bmatrix} F \\ M \end{Bmatrix} \tag{2.56}$$

Equations (3.1), (3.2), and (2.56) form a system of four equations in terms of four unknowns, i.e., F, M, κ, and γ. Once the boundary conditions imposed on the beam are specified, this system of equations can be solved. Then, other relevant unknowns, i.e., K, C, θ, and u, can be calculated using Eqs. (2.36), (2.57), (2.62), and (2.63), repeated here for convenience,

$$K = k + \kappa \tag{2.36}$$

$$\gamma = C(e_1 + u' + \tilde{k}u) - e_1 \tag{2.57}$$

$$C = \frac{\left[1 - (1/4)\theta^T\theta\right]\Delta - \tilde{\theta} + (1/2)\theta\theta^T}{1 + (1/4)\theta^T\theta} \tag{2.62}$$

$$\kappa = \left(\frac{\Delta - \frac{1}{2}\tilde{\theta}}{1 + \frac{1}{4}\theta^T\theta}\right)\theta' + Ck - k \tag{2.63}$$

Solution of Eqs. (2.57) and (2.63) that are differential equations in terms of u and θ, respectively, requires the application of proper boundary conditions for u and θ. Also, if the initial (undeformed) twist and curvature values are zero, then $k = 0$ and using Eq. (2.36), $K = \kappa$. Otherwise, the total twist and curvature K should be calculated using Eq. (2.36).

4.4 Perturbation Formulation of the Nonlinear Static Problem

The following finite difference equations have already been derived for a static problem,

$$\phi\left(x+\frac{\Delta x}{2}\right)=\frac{1}{2}\left(\phi_{i+1}+\phi_i\right)+O\left(\Delta x^2\right) \tag{3.6}$$

$$\phi'\left(x+\frac{\Delta x}{2}\right)=\frac{1}{\Delta x}\left(\phi_{i+1}-\phi_i\right)+O\left(\Delta x^2\right) \tag{3.7}$$

In order to deal with nonlinearities in a static problem, one needs to introduce space perturbations. For a fine mesh and a continuously varying variable ϕ with gradual changes, its value at the spatial node i + 1 is close to its value at node i. Therefore, spatial perturbation, $\breve{\phi}_{i+1}$, can be defined as follows:

$$\phi_{i+1}=\phi_i+\breve{\phi}_{i+1} \tag{4.12}$$

which may be compared with the time perturbation defined in Eq. (4.3). Substituting Eq. (4.12) into Eqs. (3.6) and (3.7) gives the following:

$$\phi\left(x+\frac{\Delta x}{2}\right)=\phi_i+\frac{1}{2}\breve{\phi}_{i+1} \tag{4.13}$$

$$\phi'\left(x+\frac{\Delta x}{2}\right)=\frac{1}{\Delta x}\breve{\phi}_{i+1} \tag{4.14}$$

The nonlinear terms in Eqs. (3.1) and (3.2) are products and for highly nonlinear cases these terms may be large so one cannot linearize the system just by assuming that the nonlinear terms are ignorable. That is exactly why perturbations should be used. Unlike using the original variables, when their perturbations are used, one can linearize the resulting equations based on the fact that perturbations are small and therefore their product (i.e., the nonlinear term) is negligible.

Now considering a generic nonlinear product term, $\phi\left(x+\frac{\Delta x}{2}\right)\times\gamma\left(x+\frac{\Delta x}{2}\right)$, one may try to express it in terms of the nodal functional values and their perturbations. Using Eq. (4.13), one obtains the following:

$$\phi\left(x+\frac{\Delta x}{2}\right)\times\gamma\left(x+\frac{\Delta x}{2}\right)=\left(\phi_i+\frac{1}{2}\breve{\phi}_{i+1}\right)\left(\gamma_i+\frac{1}{2}\breve{\gamma}_{i+1}\right) \tag{4.15}$$

Since perturbations are small, one may ignore the small nonlinear perturbation term, $\frac{1}{4}\breve{\phi}_{i+1}\breve{\gamma}_{i+1}$ to get,

$$\phi\left(x+\frac{\Delta x}{2}\right)\times\gamma\left(x+\frac{\Delta x}{2}\right)=\phi_i\gamma_i+\frac{1}{2}\phi_i\breve{\gamma}_{i+1}+\frac{1}{2}\breve{\phi}_{i+1}\gamma_i \tag{4.16}$$

On the other hand, assuming zero initial twist and curvatures, i.e., k = 0, Eq. (3.1) becomes as follows:

$$F' + \tilde{\kappa} F + f = 0 \tag{4.17}$$

Using Eqs. (3.6), (4.14), and (4.16) in Eq. (4.17) results in the following equation:

$$\frac{1}{\Delta x}\breve{F}_{i+1} + \left(\tilde{\kappa}_i F_i + \frac{1}{2}\tilde{\kappa}_i \breve{F}_{i+1} + \frac{1}{2}\breve{\tilde{\kappa}}_{i+1} F_i\right) + \frac{1}{2}(f_{i+1} + f_i) = 0 \tag{4.18}$$

or

$$\begin{aligned} &\frac{1}{\Delta x}\begin{Bmatrix} \breve{F}_1 \\ \breve{F}_2 \\ \breve{F}_3 \end{Bmatrix}_{i+1} + \begin{bmatrix} 0 & -\kappa_3 & \kappa_2 \\ \kappa_3 & 0 & -\kappa_1 \\ -\kappa_2 & \kappa_1 & 0 \end{bmatrix}_i \begin{Bmatrix} F_1 \\ F_2 \\ F_3 \end{Bmatrix}_i + \frac{1}{2}\begin{bmatrix} 0 & -\kappa_3 & \kappa_2 \\ \kappa_3 & 0 & -\kappa_1 \\ -\kappa_2 & \kappa_1 & 0 \end{bmatrix}_i \begin{Bmatrix} \breve{F}_1 \\ \breve{F}_2 \\ \breve{F}_3 \end{Bmatrix}_{i+1} \\ &\qquad + \frac{1}{2}\begin{bmatrix} 0 & -\breve{\kappa}_3 & \breve{\kappa}_2 \\ \breve{\kappa}_3 & 0 & -\breve{\kappa}_1 \\ -\breve{\kappa}_2 & \breve{\kappa}_1 & 0 \end{bmatrix}_{i+1} \begin{Bmatrix} F_1 \\ F_2 \\ F_3 \end{Bmatrix}_i + \frac{1}{2}\begin{Bmatrix} f_{1,i+1} + f_{1,i} \\ f_{2,i+1} + f_{2,i} \\ f_{3,i+1} + f_{3,i} \end{Bmatrix} = 0 \end{aligned} \tag{4.19}$$

Similarly, for $k = 0$, Eq. (3.2) becomes the following:

$$\begin{aligned} &\frac{1}{\Delta x}\breve{M}_{i+1} + \left(\tilde{\kappa}_i M_i + \frac{1}{2}\tilde{\kappa}_i \breve{M}_{i+1} + \frac{1}{2}\breve{\tilde{\kappa}}_{i+1} M_i\right) + \tilde{e}_1\left(F_i + \frac{1}{2}\breve{F}_{i+1}\right) \\ &\qquad + \left(\tilde{\gamma}_i F_i + \frac{1}{2}\tilde{\gamma}_i \breve{F}_{i+1} + \frac{1}{2}\breve{\tilde{\gamma}}_{i+1} F_i\right) + \frac{1}{2}(m_{i+1} + m_i) = 0 \end{aligned} \tag{4.20}$$

Next, for an arbitrary node i, the first part of the constitutive equation (2.56) gives the following equation:

$$\gamma_i = RF_i + ZM_i, \quad \gamma_{i+1} = RF_{i+1} + ZM_{i+1} \tag{4.21}$$

Subtracting the two parts of Eq. (4.21) and using Eq. (4.12) for γ gives the following equation:

$$\breve{\gamma}_{i+1} = R\breve{F}_{i+1} + Z\breve{M}_{i+1} \tag{4.22}$$

Similarly, for the second part of Eq. (2.56),

$$\breve{\kappa}_{i+1} = Z^T \breve{F}_{i+1} + T\breve{M}_{i+1} \tag{4.23}$$

Equations (4.18), (4.20), (4.22), and (4.23) form a system of twelve linear algebraic equations for twelve unknown perturbations corresponding to variables F, M, γ, and κ at every node $i + 1$. These equations can be organized in the matrix form shown in Eqs. (4.24) and (4.25).

$$\begin{bmatrix} \frac{1}{\Delta x} & \frac{-1}{2}\kappa_3 & \frac{1}{2}\kappa_2 & 0 & 0 & 0 & 0 & 0 & 0 & 0 & \frac{1}{2}F_3 & -\frac{1}{2}F_2 \\ \frac{1}{2}\kappa_3 & \frac{1}{\Delta x} & \frac{-1}{2}\kappa_1 & 0 & 0 & 0 & 0 & 0 & 0 & -\frac{1}{2}F_3 & 0 & \frac{1}{2}F_1 \\ \frac{-1}{2}\kappa_2 & \frac{1}{2}\kappa_1 & \frac{1}{\Delta x} & 0 & 0 & 0 & 0 & 0 & 0 & \frac{1}{2}F_2 & -\frac{1}{2}F_1 & 0 \\ 0 & -\gamma_{13} & \gamma_{12} & \frac{1}{\Delta x} & \frac{-1}{2}\kappa_3 & \frac{1}{2}\kappa_2 & 0 & \frac{1}{2}F_3 & -\frac{1}{2}F_2 & 0 & \frac{1}{2}M_3 & -\frac{1}{2}M_2 \\ \gamma_{13} & 0 & -\frac{1}{2}-\frac{1}{2}\gamma_{11} & \frac{1}{2}\kappa_3 & \frac{1}{\Delta x} & \frac{-1}{2}\kappa_1 & -\frac{1}{2}F_3 & 0 & \frac{1}{2}F_1 & -\frac{1}{2}M_3 & 0 & \frac{1}{2}M_1 \\ -\gamma_{12} & \frac{1}{2}+\frac{1}{2}\gamma_{11} & 0 & \frac{-1}{2}\kappa_2 & \frac{1}{2}\kappa_1 & \frac{1}{\Delta x} & \frac{1}{2}F_2 & -\frac{1}{2}F_1 & 0 & \frac{1}{2}M_2 & -\frac{1}{2}M_1 & 0 \\ R_{11} & R_{12} & R_{13} & Z_{11} & Z_{12} & Z_{13} & -1 & 0 & 0 & 0 & 0 & 0 \\ R_{21} & R_{22} & R_{23} & Z_{21} & Z_{22} & Z_{23} & 0 & -1 & 0 & 0 & 0 & 0 \\ R_{31} & R_{32} & R_{33} & Z_{31} & Z_{32} & Z_{33} & 0 & 0 & -1 & 0 & 0 & 0 \\ Z_{11} & Z_{21} & Z_{31} & T_{11} & T_{12} & T_{13} & 0 & 0 & 0 & -1 & 0 & 0 \\ Z_{12} & Z_{22} & Z_{32} & T_{21} & T_{22} & T_{23} & 0 & 0 & 0 & 0 & -1 & 0 \\ Z_{13} & Z_{23} & Z_{33} & T_{31} & T_{32} & T_{33} & 0 & 0 & 0 & 0 & 0 & -1 \end{bmatrix} \begin{Bmatrix} \breve{F}_1 \\ \breve{F}_2 \\ \breve{F}_3 \\ \breve{M}_1 \\ \breve{M}_2 \\ \breve{M}_3 \\ \breve{\gamma}_{11} \\ 2\breve{\gamma}_{12} \\ 2\breve{\gamma}_{13} \\ \breve{\kappa}_1 \\ \breve{\kappa}_2 \\ \breve{\kappa}_3 \end{Bmatrix}_i = b_i \tag{4.24}$$

$$b_i = \begin{Bmatrix} \kappa_3 F_2 - \kappa_2 F_3 - \frac{1}{2}\left(f_{1,i} + f_{1,i+1}\right) \\ -\kappa_3 F_1 + \kappa_1 F_3 - \frac{1}{2}\left(f_{2,i} + f_{2,i+1}\right) \\ \kappa_2 F_1 - \kappa_1 F_2 - \frac{1}{2}\left(f_{3,i} + f_{3,i+1}\right) \\ \kappa_3 M_2 - \kappa_2 M_3 + 2\gamma_{13} F_2 - 2\gamma_{12} F_3 - \frac{1}{2}\left(m_{1,i} + m_{1,i+1}\right) \\ -\kappa_3 M_1 + \kappa_1 M_3 + F_3 - 2\gamma_{13} F_1 + \gamma_{11} F_3 - \frac{1}{2}\left(m_{2,i} + m_{2,i+1}\right) \\ \kappa_2 M_1 - \kappa_1 M_2 - F_2 + 2\gamma_{12} F_1 - \gamma_{11} F_2 - \frac{1}{2}\left(m_{3,i} + m_{3,i+1}\right) \\ 0 \\ 0 \\ 0 \\ 0 \\ 0 \\ 0 \end{Bmatrix} \tag{4.25}$$

4.5 Algorithm of Solution

Consider the case of a cantilever beam with N nodes along the longitudinal direction as shown in Fig. 2.5. At the free end or tip of the beam (i.e., at node N), the force and moment boundary conditions are known. Therefore, the corresponding values of κ and γ can be calculated using the constitutive equation (2.56). Now that F, M, κ, and γ at the tip are all known, one may use Eqs. (4.24) and (4.25) to calculate the corresponding perturbation values at this location (i.e., at node N). Having calculated the mentioned perturbations at node N, one can use Eq. (4.12), or equivalently,

$$\phi_{i-1} = \phi_i - \breve{\phi}_i \tag{4.26}$$

in order to calculate variables F, M, κ, and γ at node $N-1$ right beside the tip of the blade. The mentioned procedure can be repeated until F, M, κ, and γ values at all nodes are calculated.

While for F and M the boundary conditions are known at the tip of the beam, for u and θ the boundary conditions are known at the root of the beam (i.e., at the clamped end). Such boundary conditions are going to be used in this step. Having already calculated κ along the beam, and knowing θ at the root, Eq. (2.63) can be used for calculating θ along the beam. Assuming $k = 0$, Eq. (2.63) reduces to the following:

$$\kappa = \left(\frac{\Delta - \frac{1}{2}\tilde{\theta}}{1 + \frac{1}{4}\theta^T\theta} \right) \theta' \tag{4.27}$$

Using the perturbation Eqs. (3.6), (4.12), (4.13), and (4.14) for θ, one obtains the following:

$$\theta_{i+1} = \theta_i + \breve{\theta}_{i+1} \tag{4.28}$$

$$\theta\left(x + \frac{\Delta x}{2} \right) = \frac{1}{2}\left(\theta_{i+1} + \theta_i \right) \tag{4.29}$$

$$\theta\left(x + \frac{\Delta x}{2} \right) = \theta_i + \frac{1}{2}\breve{\theta}_{i+1} \tag{4.30}$$

$$\theta'\left(x + \frac{\Delta x}{2} \right) = \frac{1}{\Delta x}\breve{\theta}_{i+1} \tag{4.31}$$

Equation (4.30) can be used to rewrite the denominator of Eq. (4.27) as follows:

$$1 + \frac{1}{4}\theta^T\theta = 1 + \frac{1}{4}\theta_i^T\theta_i + \frac{1}{8}\theta_i^T\breve{\theta}_{i+1} + \frac{1}{8}\breve{\theta}_{i+1}^T\theta_i \tag{4.32}$$

However, $\theta^T\theta$ is a scalar, and also $\theta_i^T\breve{\theta}_{i+1} = \breve{\theta}_{i+1}^T\theta_i$ for the same reason. Thus,

$$1 + \frac{1}{4}\theta^T\theta = 1 + \frac{1}{4}\left(\theta_i^T\theta_i + \theta_i^T\breve{\theta}_{i+1} \right) \tag{4.33}$$

Substitution of Eq. (4.33) into Eq. (4.27) gives the following:

$$\left[1 + \frac{1}{4}\left(\theta_i^T\theta_i + \theta_i^T\breve{\theta}_{i+1} \right) \right] \kappa = \theta' - \frac{1}{2}\tilde{\theta}\theta' \tag{4.34}$$

Using Eqs. (4.28) to (4.31), Eq. (4.34) reduces to the following:

$$\begin{aligned}\left[1+\frac{1}{4}\left(\theta_i^T\theta_i+\theta_i^T\breve{\theta}_{i+1}\right)\right]\left(\kappa_i+\frac{1}{2}\breve{\kappa}_{i+1}\right) &= \frac{1}{\Delta x}\breve{\theta}_{i+1} \\ &\quad -\frac{1}{2}\left(\tilde{\theta}_i+\frac{1}{2}\breve{\tilde{\theta}}_{i+1}\right)\left(\frac{1}{\Delta x}\breve{\theta}_{i+1}\right)\end{aligned} \tag{4.35}$$

Ignoring higher order terms of perturbations in Eq. (4.35) and expanding the rest in terms of the vector components results in the following:

$$\begin{bmatrix} \frac{1}{\Delta x}-\frac{1}{4}\theta_1\kappa_1 & \frac{1}{2\Delta x}\theta_3-\frac{1}{4}\theta_2\kappa_1 & -\frac{1}{2\Delta x}\theta_2-\frac{1}{4}\theta_3\kappa_1 \\ -\frac{1}{2\Delta x}\theta_3-\frac{1}{4}\theta_1\kappa_2 & \frac{1}{\Delta x}-\frac{1}{4}\theta_2\kappa_2 & \frac{1}{2\Delta x}\theta_1-\frac{1}{4}\theta_3\kappa_2 \\ \frac{1}{2\Delta x}\theta_2-\frac{1}{4}\theta_1\kappa_3 & -\frac{1}{2\Delta x}\theta_1-\frac{1}{4}\theta_2\kappa_3 & \frac{1}{\Delta x}-\frac{1}{4}\theta_3\kappa_3 \end{bmatrix}\begin{Bmatrix}\breve{\theta}_1\\ \breve{\theta}_2\\ \breve{\theta}_3\end{Bmatrix}_{i+1} = \left[1+\frac{1}{4}\left(\theta_1^2+\theta_2^2+\theta_3^2\right)\right]\begin{Bmatrix}\kappa_1+\frac{\breve{\kappa}_1}{2}\\ \kappa_2+\frac{\breve{\kappa}_2}{2}\\ \kappa_3+\frac{\breve{\kappa}_3}{2}\end{Bmatrix}_i \tag{4.36}$$

The solution of Eq. (4.36) starts by using the θ-boundary condition at $i = 1$, or at the root of the beam. For a cantilever beam, u and θ are zero at the root, whereas M and F are given at the tip. Using the known value of θ at $i = 1$ in Eq. (4.36), one can then solve this equation for the perturbation values of θ at $i = 1$. The θ-perturbations at the root and Eq. (4.12) for θ are used to calculate θ at $i = 2$, i.e., at the node beside the clamped end. The procedure is then repeated for each node and in this way, using θ and its perturbation at node i, the value of θ_{i+1} is calculated. By continuing this procedure, values of θ at all nodes will be obtained.

Having calculated θ at all nodes, those values are substituted into Eq. (2.62) to give C matrices at every cross section without performing any simplification. Finally, Eq. (2.57) is solved for u. For no initial curvature and twist, i.e., for $k = 0$, Eq. (2.57) reduces to the following:

$$\gamma = C(e_1+u')-e_1 \tag{4.37}$$

At this stage of the solution, all other quantities in Eq. (4.37) at every nodal point are known. So, this equation can be solved for the only remaining unknown, i.e., for u. To this end, first Eq. (4.37) is rewritten as follows:

$$u' = C^{-1}(e_1+\gamma)-e_1 \tag{4.38}$$

Using Eqs. (3.6) and (4.14), Eq. (4.38) is evaluated at $x + \dfrac{\Delta x}{2}$ as follows:

$$\breve{u}_{i+1} = \Delta x \left\{ \left[\frac{1}{2} (C_i + C_{i+1})^{-1} \right] \left[\frac{1}{2} (\gamma_i + \gamma_{i+1}) + e_1 \right] - e_1 \right\} \tag{4.39}$$

Having already calculated γ and C at all nodes along the beam, Eq. (4.39) can provide all u-perturbation values. Now, to use,

$$u_{i+1} = u_i + \breve{u}_{i+1} \tag{4.40}$$

that is the application of Eq. (4.12) for u, one needs to know a starting value (i.e., a boundary condition) for u. For a cantilever beam, the value of u at the root, i.e., u at $i = 1$, is zero. So, by using Eq. (4.40) and the calculated $\breve{u}_2$, the value of u at $i = 2$ is obtained. This procedure can be repeated until displacement vectors at all nodes are calculated. The algorithm of solution presented by Eqs. (4.24), (4.25), (4.36), and (4.39) provides the most basic variables of interest along the beam.

It should be noted that the difference between Eqs. (4.26) and (4.40) is in the direction of marching. Recalling Fig. 2.5 when Eq. (4.26) is used the marching direction is to the left, whereas when Eq. (4.40) is used the marching direction is switched to the right. The reason for such a choice is the way the boundary conditions (that provide the starting points for the solution) are defined in a cantilever beam problem. At the free end at right, F and M are the known variables so we should march to the left to calculate these variables at other nodes. However, at the root at left, values of u and θ are known. So, marching to the right is necessary for providing u and θ at other nodes. That is why during the numerical solution the directions of marching for the two cases are opposite.

4.6 Use of Foreshortening for Verification

Having calculated the displacement components along the beam, one may now use these results in order to calculate the nonlinear quantity of foreshortening. Foreshortening, as is shown in Fig. 4.2, is the axial contraction of the projected length of a beam due to a lateral load. This is a nonlinear phenomenon, and it is not predictable by linear modeling. In this section, exact and perturbation equations for

Fig. 4.2 Foreshortening in nonlinear bending of a cantilever beam

foreshortening are given and the corresponding results are compared. Such a comparison can be used as a verification tool to ensure that the nonlinear perturbation algorithm works properly.

Referring to Fig. 4.2, the beam that is originally in the longitudinal x_1 direction is displaced laterally in the transversal x_2 direction while it remains in the x_1-x_2 plane. In this case, the exact foreshortening value at x_1 is given as follows:

$$\Delta_{x_1} = -\frac{1}{2}\int_0^{x_1} u_2'^2 \mathrm{d}\xi_1 \tag{4.41}$$

Using Eq. (4.31), the integral in Eq. (4.41) can be approximated with the finite summation

$$\Delta_{x_{1,n}} = -\frac{1}{2\Delta x}\sum_{i=1}^{n}\left(\breve{u}_{2,i}\right)^2 \tag{4.42}$$

Nodes are numbered from the fixed end and the upper limit of the summation is n; that is, the node number up to which foreshortening is to be calculated. For $n = N$, foreshortening of the whole beam is calculated at its free end (shown in Fig. 4.2).

For a beam that has been displaced laterally in both the x_2 and x_3 directions, Eq. (4.41) can be generalized to

$$\Delta_{x_1} = -\frac{1}{2}\int_0^{x_1} \left(u_2'^2 + u_3'^2\right)\mathrm{d}\xi_1 \tag{4.43}$$

Using Eq. (4.31), the integral in Eq. (4.43) can be approximated as follows:

$$\Delta_{x_{1,n}} = -\frac{1}{2\Delta x}\sum_{i=1}^{n}\left[\left(\breve{u}_{2,i}\right)^2 + \left(\breve{u}_{3,i}\right)^2\right] \tag{4.44}$$

4.7 Case Study: Isotropic Rectangular Solid Model

The isotropic rectangular solid example introduced in Sect. 3.3 is considered here again and three load cases are analyzed—F_2 only, F_3 only, and a combination of F_2, F_3, and M_1, all applied at the tip of the cantilever beam. The latter case is lightly loaded so that one may expect that the nonlinear results should be very close to the linear ones. In this way, the linear results can be used to verify the outcome of the nonlinear analysis. In each case, 1000 nodes have been used in performing the calculations but only 10 nodes have been used to draw the figures.

4.7.1 Load Case 1: Loading in the x_2 Direction

Consider a concentrated transversal load at the tip of the cantilever beam,

$$\begin{gathered} F_1 = 0\ \text{N},\ F_2 = 100\ \text{kN},\ F_3 = 0\ \text{N} \\ M_1 = 0\ \text{N.m},\ \text{M}_2 = 0\ \text{N.m},\ \text{M}_3 = 0\ \text{N.m} \end{gathered} \tag{4.45}$$

Figures 4.3, 4.4, 4.5, and 4.6 illustrate the output of the linear and nonlinear perturbation analyses. It is observed that in most cases the results of the two solutions are close. In addition, Fig. 4.6 illustrates that the applied load in the x_2 direction generates a rotation about the x_3 axis, which is expected. Interestingly, however, in Fig. 4.3, the nonlinear analysis predicts the existence of a longitudinal force, whereas the linear theory fails to do so. As to foreshortening, a review of Fig. 4.5 reveals that the approximate nonlinear solution explained in this chapter and the exact solution given by Eq. (4.41) provide almost identical results. In addition, as shown in Fig. 4.5, since foreshortening is a nonlinear phenomenon the linear model does not predict it and provides a zero value for u_1. A linear approximation for the value of the static deflection at the tip of the beam u_2 due to F_2 (in the same direction) can be calculated as follows:

$$u_2 = \frac{F_2 L^3}{3EI} = \frac{10^5 \cdot 1^3}{3 \times 1.7926 \times 10^{13} \times \frac{0.1 \times 0.2^3}{12}} = 2.7892 \times 10^{-5}\ \text{m} \tag{4.46}$$

which is close to what is shown in Fig. 4.5.

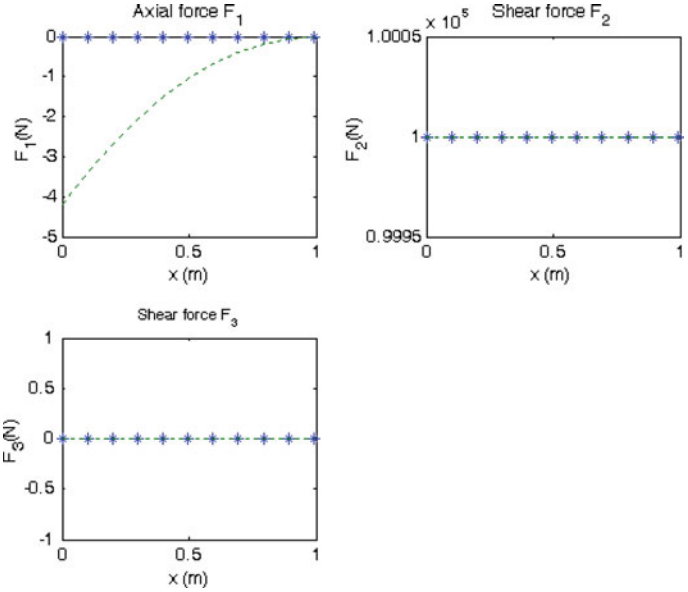

Fig. 4.3 The distribution of internal force components along the beam: linear static (asterisks) and nonlinear static (dashed) under Load Case 1

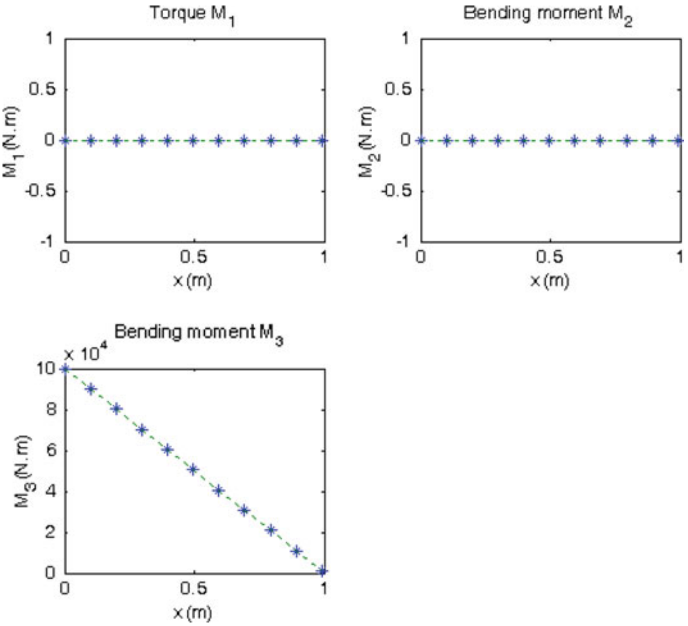

Fig. 4.4 The distribution of internal moment components along the beam: linear static (asterisks) and nonlinear static (dashed) under Load Case 1

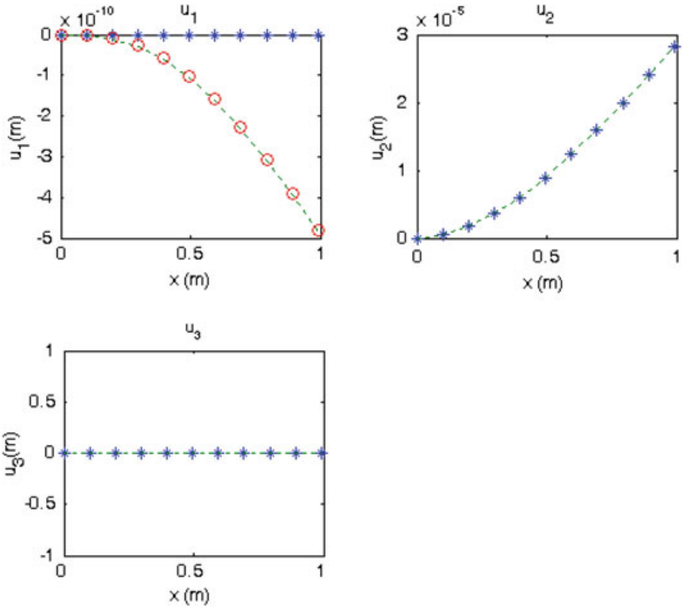

Fig. 4.5 The distribution of displacement components along the beam: linear static (asterisks), nonlinear static (dashed), and Eq. (4.41) (circles) under Load Case 1

4.7.2 Load Case 2: Loading in the x_3 Direction

Now consider the following loading at the tip of the beam,

$$\begin{aligned} F_1 &= 0\ \text{N},\ F_2 = 0\ \text{N},\ F_3 = 100\ \text{kN} \\ M_1 &= 0\ \text{N.m},\ \text{M}_2 = 0\ \text{N.m},\ \text{M}_3 = 0\ \text{N.m} \end{aligned} \tag{4.47}$$

The corresponding results have been presented in Figs. 4.7, 4.8, 4.9, and 4.10. Using the linear theory, the static deflection at the tip of the beam, u_3, due to F_3 is calculated as follows:

$$u_3 = \frac{F_3 L^3}{3EI} = \frac{10^5 \cdot 1^3}{3 \times 1.7926 \times 10^{13} \times \frac{0.2\times0.1^3}{12}} = 1.1157 \times 10^{-4}\ \text{m} \tag{4.48}$$

This is close to what is shown in Fig. 4.9. On the same figure, the foreshortening results obtained by the nonlinear procedure explained in this chapter are observed to be in agreement with the results of Eq. (4.41), as expected.

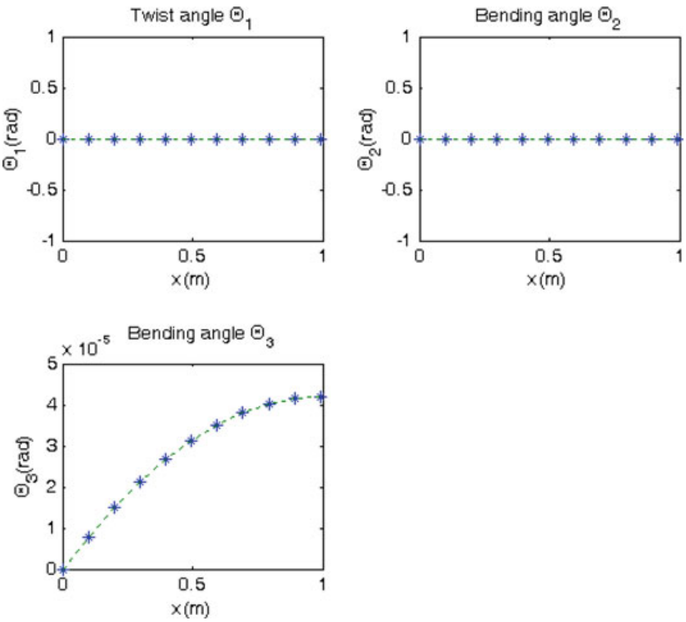

Fig. 4.6 The distribution of rotation components along the beam: linear static (asterisks) and nonlinear static (dashed) under Load Case 1

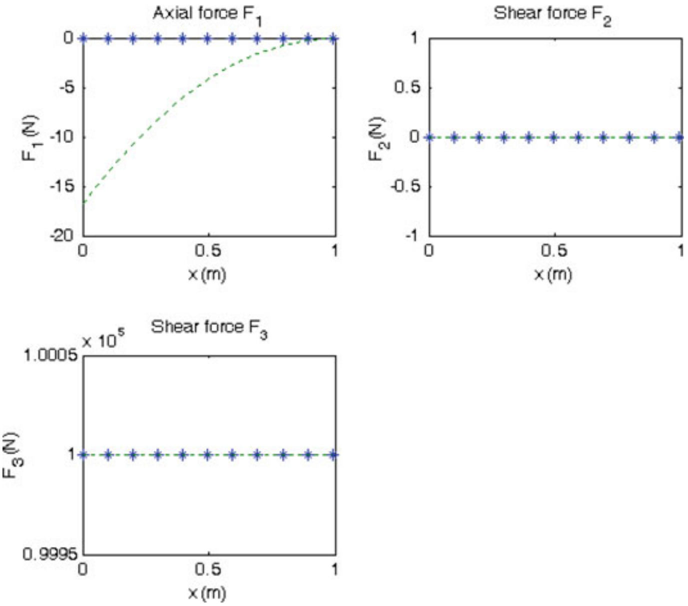

Fig. 4.7 The distribution of internal force components along the beam: linear static (asterisks) and nonlinear static (dashed) under Load Case 2

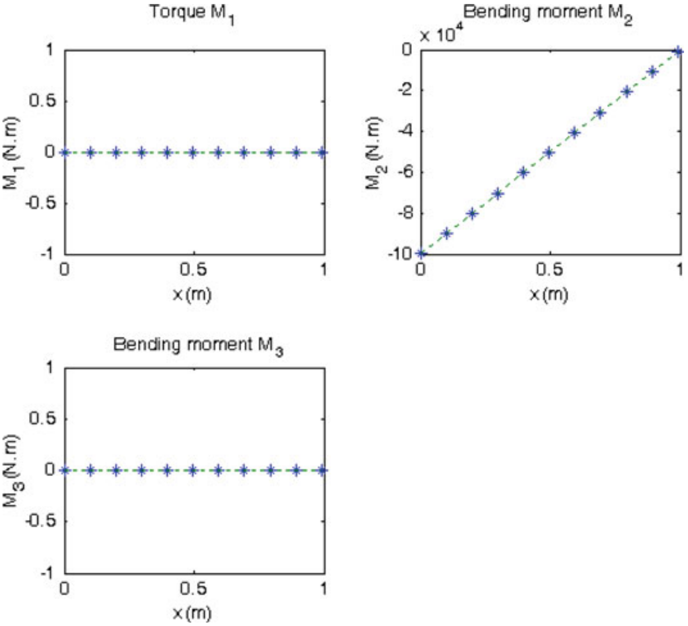

Fig. 4.8 The distribution of internal moment components along the beam: linear static (asterisks) and nonlinear static (dashed) under Load Case 2

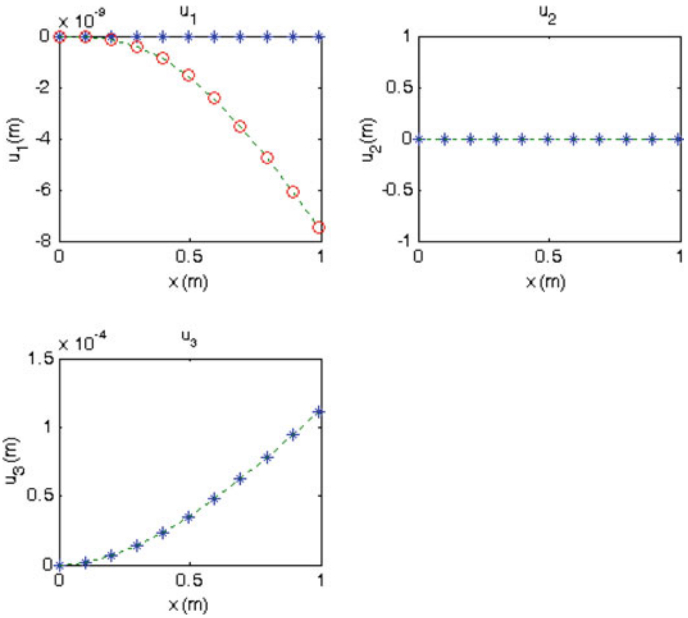

Fig. 4.9 The distribution of displacement components along the beam: linear static (asterisks), nonlinear static (dashed), and Eq. (4.41) (circles) under Load Case 2

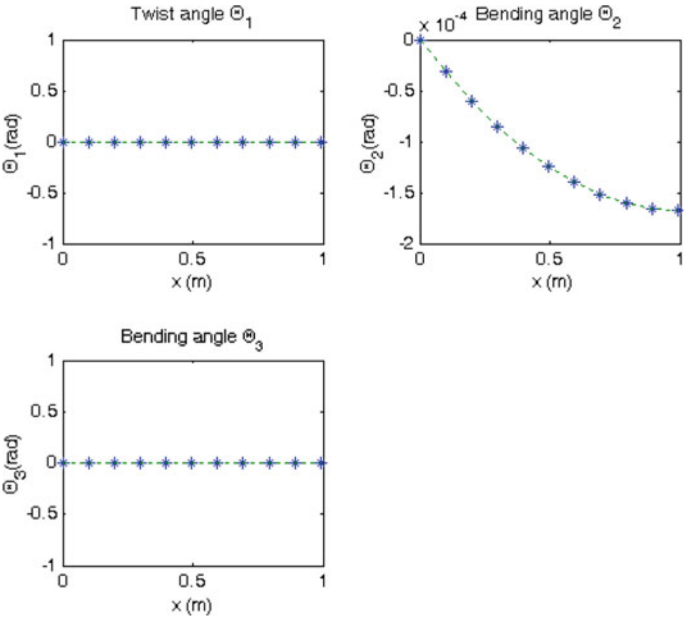

Fig. 4.10 The distribution of rotation components along the beam: linear static (asterisks) and nonlinear static (dashed) under Load Case 2

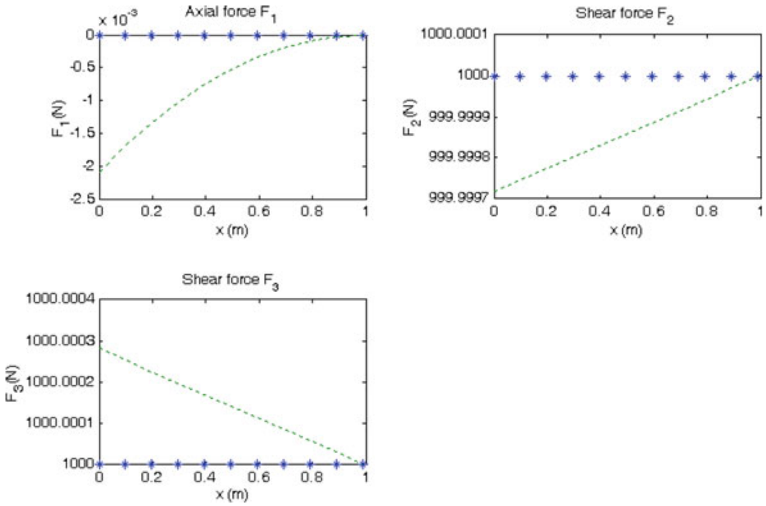

Fig. 4.11 The distribution of internal force components along the beam: linear static (asterisks) and nonlinear static (dashed) under Load Case 3

4.7.3 *Load Case 3: Combined Loading*

For the following combined loading at the tip of the beam,

$$\begin{aligned} F_1 &= 0\ \text{N},\ F_2 = 1000\ \text{N},\ F_3 = 1000\ \text{N} \\ M_1 &= 100\ \text{N.m},\ \text{M}_2 = 0\ \text{N.m},\ \text{M}_3 = 0\ \text{N.m} \end{aligned} \tag{4.49}$$

The corresponding solution using the linear and nonlinear methods is presented in Figs. 4.11, 4.12, 4.13, and 4.14.

As a verification checkpoint, it is observed that the calculated linear and nonlinear solutions for forces, moments, displacements, and rotations for this relatively light loading are very close. Also, the nonlinear solution and the exact solution Eq. (4.41) provide identical foreshortening results.

4.8 Case Study: Composite Box Model

Consider the composite box model discussed in Sect. 3.4. This time, linear and nonlinear analyses of this beam subjected to various loadings at its tip are presented.

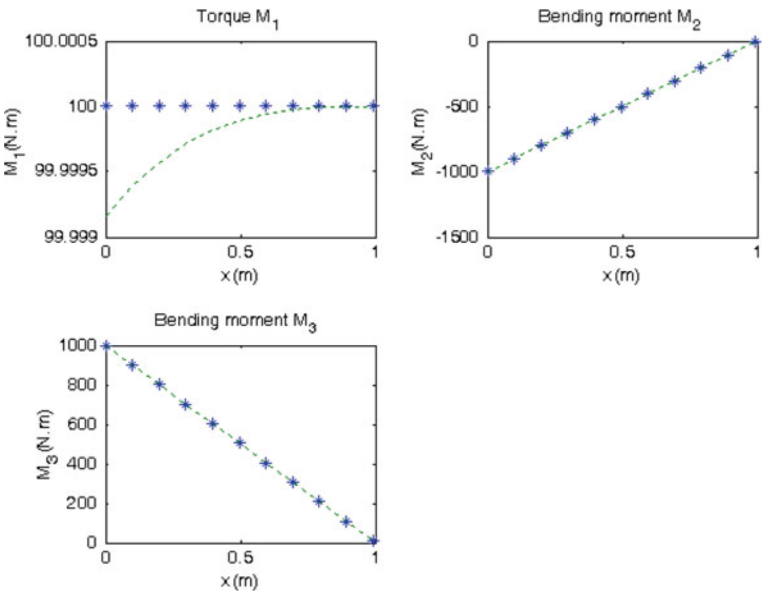

Fig. 4.12 The distribution of internal moment components along the beam: linear static (asterisks) and nonlinear static (dashed) under Load Case 3

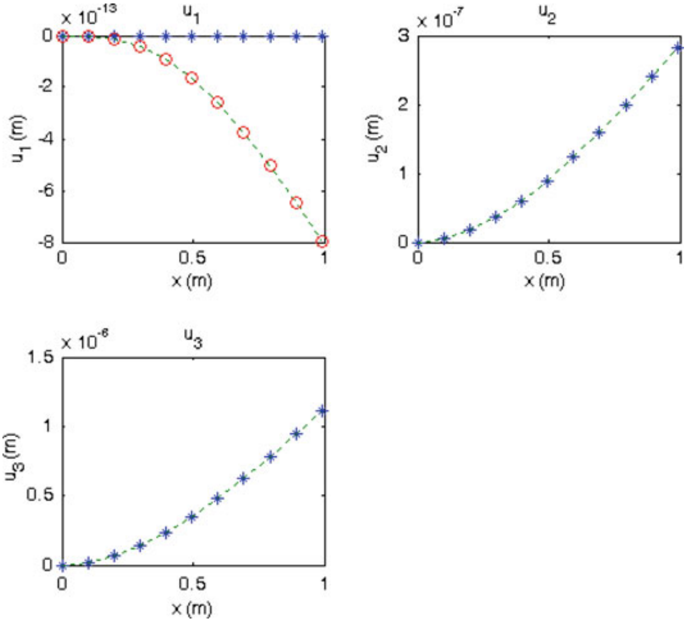

Fig. 4.13 The distribution of displacement components along the beam: linear static (asterisks), nonlinear static (dashed), and Eq. (4.41) (circles) under Load Case 3

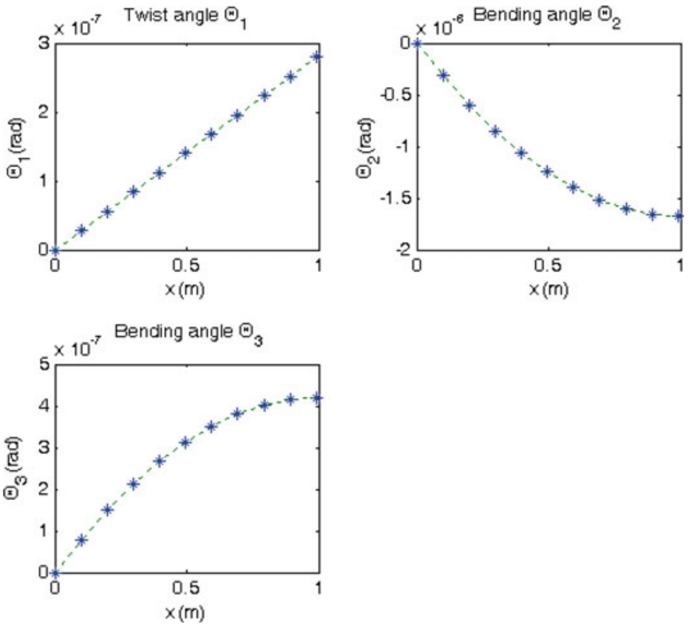

Fig. 4.14 The distribution of rotation components along the beam: linear static (asterisks) and the nonlinear static (dashed) under the Load Case 3

4.8.1 Load Case 1: Loading in the x_2 Direction

Consider a concentrated load at the tip of the beam that acts in the x_2 direction,

$$\begin{aligned} F_1 &= 0\ \mathrm{N},\ F_2 = 100\ \mathrm{N},\ F_3 = 0\ \mathrm{N} \\ M_1 &= 0\ \mathrm{N.m},\ \mathrm{M}_2 = 0\ \mathrm{N.m},\ \mathrm{M}_3 = 0\ \mathrm{N.m} \end{aligned} \tag{4.50}$$

Figures 4.15, 4.16, 4.17, and 4.18 illustrate the results of the linear and nonlinear perturbation analyses.

In Fig. 4.15, it is observed that while the static equilibrium should be valid, the end shear force F_2 is not equal to the applied force in the x_2 direction. The reason of such a difference is that in the nonlinear analysis the forces are measured in the deformed coordinates, whereas the static equilibrium conditions are written in the undeformed coordinate system (in which the applied and the internal F_2 forces remain parallel). To satisfy static equilibrium in the deformed system, a component of the deformed F_1 is combined with a component of F_2 in the deformed system to result in F_2 in the undeformed system. This force will then be equal and opposite of the applied load, F_2. This matter will be explained in more detail in the next load case.

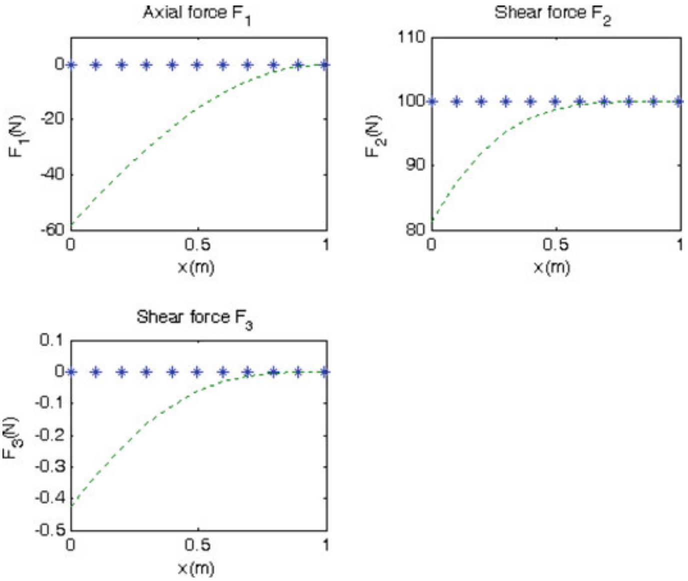

Fig. 4.15 The distribution of internal force components along the beam: linear static (asterisks) and nonlinear static (dashed) under Load Case 1

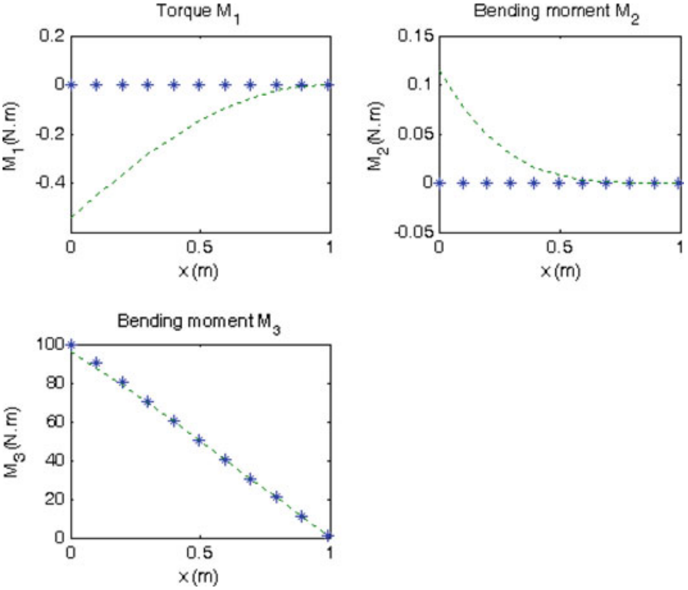

Fig. 4.16 The distribution of internal moment components along the beam: linear static (asterisks) and nonlinear static (dashed) under Load Case 1

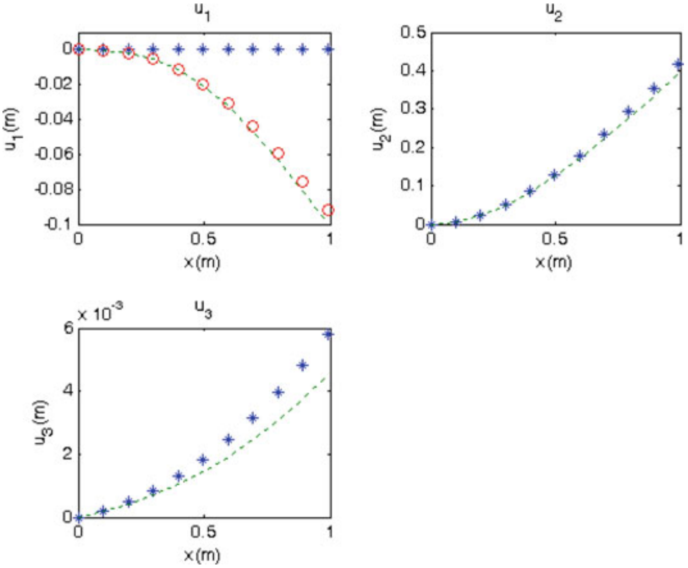

Fig. 4.17 The distribution of displacement components along the beam: linear static (asterisks), nonlinear static (dashed), and Eq. (4.41) (circles) under Load Case 1

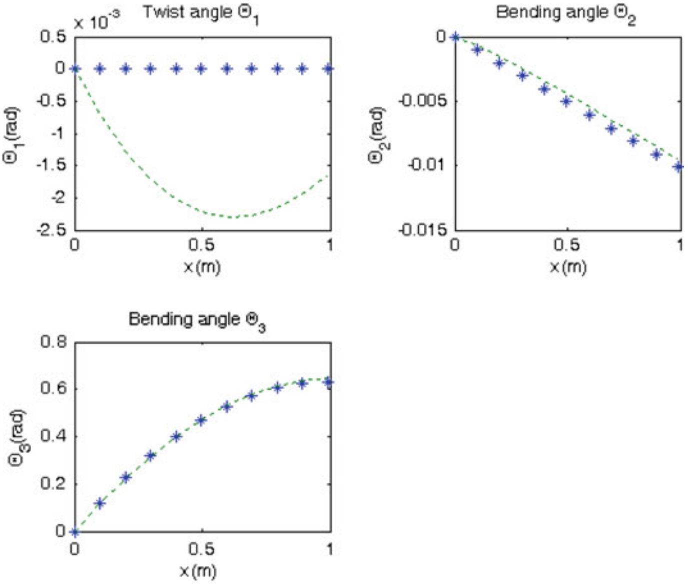

Fig. 4.18 The distribution of rotation components along the beam: linear static (asterisks) and nonlinear static (dashed) under Load Case 1

4.8.2 Load Case 2: Loading in the x_3 Direction

Another concentrated load at the tip of the beam is now considered that is applied in the x_3 direction,

$$\begin{aligned} F_1 &= 0\ \text{N},\ F_2 = 0\ \text{N},\ F_3 = 100\ \text{N} \\ M_1 &= 0\ \text{N.m},\ \text{M}_2 = 0\ \text{N.m},\ \text{M}_3 = 0\ \text{N.m} \end{aligned} \tag{4.51}$$

The corresponding results are presented in Figs. 4.19, 4.20, 4.21, and 4.22.

In Fig. 4.19, it is observed that using the linear model, when the 100 N force is applied, the induced shear force F_2 remains constant along the span of the beam. However (interestingly, and similar to the previous load case), if one uses the nonlinear model, under the application of the same loading in the x_3 direction, the shear force is observed to reduce from the original 100 N value at the free end to 79.45 N at the clamped end. One wonders how this significant difference might have happened especially since the static equilibrium equations should clearly be satisfied.

The reason is that in the nonlinear model the deformed coordinate system is used which tends to orient itself with the deformed beam and is not pointing in a fixed way (unlike the undeformed coordinate system). As shown in Fig. 4.23, the result of using the deformed coordinate system is that while F_3 decreases, F_1 and F_2

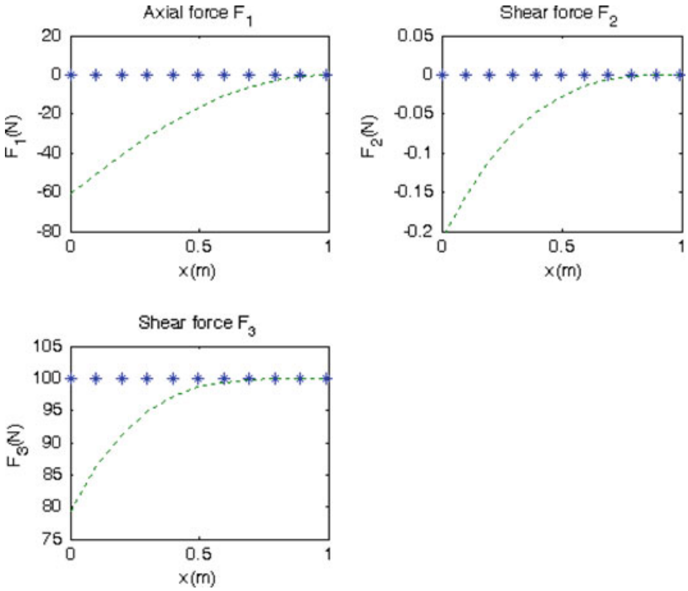

Fig. 4.19 The distribution of internal force components along the beam: linear static (asterisks) and nonlinear static (dashed) under Load Case 2

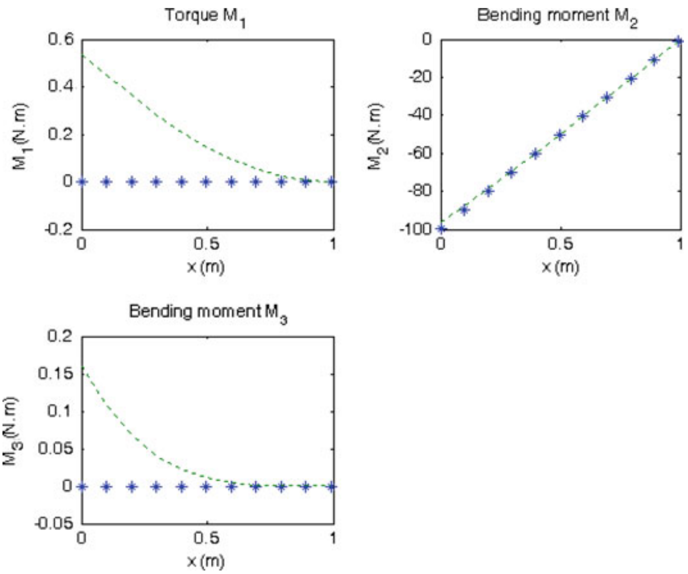

Fig. 4.20 The distribution of internal moment components along the beam: linear static (solid line) and nonlinear static (dashed) under Load Case 2

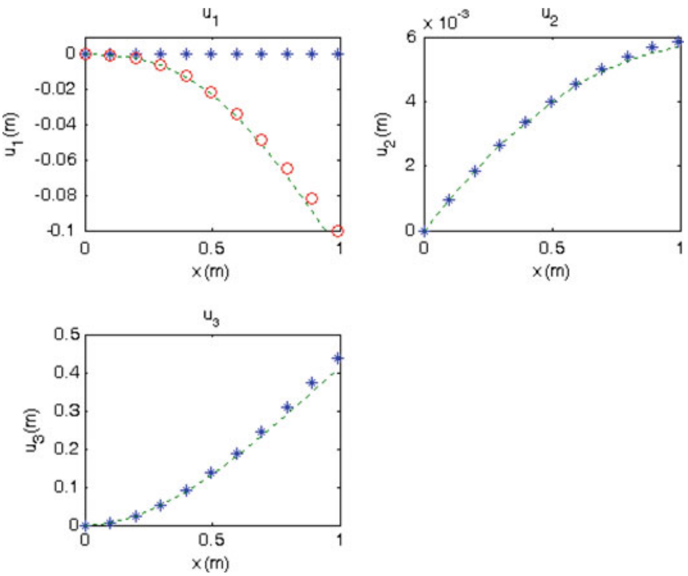

Fig. 4.21 The distribution of displacement components along the beam: linear static (asterisks), nonlinear static (dashed), and Eq. (4.41) (circles) under Load Case 2

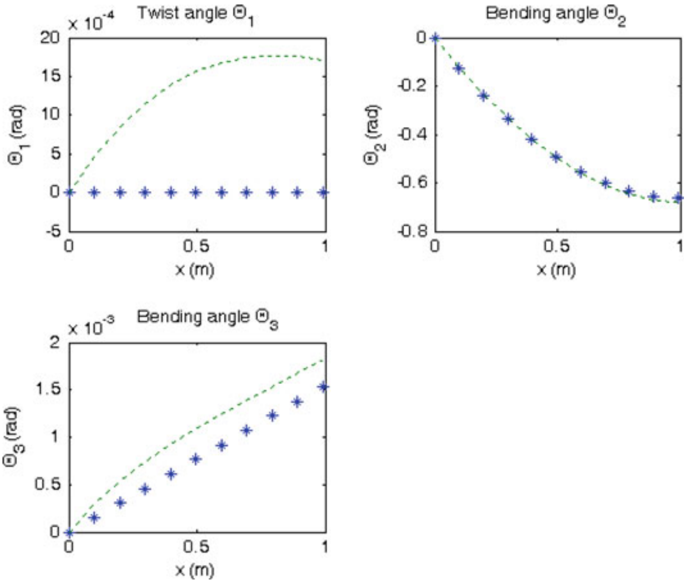

Fig. 4.22 The distribution of rotation components along the beam: linear static (asterisks) and nonlinear static (dashed) under the Load Case 2

increase in such a way that the vectorial summation of these forces along the span of the beam remains equal in magnitude and opposite in direction to the applied loading. For example, at the clamped end of the beam, the applied 100 N load is balanced with the following resultant,

$$\sqrt{(-60.826)^2 + (-0.208)^2 + (79.445)^2} = 100.057 \text{ N} \tag{4.52}$$

This phenomenon was not observed in Sect. 4.7 because in that case the rotation angles were very small.

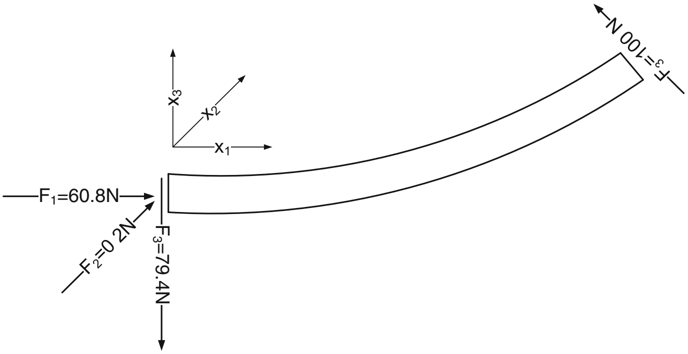

Fig. 4.23 Free body diagram of the beam using deformed coordinates

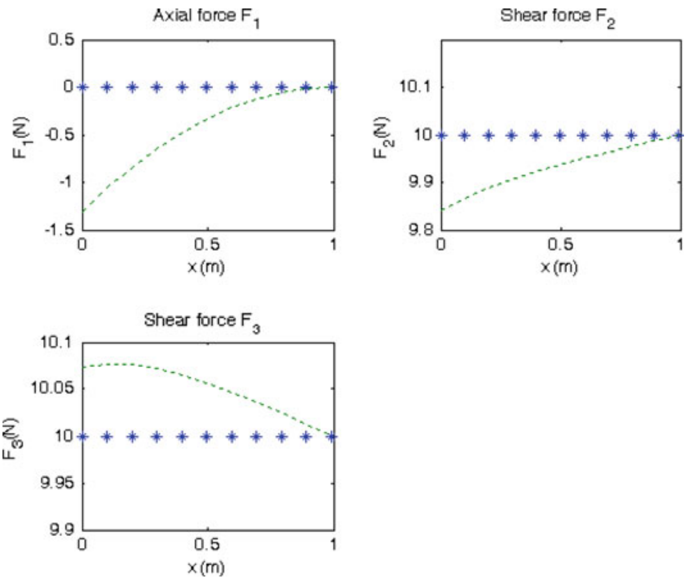

Fig. 4.24 The distribution of internal force components along the beam: linear static (asterisks) and nonlinear static (dashed) under Load Case 3

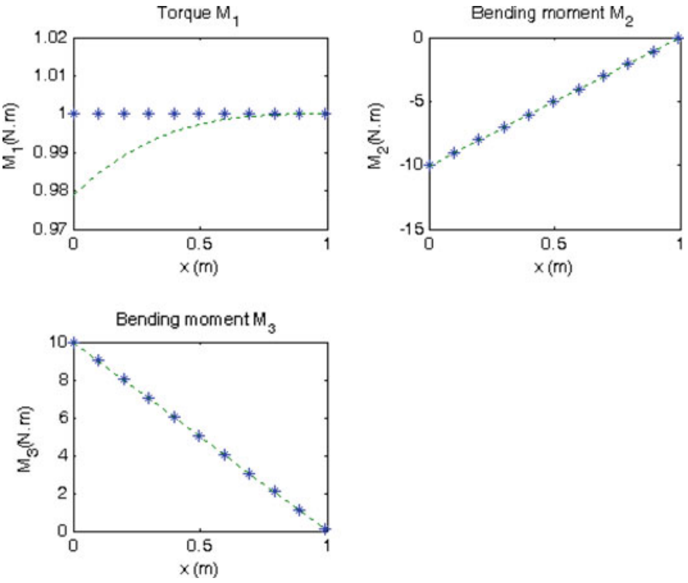

Fig. 4.25 The distribution of internal moment components along the beam: linear static (asterisks) and nonlinear static (dashed) under Load Case 3

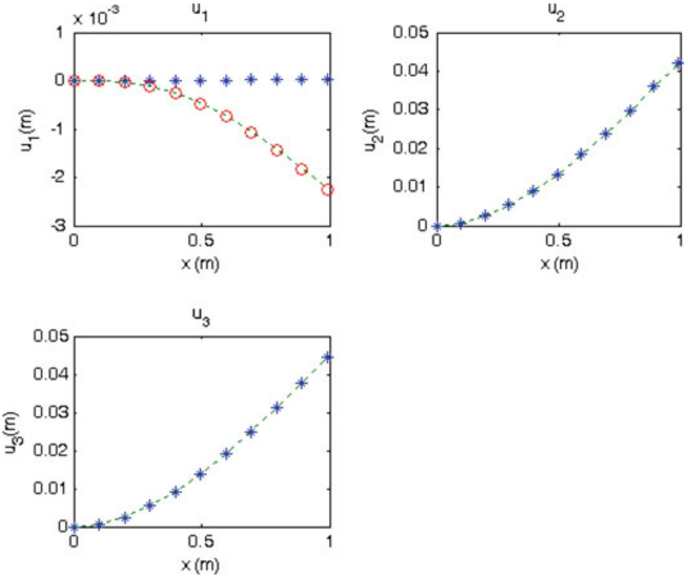

Fig. 4.26 The distribution of displacement components along the beam: linear static (asterisks), nonlinear static (dashed), and Eq. (4.41) (circles) under Load Case 3

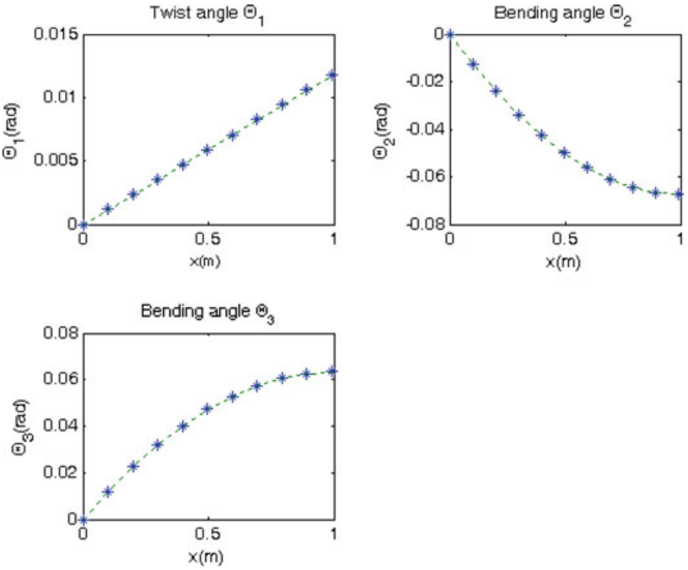

Fig. 4.27 The distribution of rotation components along the beam: linear static (asterisks) and nonlinear static (dashed) under Load Case 3

4.8.3 Load Case 3: Combined Loading

Having verified the validity of the calculation procedure in the preceding load cases, in this section a combined loading at the tip of the composite beam is applied as follows:

$$\begin{aligned} F_1 &= 0\,\mathrm{N},\ F_2 = 10\ \mathrm{N},\ F_3 = 10\ \mathrm{N} \\ M_1 &= 1\ \mathrm{N.m},\ \mathrm{M}_2 = 0\,\mathrm{N.m},\ \mathrm{M}_3 = 0\,\mathrm{N.m} \end{aligned} \tag{4.53}$$

The corresponding solution is illustrated in Figs. 4.24, 4.25, 4.26, and 4.27.

Chapter 5
Transient Nonlinear Dynamics of Accelerating Hingeless Rotating Blades

5.1 Introduction

In Chaps. 3 and 4, linear and nonlinear static solutions for beams made of composite materials were developed. In this chapter, a nonlinear dynamic model for analyzing the transient behavior of a rotating blade is presented. In the coming sections, static analysis serves two purposes. First, in order to run the nonlinear dynamic model, initial conditions for the internal forces and moments as well as the deflection and curvature distributions due to static forces (especially gravity) are required. The nonlinear static model can be used to provide such initial conditions. In this way, first static loads are applied to the nonlinear static computer program, and then, the calculated output (internal force and moment, as well as deflection and curvature distributions) are given as input to the nonlinear dynamics code. The second application of the static code in this chapter is for verification purposes as it will be explained later in Sect. 5.8.

The dynamic analysis, among other things, can be used for studying the straightening of initially sagged helicopter blades (due to their weight) as they rotate. The solution starts by setting the initial curvature, k, in the static problem equal to the undeformed curvature of the blade. Then, after running the static code and calculating the deformed curvature, κ, of the static problem, the total static curvature K is used as the undeformed curvature, k, for solving the dynamic problem.

To obtain the transient nonlinear dynamics of an accelerating rotating blade, the dynamic form of the nonlinear intrinsic equations, which were presented in Chap. 2, should be solved. One way of solving this problem is to use the direct (explicit) method. The explicit method uses direct integration expressions in terms of finite differences or perturbations, as was done in the past for solving the nonlinear static problem presented in Chap. 4. To perform the solution, the finite difference and the perturbation methods used in Chap. 4 for solving the nonlinear static problem are expanded to include time-dependent variables. While the direct approach provides a

M. Ghorashi, *Statics and Rotational Dynamics of Composite Beams*,
DOI 10.1007/978-3-319-14959-2_5

relatively easy algorithm of solution, there are possibilities of error accumulation and numerical instability, which should be taken into account.

Using the direct approach in this chapter, a blade model is analyzed that starts its motion from rest, accelerates, and finally reaches its steady-state rotational speed. In this way, the complete sequence of the nonlinear motion of a rotating composite beam is analyzed. Most of the contents of this chapter have been presented in Ghorashi (2009) and published in Ghorashi and Nitzsche (2009).

An alternative way is to use the indirect (implicit or iterative) method to calculate the steady-state response. As will be seen in Chap. 6, the solution using this method is more complex and time-consuming. However, the risk of error accumulation and numerical stability would be significantly reduced since the solution is unconditionally stable. In Chap. 6, the steady-state solution that will be calculated in Chap. 5 will be compared with the result of the shooting method.

5.2 Governing Equations of Motion

The set of equations to be solved for analyzing the dynamics of a rotating blade are presented in Chap. 2 and are reminded below. The nonlinear intrinsic equations of motion are

$$F' + \tilde{K}F + f = \dot{P} + \tilde{\Omega}P \tag{2.26}$$

$$M' + \tilde{K}M + (\tilde{e}_1 + \tilde{\gamma})F + m = \dot{H} + \tilde{\Omega}H + \tilde{V}P \tag{2.27}$$

and in scalar form,

$$F_1' + K_2F_3 - K_3F_2 + f_1 = \dot{P}_1 + \Omega_2P_3 - \Omega_3P_2 \tag{2.28}$$

$$F_2' + K_3F_1 - K_1F_3 + f_2 = \dot{P}_2 + \Omega_3P_1 - \Omega_1P_3 \tag{2.29}$$

$$F_3' + K_1F_2 - K_2F_1 + f_3 = \dot{P}_3 + \Omega_1P_2 - \Omega_2P_1 \tag{2.30}$$

$$\begin{aligned} &M_1' + K_2M_3 - K_3M_2 + 2\gamma_{12}F_3 - 2\gamma_{13}F_2 + m_1 \\ &\quad = \dot{H}_1 + \Omega_2H_3 - \Omega_3H_2 + V_2P_3 - V_3P_2 \end{aligned} \tag{2.31}$$

$$\begin{aligned} &M_2' + K_3M_1 - K_1M_3 + 2\gamma_{13}F_1 - (1+\gamma_{11})F_3 + m_2 \\ &\quad = \dot{H}_2 + \Omega_3H_1 - \Omega_1H_3 + V_3P_1 - V_1P_3 \end{aligned} \tag{2.32}$$

$$\begin{aligned} &M_3' + K_1M_2 - K_2M_1 + (1+\gamma_{11})F_2 - 2\gamma_{12}F_1 + m_3 \\ &\quad = \dot{H}_3 + \Omega_1H_2 - \Omega_2H_1 + V_1P_2 - V_2P_1 \end{aligned} \tag{2.33}$$

The nonlinear intrinsic kinematical equations are

$$V' + \tilde{K}V + (\tilde{e}_1 + \tilde{\gamma})\Omega = \dot{\gamma} \tag{2.37}$$

$$\Omega' + \tilde{K}\Omega = \dot{\kappa} \tag{2.38}$$

and in scalar form,

$$V_2' + K_2 V_3 - K_3 V_2 + 2\gamma_{12}\Omega_3 - 2\gamma_{13}\Omega_2 = \dot{\gamma}_{11} \tag{2.39}$$

$$V_2' + K_3 V_1 - K_1 V_3 - (1 + \gamma_{11})\Omega_3 + 2\gamma_{13}\Omega_1 = 2\dot{\gamma}_{12} \tag{2.40}$$

$$V_3' + K_1 V_2 - K_2 V_1 + (1 + \gamma_{11})\Omega_2 - 2\gamma_{12}\Omega_1 = 2\dot{\gamma}_{13} \tag{2.41}$$

$$\Omega_1' + K_2\Omega_3 - K_3\Omega_2 = \dot{\kappa}_1 \tag{2.42}$$

$$\Omega_2' + K_3\Omega_1 - K_1\Omega_3 = \dot{\kappa}_2 \tag{2.43}$$

$$\Omega_3' + K_1\Omega_2 - K_2\Omega_1 = \dot{\kappa}_3 \tag{2.44}$$

Equations (2.26), (2.27), (2.37), and (2.38) are fourth order in space and fourth order in time, so in general, four vector boundary conditions and four vector initial conditions are required for solving them.

The total curvature is the summation of the undeformed (initial) curvature and the contribution of deformation. So,

$$K = k + \kappa \tag{2.36}$$

Equations (2.26), (2.27), (2.37), and (2.38) are to be solved for the main variables, *F, M, V,* and Ω. But such a solution is impossible without first expressing γ, κ, *P,* and *H* in terms of *F, M, V,* and Ω. For this purpose, one may use the momentum–velocity equation,

$$\begin{Bmatrix} P \\ H \end{Bmatrix} = \begin{bmatrix} \mu\Delta & -\mu\tilde{\bar{\xi}} \\ \mu\tilde{\bar{\xi}} & i \end{bmatrix} \begin{Bmatrix} V \\ \Omega \end{Bmatrix} \tag{2.45}$$

and the constitutive equation,

$$\begin{Bmatrix} \gamma \\ \kappa \end{Bmatrix} = \begin{bmatrix} R & Z \\ Z^{\mathrm{T}} & T \end{bmatrix} \begin{Bmatrix} F \\ M \end{Bmatrix} \tag{2.56}$$

In Eqs. (2.26), (2.27), (2.37), and (2.38), $\tilde{K}F, \tilde{\Omega}P, \tilde{K}M, \tilde{\gamma}F, \tilde{\Omega}H, \tilde{V}P, \tilde{K}\Omega$, $\tilde{K}V$ and $\tilde{\gamma}\Omega$ are the terms that make the problem nonlinear. By developing expressions for these terms using the nodal values of the variables and their perturbations (in time or space), a solution algorithm can be presented. However, before trying to solve the nonlinear problem, one may want to investigate whether the presented formulation can be linearized in a meaningful way.

5.3 An Attempt on Solving a Linearized Version of the Dynamics Equations

As an analog to the solution method discussed in Chap. 3, one may want to try to linearize Eqs. (2.26), (2.27), (2.37), and (2.38) by just dropping their nonlinear terms. Such a simplification would be meaningful only if the dropped terms are small. In what follows it is shown that this simplification, especially for the case of rotor blades, is meaningless. In order to demonstrate this fact, let us proceed with the mentioned linearization plan (by dropping the nonlinear terms) and see what the outcome will be.

First, of course, we should detect the nonlinear terms. The term, $\tilde{\Omega}P$, in Eq. (2.26) is a nonlinear term. The reason is that if a given torque generates the rotational motion of the blade, both components of this term would be unknown dependent variables, and therefore, their product is nonlinear. By neglecting all of such nonlinear terms in Eqs. (2.26), (2.27), (2.37), and (2.38), one obtains,

$$F' + \tilde{k}F + f = \dot{P} \tag{5.1}$$

$$M' + \tilde{k}M + \tilde{e}_1F + m = \dot{H} \tag{5.2}$$

$$V' + \tilde{k}V + \tilde{e}_1\Omega = \dot{\gamma} \tag{5.3}$$

$$\Omega' + \tilde{k}\Omega = \dot{\kappa} \tag{5.4}$$

But, interestingly, it can be demonstrated that $\tilde{\Omega}P$ is nothing but the centripetal force generated in the blade as a result of rotation. To demonstrate this fact and for simplicity, consider a case in which the origin of the reference frame (i.e., the shear center) and the centroid at each section coincide. Thus,

$$\bar{x}_2 = \bar{x}_3 = 0 \tag{2.54}$$

Therefore,

$$\bar{\xi} = 0 \quad \tilde{\bar{\xi}} = 0 \tag{2.55}$$

In this case, Eq. (2.47) reduces to,

$$P = \mu \,.\, V \tag{5.5}$$

$$H = i \,.\, \Omega \tag{5.6}$$

Using Eq. (5.5), the term $\tilde{\Omega}P$ for a beam that is rotating about the x_3 axis becomes

$$\tilde{\Omega}P = \begin{bmatrix} 0 & -\Omega_3 & 0 \\ \Omega_3 & 0 & 0 \\ 0 & 0 & 0 \end{bmatrix} \begin{Bmatrix} \mu V_1 \\ \mu V_2 \\ \mu V_3 \end{Bmatrix} = \begin{Bmatrix} -\mu \Omega_3 V_2 \\ \mu \Omega_3 V_1 \\ 0 \end{Bmatrix} \tag{5.7}$$

where the transversal velocity V_2 is,

$$V_2 = x_1 \Omega_3 \tag{5.8}$$

Using Eq. (5.8), the first term in Eq. (5.7) becomes, $-\mu x_1 \Omega_3^2$ which is the centripetal force. Therefore, dropping $\tilde{\Omega}P$ in Eq. (2.26) to get Eq. (5.1) is equivalent to ignoring the centripetal force in a rotating blade problem. In other words, such a linear model can be valid only when the centrifugal force is negligible. This condition is clearly not valid in a rotating blade problem.

Another alternative is to keep the $\tilde{\Omega}P$ term in the formulation but try to make it linear. For this purpose, one might assume that the resulting angular velocity is constant along the blade and its dependency on time has been given. Then, one can search for the corresponding loadings f and m that can generate this velocity. While it may seem a reasonable solution, it is not. The problem is that one cannot assume that the angular velocity along the blade is constant (i.e., it is not a function of x_1). In fact, a constant angular velocity along the blade requires that the blade can be treated as a rigid body and its longitudinal axis remains a straight line. Such an assumption, however, is in contradiction with the elasticity of the behavior of the blade. So, one cannot consider a constant angular velocity Ω_3 along the beam as a known input to the problem in order to keep the $\tilde{\Omega}P$ term in the formulation without making it nonlinear.

Finally, considering a rotating cantilever blade, one might want to keep $\tilde{\Omega}P$ in the formulation, by assuming that Ω_3 has been given (accelerating from rest and to a steady-state) only at the root of the blade. While this method does not contradict the elasticity of the blade, it makes the problem nonlinear again. If this input is given only at the root of the blade, Ω_3 will still be unknown along the blade. Therefore, $\tilde{\Omega}P$ will remain to be a nonlinear term that cannot be neglected. So, it is concluded that $\tilde{\Omega}P$ is an essential nonlinearity and cannot be ignored in a rotating blade problem.

5.4 Derivation of the Generic Nonlinear Term

The system of equations to be solved includes Eqs. (2.26), (2.27), (2.37), and (2.38). In these equations, all of the nine nonlinear terms, i.e., $\tilde{K}F, \tilde{\Omega}P, \tilde{K}M, \tilde{\gamma}F$, $\tilde{\Omega}H, \tilde{V}P, \tilde{K}\Omega, \tilde{K}V$ and $\tilde{\gamma}\Omega$, have the same structure. Therefore, for developing equations, one may analyze only a single generic nonlinear vector term, $\tilde{\phi}\lambda$. This term can be expanded as,

$$\tilde{\phi}\lambda = \begin{bmatrix} 0 & -\phi_3 & \phi_2 \\ \phi_3 & 0 & -\phi_1 \\ -\phi_2 & \phi_1 & 0 \end{bmatrix} \begin{Bmatrix} \lambda_1 \\ \lambda_2 \\ \lambda_3 \end{Bmatrix} = \begin{Bmatrix} -\phi_3\lambda_2 + \phi_2\lambda_3 \\ -\phi_1\lambda_3 + \phi_3\lambda_1 \\ -\phi_2\lambda_1 + \phi_1\lambda_2 \end{Bmatrix} \tag{5.9}$$

Denoting a generic scalar nonlinear term in Eq. (5.9) by $\phi_m\lambda_n$ (m = 1:3, n = 1:3), this term can now be evaluated at the center of a space–time grid, shown in Fig. 2.6, using the nodal values of variables ϕ_m and λ_n and perturbations in time and space.

First, recalling Eqs. (2.75) and (4.12), perturbation in space in the next time step, $\breve{\phi}_{m,i+1}$, is introduced as,

$$\overset{+}{\phi}_{m,i+1} = \overset{+}{\phi}_{m,i} + \breve{\phi}_{m,i+1} \tag{5.10}$$

where the function values with a plus superscript are evaluated at the next time step. In this way, Eq. (5.10) relates function values at node i to those at node i + 1, both measured at the next time step. Similarly, for the perturbations in time, $\overset{\frown}{\phi}_{m,i}$

$$\overset{+}{\phi}_{m,i} = \phi_{m,i} + \overset{\frown}{\phi}_{m,i} \tag{5.11}$$

Equation (5.11) relates function values at a node on two consecutive time steps. Now, using Eq. (2.87) for ϕ_m and λ_n, one obtains,

$$\phi_m\left(x + \frac{\Delta x}{2}, t + \frac{\Delta t}{2}\right) = \frac{1}{4}\left(\overset{+}{\phi}_{m,\,i+1} + \overset{+}{\phi}_{m,\,i} + \phi_{m,\,i+1} + \phi_{m,\,i}\right) + O\left(\Delta x^2, \Delta t^2\right) \tag{5.12}$$

$$\lambda_n\left(x + \frac{\Delta x}{2}, t + \frac{\Delta t}{2}\right) = \frac{1}{4}\left(\overset{+}{\lambda}_{n,i+1} + \overset{+}{\lambda}_{n,i} + \lambda_{n,i+1} + \lambda_{n,i}\right) + O\left(\Delta x^2, \Delta t^2\right) \tag{5.13}$$

Substituting space perturbation Eq. (5.10) in (5.12) and ignoring the higher order terms result in,

$$\phi_m\left(x + \frac{\Delta x}{2}, t + \frac{\Delta t}{2}\right) = \frac{1}{4}\left(2\overset{+}{\phi}_{m,\,i} + \breve{\phi}_{m,i+1} + \phi_{m,\,i+1} + \phi_{m,\,i}\right) \tag{5.14}$$

Now, using time perturbation Eq. (5.11) in (5.14) gives,

$$\phi_m\left(x+\frac{\Delta x}{2}, t+\frac{\Delta t}{2}\right)=\frac{1}{4}\left(3\phi_{m,i}+2\overset{\frown}{\phi}_{m,i}+\overset{\smile}{\phi}_{m,i+1}+\phi_{m,i+1}\right) \tag{5.15}$$

Using Eq. (5.15) and a similar expression for λ_n, the generic nonlinear term $\phi_m\lambda_n$ at the center of the space–time grid of Fig. 2.6 becomes

$$\phi_m\lambda_n=\frac{1}{16}\left(3\phi_{m,i}+2\overset{\frown}{\phi}_{m,i}+\overset{\smile}{\phi}_{m,i+1}+\phi_{m,i+1}\right)\left(3\lambda_{n,i}+2\overset{\frown}{\lambda}_{n,i}+\overset{\smile}{\lambda}_{n,i+1}+\lambda_{n,i+1}\right) \tag{5.16}$$

After some mathematical manipulations, and by assuming the perturbations to be small enough to justify elimination of the second-order terms, Eq. (5.16) reduces to,

$$\begin{aligned}\phi_m\lambda_n=&\frac{1}{16}\left(9\phi_{m,i}\lambda_{n,i}+3\phi_{m,i}\lambda_{n,i+1}+3\phi_{m,i+1}\lambda_{n,i}+\phi_{m,i+1}\lambda_{n,i+1}\right)\\&+\frac{1}{16}\Big[2\overset{\frown}{\phi}_{m,i}\left(3\lambda_{n,i}+\lambda_{n,i+1}\right)+\overset{\smile}{\phi}_{m,i+1}\left(3\lambda_{n,i}+\lambda_{n,i+1}\right)\\&+2\overset{\frown}{\lambda}_{n,i}\left(3\phi_{m,i}+\phi_{m,i+1}\right)+\overset{\smile}{\lambda}_{n,i+1}\left(3\phi_{m,i}+\phi_{m,i+1}\right)\Big]\end{aligned} \tag{5.17}$$

Equation (5.17) is a linear expression in terms of the four unknown perturbations. This equation, by using Eqs. (5.10) and (5.11), can also be written in terms of the nodal values of variables,

$$\begin{aligned}\phi_m\lambda_{\mathrm{n}}=&\frac{1}{16}\left[\left(\overset{+}{\phi}_{m,i+1}+\overset{+}{\phi}_{m,i}\right)\left(\lambda_{n,i+1}+3\lambda_{n,i}\right)+\left(\overset{+}{\lambda}_{n,i+1}+\overset{+}{\lambda}_{n,i}\right)\left(\phi_{m,i+1}+3\phi_{m,i}\right)\right]\\&+\frac{1}{16}\left(\phi_{m,i+1}\lambda_{n,i+1}+\phi_{m,i+1}\lambda_{n,i}+\phi_{m,i}\lambda_{n,i+1}-3\phi_{m,i}\lambda_{n,i}\right)\end{aligned} \tag{5.18}$$

Equation (5.18) is a generic equation for expressing the nonlinear terms that are seen in Eq. (5.9).

5.5 The Finite Difference Formulation and Solution Algorithm

One may use Eq. (5.18) for expressing $\tilde{K}F, \tilde{\Omega}P, \tilde{K}M, \tilde{\gamma}F, \tilde{\Omega}H, \tilde{V}P, \tilde{K}\Omega, \tilde{K}V$ and $\tilde{\gamma}\Omega$ (i.e., for all of the nonlinear terms in Eqs. (2.26), (2.27), (2.37), and (2.38)) at any two adjacent nodes i and $i + 1$ along the longitudinal direction of the rotating blade, and at every time step. By using Eq. (5.18) for each one of the nonlinear terms, four unknowns (the ones with a plus superscript) and four known terms (the ones without a plus superscript) are added to the finite difference equations. By summing up all of these terms, using Eqs. (2.87), (2.98), and (2.109), and after mathematical manipulations, one can convert the system of vector Eqs. (2.26), (2.27), (2.37), (2.38), (2.36), (2.45), and (2.56) into the following matrix equation,

$$A_i q_i^+ + B_i q_{i+1}^+ = J_i; \quad i = 1, \ldots, N-1 \tag{5.19}$$

where N is the number of nodes in the model, and at a certain time step, all of the quantities at the right-hand side of Eq. (5.19) are known from the initial conditions, given data, or from the previous time step. Matrices A_i and B_i are 24 × 24 matrices and q_i and J_i are 24 × 1 column vectors. Expressions for matrices A_i and B_i as well as the vector J_i have been given in the Appendix.

The column state vector, q, has 24 elements that include all of the variables of interest in this problem,

$$\begin{aligned} q = [&F_1\, F_2\, F_3\, M_1\, M_2\, M_3\, V_1\, V_2\, V_3\, \Omega_1\, \Omega_2\, \Omega_3\, P_1\, P_2\, P_3\, H_1\, H_2\, H_3 \\ &\gamma_{11}\, 2\gamma_{12}\, 2\gamma_{13}\, \kappa_1\, \kappa_2\, \kappa_3]^{\mathrm{T}} \end{aligned} \tag{5.20}$$

So, Eq. (5.19) relates unknown quantities at node i to those of node i + 1. It is interesting to note that the corresponding elements of the A_i and B_i matrices are almost identical. The only exception happens when it comes to the derivatives with respect to x_1 for which a sign difference is observed [due to the application of Eq. (2.98)].

Referring to Fig. 2.5, for each i = 1, …, N − 1, Eq. (5.19) relates q_i to q_{i+1} and it is composed of 24 algebraic equations with 48 unknowns. Therefore, Eq. (5.19) cannot be solved without the application of the boundary conditions. This method has been applied for similar formulations in Ghorashi (1994) and Esmailzadeh and Ghorashi (1997).

In order to apply the boundary conditions at the two ends of the blade, one should relate the state vectors at these points at the next time step, i.e., q_1^+ and q_N^+, directly to each other. By successive use of Eq. (5.19), it can be shown that,

$$q_1^+ = M_{N-1}^{\mathrm{tot}} . q_N^+ + T_{N-1}^{\mathrm{tot}} \tag{5.21}$$

where,

$$M_{N-1}^{\mathrm{tot}} = a_1\, a_2\, a_3\, a_4 \ldots a_{N-1}, \quad a_i = -A_i^{-1} B_i \tag{5.22}$$

$$T_{N-1}^{\mathrm{tot}} = b_1 + a_1 b_2 + a_1 a_2 b_3 + \cdots + a_1 a_2 a_3 \ldots a_{N-2} b_{N-1}, \quad b_i = A_i^{-1} J_i \tag{5.23}$$

Once the boundary conditions are applied (as it will be shown in the following section) and since half of the variables at the two end nodes are already known from the boundary conditions, Eq. (5.21) would be a solvable set of 24 equations with 24 unknowns. Therefore, it can be solved for the remaining unknowns at the two ends of the blade. Having completely solved the problem at the boundary nodes 1 and N, one can use Eq. (5.19) in order to obtain the unknowns at all of the interior nodes at the next time step by starting either from node 1 or node N. The procedure can be repeated to solve the problem at all time steps and spatial nodes.

The logic of the mentioned solution is like that of the boundary element method where the solution is first obtained at the boundary, and then, the boundary solution is used for the calculation of the solution inside the domain.

The order of variables in the state vector is identical to the order of the corresponding equations so that the diagonal elements of A_i and B_i be nonzero. This choice reduces the risk of ill-conditioning in which matrices are nearly singular and therefore the solution is highly sensitive to the slightest changes in the boundary conditions or to the numerical values of other physical quantities.

It should be noted that the likelihood of ill-conditioning in a matrix increases if the ratio of the largest diagonal element divided by the smallest one is a large number. Usually, non-dimensionalization reduces the mentioned ratio and brings the values of all diagonal elements closer to each other.

5.6 The Case of a Rotating Hingeless Beam

In a rotating-wing aircraft, the rotor is unique because, unlike a propeller, it must provide both a lifting force (in opposition to the aircraft weight) and a propulsive force (to overcome the rotor and airframe drag) in forward flight. There are basically four types of helicopter rotor hubs in use. These are the teetering, articulated, hingeless, and the bearingless designs.

A hingeless rotor design eliminates the flap and lead–lag hinges by using flexure to accommodate blade motion. A feathering bearing is still used to allow for pitch changes on each blade. The advantages of a hingeless design are low aerodynamic drag and being mechanically simple with a low parts count. However, because blade articulation is achieved by the elastic flexing of a structural beam, the design of such rotors is rather complicated, Leishman (2006, p. 174).

The solution method explained in Sect. 5.5 is now applied to the analysis of the nonlinear dynamic behavior of a rotating hingeless (cantilever) composite blade. The aim is to calculate the transient and the steady-state responses of the blade as it is gently accelerated. The angular velocity $\Omega_3(t)$ at the root of the blade is assumed to vary as follows:

$$\Omega_3(t) = \Omega_{3,\mathrm{ss}} \times \frac{t^2}{k_\Omega^2 + t^2} \tag{5.24}$$

Therefore, the blade starts its motion from rest and accelerates until it reaches the steady-state rotational speed, $\Omega_{3,\mathrm{ss}}$ (k_Ω is a constant). In this formulation, even if one only wishes to analyze the response of the blade at the steady-state speed, calculating the whole dynamic response starting from zero velocity is necessary.

To simplify the analysis, consider the case in which the origin of the reference frame (i.e., the shear center) and the centroid of each section coincide. Thus,

$$\bar{x}_2 = \bar{x}_3 = 0 \tag{2.54}$$

Therefore,

$$\bar{\xi} = 0 \quad \tilde{\bar{\xi}} = 0 \tag{2.55}$$

For a hingeless rotating blade with its root ($i = 1$) on the axis of rotation, and the angular velocity at the root as the given kinematic input, the root boundary conditions are

$$V = \begin{Bmatrix} 0 \\ 0 \\ 0 \end{Bmatrix}, \quad \Omega = \begin{Bmatrix} 0 \\ 0 \\ \Omega_3 \end{Bmatrix} \tag{5.25}$$

Substituting Eqs. (5.25) and (2.54) into Eq. (2.45) results in the values of P and H at node 1. Now, at the tip of the blade ($i = N$), the boundary conditions are kinetic,

$$F = \begin{Bmatrix} 0 \\ 0 \\ 0 \end{Bmatrix}, \quad M = \begin{Bmatrix} 0 \\ 0 \\ 0 \end{Bmatrix} \tag{5.26}$$

Using Eq. (2.56) at the tip, one obtains: $\gamma = 0, \quad \kappa = 0$. So, together with Eq. (5.26), there are four vector boundary conditions at the tip that represent a total of 12 scalar equations. Recalling the other set of 12 scalar boundary conditions at the root ($i = 1$), in all 24 quantities [i.e., half of the number of variables in Eq. (5.21)] are known from the boundary conditions. Therefore, enough number of boundary conditions are now available to solve the problem. Substitution of Eqs. (5.25) and (5.26) into (5.21) gives

$$\begin{Bmatrix} F^+ \\ M^+ \\ 0 \\ \overbrace{\Omega^+}^{\text{given}} \\ 0 \\ \overbrace{H^+}^{\text{given}} \\ \gamma^+ \\ \kappa^+ \end{Bmatrix}_1 = M_{N-1}^{\text{tot}} \begin{Bmatrix} 0 \\ 0 \\ V^+ \\ \Omega^+ \\ P^+ \\ H^+ \\ 0 \\ 0 \end{Bmatrix}_N + T_{N-1}^{\text{tot}} \tag{5.27}$$

Equation (5.27) relates the remaining unknowns at node 1 to the remaining unknowns at node N. This equation should be solved for the eight unknown vectors at the two nodes. To this end, a sub-matrix of M_{N-1} and a sub-vector of T_{N-1} are made. To form these sub-matrices, one should keep elements on the row numbers which are the same as the row numbers of the *known* boundary conditions at node 1 and for M_{N-1} keep elements on the column numbers which are the same as the row numbers of the *unknown* boundary conditions at node N to get

$$\underbrace{\begin{Bmatrix} V^+ \\ \Omega^+ \\ P^+ \\ H^+ \end{Bmatrix}_1}_{\text{all known}} = M_{N-1}^{\text{tot}}(7:18, 7:18). \underbrace{\begin{Bmatrix} V^+ \\ \Omega^+ \\ P^+ \\ H^+ \end{Bmatrix}_N}_{\text{all unknown}} + T_{N-1}^{\text{tot}}(7:18) \tag{5.28}$$

or,

$$\begin{Bmatrix} V^+ \\ \Omega^+ \\ P^+ \\ H^+ \end{Bmatrix}_N = \left[M_{N-1}^{\text{tot}}(7:18, 7:18)\right]^{-1} . \left(\begin{Bmatrix} V^+ \\ \Omega^+ \\ P^+ \\ H^+ \end{Bmatrix}_1 - T_{N-1}^{\text{tot}}(7:18) \right) \tag{5.29}$$

Equation (5.29) provides all of the remaining unknowns at node N. Substituting the results obtained from solving Eq. (5.29) at node N, back into Eq. (5.27) results in the remaining unknowns at node 1. Having calculated all of the unknowns at nodes 1 and N, one may now use Eq. (5.19) to calculate the unknowns at all interior nodes, starting from either node 1 or node N. Starting from node N, and in order to march toward node 1, the following may be used:

$$q_i^+ = -A_i^{-1} B_i q_{i+1}^+ + A_i^{-1} J_i; \quad i = N-1 \text{ to } 1 \tag{5.30}$$

or,

$$q_i^+ = a_i q_{i+1}^+ + b_i; \quad i = N-1 \text{ to } 1 \tag{5.31}$$

Using Eq. (5.31), and having already calculated q_N^+, one may calculate q_{N-1}^+ and then continue to find q_{N-2}^+ and so on until eventually another approximate solution for q_1^+ is obtained. This result may then be compared with the other q_1^+ value calculated using Eq. (5.27). This comparison provides a measure for the accuracy of the solution procedure and the impact of round-off errors.

5.6.1 Approximate Equation of the Axial Force

Since the most significant force that is generated in the rotating blade is the axial force, F_1, it would be beneficial to derive an alternative expression for this force and use it for verification. Figure 5.1 illustrates the free body diagram of an element of the blade of length, $\mathrm{d}x_1$, where only the axial forces are shown. Using Newton's second law of motion,

$$\sum F_1 = ma_1 \tag{5.32}$$

one obtains,

$$\mathrm{d}F_1 = \overbrace{(\rho A)}^{\mu}\,\mathrm{d}x_1\left(-x_1\Omega_3^2\right) \tag{5.33}$$

or,

$$\frac{\mathrm{d}F_1}{\mathrm{d}x_1} = -\rho A x_1 \Omega_3^2 \tag{5.34}$$

Integrating Eq. (5.34) and satisfying the free end boundary condition give

$$F_1 = \frac{1}{2}\rho A\Omega_3^2\left(L^2 - x_1^2\right) \tag{5.35}$$

Equation (5.35) provides an approximate expression for F_1 which can be used as a benchmark to evaluate the accuracy of the corresponding results provided by other methods.

5.6.2 Effect of Weight

To make the model more realistic, the effect of the weight of the blade in its dynamic response is taken into account. To this end, weight is modeled by the following gradually increasing force per unit length,

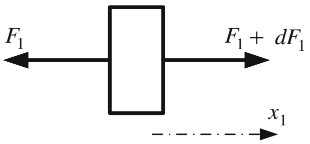

Fig. 5.1 Free body diagram of the blade for the axial tensile force component

$$f_3(t) = \rho A g \times \frac{t^2}{k_g^2 + t^2} \tag{5.36}$$

where k_g is a constant. This gradually varying time function smoothens the convergence of the solution, and k_g can be tuned so that the speed of convergence to the nominal gravity force can be adjusted.

5.7 Case Study: Isotropic Rectangular Solid Model

The isotropic rectangular solid model introduced in Sect. 3.3 is considered here again. The blade rotates about the x_3 axis at the angular velocity shown in Fig. 5.2a and gently reaches a steady-state velocity. The response of the blade to this angular velocity input has been illustrated in Figs. 5.2b, 5.3, 5.4, 5.5, 5.6, 5.7, 5.8, 5.9, and 5.10. Two cases have been considered—with the effect of gravity and without it.

The resulting variation of the induced moment at the clamped end versus time has been illustrated in Fig. 5.2b. It is observed that when the blade reaches its steady-state velocity, since tangential acceleration is zero and as expected, the bending moment converges to zero as well. Furthermore, it can be seen that the maximum absolute value of the bending moment corresponds to an instant at which the angular velocity curve has an inflection point, i.e., when the angular acceleration is maximum.

Figure 5.3 illustrates the variation of the induced bending moment along the blade and versus time. At x = 0, it shows the same variations as were observed in Fig. 5.2b, and at x = 1 m, the free boundary condition value of zero is seen.

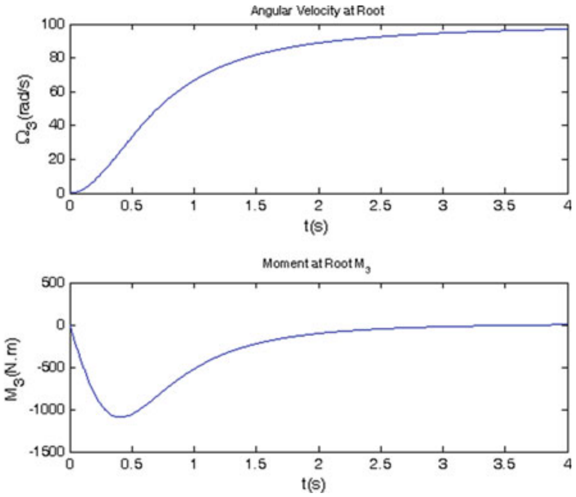

Fig. 5.2 **a** Time history diagram of the angular velocity Ω_3 at the root, **b** corresponding bending moment at the clamped root

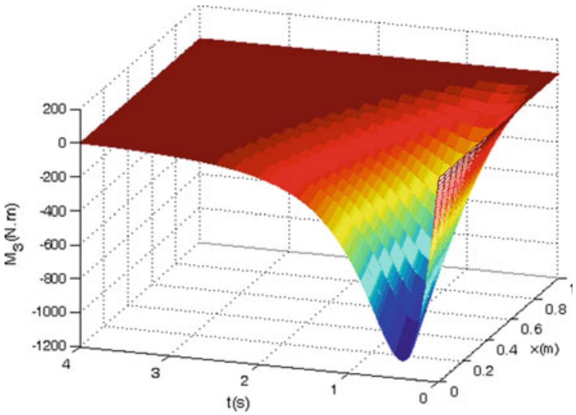

Fig. 5.3 Time history variation of the induced bending moment M_3 along the blade

Distribution of the induced internal forces along the blade span at $t = 2$ s is shown in Fig. 5.4. In Fig. 5.5, the time history diagrams of the induced internal forces at the mid-span of the blade are plotted. Figure 5.6 is the same as Fig. 5.5 except for the fact that it includes the effect of the weight of the blade. It can be seen that weight, which acts in the x_3 direction, mostly affects the F_3 component, as expected. Figures 5.5 and 5.6 also reveal that the obtained results for F_1 are very

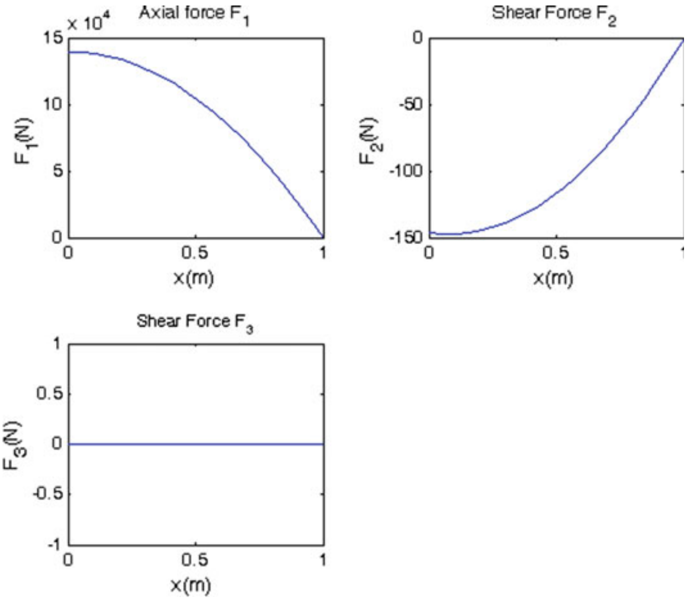

Fig. 5.4 Distributions of the internal force components along the blade at $t = 2$ s; weight not included

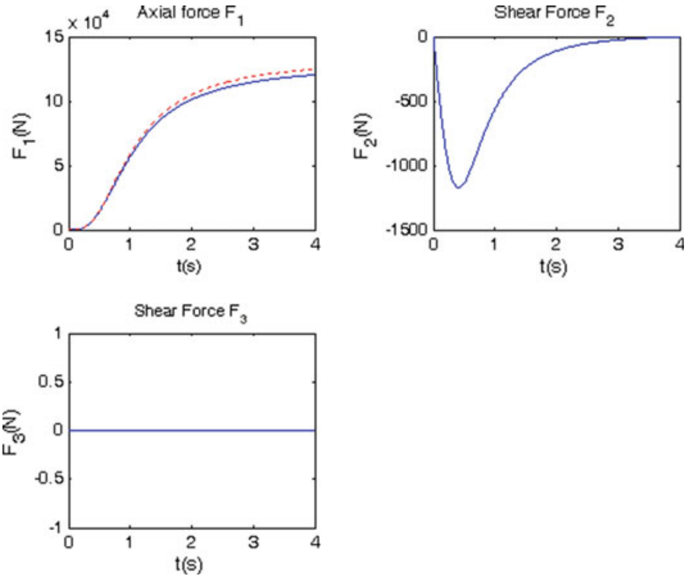

Fig. 5.5 Time history diagrams of the internal forces at the mid-span (*solid line*) Eq. (5.35) (*dashed*); weight not included

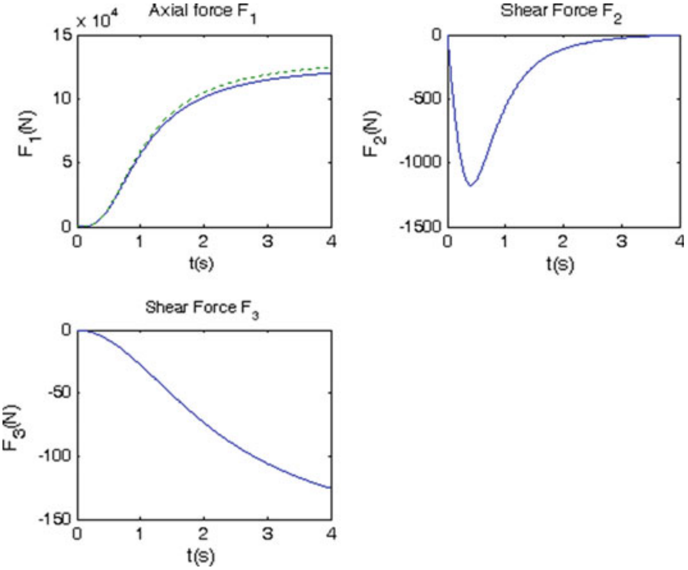

Fig. 5.6 Time history diagrams of the internal forces at the mid-span (*solid line*) Eq. (5.35) (*dashed*); weight included

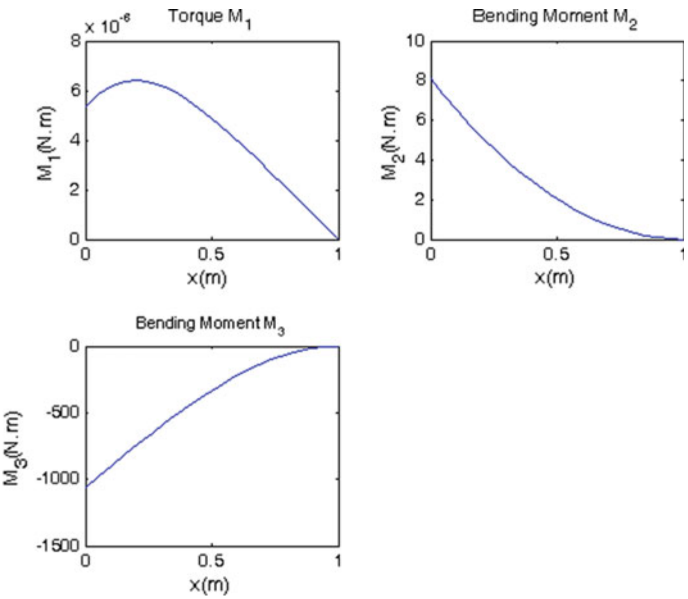

Fig. 5.7 Distributions of the internal moment components along the blade at $t = 0.5$ s; weight included

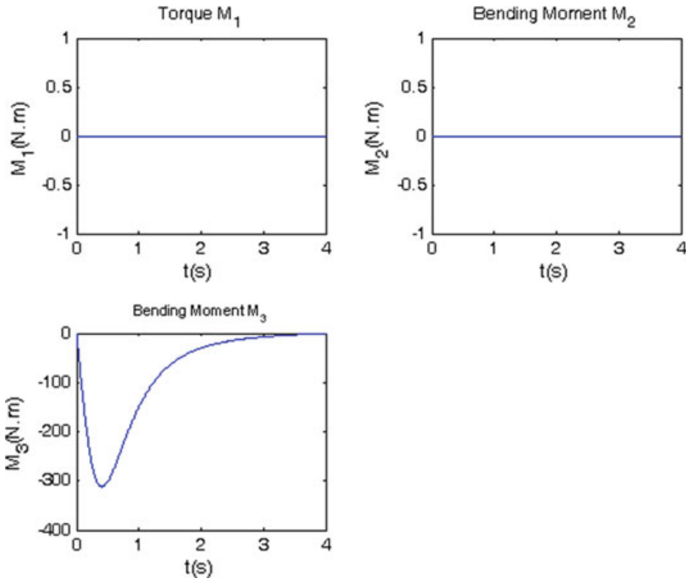

Fig. 5.8 Time history diagrams of the internal moment components at the mid-span; weight not included

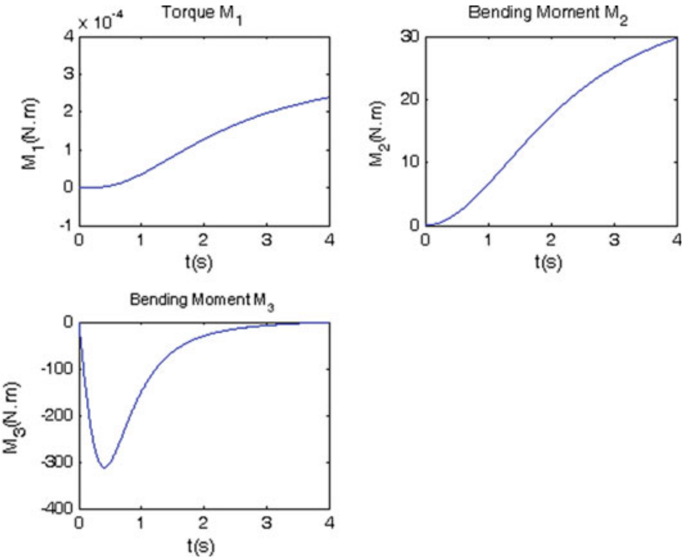

Fig. 5.9 Time history diagrams of the internal moment components at the mid-span; weight included

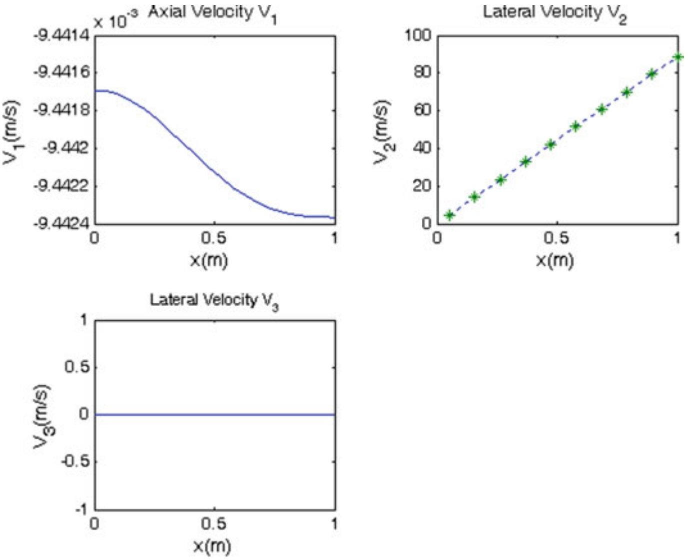

Fig. 5.10 Distributions of the velocity components along the blade at $t = 2$ s (*solid and dashed lines*) and according to Eq. (5.8) (*asterisk*)

close to those predicted by Eq. (5.35). This force, as shown in Figs. 5.5 and 5.6, is the prominent force generated in the blade.

Figure 5.7 presents the distributions of the induced moments along the blade. The time history diagrams of the moments induced at the mid-span of the blade are illustrated in Figs. 5.8 and 5.9. It is observed that if the weight of the blade is not included in the analysis, M_3 is the only significant moment that is generated. However, in Fig. 5.9, with addition of gravity to the model, a nonzero moment M_2 is also produced, as expected. The variation of the linear velocity along the blade is illustrated in Fig. 5.10. As to V_2, the calculated distribution is very close to the linear distribution of Eq. (5.8), as expected.

5.8 Verification by the Nonlinear Static Model

The results of the nonlinear static model of Chap. 4 are now compared with those calculated for the nonlinear dynamic model of a non-rotating hingeless blade that is subjected to a gradually applied lateral load. If the load application in the dynamic model is gradual enough, the outcome of this quasi-static loading should be close to (and actually converge to) that of the nonlinear static model.

Since the blade is almost stationary, the clamped root boundary conditions, i.e., Eq. (5.25), reduce to

$$V = \begin{Bmatrix} 0 \\ 0 \\ 0 \end{Bmatrix}, \quad \Omega = \begin{Bmatrix} 0 \\ 0 \\ 0 \end{Bmatrix} \tag{5.37}$$

At the tip Eq. (5.26) is still valid.

As an example, consider the isotropic rectangular solid model introduced in Sect. 3.3 that is subjected to a concentrated static load, $F_2 = 25$ N, at the tip of the beam. The equivalent dynamic model can be built by dividing the 1-m-long beam into 19 elements (similar to what is seen in Fig. 2.5) in which only the 19th element (the tip element) is subjected to a triangularly distributed load $f_2 = 950$ N/m (it varies between zero at the 19th node and 950 N/m at the 20th node). This distributed load is applied gradually to the beam, and at its full value, it is equivalent to a concentrated load of: $950 \times (1/19)/2 = 25$ N, which is the same as the applied static load. However, this equivalent point force is not applied at the tip of the last element but at an intermediate point along that element. Because of the slightly shorter moment arm, the steady-state value of the bending moment induced by this gradually applied dynamic load about the mid-span of the beam would be somewhat less than the corresponding static force moment. In fact, the moment of the dynamic load about the mid-span of the blade would be $25 \times [0.5 - (1/3)/19] = 12.1$ N.m, whereas the corresponding static moment is 12.5 N.m.

While in the static formulation the tip values of F and M are the applied loads at the tip of the blade, in the dynamic formulation f and m are the applied loads per unit length. This difference should be accounted for in order to get meaningful and comparable results.

As it was mentioned, the load is applied gently to the nonlinear dynamic model. The gradual application of the load is necessary to assure the effective performance of the perturbation scheme. It is also compatible with the main assumption in the application of the perturbation method according to which perturbations are small and variations of variables in time and space happen gradually. If this is not the case, the method fails to provide smooth and stable solutions. The gentle variation of the applied distributed load is expressed by

$$f(t) = f_{ss} \times \frac{t^2}{2+t^2} \tag{5.38}$$

where, f_{ss} is the target steady-state value of the distributed load, and the number in the denominator is an arbitrary constant that tunes the speed of convergence of $f(t)$ to f_{ss}.

Using the gradually applied load in the nonlinear dynamic model, the induced moment components at the mid-span of the beam have been calculated and illustrated in Fig. 5.11.

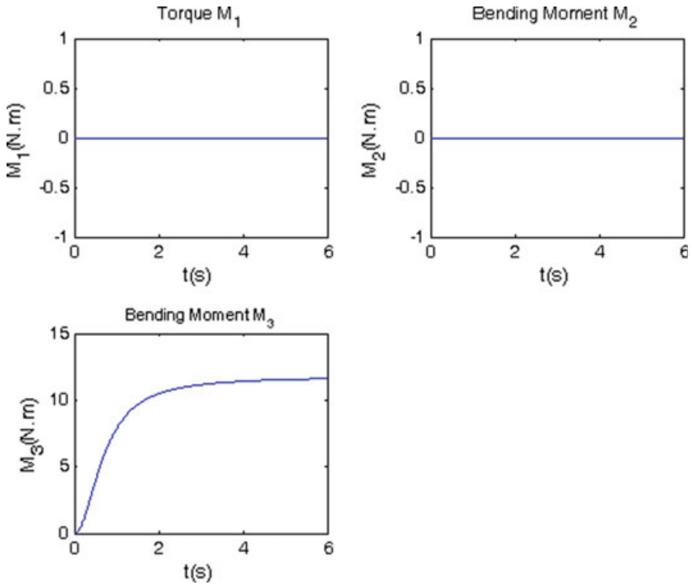

Fig. 5.11 Time history diagrams of internal moment components at the mid-span of the clamped beam using the nonlinear dynamic model

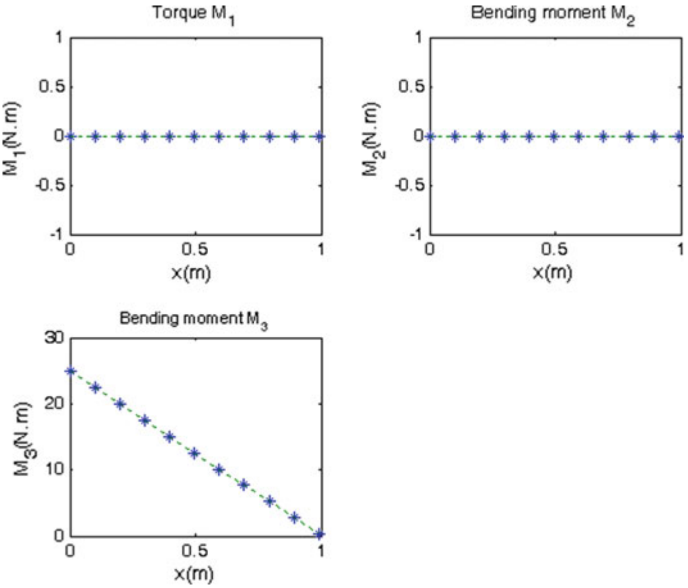

Fig. 5.12 Internal moment components along the beam under the application of an $F_2 = 25$ N tip load using the linear static model (*asterisk*) and the nonlinear static model (*dashes*)

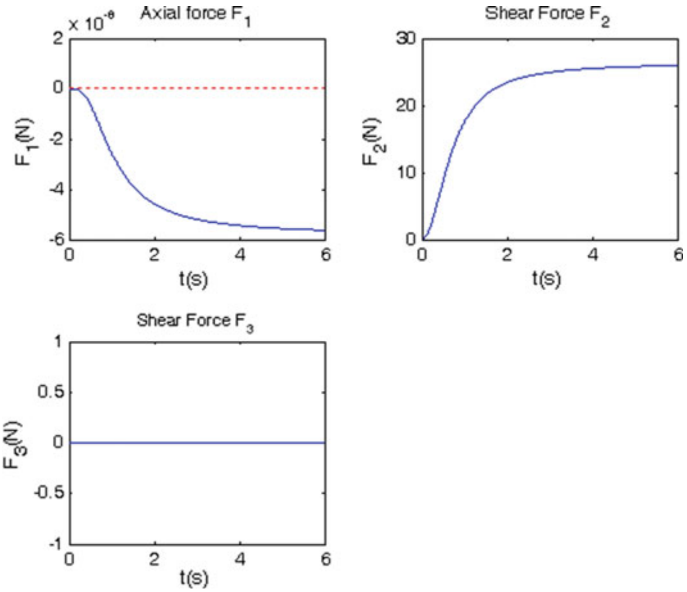

Fig. 5.13 Time history diagrams of internal force components at the mid-span of the clamped beam using the nonlinear dynamic model

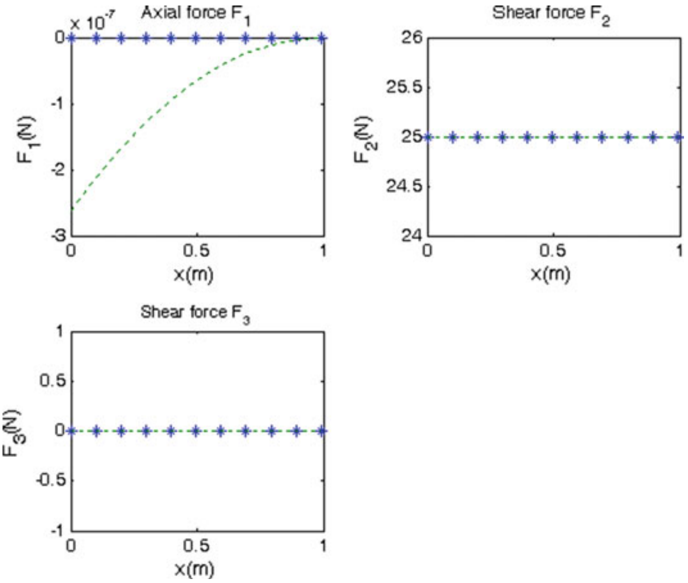

Fig. 5.14 Internal force components along the beam under the application of an $F_2 = 25$ N tip load using the linear static model (*asterisk*) and the nonlinear static model (*dashes*)

Figure 5.12 presents the corresponding nonlinear static model results for the induced moment distribution along the length of the beam. It can be seen that the value to which the M_3 component is converging at the mid-span of the beam in Fig. 5.11 is very close to the corresponding static moment value at the same point shown in Fig. 5.12. The corresponding results for the nonlinear dynamic and the nonlinear static values of the shear force, F_2, at the mid-span of the blade have been plotted in Figs. 5.13 and 5.14, respectively. Conclusions similar to those made about the moments can be presented for these forces as well, and it can be seen that the dynamic value of F_2 converges to the nonlinear static shear force given in Fig. 5.14.

5.9 Case Study: Composite Box Model

Having demonstrated the validity of the analysis in Sect. 5.8, one can now extend the nonlinear dynamic solution to the composite box beam example discussed in Sect. 3.4. The cross-sectional area of the composite material (excluding the hollow part) is 5.08×10^{-5} m^2. The model has 50 nodes along its span and 1600 nodes in the cross section.

The blade accelerates from rest and gradually reaches its steady-state speed of 100 rad/s, as it is shown in Fig. 5.15a. The dynamic response of the blade is illustrated in Figs. 5.15b, 5.16, 5.17, 5.18, 5.19, 5.20, and 5.21. It is seen that by using the full nonlinear model, one may start with the rest initial conditions, accelerate the blade, and get its whole elasto-dynamic behavior until it reaches the steady state.

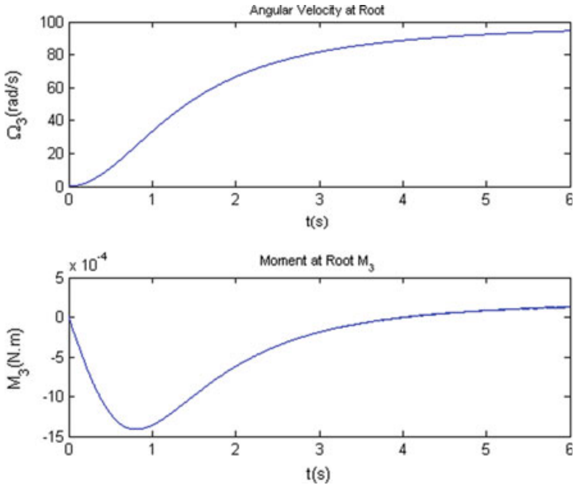

Fig. 5.15 **a** Time history diagram of the angular velocity Ω_3 at the root, **b** corresponding bending moment at the clamped root

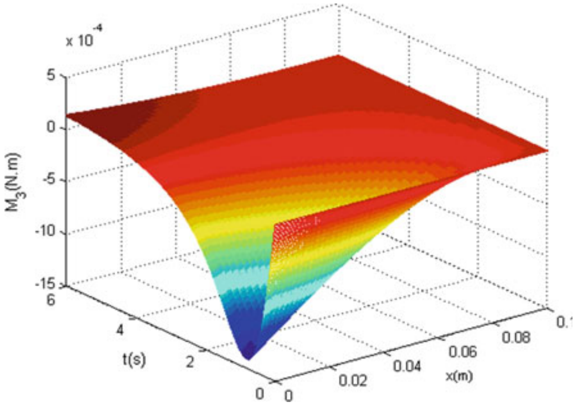

Fig. 5.16 Time history variation of the induced bending moment M_3 along the blade

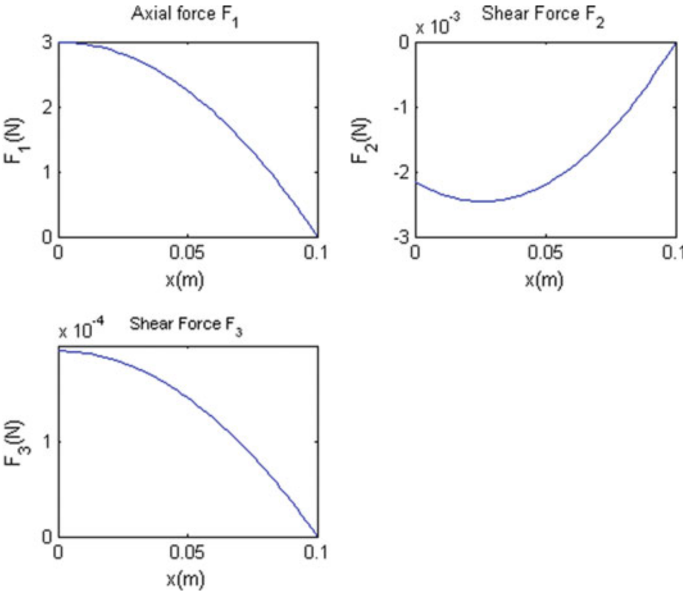

Fig. 5.17 Distribution of the internal force components along the blade at $t = 3$ s

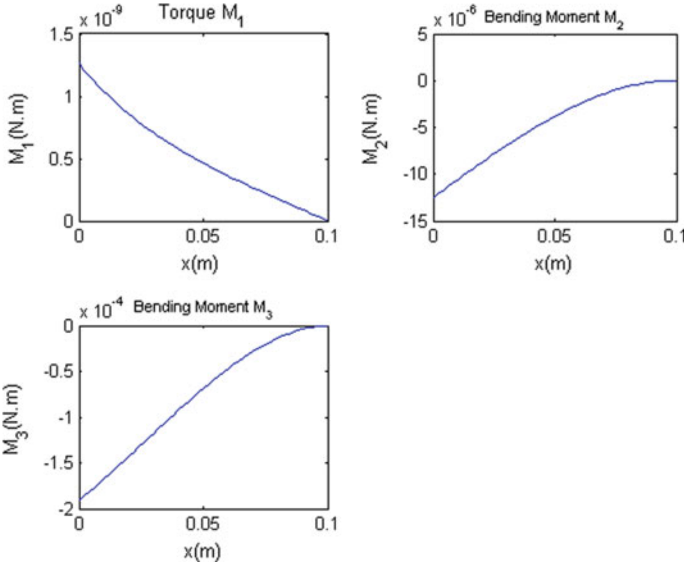

Fig. 5.18 Distributions of the internal moment components along the blade at $t = 3$ s

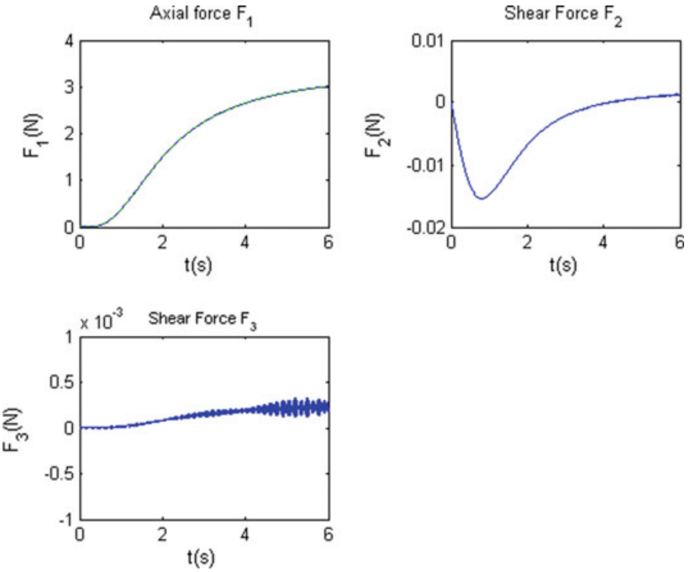

Fig. 5.19 Time history diagrams of the internal forces at the mid-span

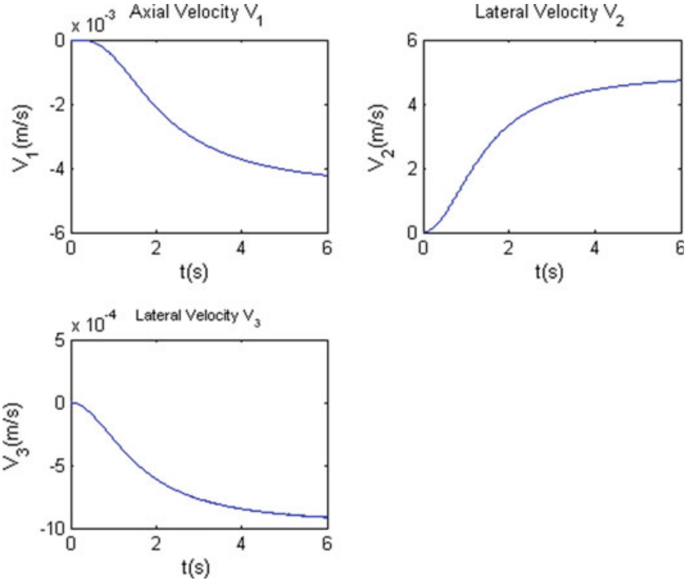

Fig. 5.20 Time history diagrams of the velocity components at the mid-span

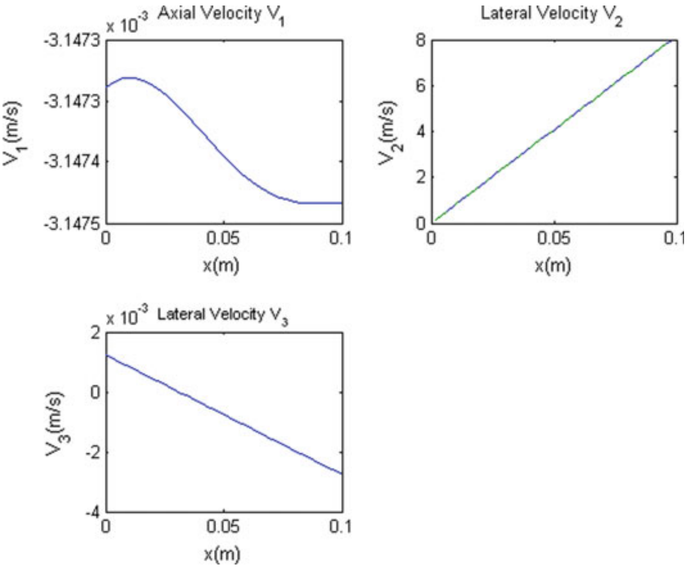

Fig. 5.21 Distributions of the velocity components along the blade at $t = 3$ s

References

Esmailzadeh, E., & Ghorashi, M. (1997). Vibration analysis of a Timoshenko Beam subjected to a traveling mass. *Journal of Sound and Vibration, 199*(4), 615–628.

Ghorashi, M. (1994). *Dynamic and vibratory analysis of beams under dynamic loads induced by traveling masses and vehicles*. Ph.D. Thesis, Mechanical Engineering Department, Sharif University of Technology.

Ghorashi, M. (2009). *Dynamics of elastic nonlinear rotating composite beams with embedded actuators.* Ph.D. Thesis, Mechanical and Aerospace Engineering Department, Carleton University.

Ghorashi, M., & Nitzsche, F. (2009). Nonlinear dynamic response of an accelerating composite rotor blade using perturbations. *Journal of Mechanics of Materials and Structures, 4*, 693–718.

Leishman, J. G. (2006). *Principles of helicopter aerodynamics* (2nd ed.). NewYork: Cambridge University Press.

Chapter 6
Steady-State and Perturbed Steady-State Nonlinear Dynamics of Hingeless Rotating Blades

6.1 Introduction

The finite difference solution presented in Chap. 5 can provide the full dynamic (transient and steady-state) response of a rotating blade. However, one may only be interested in finding the steady-state response. In this chapter, finding an alternative solution method with this capability is in order. Such an alternative solution can also provide a means for verifying the steady-state results obtained by using the method presented in Chap. 5.

To perform a numerical solution, one may use an explicit finite difference method where explicit (direct) integration is performed. An explicit solution, as was implemented in Chap. 5, is a straightforward method, but it may result in numerical instability. While in a stable difference scheme small changes in the initial and boundary data do not change the solution greatly, an unstable difference scheme shows great sensitivity to the initial and boundary data.

Contrary to the direct methods, in an implicit (indirect or iterative) integration method, there is not an explicit formula at a point for the value of the unknown functions appearing in the differential equation. Generally, using implicit methods, a nonlinear algebraic equation must be solved to determine a function value at a given point. However, even though the solution algorithm of implicit methods is more involved, they have the advantage of providing unconditionally stable solutions.

In analyzing rotor blades, at the steady state, the governing equations are no longer time-dependent, and therefore, they have no partial derivatives with respect to time and no time-dependent applied forces. They form a two-point boundary value problem with boundary conditions at the root (first point) and at the tip (second point). Such a boundary value problem can be solved by using the shooting method—as it was done by the author before in Esmailzadeh et al. (1995), for example.

M. Ghorashi, *Statics and Rotational Dynamics of Composite Beams*,
DOI 10.1007/978-3-319-14959-2_6

In this chapter, an implicit integration method that uses the shooting method for the numerical solution of nonlinear boundary value problems is developed in order to calculate the nonlinear steady-state response of a hingeless rotating blade. The outcome is the steady-state response of the nonlinear hingeless (cantilevered) rotating blade.

The applied implicit method converts the original boundary value problem to a series of equivalent initial value problems in terms of the space variable where the unknown initial conditions are calculated through an iterative process using the Newton-Raphson method. These initial conditions correspond to the boundary conditions of the original boundary value problem. In each iteration, the Newton-Raphson algorithm improves the unknown but guessed initial conditions. The solution is repeated until it satisfies a convergence criterion that is checked at the end of every iteration. When the convergence criterion is satisfied, the correct solution of the boundary value problem and the steady-state response of the blade are obtained. The solution includes the steady-state internal forces, moments, velocities, and angular velocities along the blade. This solution is used to verify the results of the explicit (or direct) method presented in Chap. 5.

Finally, the response of the system to small perturbations applied to the system when it is already in its steady-state motion is calculated. In order to do that, the complete solution is written as a summation of the steady-state and the perturbation terms representing small changes in the response. This function is then substituted into the original time-dependent equations, and the result is solved for the unknown perturbations. Unlike the method used in Chap. 5 which produced the whole dynamics of the blade in this chapter, the blade dynamics is calculated only in the vicinity of the steady-state response.

Most of the contents of this chapter have been presented in Ghorashi (2009) and published in Ghorashi and Nitzsche (2008, 2009). In Cesnik et al. (2001) and Shin et al. (2008), the steady-state dynamics of rotating blades and their perturbed solutions around the steady-state solution have been presented.

6.2 Formulation of the Boundary Value Problem and Its Conversion to a Series of Initial Value Problems

The steady-state form of the governing differential equations (2.26), (2.27), (2.37), and (2.38) can be obtained by dropping all of the time-dependent terms and all terms with derivatives with respect to time. Also, the applied loads $f(x_1, t)$ and $m(x_1, t)$ are now treated as functions of x_1 only. The resulting set of nonlinear ordinary differential equations forms a boundary value problem. The steady-state form of the governing differential equations (2.26), (2.27), (2.37), and (2.38) is as follows:

$$F_1' = -K_2F_3 + K_3F_2 + \Omega_2P_3 - \Omega_3P_2 - f_1 \tag{6.1}$$

$$F_2' = -K_3F_1 + K_1F_3 + \Omega_3P_1 - \Omega_1P_3 - f_2 \tag{6.2}$$

$$F_3' = -K_1F_2 + K_2F_1 + \Omega_1P_2 - \Omega_2P_1 - f_3 \tag{6.3}$$

$$M_1' = -K_2M_3 + K_3M_2 - 2\gamma_{12}F_3 + 2\gamma_{13}F_2 + \Omega_2H_3 - \Omega_3H_2 + V_2P_3 - V_3P_2 - m_1 \tag{6.4}$$

$$M_2' = -K_3M_1 + K_1M_3 - 2\gamma_{13}F_1 + (1+\gamma_{11})F_3 + \Omega_3H_1 - \Omega_1H_3 + V_3P_1 - V_1P_3 - m_2 \tag{6.5}$$

$$M_3' = -K_1M_2 + K_2M_1 - (1+\gamma_{11})F_2 + 2\gamma_{12}F_1 + \Omega_1H_2 - \Omega_2H_1 + V_1P_2 - V_2P_1 - m_3 \tag{6.6}$$

$$V_1' = -K_2V_3 + K_3V_2 - 2\gamma_{12}\Omega_3 + 2\gamma_{13}\Omega_2 \tag{6.7}$$

$$V_2' = -K_3V_1 + K_1V_3 + (1+\gamma_{11})\Omega_3 - 2\gamma_{13}\Omega_1 \tag{6.8}$$

$$V_3' = -K_1V_2 + K_2V_1 - (1+\gamma_{11})\Omega_2 + 2\gamma_{12}\Omega_1 \tag{6.9}$$

$$\Omega_1' = -K_2\Omega_3 + K_3\Omega_2 \tag{6.10}$$

$$\Omega_2' = -K_3\Omega_1 + K_1\Omega_3 \tag{6.11}$$

$$\Omega_3' = -K_1\Omega_2 + K_2\Omega_1 \tag{6.12}$$

One may use Eqs. (2.36), (2.47), and (2.56) in order to express all variables in Eqs. (6.1)–(6.12) only in terms of the four vector variables F, M, V, and Ω (or the corresponding twelve scalar variables).

For simplicity, consider a case in which the origin of the reference frame (i.e., the shear center) and the centroid of cross sections coincide. Then, using Eq. (5.5), Eqs. (6.4)–(6.6) reduce to the following:

$$M_1' = -K_2M_3 + K_3M_2 - 2\gamma_{12}F_3 + 2\gamma_{13}F_2 + \Omega_2H_3 - \Omega_3H_2 - m_1 \tag{6.13}$$

$$M_2' = -K_3M_1 + K_1M_3 - 2\gamma_{13}F_1 + (1+\gamma_{11})F_3 + \Omega_3H_1 - \Omega_1H_3 - m_2 \tag{6.14}$$

$$M_3' = -K_1M_2 + K_2M_1 - (1+\gamma_{11})F_2 + 2\gamma_{12}F_1 + \Omega_1H_2 - \Omega_2H_1 - m_3 \tag{6.15}$$

The system of Eqs. (6.1)–(6.3) and (6.7)–(6.15) is a system of twelve scalar nonlinear ordinary differential equations in terms of the twelve components of F, M, V, and Ω. They should be solved together with the hingeless boundary conditions (5.25) and (5.26) at the root and at the tip of the blade, respectively. Having solved this system, other variables of interest such as the 1-D displacement field u, deformed curvature κ, Rodrigues parameters θ, and the finite rotation tensor C can be calculated using Eqs. (2.36), (2.57), (2.58), and (2.62). In the coming sections, it will be shown how this problem can be solved by conversion to an equivalent initial value problem that is solved iteratively.

6.3 The Solution Algorithm and Formulation

In Sect. 6.2, it was shown that the steady-state analysis of a rotating blade includes the solution of a system of twelve scalar nonlinear ordinary differential equations (6.1)–(6.3) and (6.7)–(6.15) in terms of the twelve components of F, M, V, and Ω. The objective here is to calculate the steady-state response of a composite rotating blade by solving the nonlinear boundary value problem formulated in Sect. 6.2 and by using the shooting method. To this end, at the steady-state, the boundary value problem will be converted to a series of initial value problems (in terms of the longitudinal coordinate, x_1).

In the case of a fixed-free (hingeless or cantilever) blade, while based on the root boundary condition given in Eq. (5.25), at $x_1 = 0$, Ω and V are known, magnitudes of F and M at this point are unknown. Therefore, in the equivalent initial value problem, the fixed boundary provides the required initial conditions for velocity and angular velocity. However, for the rest of the variables, i.e., forces and moments, such initial conditions at the root are not known. So, for converting this two-point boundary value problem (with boundaries at the root and at the tip of the blade) to an initial value problem, initial conditions for variables whose boundary values at the root are not known should be guessed (in order to solve the initial value problem) and then corrected iteratively. After guessing them, a complete set of known and assumed initial conditions at the root would be available. The initial value problem is then solved by the Runge-Kutta method, and the solution along the blade and especially at its other end (the free end or tip) is calculated.

At this step, the error that the current solution has at the known boundary conditions at the tip of the blade is computed. The checkpoint for the accuracy of the guessed initial conditions at the root is to see whether the calculated solution satisfies the known boundary conditions at the tip of the blade, i.e., Eq. (5.26). If these conditions are satisfied by the obtained solution, a solution of the boundary value problem which satisfies all imposed boundary conditions is obtained. It is, therefore, the correct solution to the boundary value problem. Otherwise, the guessed initial conditions at the root are in error and they should be modified. The modification is performed iteratively by the use of the Newton-Raphson algorithm. It provides the best corrective increments for the guessed initial conditions. The solution of the initial value problem and the updating of the initial conditions at the root are repeated until the correct solution to the problem that satisfies the boundary conditions at the tip of the blade is obtained.

Now, let us formulate the mentioned discussion. Consider an arbitrary iteration number, k, and let us denote the known (target) values of the boundary conditions at the tip of the blade by β_j (j = 1 to 6)—three indices are used for the three force components and three indices for the three moment components. These known values can be compared with the current (kth iteration) values, g_{jk} (j = 1 to 6), that have been calculated at the tip of the blade using the solution of the initial value problem with the guessed initial conditions at the root. The closeness of β_j to g_{jk} at the tip of the blade is a measure of the accuracy of the applied initial conditions at the root of the blade.

Let us assume that α_i (i = 1 to 6) are the correct values of the initial conditions at the root (point one in the 2-point boundary value problem) that are unknown. These are the values for which correct boundary conditions β_j at the tip of the blade can be obtained:

$$g_j(\alpha_i, L) = \beta_j; \quad j = 1\,\text{to}\,6 \tag{6.16}$$

In Eq. (6.16), the β_j values are known from the tip boundary conditions of the blade. The aim is to calculate an estimation for initial conditions, α_i. The initial guess values for these unknown initial conditions at the root are denoted by α_{i0} (i = 1 to 6). All g_j quantities, i.e., function values at the tip of the blade (point two in the 2-point boundary value problem), that are calculated based on the guessed root initial conditions are functions of the selected values of the initial conditions (or initial guesses), α_{i0}. Using α_{i0} as initial condition, a corresponding estimation for β_j at the free end is obtained that is denoted by β_{j0}:

$$g_j(\alpha_{i0}, L) = \beta_{j0}; \quad j = 1\,\text{to}\,6 \tag{6.17}$$

Now, a Taylor series expansion can be written that may be used to calculate the necessary changes in the guessed initial conditions in order to improve them. To improve the initial guess values, α_{i0}, increments $\Delta\alpha_{i1}$ are applied on them. The modified values of g_j are related to their current values, g_j (α_{i0}, L), using the following Taylor series expansion:

$$g_j(\alpha_{i1}, L) \approx g_j(\alpha_{i0}, L) + \sum_{i=1}^{6} \left(\frac{\partial g_j}{\partial \alpha_i} (\alpha_{i0}, L).\Delta\alpha_{i1} \right) \tag{6.18}$$

At the free end of a cantilever blade, all β_j (that correspond to the force and moment boundary conditions) are zero. Therefore, using Eq. (6.18), the ideal initial condition increments $\Delta\alpha_{i1}$ are the ones for which the left-hand side of Eq. (6.18) vanishes. So, in an expanded form,

$$0 \approx \begin{Bmatrix} g_1(\alpha_{i0}, L) \\ g_2(\alpha_{i0}, L) \\ g_3(\alpha_{i0}, L) \\ g_4(\alpha_{i0}, L) \\ g_5(\alpha_{i0}, L) \\ g_6(\alpha_{i0}, L) \end{Bmatrix} + \begin{bmatrix} \frac{\partial g_1}{\partial \alpha_1} & \frac{\partial g_1}{\partial \alpha_2} & \frac{\partial g_1}{\partial \alpha_3} & \frac{\partial g_1}{\partial \alpha_4} & \frac{\partial g_1}{\partial \alpha_5} & \frac{\partial g_1}{\partial \alpha_6} \\ \frac{\partial g_2}{\partial \alpha_1} & \frac{\partial g_2}{\partial \alpha_2} & \frac{\partial g_2}{\partial \alpha_3} & \frac{\partial g_2}{\partial \alpha_4} & \frac{\partial g_2}{\partial \alpha_5} & \frac{\partial g_2}{\partial \alpha_6} \\ \frac{\partial g_3}{\partial \alpha_1} & \frac{\partial g_3}{\partial \alpha_2} & \frac{\partial g_3}{\partial \alpha_3} & \frac{\partial g_3}{\partial \alpha_4} & \frac{\partial g_3}{\partial \alpha_5} & \frac{\partial g_3}{\partial \alpha_6} \\ \frac{\partial g_4}{\partial \alpha_1} & \frac{\partial g_4}{\partial \alpha_2} & \frac{\partial g_4}{\partial \alpha_3} & \frac{\partial g_4}{\partial \alpha_4} & \frac{\partial g_4}{\partial \alpha_5} & \frac{\partial g_4}{\partial \alpha_6} \\ \frac{\partial g_5}{\partial \alpha_1} & \frac{\partial g_5}{\partial \alpha_2} & \frac{\partial g_5}{\partial \alpha_3} & \frac{\partial g_5}{\partial \alpha_4} & \frac{\partial g_5}{\partial \alpha_5} & \frac{\partial g_5}{\partial \alpha_6} \\ \frac{\partial g_6}{\partial \alpha_1} & \frac{\partial g_6}{\partial \alpha_2} & \frac{\partial g_6}{\partial \alpha_3} & \frac{\partial g_6}{\partial \alpha_4} & \frac{\partial g_6}{\partial \alpha_5} & \frac{\partial g_6}{\partial \alpha_6} \end{bmatrix} \begin{Bmatrix} \Delta\alpha_{11} \\ \Delta\alpha_{21} \\ \Delta\alpha_{31} \\ \Delta\alpha_{41} \\ \Delta\alpha_{51} \\ \Delta\alpha_{61} \end{Bmatrix} \tag{6.19}$$

Elements of the Jacobian matrix in Eq. (6.19) are determined by analyzing the sensitivity of the current boundary condition values at point two (i.e., at the tip of the blade) with respect to slight variations of the guessed values of the initial conditions (i.e., the unknown boundary condition values) at point one or the root. Such a sensitivity analysis can be performed by numerical differentiation. The matrix of the calculated derivatives would be the Jacobian matrix of the problem. In calculating the Jacobian for the hingeless case, the increments are applied at the root and on variables whose values are not known at the root (i.e., on, F_1, F_2, F_3, M_1, M_2, M_3) and their effects on variables whose values at the tip are known are evaluated (i.e., on, F_1, F_2, F_3, M_1, M_2, M_3). Interestingly, for the hingeless blade, these variables are the same. This will not be the case for the articulated blade where the unknown values at the root are not the same as the known values at the tip.

The sensitivities (or partial derivatives) in Eq. (6.19) are calculated numerically using the central difference formula and the definition of a partial derivative. To this end, first a small positive (i.e., ε) increment and then a small negative (i.e., $-\varepsilon$) increment are given to the guessed initial condition of interest, and then the effect of the imposed two increments on the boundary values at the tip is obtained by solving Eqs. (6.1)–(6.3) and (6.7)–(6.15) as an initial value problem. Then, the derivatives are estimated based on a 2ε increment in the initial conditions at the root. As an example,

$$\frac{\partial g_j}{\partial \alpha_2}(\alpha_{i0}, L) \approx \frac{g_j(\alpha_{10}, \alpha_{20} + \varepsilon, \alpha_{30}, \alpha_{40}, \alpha_{50}, \alpha_{60}, L) - g_j(\alpha_{10}, \alpha_{20} - \varepsilon, \alpha_{30}, \alpha_{40}, \alpha_{50}, \alpha_{60}, L)}{2\varepsilon} \tag{6.20}$$

So, by using Eq. (6.19), the best modifications to the initial conditions (increments) can be calculated as follows:

$$\begin{Bmatrix} \Delta\alpha_{11} \\ \Delta\alpha_{21} \\ \Delta\alpha_{31} \\ \Delta\alpha_{41} \\ \Delta\alpha_{51} \\ \Delta\alpha_{61} \end{Bmatrix} = - \begin{bmatrix} \frac{\partial g_1}{\partial \alpha_1} & \frac{\partial g_1}{\partial \alpha_2} & \frac{\partial g_1}{\partial \alpha_3} & \frac{\partial g_1}{\partial \alpha_4} & \frac{\partial g_1}{\partial \alpha_5} & \frac{\partial g_1}{\partial \alpha_6} \\ \frac{\partial g_2}{\partial \alpha_1} & \frac{\partial g_2}{\partial \alpha_2} & \frac{\partial g_2}{\partial \alpha_3} & \frac{\partial g_2}{\partial \alpha_4} & \frac{\partial g_2}{\partial \alpha_5} & \frac{\partial g_2}{\partial \alpha_6} \\ \frac{\partial g_3}{\partial \alpha_1} & \frac{\partial g_3}{\partial \alpha_2} & \frac{\partial g_3}{\partial \alpha_3} & \frac{\partial g_3}{\partial \alpha_4} & \frac{\partial g_3}{\partial \alpha_5} & \frac{\partial g_3}{\partial \alpha_6} \\ \frac{\partial g_4}{\partial \alpha_1} & \frac{\partial g_4}{\partial \alpha_2} & \frac{\partial g_4}{\partial \alpha_3} & \frac{\partial g_4}{\partial \alpha_4} & \frac{\partial g_4}{\partial \alpha_5} & \frac{\partial g_4}{\partial \alpha_6} \\ \frac{\partial g_5}{\partial \alpha_1} & \frac{\partial g_5}{\partial \alpha_2} & \frac{\partial g_5}{\partial \alpha_3} & \frac{\partial g_5}{\partial \alpha_4} & \frac{\partial g_5}{\partial \alpha_5} & \frac{\partial g_5}{\partial \alpha_6} \\ \frac{\partial g_6}{\partial \alpha_1} & \frac{\partial g_6}{\partial \alpha_2} & \frac{\partial g_6}{\partial \alpha_3} & \frac{\partial g_6}{\partial \alpha_4} & \frac{\partial g_6}{\partial \alpha_5} & \frac{\partial g_6}{\partial \alpha_6} \end{bmatrix} \times \begin{Bmatrix} g_1(\alpha_{i0}, L) \\ g_2(\alpha_{i0}, L) \\ g_3(\alpha_{i0}, L) \\ g_4(\alpha_{i0}, L) \\ g_5(\alpha_{i0}, L) \\ g_6(\alpha_{i0}, L) \end{Bmatrix} \tag{6.21}$$

At the end of the first iteration, the calculated increments are used to improve the initial guess values:

$$\alpha_{i1} = \alpha_{i0} + \Delta\alpha_{i1} \tag{6.22}$$

Now, by using the new set of assumed initial conditions (6.22), the whole algorithm can be repeated. By doing so repeatedly, at the end of the *k*th iteration, one obtains,

$$\alpha_{ik} = \alpha_{ik-1} + \Delta\alpha_{ik} \tag{6.23}$$

In this way, the estimations for the unknown 'initial conditions' are gradually improved until finally a solution is obtained in which all of the blade tip boundary conditions are approximately satisfied. The algorithm is stopped when a convergence criterion is satisfied. The selected convergence criterion checks to see whether the summation of the absolute errors at the tip of the blade is small enough. So, the algorithm will stop when the following convergence criterion is satisfied:

$$\sum_{j=1}^{6} \left| g_j(\alpha_{ik}, L) \right| < \varepsilon \tag{6.24}$$

Once condition (6.24) is satisfied, the correct initial conditions and, consequently, the correct steady-state solution of the problem are obtained with acceptable accuracy. The level of accuracy of this solution can be tuned by adjusting ε.

The foregoing solution algorithm may be summarized as follows:

1. Guess initial values for the unknown variables at the root of the blade.
2. Solve the resulting initial value problem using the Runge-Kutta method.
3. Calculate the error of boundary condition values at the tip of the blade, shown by Eq. (6.17).
4. Terminate the process when the convergence criterion (6.24) is satisfied.
5. Calculate the Jacobian matrix using the sensitivity analysis of the solution for values of boundary conditions at point 2 (tip) with respect to the guessed variable values at point 1 (root) by equations similar to Eq. (6.20).
6. Use the Newton-Raphson method to get improved values of the initial guesses for the unknown initial conditions as given by Eq. (6.22).
7. Repeat the process from step 2.

6.4 Case Study: Isotropic Rectangular Solid Model

The isotropic rectangular solid model of Sect. 3.3 is considered here again. Root angular velocity of Ω_3 = 100 rad/s is applied, and the steady-state response of the blade is sought.

Table 6.1 shows the sequence of guessed and then improved initial conditions at the root using the method discussed in Sect. 6.3. The corresponding sequence of error values at the tip has been listed in Table 6.2. It is observed that even though the initial guesses at the root have been far from correct, the mentioned algorithm has been able to obtain the correct solution that satisfies the tip boundary conditions listed in Eq. (5.26) in just a few iterations.

Figures 6.1, 6.2, 6.3, and 6.4 illustrate the calculated steady-state response of the blade. As expected, the axial force F_1 is the dominant force component. In addition,

Table 6.1 The initial conditions at the root for various iterations (all F in N and all M in N.m)

Iteration	$\alpha_1 = F_1(0)$	$\alpha_2 = F_2(0)$	$\alpha_3 = F_3(0)$	$\alpha_4 = M_1(0)$	$\alpha_5 = M_2(0)$	$\alpha_6 = M_3(0)$
1	100	100	1000	1000	1000	1000
2	1.77e+5	1.437e−1	−8.897e−1	−3.561e−3	4.973e−1	7.132e−2
3	1.77e+5	8.935e−12	5.735e−13	−2.697e−11	−1.541e−12	4.315e−12

Table 6.2 Calculated tip boundary conditions for the initial conditions in Table 6.1 (all F in N and all M in N.m)

Iteration	$g_1 = F_1(L)$	$g_2 = F_2(L)$	$g_3 = F_3(L)$	$g_4 = M_1(L)$	$g_5 = M_2(L)$	$g_6 = M_3(L)$
1	−1.769e+5	1.001e+2	9.99e+2	1.00e+3	1.9998e+3	8.999e+2
2	−4.948e−3	1.437e−1	−8.897e−1	−3.561e−3	−3.924e−1	−7.236e−2
3	1.4188e−1	8.935e−12	5.735e−13	−2.697e−11	−9.678e−13	−4.619e−12

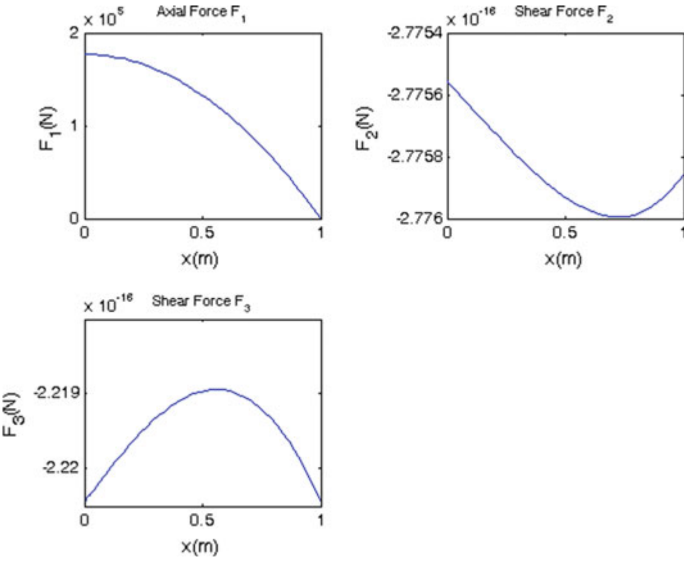

Fig. 6.1 Steady-state internal force components along the blade

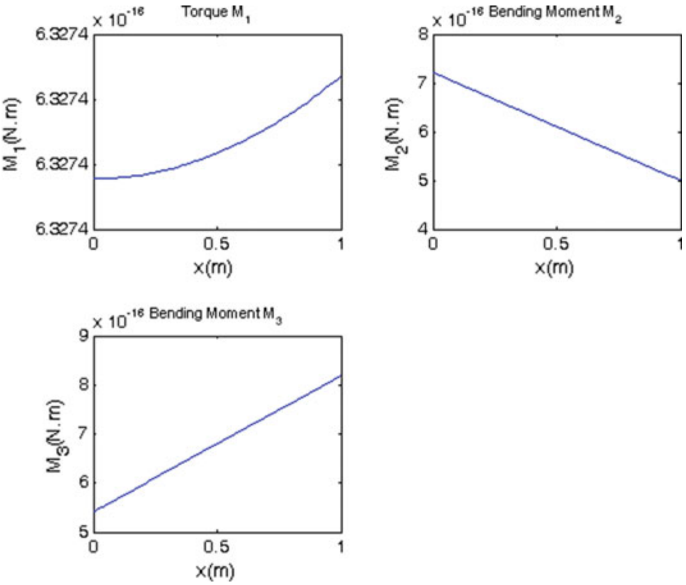

Fig. 6.2 Steady-state internal moment components along the blade

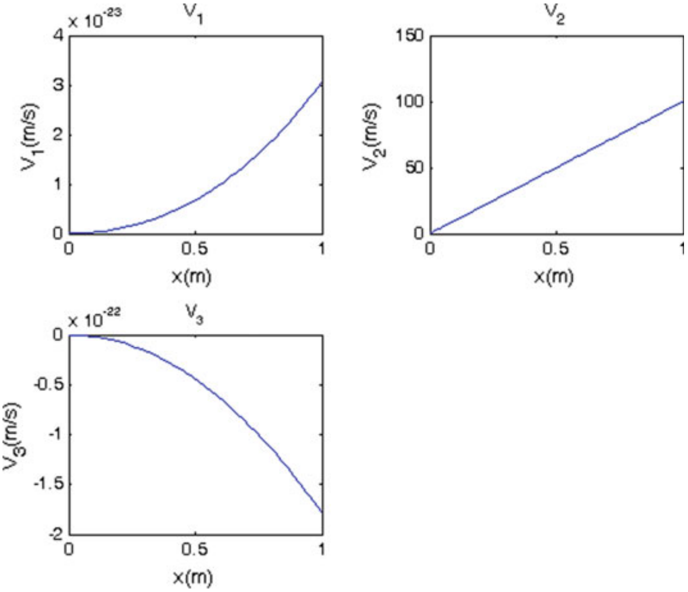

Fig. 6.3 Steady-state velocity components along the blade

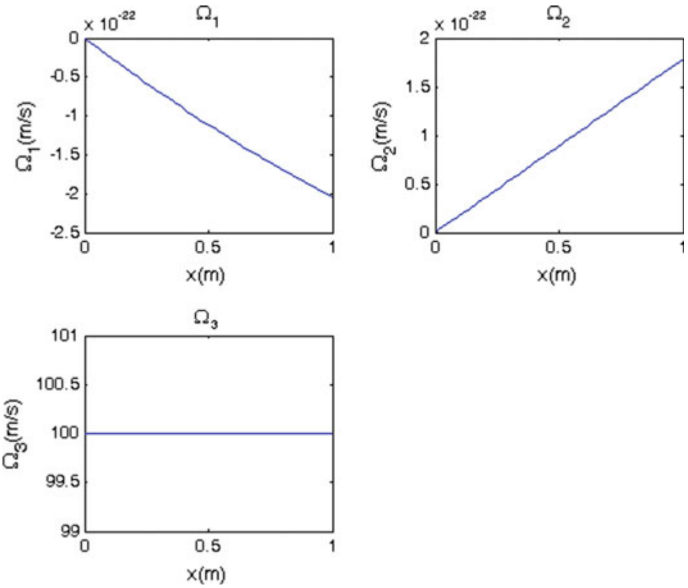

Fig. 6.4 Steady-state angular velocity components along the blade

the linear variation of V_2 along the blade is compatible with the constant value of Ω_3 along the blade.

To verify the results, the obtained steady-state solution has been compared with the results of the transient solution discussed in Chap. 5. The transient solution is expected to converge to the steady-state response obtained by the shooting method. The two steady-state solutions are illustrated in Fig. 6.5 and are seen to be almost identical.

Fig. 6.5 Steady-state values of the internal force F_1 along the blade using the shooting method (*solid line*) and the finite difference method (*circles*)

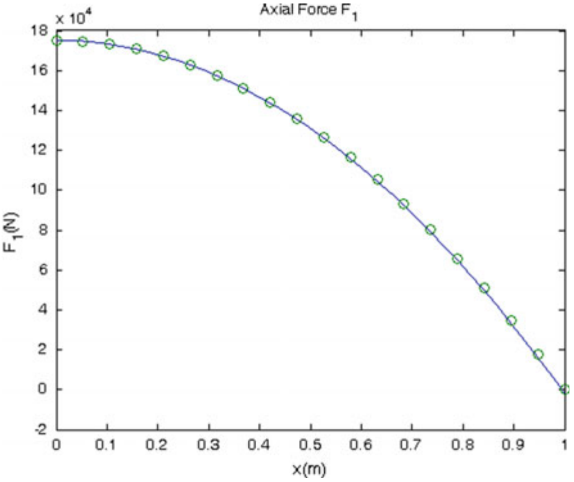

The developed computer program that implements the shooting method provides the steady-state solution in just a few seconds. In comparison, another program that calculates the transient finite difference solution has to run for a few minutes in order to converge to the steady-state solution.

6.5 Case Study: Verification Example

The case of a rotating blade with the following non-dimensional data has been given in Hodges (2008):

$$\begin{array}{llll} \Omega_3 = 1.4426 & L = 10 & k = 0 & R(1,1) = 1 \times 10^{-7} \\ Z = 0 & T(1,1) = 1 \times 10^{-6} & T(2,2) = 1 \times 10^{-6} & T(3,3) = 1 \times 10^{-8} \\ & \mu = 4 & i(1,1) = 0.1 & \end{array} \tag{6.25}$$

Other elements of R and i are assumed to be zero. Figures 6.6, 6.7, 6.8, and 6.9 illustrate the results obtained by the present method and those of Hodges (2008). It is clear that the two steady-state solutions are dominated by the axial force and the results obtained by the two methods are very close to each other.

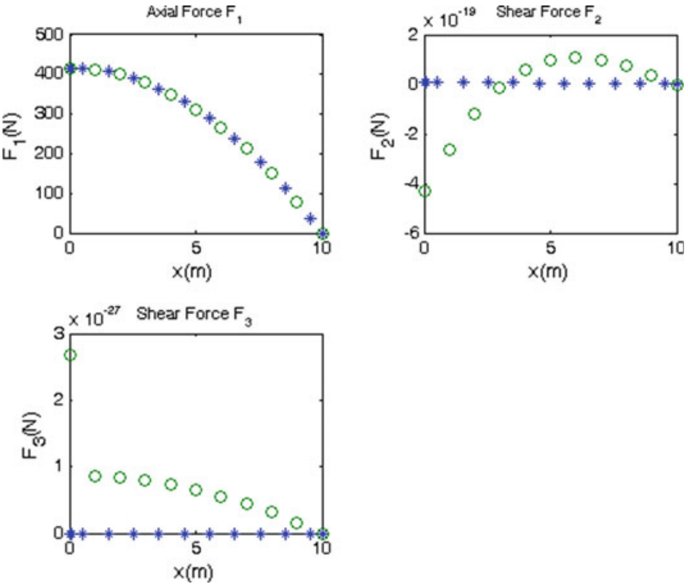

Fig. 6.6 Steady-state internal force components along the blade; present solution (*asterisk*) Hodges (2008) (*circles*)

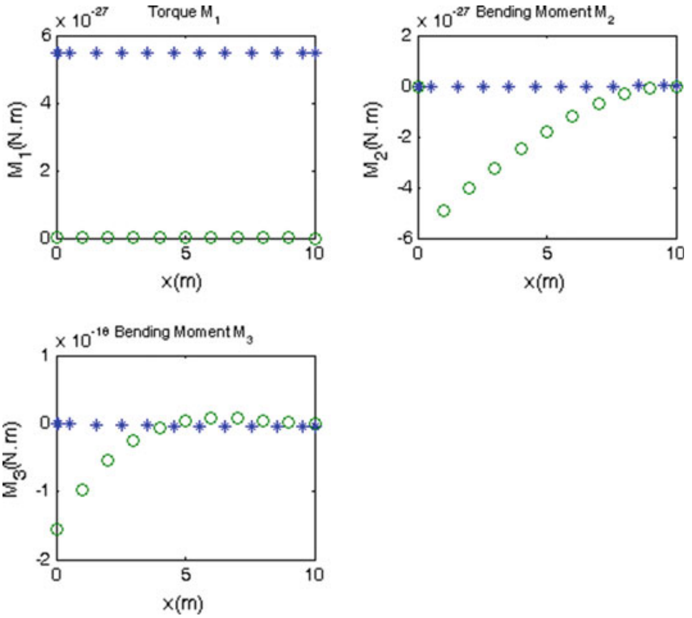

Fig. 6.7 Steady-state internal moment components along the blade; present solution (*asterisk*) Hodges (2008) (*circles*)

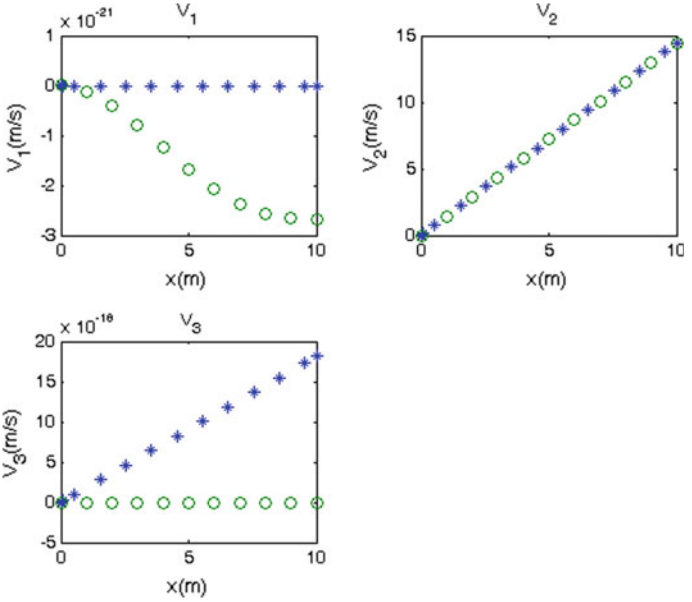

Fig. 6.8 Steady-state velocity components along the blade; present solution (*asterisk*) Hodges (2008) (*circles*)

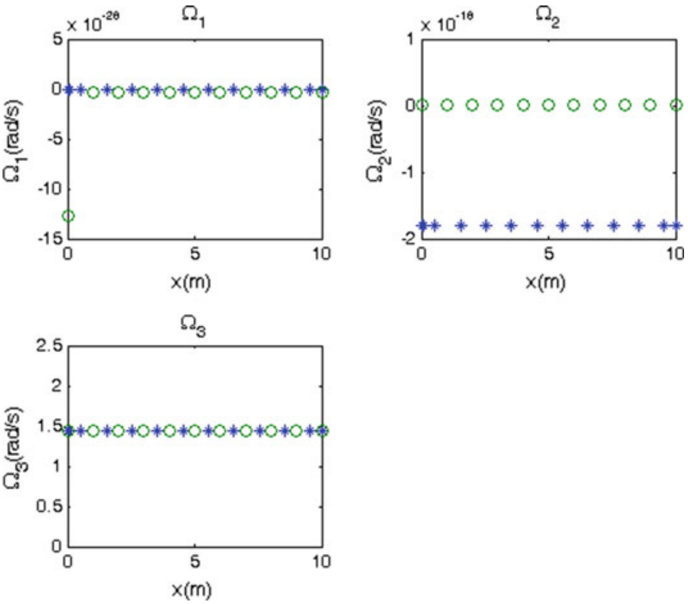

Fig. 6.9 Steady-state angular velocity components along the blade; present solution (*asterisk*) Hodges (2008) (*circles*)

6.6 Case Study: Passive Airfoil Model

The case of a passive composite airfoil is discussed in Hodges et al. (2007). The blade comprises of a spanwise uniform cantilever beam with the representative helicopter airfoil cross-sectional configuration VR-7 shown in Fig. 6.10. The blade section has a chord length of 20.2 in. and a web located 8.4025 in. from the leading edge. The layup orientations for the D-spar, from outside to inside, are [45°/−45°/0°/0°/0°]. The layup angle is 45° for the trailing edge skin and 0° for the web.

The shear center has been located at a point 5.889-in. back and 0.6579-in. up from the leading edge. VABS has been run with the origin of the sectional coordinate system reset to this point. The center of mass was located slightly to the rear and above the shear center at $\bar{x}_2 = -0.00351124$ - in. and $\bar{x}_3 = -0.196410$ - in. The sectional mass properties have been calculated as follows:

$$\begin{aligned} &\mu = 1.54601 \times 10^{-3}\text{lb.s}^2/\text{in.}^2 \quad i_2 = 1.28544 \times 10^{-3}\text{lb.s}^2 \\ &i_3 = 2.68960 \times 10^{-2}\text{lb.s}^2 \end{aligned} \tag{6.26}$$

where μ is the mass per unit length, i_2 is the cross-sectional mass moment of inertia about the direction along the chordline, and i_3 is the cross-sectional mass moment of inertia about the perpendicular direction.

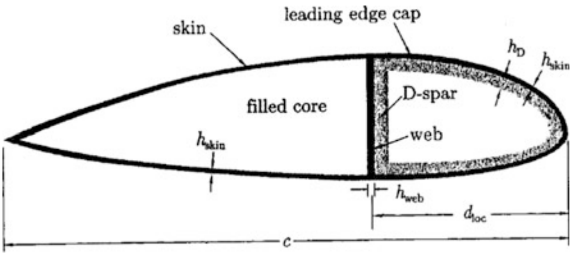

Fig. 6.10 Sketch of the rotor blade cross section, Hodges et al. (2007) © American Helicopter Society, reprinted with permission

The generalized Timoshenko model obtained from VABS for this cross section is represented by the following stiffness matrix:

$$S = \begin{bmatrix} 128.550 & -0.651479 & 0.026700 & -1.17823 & 25.0459 & -168.948 \\ -0.651479 & 9.68119 & -0.414611 & 0.021110 & 0.706635 & 1.03049 \\ 0.026700 & -0.414611 & 1.44328 & -0.001493 & -0.054592 & 0.116498 \\ -1.17823 & 0.021110 & -0.001493 & 34.5784 & 1.30984 & 1.36493 \\ 25.0459 & 0.706635 & -0.054592 & 1.30984 & 91.8417 & 25.3056 \\ -168.948 & 1.03049 & 0.116498 & 1.36493 & 25.3056 & 1492.29 \end{bmatrix} \times 10^6 \tag{6.27}$$

Reviewing Eq. (2.56) reveals that the units associated with stiffness values are S_{ij} (lb), $S_{i,j+3}$ (lb.in.), and $S_{i+3,j+3}$ (lb.in.^{2}) for $i, j = 1, 2, 3$. It should also be noted that the cross-sectional matrix for classical theory is obtained by striking the second and third rows and columns from the inverse of the 6 by 6 stiffness matrix above [in order to drop in-plane shear deformation, as seen in the scalar form of Eq. (2.56)] and then inverting the resulting 4 by 4 matrix.

In the present analysis, a 120-in.-long blade that has the cross section shown in Fig. 6.10 is considered and the blade rotates at 100 rad/s. Figure 6.11 illustrates the calculated steady-state distribution of F_1 using the shooting method algorithm described in Sect. 6.3.

6.7 Perturbed Steady-State Analysis

Consider a rotating blade that has already reached its steady-state motion. The aim is to calculate the behavior of this blade in the vicinity of its steady-state motion as a result of small disturbances. Such disturbances induce perturbations on the steady-state values of all variables. Therefore, the complete solution for each variable can be written as the summation of the steady-state component (x_1 dependent) and a perturbed part (x_1 and t dependent).

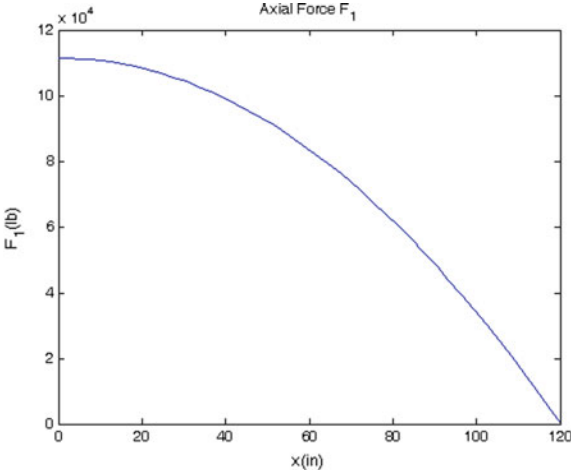

Fig. 6.11 Steady-state variation of the internal force F_1 along the blade

Referring to Fig. 2.6, for every dependent variable, one may write as follows:

$$\phi\left(x+\frac{\Delta x}{2},t+\frac{\Delta t}{2}\right)=\phi_{ss}\left(x+\frac{\Delta x}{2}\right)+\phi_p\left(x+\frac{\Delta x}{2},t+\frac{\Delta t}{2}\right)\tag{6.28}$$

in which the solution for the variable of interest has been expressed as the summation of its steady-state value and perturbations about the steady state. Using Eq. (6.28) for ϕ_m and λ_n,

$$\begin{aligned}&\phi_m\left(x+\frac{\Delta x}{2},t+\frac{\Delta t}{2}\right)\lambda_n\left(x+\frac{\Delta x}{2},t+\frac{\Delta t}{2}\right)=\\&\quad\left\{\phi_{m,ss}\left(x+\frac{\Delta x}{2}\right)+\phi_{m,p}\left(x+\frac{\Delta x}{2},t+\frac{\Delta t}{2}\right)\right\}\left\{\lambda_{n,ss}\left(x+\frac{\Delta x}{2}\right)+\lambda_{n,p}\left(x+\frac{\Delta x}{2},t+\frac{\Delta t}{2}\right)\right\}\end{aligned}\tag{6.29}$$

The purely steady-state term $\phi_{m,ss}\lambda_{n,ss}$ satisfies the steady-state differential equations, so it will not appear in the perturbations equations. Also, the product of perturbation terms, i.e., $\phi_{m,p}\lambda_{n,p}$, is small and can be neglected. So, the contribution of Eq. (6.29) in the perturbation equations would be the following:

$$\begin{aligned}&\left\{\phi_m\left(x+\frac{\Delta x}{2},t+\frac{\Delta t}{2}\right)\lambda_n\left(x+\frac{\Delta x}{2},t+\frac{\Delta t}{2}\right)\right\}_p=\\&\quad\phi_{m,ss}\left(x+\frac{\Delta x}{2}\right)\lambda_{n,p}\left(x+\frac{\Delta x}{2},t+\frac{\Delta t}{2}\right)+\phi_{m,p}\left(x+\frac{\Delta x}{2},t+\frac{\Delta t}{2}\right)\lambda_{n,ss}\left(x+\frac{\Delta x}{2}\right)\end{aligned}\tag{6.30}$$

Now, using Eq. (2.87),

$$\phi_{m,ss}\left(x+\frac{\Delta x}{2}\right)=\frac{1}{2}\left(\phi_{m,ss,i+1}+\phi_{m,ss,i}\right)+O\left(\Delta x^2\right) \tag{6.31}$$

So, the perturbational contribution of $\phi_m \lambda_n$ becomes the following:

$$\begin{aligned}&\left\{\phi_m\left(x+\frac{\Delta x}{2},t+\frac{\Delta t}{2}\right)\lambda_n\left(x+\frac{\Delta x}{2},t+\frac{\Delta t}{2}\right)\right\}_p=\\&\frac{1}{8}\left[\left(\phi_{m,ss,i+1}+\phi_{m,ss,i}\right)\left(\lambda^+_{n,p,i+1}+\lambda^+_{n,p,i}+\lambda_{n,p,i+1}+\lambda_{n,p,i}\right)\right]\\&+\frac{1}{8}\left[\left(\lambda_{n,ss,i+1}+\lambda_{n,ss,i}\right)\left(\phi^+_{m,p,i+1}+\phi^+_{m,p,i}+\phi_{m,p,i+1}+\phi_{m,p,i}\right)\right]\end{aligned} \tag{6.32}$$

Using the steady-state equations, (6.1)–(6.12) together with Eqs. (6.32), (2.87), (2.98), and (2.109), the dynamic governing Eqs. (2.26), (2.27), (2.36)–(2.38), (2.45), and (2.56) can be converted to the following matrix equation:

$$A_{ss,i}q^+_{p,i}+B_{ss,i}q^+_{p,i+1}=J_{ss,i} \tag{6.33}$$

where q_p contains the perturbations of the variables given in Eq. (5.20). Even though the expressions for A_ss, B_ss, and J_ss in Eq. (6.33) are different from those of Eq. (5.19), the solution methods are identical. Having solved Eq. (6.33), the complete solution can be recovered by using Eq. (6.28).

6.8 Case Study: Isotropic Rectangular Solid Model

Consider the isotropic rectangular solid model introduced in Sect. 3.3 that is rotating at the steady-state angular velocity, Ω_3 = 100 rad/s.

The aim is to evaluate the effects of an angular velocity perturbation of

$$\Omega_{3,p,1}=\sin(100t)\,\text{rad/s} \tag{6.34}$$

that is applied at the root.

Figures 6.12 and 6.13 illustrate the input angular velocity perturbations as well as the resulting perturbations in the bending moment and in the force components at the root. Having calculated the perturbed dependent variables, one may use Eq. (6.28) to get the complete dynamic response. In Figs. 6.14, 6.15, 6.16, 6.17, and 6.18, the steady-state results are plotted in solid lines until t = 2.667 s. At this instant, the perturbation is as follows:

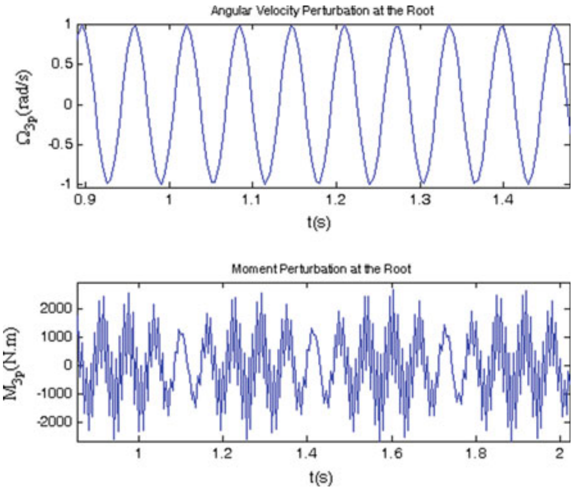

Fig. 6.12 Perturbations of angular velocity and bending moment at the root

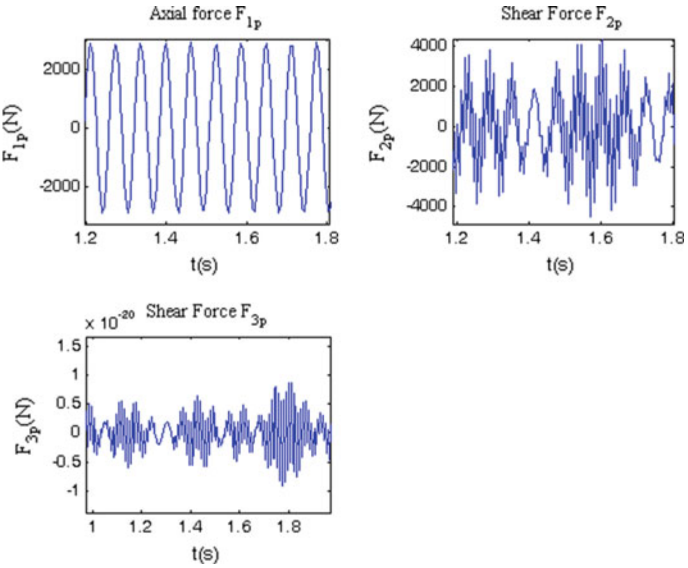

Fig. 6.13 Perturbations of force components at the root

$$\Omega_{3,p,1} = \sin(93.5t)\,\text{rad/s} \tag{6.35}$$

which is applied at the root of the blade. The effect of this perturbation, using the foregoing algorithm, is illustrated in solid lines.

Fig. 6.14 Accelerating and perturbed steady-state angular velocities at the root

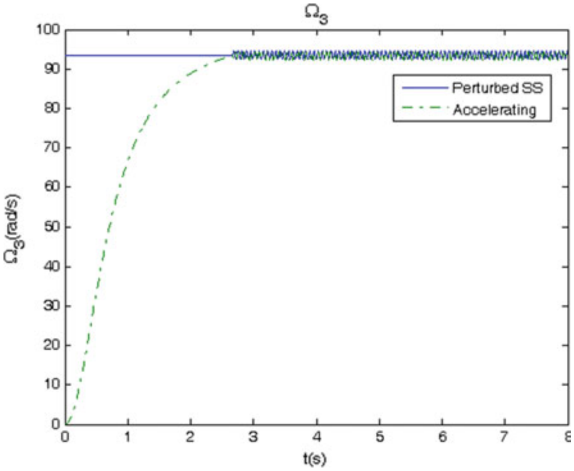

Fig. 6.15 Zoomed-in view of Fig. 6.14

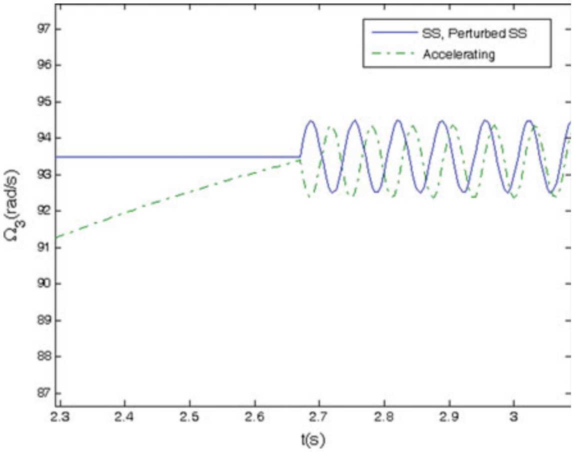

Fig. 6.16 Steady-state, accelerating, and perturbed axial force at the root

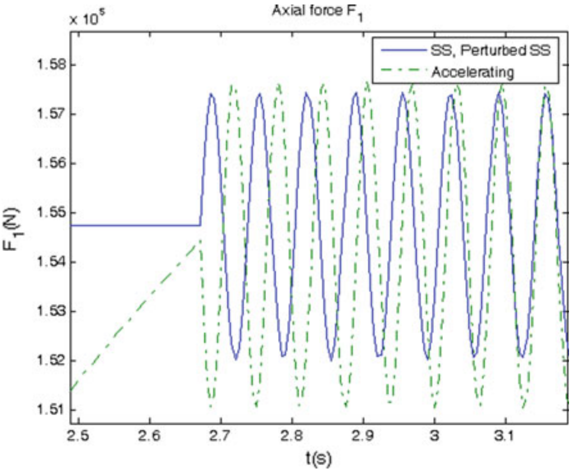

Fig. 6.17 Steady-state, accelerating, and perturbed shear force at the root

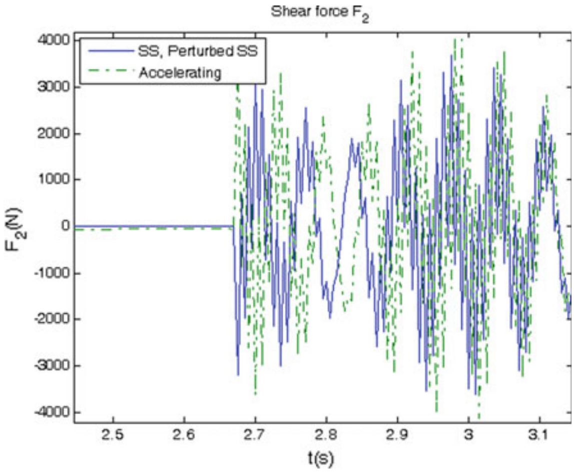

Fig. 6.18 Steady-state, accelerating, and perturbed bending moment at the root

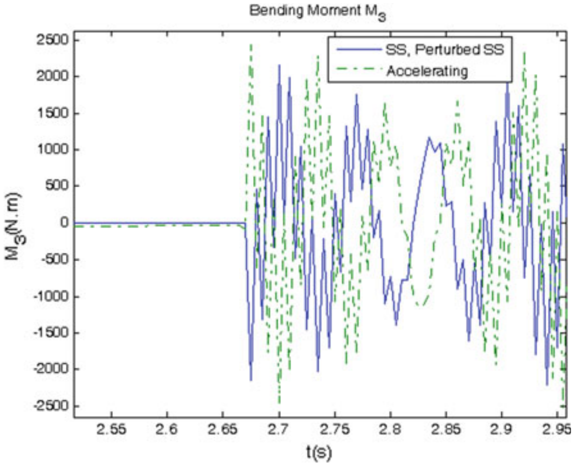

As an alternative method, the problem has also been solved using the algorithm presented in Chap. 5 for an accelerating blade. For this purpose, the blade starts to rotate from rest, and at t = 2.667 s when the beam has an angular velocity of 93.5 rad/s, the perturbation shown in Eq. (6.35) is applied. In Figs. 6.14, 6.15, 6.16, 6.17, and 6.18, the corresponding results are plotted in dash-dotted lines. It can be observed that the predictions of the perturbed steady-state method discussed in this chapter are close to those of the accelerating blade method of Chap. 5.

References

Cesnik, C. E. S., Shin, S. J., & Wilbur, M. L. (2001). Dynamic response of active twist rotor blades. *Smart Materials and Structures, 10*, 62–76.

Esmailzadeh, E., Ghorashi, M., & Mehri, B. (1995). Periodic behavior of a nonlinear dynamical system. *Nonlinear Dynamics, 7*(3), 335–344.

Ghorashi, M. (2009). *Dynamics of elastic nonlinear rotating composite beams with embedded actuators.* Ph.D. Thesis, Mechanical and Aerospace Engineering Department, Carleton University.

Ghorashi, M., & Nitzsche, F. (2008). Steady-state nonlinear dynamic response of a composite rotor blade using implicit integration of intrinsic equations of a beam. *International Review of Aerospace Engineering*, *1*, 225–233.

Ghorashi, M., & Nitzsche, F. (2009). Nonlinear dynamic response of an accelerating composite rotor blade using perturbations. *Journal of Mechanics of Materials and Structures, 4*, 693–718.

Hodges, D. H. (2008). *Personal communications*.

Hodges, D. H., Saberi, H., & Ormiston, R. A. (2007) Development of nonlinear beam elements for rotorcraft comprehensive analysis. *Journal of the American Helicopter Society, 52*(1), 36–48.

Shin, S. J., Cesnik, C. E. S., Wilkie, W. K., & Wilbur, M. L. (2008). Design and manufacturing of a model-scale active twist rotor prototype blade. *Journal of Intelligent Material Systems and Structures, 19*, 1443–1456.

Chapter 7
Rigid and Elastic Articulated Rotating Composite Blades

7.1 Introduction

In Chaps. 5 and 6, the nonlinear elasto-dynamics of rotating hingeless (cantilever) blades was analyzed. Contrary to hingeless blades that cannot perform rigid body motions, in order to reduce moment loads that are induced at the root, in many helicopters blades are articulated. Analyzing the dynamics of these articulated or hinged blades requires the inclusion of rigid body motions as a new set of unknown variables.

One may start the analysis by first ignoring the elastic deformations of the blade in comparison to its rigid body motions. In fact, for a number of important helicopter problems with hinged blades, the blade rigidity assumption is adequate. In Bramwell et al. (2001), it has been mentioned that, ‘It is fortunate that, in spite of the considerable flexibility of rotor blades, much of helicopter theory can be affected by regarding the blade as rigid, with obvious simplifications in the analysis.’ That is why the analysis of rigid body motions is so essential for understanding the behavior of articulated blades.

However, still there are cases where the flexibility of the blade and its deformations should be taken into consideration. Elastic deformations of a blade can significantly affect its aerodynamic loadings. The elasticity of a rotor blade also affects its natural frequencies and natural modes of vibration.

In this chapter, first a review of the analysis of rigid articulated rotating blades having flap, lead–lag and feathering hinges is presented. In this analysis, the angular velocity of the rotor is considered to be constant and the helicopter undergoes rectilinear motion at constant speed. A generalized solution to the coupled rigid body motion problem of helicopter blades in flap and lead–lag is derived to generate the root boundary conditions. Then, the elastic articulated rotating blades are analyzed. The root boundary condition for the elastic blades is formulated by the

M. Ghorashi, *Statics and Rotational Dynamics of Composite Beams*,
DOI 10.1007/978-3-319-14959-2_7

use of the rigid articulated blade solution. Having done that, the root boundary condition and the elastic rotating blade formulation (derived in Chap. 5) are combined in order to solve the elastic articulated rotating blade problem. The specific problem considered involves an accelerating rotor blade that starts its motion from rest and converges to a steady-state angular velocity. In this way, a direct integration method which utilizes perturbations is presented for the elasto-dynamic analysis of an accelerating articulated composite blade by solving the nonlinear intrinsic differential equations. This chapter is essentially based on the material presented in Ghorashi (2009) and published in Ghorashi (2012).

7.2 Introduction to the Dynamics of Articulated Blades

A typical hinge arrangement for an articulated blade is shown in Fig. 7.1. The use of these hinges in order to reduce the induced moments has been a main development in the manufacture of helicopters. The most important of these hinges is the flapping hinge which allows the blade to move in a plane containing the blade and the shaft. Now, a blade which is free to flap experiences large Coriolis moments in the plane of rotation. That is why a further hinge—called the drag or lead–lag hinge—is provided to relieve these moments. Lastly, the blade can be feathered about a third axis, usually parallel to the blade span, to enable the blade pitch angle to be changed, Bramwell et al. (2001).

A large number of helicopters use the conventional fully articulated rotor hubs. Hence, mechanical flap and lead–lag hinges are provided on each blade along with a feathering bearing. Furthermore, because of the relatively low drag and aerodynamic damping in the lead–lag plane, mechanical dampers are fitted at the lag hinges. The articulated rotor design is mechanically complicated, heavy, and it produces relatively high drag in forward flight. Nevertheless, the fully articulated design is the classic approach to providing the blade articulation, and in practice, it has been proven mechanically reliable but with relatively high maintenance costs because of the large number of parts (Leishman 2006).

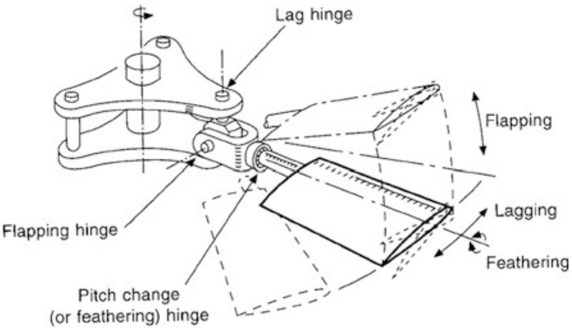

Fig. 7.1 Typical hinge arrangement, Bramwell et al. (2001), page 2 © Elsevier Ltd., reprinted with permission

The main rotational motion of a blade about its rotor is measured by the azimuth angle, ψ. It is the angle between the spanwise direction of the blade and the rear centerline of the helicopter (rearmost position of the blade). At constant rotor shaft angular velocity, the azimuth angle is related to this velocity and time by,

$$\psi = \Omega t \tag{7.1}$$

Since aerodynamic loads are periodic functions of the azimuth angle (they depend on the location of the blade with respect to the rest of the helicopter), it is sometimes advantageous to use Eq. (7.1) to replace time with the azimuth angle, as the independent variable.

The feathering mechanism is a parallel mechanism where the blades remain parallel to the swashplate at all times. The swashplate has a lower plate that does not rotate with the shaft but can be tilted in any direction by the pilot's cyclic control. The upper plate rotates with the shaft, but it is constrained to remain parallel to the lower plate.

Collective pitch is the mechanism in effect in hover and can keep the helicopter over a certain location. In hovering flight, the swashplate is used to tune the collective (constant) pitch. The collective pitch is imposed by the collective lever and the pitch link. The collective lever raises or lowers the swashplate without introducing any tilt on it; this alters the pitch angle of all the blades by the same amount. The resulting flow field is azimuthally axisymmetric and adjusts the magnitude of the thrust. In hover, each blade encounters the same aerodynamic environment. As a result, the flapping angle does not change with the azimuth angle. So, $\beta(\psi) = \beta_0$, which is a constant called the coning angle. The coning angle is calculated by solving the equation of balance of moments of the centrifugal and aerodynamic forces about the flapping hinge.

In forward flight, cyclic pitch is produced by tilting the swashplate using pilot's control. Cyclic feathering takes place relative to a plane that is perpendicular to the shaft. Feathering increases the lift in certain regions of blade rotation and decreases it in others. The resultant is that the helicopter tends to move in a certain direction, and forward flight is obtained.

In hover, with only the collective pitch, Ω_1 is zero. However, in the forward flight, due to cyclic pitch, Ω_1 is not zero and it is an input provided by the pilot at the root as a known function of time. Based on this discussion, pitch is not regarded as a degree of freedom of the blade. It, however, generates aerodynamic moments, which in turn produce flap and lag motions that are the two degrees of freedom of the blade.

Therefore, the collective pitch controls the average blade pitch angle, and consequently, it adjusts the blade lift and average rotor thrust. The cyclic pitch, on the other hand, controls the orientation of the rotor thrust vector. Finally, the yaw motion is controlled by using the tail rotor thrust that causes the nose to yaw right or left.

7.3 Euler Equations of Motion for Rigid Rotating Blades

Figure 7.1 illustrates the general case where a rotor blade rotates about a fixed point and has a hinge system, which is effectively concentrated at a single point. The relevant parameters of the system have been illustrated in Fig. 7.2. Point O is on the center axis of the rotor shaft about which the blade rotates. The hinge system is effectively concentrated at the single point P (at the root of the blade). Therefore, OP is the hinge offset.

Using Fig. 7.2, the absolute angular momentum of a representative particle, m_{i}, with position vector, ρ_i, with respect to the mass center of the blade, G, can be found by calculating the moment of the absolute linear momentum of this particle about G. By adding the contributions obtained for all of the particles in the blade, one obtains

$$\vec{H}_G = \sum_i (\vec{\rho}_i \times m_i \vec{v}_i) \tag{7.2}$$

For a rigid blade, that is modeled as a continuum and rotates at an instantaneous angular velocity ω, Eq. (7.2) can be expressed as

$$\vec{H}_G = \int [\vec{\rho} \times (\vec{\omega} \times \vec{\rho})] \mathrm{d}m \tag{7.3}$$

Similarly, if O is a fixed point in a Newtonian reference frame about which the blade is rotating, the absolute angular momentum of the rigid blade about O could be written as

$$\vec{H}_O = \sum_i (\vec{r}_i \times m_i \vec{v}_i) \tag{7.4}$$

where $\vec{r}_i$ is the position vector of particle m_i with respect to hinge O. For a continuum, Eq. (7.4) can be expressed as

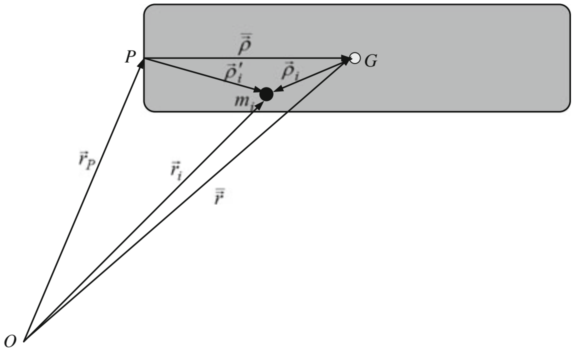

Fig. 7.2 Rotating blade with O on the shaft axis and the hinge P at the root of the blade

$$\vec{H}_O = \int [\vec{r} \times (\vec{\omega} \times \vec{r})]\mathrm{d}m \tag{7.5}$$

Equations (7.3) and (7.5) have identical forms.

In order to perform the calculations, the moment arm, r or ρ, can be written as $x\vec{i} + y\vec{j} + z\vec{k}$ where x–y–z refers to the coordinates of dm in the reference frame located at G or O, respectively. Then, the cross products may be carried out. Alternatively, to perform the calculations, one can use the triple vector product identity

$$\vec{A} \times (\vec{B} \times \vec{C}) = (\vec{A} \circ \vec{C})\vec{B} - (\vec{A} \circ \vec{B})\vec{C} \tag{7.6}$$

Either way the result is

$$\begin{aligned} \mathrm{d}\vec{H} = {} & \vec{i}[(y^2+z^2)\omega_x - xy\omega_y - xz\omega_z]\mathrm{d}m + \vec{j}[-yx\omega_x + (z^2+x^2)\omega_y - yz\omega_z]\mathrm{d}m \\ & + \vec{k}[-zx\omega_x - zy\omega_y + (x^2+y^2)\omega_z]\mathrm{d}m \end{aligned} \tag{7.7}$$

Integrating Eq. (7.7), all over the blade gives

$$\begin{aligned} \vec{H} = {} & \vec{i}(I_{xx}\omega_x - I_{xy}\omega_y - I_{xz}\omega_z) + \vec{j}(-I_{yx}\omega_x + I_{yy}\omega_y - I_{yz}\omega_z) \\ & + \vec{k}(-I_{zx}\omega_x - I_{zy}\omega_y + I_{zz}\omega_z) \end{aligned} \tag{7.8}$$

where the moments of inertia and the products of inertia (components of the inertia matrix I) are defined as

$$\begin{aligned} I_{xx} &= \int (y^2+z^2)\mathrm{d}m & I_{xy} &= I_{yx} = \int xy\mathrm{d}m \\ I_{yy} &= \int (z^2+x^2)\mathrm{d}m & I_{xz} &= I_{zx} = \int xz\mathrm{d}m \\ I_{zz} &= \int (x^2+y^2)\mathrm{d}m & I_{yz} &= I_{zy} = \int yz\mathrm{d}m \end{aligned} \tag{7.9}$$

Equation (7.8) can be expressed in the following matrix form,

$$\vec{H} = I\vec{\omega}, \quad \begin{Bmatrix} H_x \\ H_y \\ H_z \end{Bmatrix} = \begin{bmatrix} I_{xx} & -I_{xy} & -I_{xz} \\ -I_{yx} & I_{yy} & -I_{yz} \\ -I_{zx} & -I_{zy} & I_{zz} \end{bmatrix} \begin{Bmatrix} \omega_x \\ \omega_y \\ \omega_z \end{Bmatrix} \tag{7.10}$$

Equation (7.10) is the general expression for the angular momentum of a rigid blade about either its mass center, G, or a point, O, that is a fixed point in a Newtonian reference frame (about which the blade is rotating with an instantaneous angular velocity ω). In both cases, if the reference frame x–y–z with origin at G or O is attached to the rigid blade, the moment of inertia and the product of inertia integrals will be invariant with respect to time. Next, one may use

$$\sum \vec{M} = \dot{\vec{H}} \tag{7.11}$$

where the terms are calculated either about a fixed point, O, or the mass center, G. Recalling that Ω is the angular velocity vector of the moving coordinate system, application of the Coriolis theorem,

$$\dot{\vec{H}} = \left(\frac{\mathrm{d}\vec{H}}{\mathrm{d}t}\right)_{xyz} + \vec{\Omega} \times \vec{H} \tag{7.12}$$

and Eq. (7.11) result in,

$$\sum \vec{M} = \left(\frac{\mathrm{d}\vec{H}}{\mathrm{d}t}\right)_{xyz} + \vec{\Omega} \times \vec{H} \tag{7.13}$$

or,

$$\sum \vec{M} = (\dot{H}_x \vec{i} + \dot{H}_y \vec{j} + \dot{H}_z \vec{k}) + \vec{\Omega} \times \vec{H} \tag{7.14}$$

In Eq. (7.14), the terms in parentheses represent part of $\dot{\vec{H}}$ which is due to the change in the magnitude of the components of H as they are viewed by observers at G or O. The cross product term is due to changes in the direction of the components of H. Expansion of the cross product and rearrangement of the result give

$$\sum \vec{M} = (\dot{H}_x - H_y \Omega_z + H_z \Omega_y)\vec{i} + (\dot{H}_y - H_z \Omega_x + H_x \Omega_z)\vec{j} + (\dot{H}_z - H_x \Omega_y + H_y \Omega_x)\vec{k} \tag{7.15}$$

Equation (7.15) is the most general form of the moment equation of a rigid body about a fixed point, O, or mass center, G. The angular velocity vector, Ω, of the moving reference axes, in general, can be different from the angular velocity vector, ω, of the rigid blade. If the moving reference axes are attached to the rigid blade, then, $\Omega = \omega$, and Eq. (7.15) reduces to

$$\begin{aligned} \sum M_x &= \dot{H}_x - H_y \omega_z + H_z \omega_y \\ \sum M_y &= \dot{H}_y - H_z \omega_x + H_x \omega_z \\ \sum M_z &= \dot{H}_z - H_x \omega_y + H_y \omega_x \end{aligned} \tag{7.16}$$

These are the general moment equations for a rotating rigid blade using a set of reference coordinates which are attached to the blade at point, O, that is a fixed point in a Newtonian reference frame about which the blade is rotating, or at its mass center, G.

At any point in a rigid body, there are three principal axes of inertia. The products of inertia with respect to these axes are zero. If the coordinate axes x–y–z are the principal axes of inertia of the blade with origin at G or O, Eq. (7.10) reduces to

$$\begin{Bmatrix} H_x \\ H_y \\ H_z \end{Bmatrix} = \begin{bmatrix} I_{xx} & 0 & 0 \\ 0 & I_{yy} & 0 \\ 0 & 0 & I_{zz} \end{bmatrix} \begin{Bmatrix} \omega_x \\ \omega_y \\ \omega_z \end{Bmatrix} \tag{7.17}$$

If the reference axes coincide with these principal axes (at mass center G or point O), using Eqs. (7.16) and (7.17) one obtains

$$\sum M_x = I_{xx}\dot{\omega}_x - (I_{yy} - I_{zz})\omega_y\omega_z \tag{7.18}$$

$$\sum M_y = I_{yy}\dot{\omega}_y - (I_{zz} - I_{xx})\omega_z\omega_x \tag{7.19}$$

$$\sum M_z = I_{zz}\dot{\omega}_z - (I_{xx} - I_{yy})\omega_x\omega_y \tag{7.20}$$

Equations (7.18)–(7.20) are the Euler's equations of motion for a rotating rigid body and they are used for writing moment equations for rotating articulated blades with no hinge offset about a point O that is fixed in a Newtonian reference frame or about the mass center G of the blade.

7.4 Extended Euler Equations for a Rigid Rotating Blade

As it was shown in Sect. 7.3, Euler's equations of motion (7.18)–(7.20) can be written about a point O that is fixed in a Newtonian reference frame or about the mass center, G. However, as it is seen in Fig. 7.1, in rotor blades usually the offset between the hinge system and the rotor axis (shown by OP in Fig. 7.2) is not zero. Therefore, the flap/lag/pitch hinge has nonzero acceleration and it is not a stationary point in a Newtonian reference system. Consequently, while Eqs. (7.18)–(7.20) can still be written about G, they are not valid about the hinge point P.

Using the center of gravity to write moments about is inconvenient since in calculating moments of forces about G, one has to deal with the moments of unknown reaction forces at the hinge. Such a problem does not exist if moments are written about the hinge point. Nevertheless, in order to be able to write moments about the hinge location, P, when it is not fixed in a Newtonian reference system, the Euler's equations should be modified to what is called the 'extended' Euler's equations.

For a system of particles, using Fig. 7.2 and its corresponding kinetic diagram, the moment equation about an arbitrary point P can be written as, Meriam and Kraige (2003),

$$\sum \vec{M}_P = \dot{\vec{H}}_{P,\mathrm{rel}} + \overline{\vec{\rho}} \times m\vec{a}_P \tag{7.21}$$

where m is the mass of the body, and $\vec{H}_{P,\mathrm{rel}}$ is its angular momentum about P and relative to P defined as

$$\vec{H}_{P,\mathrm{rel}} = \sum_i \left(\vec{\rho}_i' \times m_i \vec{v}_{i/P}\right) \tag{7.22}$$

For a rigid blade, Eq. (7.22) can be written as

$$\vec{H}_{P,\mathrm{rel}} = \sum_i \left(m_i \vec{\rho}_i' \times (\omega \times \vec{\rho}_i')\right) \tag{7.23}$$

Finally, considering the whole blade as a continuum,

$$\vec{H}_{P,\mathrm{rel}} = \int [\vec{\rho}' \times (\vec{\omega} \times \vec{\rho}')]\mathrm{d}m \tag{7.24}$$

Equation (7.24) is similar to Eqs. (7.3) and (7.5). Starting from Eq. (7.24) and following a procedure similar to what was done in Sect. 7.3, one obtains

$$\vec{H}_{P,\mathrm{rel}} = I\vec{\omega}, \quad \begin{Bmatrix} H_{p,x} \\ H_{p,y} \\ H_{p,z} \end{Bmatrix}_{\mathrm{rel}} = \begin{bmatrix} I_{xx} & -I_{xy} & -I_{xz} \\ -I_{yx} & I_{yy} & -I_{yz} \\ -I_{zx} & -I_{zy} & I_{zz} \end{bmatrix} \begin{Bmatrix} \omega_x \\ \omega_y \\ \omega_z \end{Bmatrix} \tag{7.25}$$

If the coordinate axes x–y–z are chosen to be the principal axes of inertia of the blade with origin at the hinge point, P, Eq. (7.25) reduces to

$$\begin{Bmatrix} H_{p,x} \\ H_{p,y} \\ H_{p,z} \end{Bmatrix}_{\mathrm{rel}} = \begin{bmatrix} I_{xx} & 0 & 0 \\ 0 & I_{yy} & 0 \\ 0 & 0 & I_{zz} \end{bmatrix} \begin{Bmatrix} \omega_x \\ \omega_y \\ \omega_z \end{Bmatrix} \tag{7.26}$$

By taking the time derivative of Eq. (7.26) and using Eq. (7.12) (Coriolis theorem), one obtains

$$\left(\dot{H}_P\right)_{\mathrm{rel},x} = I_{xx}\dot{\omega}_x - (I_{yy} - I_{zz})\omega_y\omega_z \tag{7.27}$$

$$\left(\dot{\vec{H}}_P\right)_{\mathrm{rel},y} = I_{yy}\dot{\omega}_y - (I_{zz} - I_{xx})\omega_z\omega_x \tag{7.28}$$

$$\left(\dot{\vec{H}}_P\right)_{\mathrm{rel},z} = I_{zz}\dot{\omega}_z - (I_{xx} - I_{yy})\omega_x\omega_y \tag{7.29}$$

Now, the term $\overrightarrow{\rho} \times m\vec{a}_P$ in Eq. (7.21) should be calculated. The position vector of the mass center of the blade, G, with respect to hinge, P (shown in Fig. 7.2), can be written as,

$$\overrightarrow{\rho} = x_G\hat{i} + y_G\hat{j} + z_G\hat{k} \tag{7.30}$$

Considering the absolute acceleration of the hinge point P,

$$\vec{a}_P = a_{Px}\hat{i} + a_{Py}\hat{j} + a_{Pz}\hat{k} \tag{7.31}$$

one obtains

$$\overrightarrow{\rho} \times \vec{a}_P = \left(y_G a_{Pz} - z_G a_{Py}\right)\hat{i} + \left(z_G a_{Px} - x_G a_{Pz}\right)\hat{j} + \left(x_G a_{Py} - y_G a_{Px}\right)\hat{k} \tag{7.32}$$

Substitution of Eqs. (7.27)–(7.29) and (7.32) into (7.21) results in,

$$\sum M_{Px} = I_{xx}\dot{\omega}_x - (I_{yy} - I_{zz})\omega_y\omega_z + m\left(y_G a_{Pz} - z_G a_{Py}\right) \tag{7.33}$$

$$\sum M_{Py} = I_{yy}\dot{\omega}_y - (I_{zz} - I_{xx})\omega_z\omega_x + m(z_G a_{Px} - x_G a_{Pz}) \tag{7.34}$$

$$\sum M_{Pz} = I_{zz}\dot{\omega}_z - (I_{xx} - I_{yy})\omega_x\omega_y + m\left(x_G a_{Py} - y_G a_{Px}\right) \tag{7.35}$$

where m is the mass of the blade and the equations are written with respect to a principal coordinate system of inertia that is attached to the blade and its origin is at hinge, P.

Equations (7.33)–(7.35) are the 'extended' form of the Euler equations of motion (7.18)–(7.20) in which the hinge point P is a general point with nonzero acceleration. For zero offset (i.e., $OP = 0$) or zero acceleration of point P, Eqs. (7.33)–(7.35) reduce to (7.18)–(7.20), as expected.

In helicopter blades, the center of gravity is practically on the x-axis. So

$$\overrightarrow{\rho} = x_G\hat{i}, \quad y_G = 0, \quad z_G = 0 \tag{7.36}$$

Substituting Eq. (7.36) into Eqs. (7.33)–(7.35) results in

$$\sum M_{Px} = I_{xx}\dot{\omega}_x - (I_{yy} - I_{zz})\omega_y\omega_z \tag{7.37}$$

$$\sum M_{Py} = I_{yy}\dot{\omega}_y - (I_{zz} - I_{xx})\omega_z\omega_x - m x_G a_{Pz} \tag{7.38}$$

$$\sum M_{Pz} = I_{zz}\dot{\omega}_z - (I_{xx} - I_{yy})\omega_x\omega_y + m x_G a_{Py} \tag{7.39}$$

Equations (7.37)–(7.39) are the 'extended' Euler equations adapted for the case of a rotating blade with hinge offset and can be used for deriving the equations of motion of a rigid articulated blade in flapping, lagging, and feathering motions.

7.5 Uncoupled Equations of Motion of a Rigid Articulated Blade

The blades of an articulated rotor, as seen in Fig. 7.1, have two primary degrees of freedom, which are flapping and lagging, and they take place about the flap and lag hinges, respectively. The flap and lag hinges are used in order to reduce the root blade loads (since at the hinge moments must be zero). The flap hinge is usually offset slightly from the center of rotation because of mechanical constraints and to improve the helicopter handling qualities. The lead–lag hinge too must be offset from the center of rotation to provide some moment arm and for the shaft to transmit torque to the rotor.

The lag motion is only lightly damped. The small lead–lag displacements produce small aerodynamic and drag forces. These drag forces are almost two orders of magnitude less than the lift forces. Therefore, the lead–lag motion is very susceptible to instabilities. An important example is ground resonance, where the blade lead–lag motion and the lateral motion of the fuselage and rotor hub become coupled to produce a catastrophic aeromechanical instability. To prevent this phenomenon, most rotors have mechanical lag dampers, which provide artificial damping.

7.5.1 Uncoupled Flapping

Figure 7.3 illustrates a rotating blade with a flap hinge mounted at distance eR from the axis of rotation (the flap hinge offset distance is eR, where R is the rotor radius shown in the figure and the blade span is R-eR, typically, $e < 0.15$).

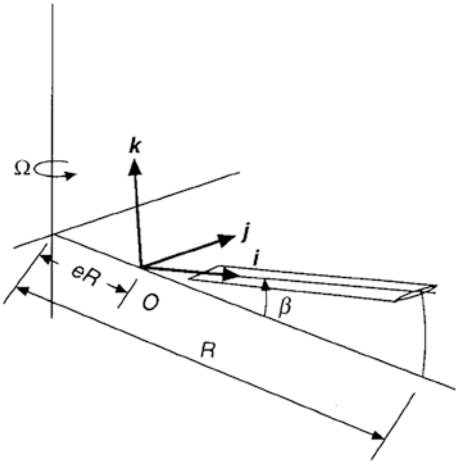

Fig. 7.3 Flapping blade, Bramwell et al. (2001), page 7 © Elsevier Ltd., reprinted with permission

In Fig. 7.3, the blade coordinate system that is attached to the blade has been shown. The origin of this system is at the hinge and the axes are in the principal directions of inertia of the blade at the root. In flapping, as it is seen in Fig. 7.4 the angular velocity of the shaft Ω is always in the plane made by x- and z-axes. The flap angle, β, is measured relative to a plane perpendicular to the rotor shaft axis, and its positive sense, as is shown in Fig. 7.4, is in the negative y direction (flapping up). Flapping up provides a balance between the moment of centrifugal forces and the moment of lift forces about the flap hinge.

In the hub coordinate system shown in Fig. 7.5, the shaft angular velocity can be written as, $\Omega.e_3$. Referring to Fig. 7.4, the total angular velocity of the blade in the blade coordinate system can be written as the summation of the transformed vector of the rotor shaft angular velocity and the flap motion, $-\dot{\beta}\hat{j}$,

$$\begin{Bmatrix} \omega_1 \\ \omega_2 \\ \omega_3 \end{Bmatrix} = \begin{bmatrix} \cos\beta & 0 & \sin\beta \\ 0 & 1 & 0 \\ -\sin\beta & 0 & \cos\beta \end{bmatrix} \begin{Bmatrix} 0 \\ 0 \\ \Omega \end{Bmatrix} - \dot{\beta}\hat{j} \tag{7.40}$$

or

$$\vec{\omega} = (\Omega\sin\beta)\hat{i} - \dot{\beta}\hat{j} + (\Omega\cos\beta)\hat{k} \tag{7.41}$$

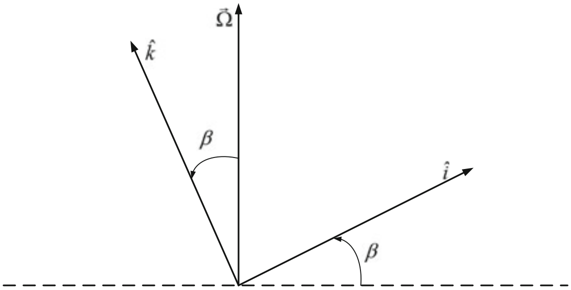

Fig. 7.4 Flapping of a rotating blade in the blade coordinate system

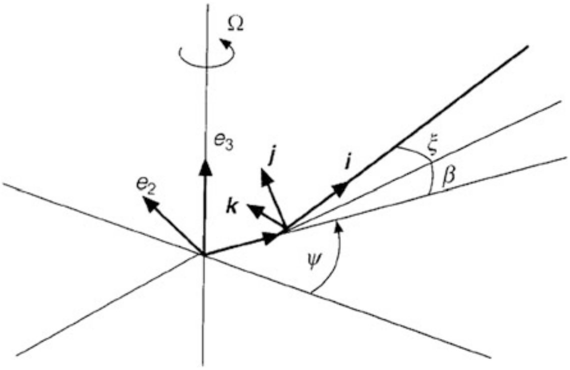

Fig. 7.5 Rotating rigid blade with hub and blade coordinate systems, Bramwell et al. (2001), page 22 © Elsevier Ltd., reprinted with permission

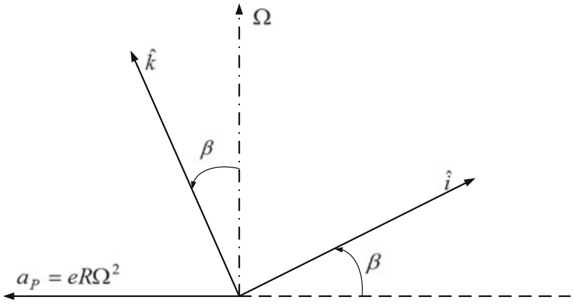

Fig. 7.6 The acceleration of the hinge point in the blade coordinate system

Equation (7.41) demonstrates the relation between the angular velocity of the shaft, Ω, and the angular velocity of the blade, ω, during flapping.

Using the hub coordinate system shown in Fig. 7.5, for constant shaft angular velocity, Ω, the acceleration of the hinge point, P, shown in Fig. 7.6 is $-eR\Omega^2 e_1$. By implementing a rotation transformation, this acceleration can be expressed in the blade coordinate system as follows:

$$\begin{Bmatrix} a_{P1} \\ a_{P2} \\ a_{P3} \end{Bmatrix} = \begin{bmatrix} \cos\beta & 0 & \sin\beta \\ 0 & 1 & 0 \\ -\sin\beta & 0 & \cos\beta \end{bmatrix} \begin{Bmatrix} -eR\Omega^2 \\ 0 \\ 0 \end{Bmatrix} \tag{7.42}$$

or

$$\vec{a}_P = (-eR\Omega^2\cos\beta)\hat{i} + 0\hat{j} + (eR\Omega^2\sin\beta)\hat{k} \tag{7.43}$$

But, using Eq. (7.9) for blades which are thin in the z direction,

$$I_{zz} \approx I_{xx} + I_{yy} \tag{7.44}$$

Since the flapping motion takes place about the y-axis, one may utilize the second of the ‘extended’ Euler equations (7.38) as well as Eqs. (7.41) and (7.44) to get

$$\sum M_{Py} = -I_{yy}\ddot{\beta} - I_{yy}(\Omega\sin\beta)(\Omega\cos\beta) - mx_G(eR\Omega^2\sin\beta)$$

or

$$-\sum M_{Py} = I_{yy}\ddot{\beta} + \Omega^2(I_{yy}\cos\beta + mx_G eR)\sin\beta \tag{7.45}$$

The non-dimensional position of the mass center, x_{Gn}, can now be defined as

$$x_G = Rx_{Gn} \tag{7.46}$$

Substituting Eq. (7.46) into (7.45) results in

$$-\sum M_{Py} = I_{yy}\ddot{\beta} + \Omega^2\left(I_{yy}\cos\beta + mx_{Gn}eR^2\right)\sin\beta \tag{7.47}$$

Equation (7.47) is the nonlinear flap-only (uncoupled) equation. The term in the left-hand side of Eq. (7.47) is the negative of the aerodynamic moment (considered positive in the positive y or in the negative β direction). The second term in the right-hand side of Eq. (7.47) is equal to the moment of centrifugal forces on the blade about the flap hinge. This moment acts like a torsional spring and tends to return the blade to its equilibrium position.

For small values of the flap angle, which is usually the case, Eq. (7.47) may be linearized to

$$\ddot{\beta} + \Omega^2 \nu_\beta^2 \beta = -\frac{1}{I_{yy}}\sum M_{Py} \tag{7.48}$$

where

$$\nu_\beta^2 = 1 + \frac{mx_{Gn}eR^2}{I_{yy}} \tag{7.49}$$

If the blade is modeled as a slender bar with uniform mass distribution along its span, since the reference of the coordinate system is roughly located at the root of the blade,

$$x_G = \frac{1}{2}(R - Re), \quad I_{yy} = \frac{1}{3}m(R - Re)^2 \tag{7.50}$$

Substituting Eq. (7.50) into Eq. (7.49) gives,

$$\nu_\beta^2 = 1 + \frac{3e}{2(1-e)} \tag{7.51}$$

So the natural frequency of flapping that according to Eq. (7.48) is $\Omega\nu_\beta$, becomes

$$\omega_{nf} = \Omega\sqrt{1 + \frac{3e}{2(1-e)}} \tag{7.52}$$

The value of eccentricity, e, is around 5 % so the natural frequency of the rotor is only slightly greater than Ω. Setting hinge offset equal to zero ($e = 0$) results in a flapping natural frequency equal to the frequency of rotation of the rotor shaft (or 1 per rev).

In hovering flight, the flap angle converges to a constant, β_0 (independent of the azimuth angle, ψ), which is called the coning angle. The coning angle is determined by a balance of the moments of aerodynamic and centrifugal forces about the flapping hinge. Using Eq. (7.48),

$$\beta_0 = -\frac{3\sum M_{Py}}{mR^2\Omega^2(1-e)(1+0.5e)} \tag{7.53}$$

Furthermore, substituting Eqs. (7.41) and (7.44) into Eq. (7.37) gives

$$\sum M_{Px} = I_{xx}\Omega\dot{\beta}\cos\beta - (-I_{xx})(-\dot{\beta})\Omega\cos\beta = 0 \tag{7.54}$$

Therefore, the flapping motion produces no feathering inertia moment. For the lead–lag motion, using Eqs. (7.41), (7.44) and Eq. (7.39) one obtains

$$\sum M_{Pz} = \left(\Omega\dot{\beta}\sin\beta\right)\left(-I_{zz} + I_{xx} - I_{yy}\right) = -2I_{yy}\Omega\dot{\beta}\sin\beta \tag{7.55}$$

The in-plane lag moment given in Eq. (7.55) is generated by flapping. The existence of this moment is, in fact, the reason for which in articulated blades a lead–lag hinge is used.

7.5.2 Uncoupled Lead–Lag

Figure 7.7 illustrates a lead–lag hinge with hinge offset distance, *eR*. This hinge is parallel to the rotor shaft axis, so the lead–lag angle, ξ, represents a change of the blade angle in the plane of the hub. The lead–lag angle is defined positive in the 'lagging' direction (opposite to the rotor shaft angular velocity, Ω). This sign convention is contrary to the one used in Bramwell et al. (2001) and is illustrated in Fig. 7.7. Therefore, due to lagging, the instantaneous angular velocity of the blade reduces to

$$\vec{\omega} = (\Omega - \dot{\xi})\hat{k} \tag{7.56}$$

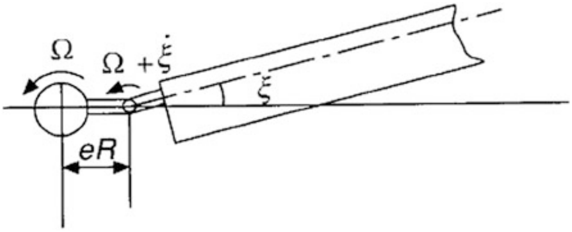

Fig. 7.7 Blade lagging, Bramwell et al. (2001), page 9 © Elsevier Ltd., reprinted with permission

For constant Ω, and due to the lead–lag rotation, ξ, the acceleration $-eR\Omega^2 e_1$ of the hinge point, P (i.e., a_P), in the hub coordinate system can be written as

$$\begin{Bmatrix} a_{P1} \\ a_{P2} \\ a_{P3} \end{Bmatrix} = \begin{bmatrix} \cos\xi & -\sin\xi & 0 \\ \sin\xi & \cos\xi & 0 \\ 0 & 0 & 1 \end{bmatrix} \begin{Bmatrix} -eR\Omega^2 \\ 0 \\ 0 \end{Bmatrix} \tag{7.57}$$

or

$$\vec{a}_P = -eR\Omega^2(\cos\xi\hat{i} + \sin\xi\hat{j}) \tag{7.58}$$

Substituting Eqs. (7.46), (7.56), and (7.58) into Eq. (7.39) gives

$$-\sum M_{Pz} = I_{zz}\ddot{\xi} + mex_{Gn}R^2\Omega^2 \sin\xi \tag{7.59}$$

For small ξ, Eq. (7.59) can be linearized to

$$\ddot{\xi} + v_\xi^2\Omega^2\xi = -\frac{1}{I_{zz}}\sum M_{Pz} \tag{7.60}$$

where

$$v_\xi^2 = \frac{mex_{Gn}R^2}{I_{zz}} \tag{7.61}$$

The negative signs of moments in the right hand side of the flap Eq. (7.48) and the lead–lag Eq. (7.60) are because the positive direction of flap is in the negative y direction and the positive direction of lead–lag is in the negative z direction.

For a blade modeled as a slender bar with uniform mass distribution along its span, using Eqs. (7.50) and (7.61) the natural frequency of lead–lag that according to Eq. (7.60) is Ωv_ξ, and it becomes

$$\omega_{nl} = \Omega\sqrt{\frac{3e}{2(1-e)}} \tag{7.62}$$

If the lead–lag offset distance is zero, Eq. (7.62) results in a zero lead–lag rigid body natural frequency and an unbounded lead–lag response. A rotor blade that is pinned in lead–lag to the axis of rotation generates the mentioned ill-conditioned problem (zero stiffness at root and zero lead–lag natural frequency).

Interestingly, the lead–lag hinge offset and the lead–lag hinge torsional spring have identical effects. With nonzero lead–lag hinge offset, but no hinge torsional spring, Eq. (7.60) is the equation of motion. On the other hand, with a torsional spring at the lead–lag hinge, when the hinge offset is zero,

$$\ddot{\xi} + K_T \xi = -\frac{1}{I_{zz}} \sum M_{Pz}$$

where K_T is the torsional spring stiffness. The above equation is equivalent to Eq. (7.60). So, the inclusion of a hinge offset is equivalent to the installation of a torsional spring at the hinge. One may conclude that to prevent the mentioned ill-conditioning either the lead–lag hinge should have an offset or a torsional spring should be put at the root to ensure nonzero stiffness, Hodges (2008).

Therefore, the lead–lag offset distance should not be designed to be zero or if it is going to be zero, the hinge should have a torsional spring to avoid the zero stiffness condition that would otherwise happen when $e = 0$. In the flapping motion, however, always the stiffening effect due to rotation of the blade exists. Therefore, the flap hinge may be located without an offset and it does not require a spring to prevent zero stiffness and ill-conditioning. In flapping, neither hinge offset nor the hinge spring is required and the $M_2 = 0$ boundary condition at the hinge does not make any trouble. These points will be explained in more detail later in this chapter.

For $I_{yy} = I_{zz}$ and coincident flap and lag hinges, Eqs. (7.52) and (7.62) result in the following relation between the flap and the lead–lag natural frequencies,

$$\omega_{\mathrm{nf}}^2 = \Omega^2 + \omega_{\mathrm{nl}}^2 \tag{7.63}$$

Therefore, the natural frequency of the lag motion is much smaller than the flapping natural frequency. The reason is mainly that the centrifugal restoring moment about the lag hinge is considerably less than the corresponding moment about the flapping hinge. For articulated rotors, the uncoupled rotating lag frequency is typically around 0.2 to 0.3Ω (Leishman 2006, page 195).

7.5.3 The Blade to Hub Coordinate Transformation

Blade and hub coordinate systems have been shown in Fig. 7.5. So far, since most analyses have focused on the blade response, the results were presented in the blade coordinates. The results can be transferred to the hub coordinates if the hub design and the dynamics of the helicopter as a whole is of interest.

Let $i, j,$ and k be the set of unit vectors attached to the blade and e_1, e_2, and e_3 be a set of unit vectors fixed in the rotating hub. When the blade is in its undeformed position, i.e., when there is no flapping or lagging (or if the blade has no hinges), the blade axes coincide with the hub axes. Now suppose the blade flaps through angle β about e_2, bringing the blade axes into a position whose unit vectors are i_1, j_1, and k_1. The unit vectors e_1, e_2, and e_3 are related to i_1, j_1, and k_1 through a rotation matrix transformation

$$\begin{Bmatrix} i_1 \\ j_1 \\ k_1 \end{Bmatrix} = \begin{bmatrix} \cos\beta & 0 & \sin\beta \\ 0 & 1 & 0 \\ -\sin\beta & 0 & \cos\beta \end{bmatrix} \begin{Bmatrix} e_1 \\ e_2 \\ e_3 \end{Bmatrix} \tag{7.64}$$

The blade now rotates about the lag axis through angle ξ, bringing the unit vectors of the blade into their final positions i, j, and k. The unit vectors i, j, and k are related to i_1, j_1, and k_1 through the following rotation matrix transformation

$$\begin{Bmatrix} i \\ j \\ k \end{Bmatrix} = \begin{bmatrix} \cos\xi & -\sin\xi & 0 \\ \sin\xi & \cos\xi & 0 \\ 0 & 0 & 1 \end{bmatrix} \begin{Bmatrix} i_1 \\ j_1 \\ k_1 \end{Bmatrix} \tag{7.65}$$

The relationship between e_1, e_2, and e_3 and i, j, and k will then be

$$\begin{Bmatrix} i \\ j \\ k \end{Bmatrix} = \begin{bmatrix} \cos\xi & -\sin\xi & 0 \\ \sin\xi & \cos\xi & 0 \\ 0 & 0 & 1 \end{bmatrix} \begin{bmatrix} \cos\beta & 0 & \sin\beta \\ 0 & 1 & 0 \\ -\sin\beta & 0 & \cos\beta \end{bmatrix} \begin{Bmatrix} e_1 \\ e_2 \\ e_3 \end{Bmatrix} \tag{7.66}$$

or

$$\begin{Bmatrix} i \\ j \\ k \end{Bmatrix} = \begin{bmatrix} \cos\xi\cos\beta & -\sin\xi & \cos\xi\sin\beta \\ \sin\xi\cos\beta & \cos\xi & \sin\xi\sin\beta \\ -\sin\beta & 0 & \cos\beta \end{bmatrix} \begin{Bmatrix} e_1 \\ e_2 \\ e_3 \end{Bmatrix} \tag{7.67}$$

If first flap is applied and then lag the above relationship enables one to express quantities measured in one set of axes in terms of the other set. For large angles, the outcome would be different if the order of implementation of rotations is reversed because matrix multiplication is not commutative. For small angles, however, Eq. (7.67) for both sets of orders of transformation reduces to

$$\begin{Bmatrix} i \\ j \\ k \end{Bmatrix} = \begin{bmatrix} 1 & -\xi & \beta \\ \xi & 1 & 0 \\ -\beta & 0 & 1 \end{bmatrix} \begin{Bmatrix} e_1 \\ e_2 \\ e_3 \end{Bmatrix} \tag{7.68}$$

In articulated blades, the existence of hinges generates a difference between the angular velocity of the rotor shaft and the angular velocity of the blade. So, one should be careful to distinguish between these two angular velocities. Equation (7.66) can be used to transform the rotor shaft angular velocity from the hub coordinate system to the blade coordinate system. Based on the previous discussion, here the flap and the lead-lag angles are small. By adding the lead–lag and the flap angular velocities to the transformed rotor angular velocity, the total angular velocity of the blade in the blade coordinate system is obtained as

$$\begin{Bmatrix} \omega_1 \\ \omega_2 \\ \omega_3 \end{Bmatrix} = \begin{bmatrix} \cos\xi & -\sin\xi & 0 \\ \sin\xi & \cos\xi & 0 \\ 0 & 0 & 1 \end{bmatrix} \begin{bmatrix} \cos\beta & 0 & \sin\beta \\ 0 & 1 & 0 \\ -\sin\beta & 0 & \cos\beta \end{bmatrix} \begin{Bmatrix} 0 \\ 0 \\ \Omega \end{Bmatrix} - \dot{\beta}\hat{j} - \dot{\xi}\hat{k} \tag{7.69}$$

or

$$\vec{\omega} = (\Omega \sin\beta \cos\xi)\hat{i} + (\Omega \sin\beta \sin\xi - \dot{\beta})\hat{j} + (\Omega \cos\beta - \dot{\xi})\hat{k} \tag{7.70}$$

7.6 Coupled Nonlinear Flap and Lead–Lag Motions of Rigid Articulated Blades

So far a simplified version of rotating blade dynamics has been presented in which the flap and lead–lag motions are assumed independent from each other. A more realistic approach based on the system of Eqs. (7.37)–(7.39) comprises the coupling of these motions. In what follows, the nonlinear and coupled flap and lead–lag equations of motion are derived for a rotating rigid blade with coincident flap and lead–lag hinges.

Referring to Figs. 7.5 and 7.6, for constant rotor shaft angular velocity, Ω, the acceleration of the hinge point P (i.e., a_P) in the hub coordinate system $-eR\Omega^2 e_1$ can be transformed to the blade coordinate system by using Eq. (7.67) to result in

$$\begin{Bmatrix} a_{P1} \\ a_{P2} \\ a_{P3} \end{Bmatrix} = \begin{bmatrix} \cos\xi\cos\beta & -\sin\xi & \cos\xi\sin\beta \\ \sin\xi\cos\beta & \cos\xi & \sin\xi\sin\beta \\ -\sin\beta & 0 & \cos\beta \end{bmatrix} \begin{Bmatrix} -eR\Omega^2 \\ 0 \\ 0 \end{Bmatrix} \tag{7.71}$$

or

$$\vec{a}_P = eR\Omega^2(-\cos\beta\cos\xi\hat{i} - \cos\beta\sin\xi\hat{j} + \sin\beta\hat{k}) \tag{7.72}$$

Substitution of Eqs. (7.70) and (7.72) into Eq. (7.39) gives

$$\begin{aligned} \sum M_{Pz} = {} & I_{zz}(-\ddot{\xi} - \dot{\beta}\Omega\sin\beta) - (I_{xx} - I_{yy})(\Omega\sin\beta\cos\xi)(\Omega\sin\beta\sin\xi - \dot{\beta}) \\ & - m(Rx_{Gn})(eR\Omega^2\cos\beta\sin\xi) \end{aligned} \tag{7.73}$$

For small β and ξ, from Eqs. (7.73) and (7.44) one obtains

$$-\sum M_{Pz} = I_{zz}\ddot{\xi} + 2I_{yy}\Omega\beta\dot{\beta} + mex_{Gn}R^2\Omega^2\xi \tag{7.74}$$

Using $I_{zz} \approx I_{yy}$ in Eq. (7.74) results in

$$-\frac{1}{I_{zz}}\sum M_{Pz} = \ddot{\xi} + \left(mex_{Gn}R^2/I_{zz}\right)\Omega^2\xi + 2\Omega\beta\dot{\beta} \tag{7.75}$$

or

$$\ddot{\xi} + \nu_{\xi}^2\Omega^2\xi + 2\Omega\beta\dot{\beta} = -\frac{1}{I_{zz}}\sum M_{Pz} \tag{7.76}$$

where

$$\nu_{\xi}^2 = \frac{mx_{Gn}eR^2}{I_{zz}} \tag{7.61}$$

Equation (7.76) is one of the two coupled flap–lead–lag equations of motion and is a generalized form of Eq. (7.60). Equation (7.76) reduces to Eq. (7.60) once the flap angle is set equal to zero. Recalling ground resonance discussed before, a mechanical lag damper can be included in the model to prevent it from happening. In such a case, Eq. (7.76) is modified to

$$\ddot{\xi} + C_{\xi}\dot{\xi} + \nu_{\xi}^2\Omega^2\xi + 2\Omega\beta\dot{\beta} = -\frac{1}{I_{zz}}\sum M_{Pz} \tag{7.77}$$

The second coupled flap–lag equation of motion can be obtained by substituting Eqs. (7.70) and (7.72) into Eq. (7.38) to give

$$\begin{aligned}\sum M_{Py} = {} & I_{yy}(-\ddot{\beta} + \Omega\dot{\beta}\cos\beta\sin\xi + \Omega\dot{\xi}\sin\beta\cos\xi) \\ & -(I_{zz} - I_{xx})(\Omega\cos\beta - \dot{\xi})(\Omega\sin\beta\cos\xi) - m(Rx_{Gn})(eR\Omega^2\sin\beta)\end{aligned} \tag{7.78}$$

Substituting Eq. (7.44) into Eq. (7.78) and for small flap and lead–lag angles one obtains

$$\ddot{\beta} + \Omega^2\left(1 + \frac{mx_{Gn}eR^2}{I_{yy}}\right)\beta - \Omega(2\dot{\xi}\beta + \dot{\beta}\xi) = -\frac{1}{I_{yy}}\sum M_{Py} \tag{7.79}$$

The flap and the lead–lag equations of motion (7.76) and (7.79) are nonlinearly coupled, and linearization decouples them. In other words, like many other nonlinear models, coupling originates from nonlinearity. If the nonlinear terms are ignored, these equations reduce to the decoupled set of linear Eqs. (7.48) and (7.60). A slightly different equation has been presented in Leishman (2006), page 197, as

$$\ddot{\beta} + \Omega^2\nu_{\beta}^2\beta - 2\Omega\dot{\xi}\beta = -\frac{1}{I_{yy}}\sum M_{Py}, \quad \nu_{\beta}^2 = 1 + \frac{mx_{Gn}eR^2}{I_{yy}} \tag{7.80}$$

In comparison with Eq. (7.79), Eq. (7.80) is missing the $-\Omega\dot{\beta}\xi$ term.

So far, time has been used as the independent variable; however, as it was mentioned before, sometimes it is advantageous to change the independent variable to the azimuth angle, ψ, shown in Fig. 7.5. Azimuth angle is related to the constant angular velocity of the rotor shaft as

$$\psi = \Omega t \tag{7.1}$$

At constant rotational speed, using the chain rule, Eq. (7.1) gives

$$\frac{\mathrm{d}(\bullet)}{\mathrm{d}t} = \frac{\mathrm{d}(\bullet)}{\mathrm{d}\psi}\frac{\mathrm{d}\psi}{\mathrm{d}t} = \frac{\mathrm{d}(\bullet)}{\mathrm{d}\psi}\Omega \tag{7.81}$$

and

$$\frac{\mathrm{d}^2(\bullet)}{\mathrm{d}t^2} = \frac{\mathrm{d}^2(\bullet)}{\mathrm{d}\psi^2}\left(\frac{\mathrm{d}\psi}{\mathrm{d}t}\right)^2 = \frac{\mathrm{d}^2(\bullet)}{\mathrm{d}\psi^2}\Omega^2 \tag{7.82}$$

Therefore, the coupled nonlinear flap–lag Eqs. (7.77) and (7.79) convert to,

$$\frac{\mathrm{d}^2\beta}{\mathrm{d}\psi^2} + \left(1 + \frac{mx_{Gn}eR^2}{I_{yy}}\right)\beta - \left(2\beta\frac{\mathrm{d}\xi}{\mathrm{d}\psi} + \xi\frac{\mathrm{d}\beta}{\mathrm{d}\psi}\right) = -\frac{1}{\Omega^2 I_{yy}}\sum M_{Py} \tag{7.83}$$

$$\frac{\mathrm{d}^2\xi}{\mathrm{d}\psi^2} + \frac{C_\xi}{\Omega}\frac{\mathrm{d}\xi}{\mathrm{d}\psi} + \left(\frac{mx_{Gn}eR^2}{I_{zz}}\right)\xi + 2\beta\frac{\mathrm{d}\beta}{\mathrm{d}\psi} = -\frac{1}{\Omega^2 I_{zz}}\sum M_{Pz} \tag{7.84}$$

7.7 Case Study: Undamped Coupled Motion of Rigid Articulated Blades

The isotropic rectangular solid model introduced in Sect. 3.3 is considered here again. In this case, the moments of inertia of the beam about its root are

$$I_{yy} = I_{x_2x_2} = 11.8295\,\mathrm{kg.m^2}, \quad I_{zz} = I_{x_3x_3} = 11.9180\,\mathrm{kg.m^2}, \tag{7.85}$$

Also,

$$x_{Gn} = 0.48 \quad e = 0.04 \quad R = 1.04\,\mathrm{m} \tag{7.86}$$

In a helicopter, the pitch command (the summation of the collective and cyclic pitches) given by the pilot controls lift and drag and therefore, M_y and M_z. These moments in turn produce nonzero flap and lead–lag motions. In this simple blade model in hover, a steady-state shaft angular velocity of Ω = 100 rad/s and applied moments M_y = −1000 N.m and M_z = −10 N.m are assumed. These constant moments model the application of a collective pitch in hover where the moments are not functions of the azimuth angle and they adjust the flap angle β in order to provide the necessary thrust. So, the coupled flap–lag Eqs. (7.77) and (7.79) without including the mechanical damper in lead–lag become

$$\ddot{\beta} + 10621\beta - 100(2\dot{\xi}\beta + \dot{\beta}\xi) = 84.53 \tag{7.87}$$

$$\ddot{\xi} + 617\xi + 200\beta\dot{\beta} = 0.839 \tag{7.88}$$

Figures 7.8 and 7.9 illustrate the solution of Eqs. (7.87) and (7.88) that is labeled as 'present.' The 'Leishman' solution corresponds to the use of Eq. (7.80) for the numerical values given in this case study. The contribution of the missing term in Eq. (7.80) can be deduced from the figures. The 'uncoupled' response is obtained by solving a modified version of Eqs. (7.48) and (7.60) that does not have the nonlinear terms.

It is seen that the flap motion has a one per rev frequency, as expected. The lead–lag oscillations, however, because of the small hinge offset are much slower (have a larger period). The mean flap and lead–lag values, determined mainly by the collective pitch that controls the forcing terms in Eqs. (7.87) and (7.88), are seen to be positive, as expected. In this case, even though a collective pitch is applied, the coning angle does not converge to a constant value. The reason is that there is no damping in this model.

In this problem, if the hinge offset is set equal to zero, the linear lead–lag frequency becomes zero and the lead–lag solution becomes unbounded, as it is

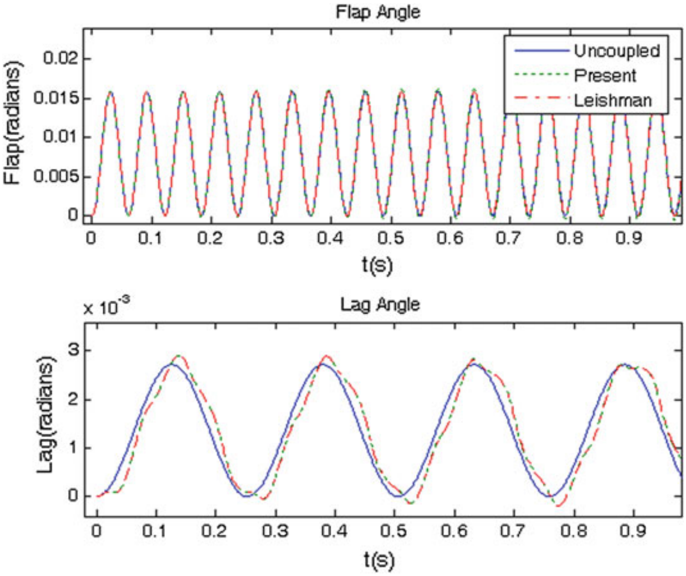

Fig. 7.8 Time history diagrams for lead–lag and flap motions

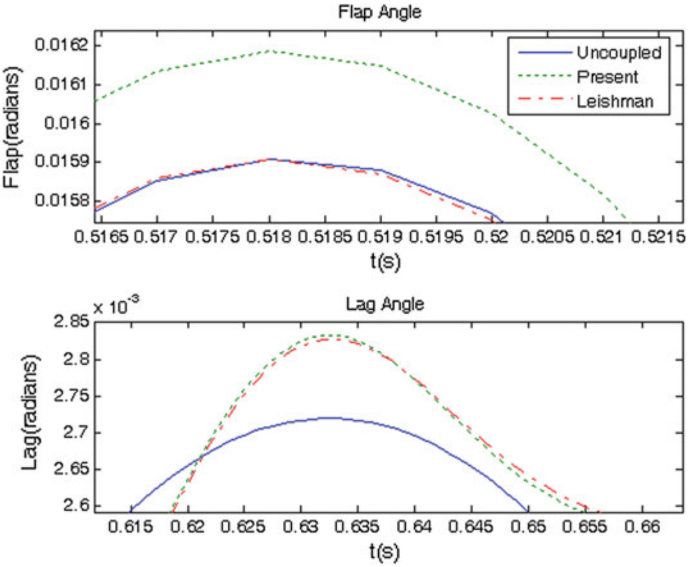

Fig. 7.9 Zoomed-in view of Fig. 7.8

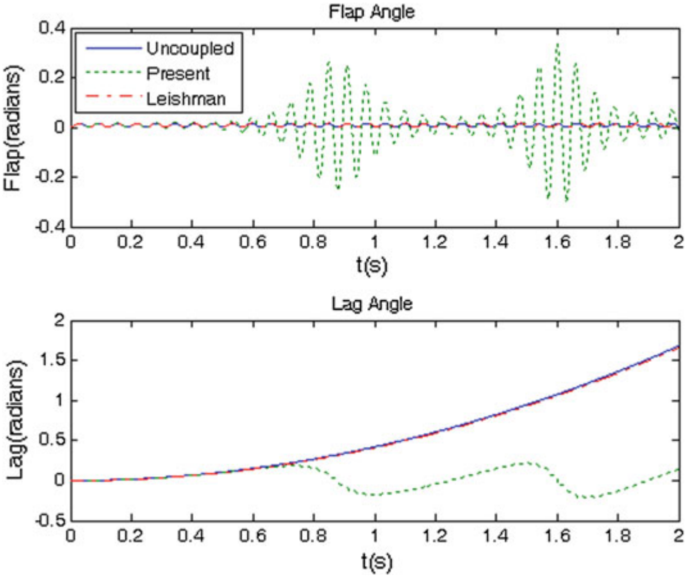

Fig. 7.10 Time history diagrams for lead–lag and flap motions with zero hinge offset

observed in Fig. 7.10. In such a case, as it is mentioned in Sect. 7.5, in order to control the lead–lag motion, a torsional spring should be installed at the hinge.

7.8 Aerodynamically Damped Flap and Lead–Lag Motions of Rigid Articulated Blades

7.8.1 Aerodynamic Damping Effect in Flap Motion with no Hinge Offset

By ignoring the free-stream velocity and axial climbing and including the effects of blade pitch, flap motion, and the induced velocity field, the lift force per unit length is (Leishman 2006, page 179)

$$L = \frac{1}{2}\rho U_T^2 c C_{L\alpha}\left(\theta - \frac{\dot{\beta} r}{U_\mathrm{T}} - \frac{v_i}{U_T}\right) \tag{7.89}$$

In Eq. (7.89), the induced velocity v_i is the velocity imparted to the mass of air contained in the control volume at the rotor disk. In addition, the tangential velocity of the blade element in hover or axial climb is

$$U_\mathrm{T} = r\Omega \tag{7.90}$$

Furthermore, c is the local blade chord. By ignoring the hinge offset for now, the aerodynamic moment about the hinge would be

$$-\sum M_{Py} = \int_0^R L r \mathrm{d}r = \frac{1}{2}\rho\Omega^2 c C_{L\alpha}\int_0^R r^3\left(\theta - \frac{\dot{\beta}}{\Omega} - \frac{v_i}{r\Omega}\right)\mathrm{d}r$$

or

$$-\sum M_{Py} = \frac{1}{2}\rho\Omega^2 c C_{L\alpha}\int_0^R r^3\left(\theta - \frac{\dot{\beta}}{\Omega} - \lambda_i\frac{R}{r}\right)\mathrm{d}r = \frac{1}{8}\rho\Omega^2 c C_{L\alpha}R^4\left(\theta - \frac{\dot{\beta}}{\Omega} - \frac{4\lambda_i}{3}\right) \tag{7.91}$$

where the rotor-induced inflow ratio is defined as

$$\lambda_i = \frac{v_i}{R\Omega} \tag{7.92}$$

The linear uncoupled version of Eq. (7.83) with no hinge offset is

$$\frac{\mathrm{d}^2\beta}{\mathrm{d}\psi^2} + \beta = -\frac{1}{\Omega^2 I_{yy}}\sum M_{Py} \tag{7.93}$$

Substitution of Eq. (7.91) into Eq. (7.93) gives,

$$\frac{\mathrm{d}^2\beta}{\mathrm{d}\psi^2}+\beta=\frac{\rho\, c\, C_{L\alpha}R^4}{I_{yy}}\left(\frac{1}{8}\right)\left(\theta-\frac{\mathrm{d}\beta}{\mathrm{d}\psi}-\frac{4\lambda_i}{3}\right)$$

Therefore, the uncoupled flapping equation with pitch and aerodynamics is

$$\frac{\mathrm{d}^2\beta}{\mathrm{d}\psi^2}+\left(\frac{\gamma}{8}\right)\frac{\mathrm{d}\beta}{\mathrm{d}\psi}+\beta=\frac{\gamma}{8}\left(\theta-\frac{4\lambda_i}{3}\right) \tag{7.94}$$

where the Lock number is defined as

$$\gamma=\frac{\rho c C_{L\alpha}R^4}{I_{yy}} \tag{7.95}$$

Lock number is a measure of the ratio of aerodynamic forces to inertia forces. The Lock number, for a helicopter rotor blade, is approximately eight.

Equation (7.94) is the flapping equation for a hinged blade with no offset. It is seen that the undamped natural frequency of the flapping blade about a hinge located at the axis of rotation is one per rev. The obtained equation is that of a damped motion, the damping is provided by the moment of aerodynamic forces about the flap hinge and it is proportional to the flap rate. The restoring moment, however, is produced by the centrifugal force.

7.8.2 Hinge Offset Effect on Nonlinear Aerodynamically Damped Flap Motion

So far, the contributions of hinge offset and aerodynamic forces on the flap motion have been considered separately. In this section, the combined effect of these two factors on the flapping motion is formulated.

Equation (7.83) includes the effects of hinge offset and flap–lag coupling. The moment of aerodynamic forces about the hinge location at, $r = eR$, can be stated as

$$-\sum M_{Py}=\int_{eR}^{R}L(r-eR)\mathrm{d}r \tag{7.96}$$

A modified version of Eq. (7.89) for the lift force per unit length of the blade that includes the hinge offset effect can be written as

$$L=\frac{1}{2}\rho U_T^2 c C_{L\alpha}\left(\theta-\frac{\dot{\beta}(r-eR)}{U_T}-\frac{v_i}{U_T}\right) \tag{7.97}$$

Combining Eqs. (7.96) and (7.97) results in

$$-\sum M_{Py} = \frac{1}{2}\rho\Omega^2 cC_{L\alpha}\int_{eR}^{R} r^2(r-eR)\left[\theta - \frac{\dot{\beta}(r-eR)}{\Omega r} - \lambda_i\frac{R}{r}\right]\mathrm{d}r$$

or

$$\begin{aligned}-\sum M_{Py} &= \frac{1}{2}\rho\Omega^2 cC_{L\alpha}\\ &\quad\times\left[R^4(\frac{1}{4}+\frac{1}{12}e^4-\frac{1}{3}e)\theta - \frac{1}{4}R^4(1-e)^3(1+\frac{1}{3}e)\frac{\mathrm{d}\beta}{\mathrm{d}\psi}\right.\\ &\qquad\left.-\left(\frac{1}{3}R^3(1-e^3)-\frac{1}{2}eR^3(1-e^2)\right)\lambda_i R\right]\end{aligned}\tag{7.98}$$

Substituting Eq. (7.98) into (7.83) gives

$$\begin{aligned}&\frac{\mathrm{d}^2\beta}{\mathrm{d}\psi^2}+\left(1+\frac{mx_{Gn}eR^2}{I_{yy}}\right)\beta-\left(2\beta\frac{\mathrm{d}\xi}{\mathrm{d}\psi}+\xi\frac{\mathrm{d}\beta}{\mathrm{d}\psi}\right)\\ &=\frac{1}{2I_{yy}}\rho cC_{L\alpha}\times\left[R^4(\frac{1}{4}+\frac{1}{12}e^4-\frac{1}{3}e)\theta-\frac{1}{4}R^4(1-e)^3(1+\frac{1}{3}e)\frac{\mathrm{d}\beta}{\mathrm{d}\psi}\right.\\ &\quad\left.-\left(\frac{1}{3}R^3(1-e^3)-\frac{1}{2}eR^3(1-e^2)\right)\lambda_i R\right]\end{aligned}$$

or, after rearrangements,

$$\begin{aligned}&\frac{\mathrm{d}^2\beta}{\mathrm{d}\psi^2}+\left(\frac{1}{8I_{yy}}\rho cC_{L\alpha}R^4(1-e)^3\left(1+\frac{1}{3}e\right)\right)\frac{\mathrm{d}\beta}{\mathrm{d}\psi}+\left(1+\frac{mx_{Gn}eR^2}{I_{yy}}\right)\beta-\left(2\beta\frac{d\xi}{d\psi}+\xi\frac{\mathrm{d}\beta}{\mathrm{d}\psi}\right)\\ &=\frac{1}{2I_{yy}}\rho cC_{L\alpha}\left[\left(R^4\left(\frac{1}{4}+\frac{1}{12}e^4-\frac{1}{3}e\right)\right)\theta-\left(\frac{1}{3}R^3(1-e^3)-\frac{1}{2}eR^3(1-e^2)\right)\lambda_i R\right]\end{aligned}$$

Recalling the Lock number as defined in Eq. (7.95), the general form of the coupled nonlinear flap–lag equation of motion including aerodynamic damping and hinge offset is

$$\begin{aligned}&\frac{\mathrm{d}^2\beta}{\mathrm{d}\psi^2}+\left[\frac{\gamma}{8}(1-e)^3\left(1+\frac{1}{3}e\right)\right]\frac{\mathrm{d}\beta}{\mathrm{d}\psi}+\left(1+\frac{mx_{Gn}eR^2}{I_{yy}}\right)\beta-\left(2\beta\frac{\mathrm{d}\xi}{\mathrm{d}\psi}+\xi\frac{\mathrm{d}\beta}{\mathrm{d}\psi}\right)\\ &=\frac{\gamma}{2}\left[\left(\frac{1}{4}+\frac{1}{12}e^4-\frac{1}{3}e\right)\theta-\left(\frac{1}{3}(1-e^3)-\frac{1}{2}e(1-e^2)\right)\lambda_i\right]\end{aligned}\tag{7.99}$$

In order to verify this result, a few special cases are considered. If the hinge offset is zero, Eq. (7.99) reduces to (7.94), as expected. Alternatively, if no flap–lag coupling and no cyclic pitch or induced velocity exist, Eq. (7.99) reduces to

$$\frac{\mathrm{d}^2\beta}{\mathrm{d}\psi^2}+\left[\frac{1}{8}\gamma(1-e)^3\left(1+\frac{1}{3}e\right)\right]\frac{\mathrm{d}\beta}{\mathrm{d}\psi}+\left(1+\frac{mx_{Gn}eR^2}{I_{yy}}\right)\beta=0 \tag{7.100}$$

which has been derived in Bramwell et al. (2001). Therefore, Eq. (7.99) is the general flap equation of motion where the effects of hinge offset, aerodynamic damping, and nonlinear coupling have all been taken into account.

7.8.3 Aerodynamic Damping Effect in the Lead–Lag Motion

For the lead–lag motion, if P denotes the power required to drive one blade, the corresponding moment would be (Leishman 2006)

$$\sum M_{Pz}=-\left(\frac{P}{\Omega}\right)\left(1-\frac{2\dot{\xi}}{\Omega}\right) \tag{7.101}$$

Substituting Eq. (7.101) into Eq. (7.84) and using Eq. (7.81) one obtains the following equation for the lead–lag motion of a rotating blade with a mechanical lag damper,

$$\frac{\mathrm{d}^2\xi}{\mathrm{d}\psi^2}+\left(\frac{C_\xi}{\Omega}+\frac{2P}{\Omega^3 I_{zz}}\right)\frac{\mathrm{d}\xi}{\mathrm{d}\psi}+\left(\frac{mx_{Gn}eR^2}{I_{zz}}\right)\xi+2\beta\frac{\mathrm{d}\beta}{\mathrm{d}\psi}=\frac{1}{\Omega^2 I_{zz}}\left(\frac{P}{\Omega}\right) \tag{7.102}$$

The linearized version of (7.102) represents a damped harmonic motion about the following steady value,

$$\xi_0=\frac{P}{\varepsilon\Omega^3 I_{zz}},\quad \varepsilon=\left(\frac{mx_{Gn}eR^2}{I_{zz}}\right) \tag{7.103}$$

Typical values of $\frac{P}{\Omega^3 I_{zz}}$ and ε are 0.006 and 0.075, respectively. Consequently, the steady value of ξ would be about 4.5°. Equations (7.99) and (7.102) are the general set of coupled nonlinear flap and lead–lag equations of motion with aerodynamic damping in flap and mechanical damping in lead–lag for a rigid blade with offset hinge.

7.9 Case Study: Articulated Rotating Blade with Aerodynamic Damping

The articulated blade model discussed in Sect. 7.7 is considered here again. Using Eqs. (7.99) and (7.102) with the drag moment $M_z = -10$ N.m, steady-state angular velocity of $\Omega = 100$ rad/s, $\gamma = 8$, and a collective pitch angle of 2° (which should tune the average value of β in order to provide the necessary thrust), the set of nonlinear flap–lag equations of motion becomes

$$\ddot{\beta} + 89.6\dot{\beta} + 10621\beta - 100(2\dot{\xi}\beta + \dot{\beta}\xi) = 330.45 \tag{7.104}$$

$$\ddot{\xi} + 617\xi + 200\beta\dot{\beta} = 0.839 \tag{7.105}$$

where time has replaced azimuth angle as the independent variable.

Figures 7.11 and 7.12 illustrate the solutions of Eqs. (7.104) and (7.105) that are labeled as, 'present.' The 'Leishman' label corresponds to the solution of Eqs. (7.104) and (7.105) with the $\dot{\beta}\xi$ missing from the flapping Eq. (7.104). The 'uncoupled' solution is obtained by solving Eqs. (7.104) and (7.105) in which all nonlinear terms have been ignored. Interestingly, since all of the nonlinear terms in Eqs. (7.104) and (7.105) are dynamic, all three solutions for the flap angle converge to the same steady-state result.

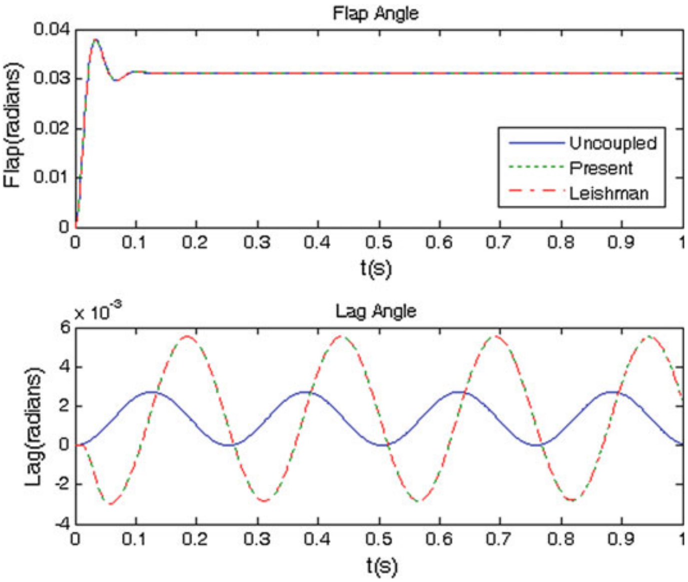

Fig. 7.11 Time history diagrams of flap and lead–lag motions with aerodynamic damping included

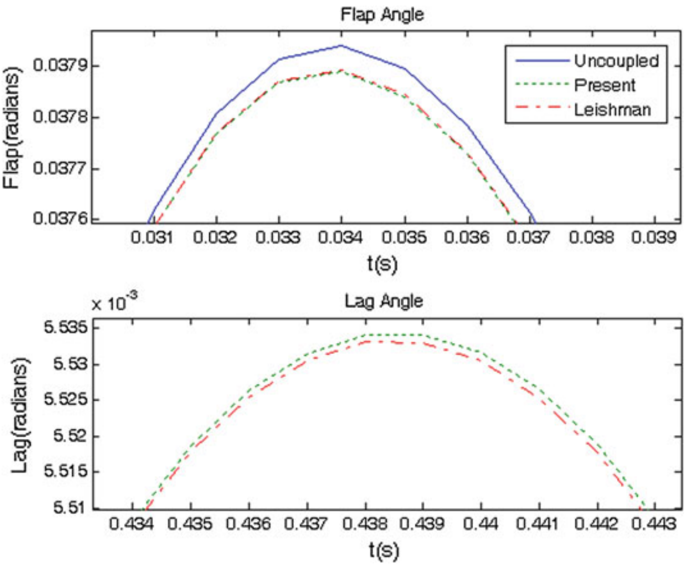

Fig. 7.12 Zoomed-in view of Fig. 7.11

Figure 7.12 illustrates a zoomed-in view of Fig. 7.11 and highlights the differences among the obtained solutions. It is observed that because of the aerodynamic damping and due to the application of the step input, which represents the collective pitch, the flap motion converges to a new steady-state position which corresponds to a coning angle. However, the aerodynamic damping that exists in the flap motion does not have any damping effect on the lead–lag motion through the nonlinear coupling.

To control the lead–lag motion, that is otherwise naturally undamped, mechanical dampers can be implemented. In order to illustrate this effect, Eqs. (7.104) and (7.105) are modified as

$$\ddot{\beta} + 89.6\dot{\beta} + 10621\beta - 100(2\dot{\xi}\beta + \dot{\beta}\xi) = 330.45 \tag{7.106}$$

$$\ddot{\xi} + 10\dot{\xi} + 617\xi + 200\beta\dot{\beta} = 0.839 \tag{7.107}$$

Figures 7.13 and 7.14 illustrate the corresponding solutions where the effect of damping on both motions is observed. The three solutions, i.e., ‘present,’ ‘Leishman,’ and ‘uncoupled,’ are presented, and they have the same meaning here as they had before in Figs. 7.11 and 7.12. It is seen that due to the application of the step input (i.e., the collective pitch), both flap and lead–lag motions converge to new steady states. These steady states represent a coning angle and a steady lag angle for the blade. Figures 7.13 and 7.14 reveal that while there are some differences in the dynamic responses, all of the three solutions predict the same steady-state outcome. This is expected as the nonlinear terms in Eqs. (7.106) and (7.107) are all dynamic and hence they have no effect on the steady-state response.

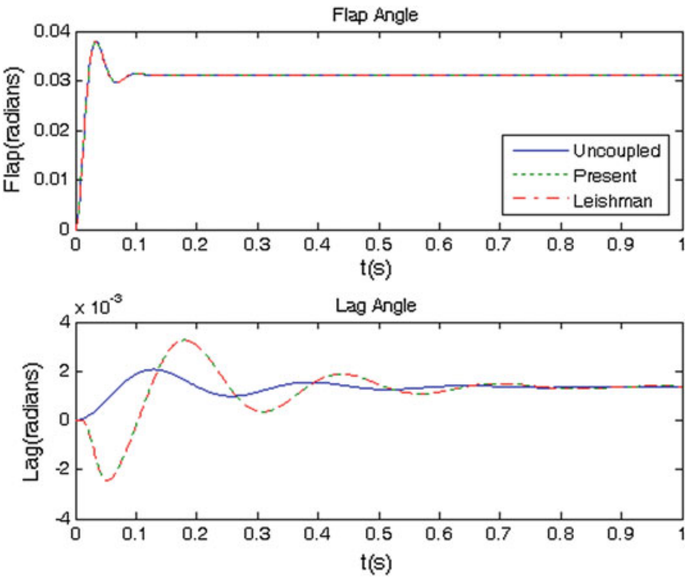

Fig. 7.13 Time history diagrams of flap and lead–lag motions; aerodynamic damping and lead–lag dampers are included

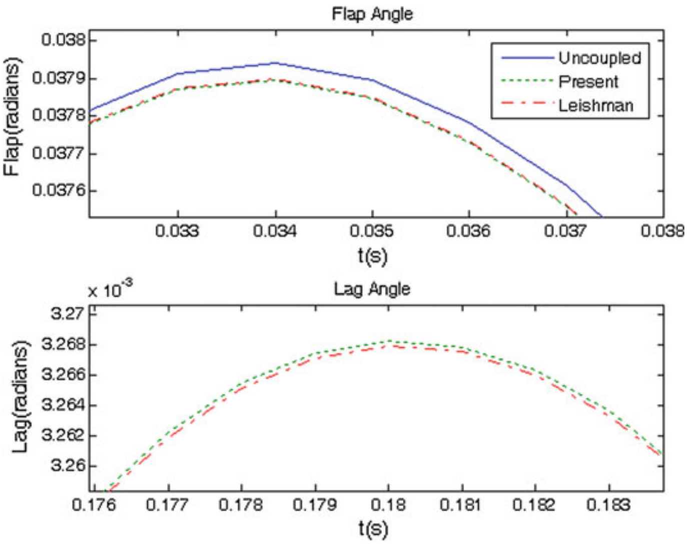

Fig. 7.14 Zoomed-in view of Fig. 7.13

7.10 Elastic Articulated Composite Rotating Blades

In the previous sections of this chapter, the articulated blades were assumed to be rigid. They were considered to rotate at a constant angular velocity and had articulated boundary conditions at the root. In comparison, in Chap. 5 the elasto-dynamic analysis of hingeless rotor blades was presented in which the angular velocity of the rotor was a variable. The root boundary conditions of the considered hingeless blades were clamped and the blades were modeled as elastic members.

In this section, to present a more realistic model of articulated rotor blades, they are modeled as elastic members. To perform the analysis of elastic articulated rotating blades, a solution algorithm that is a combination of the mentioned two solution methods is presented.

While for a rigid blade one can calculate the flap and lead–lag motions by solving the set of two coupled nonlinear differential Eqs. (7.99) and (7.102), the same is not easily achievable for elastic blades. The main problem is that one should solve a combined initial and boundary value problem whose root boundary conditions depend on the unknown solution of the differential equations of motion. This dependence creates an endless cycle in which solving the differential equations of motion for the elastic blade requires the knowledge of the boundary conditions and finding the boundary conditions, on the other hand, is possible only after the differential equation of motion has been solved. In other words, without solving the differential equations of motion the boundary conditions would not be known and without knowing the boundary conditions one cannot solve the differential equations of motion.

In this section, in order to circumvent the mentioned problem, the unknown angular velocity boundary conditions of the elastic blade at its root are taken from the corresponding solution of its rigid articulated blade analog. Therefore, first the rigid body motions of lead–lag and flap are calculated by analyzing the rigid body dynamics of the blade. Then, these solutions are utilized for obtaining the angular velocity boundary conditions of the elastic blade at its root.

Having obtained the root boundary conditions of the elastic blade, in the rest of the solution the blade is treated as an elastic member and the nonlinear elastic problem of the rotating blade is solved using the perturbation method discussed in Chap. 5. It is expected that the impact of the rigid body approximation in the first part of the solution be minor unless the blade deforms in higher modes with significant deformations.

Combining the algorithms for analyzing the rigid articulated blade and the elastic hingeless blade problems generates an algorithm, which is suitable for analyzing elastic articulated rotating blades. Such an analysis is performed in the following steps:

Step 1 The elastic blade, initially modeled as hingeless, is accelerated from rest to its full speed (the steady-state speed). The blade gently starts its rotation from rest and then using angular velocity functions like Eq. (5.24) gently converges to full speed. For such an accelerating rotor, one cannot use the hinged blade equations because they were obtained for a blade that rotates at constant angular velocity. So, in this first part of motion the methods that were developed in Chap. 5 could be utilized in the solution.

Step 2 Achieving the steady-state speed does not, of course, mean that the response of the blade is steady state. So, the blade is given some time (shown by T_{lim}) to continue to rotate at full speed and reach its steady-state response after the end of the acceleration phase and before the aerodynamic loads are applied and the hinges function.

Step 3 While the blade is still rotating at its steady-state speed, it is subjected to aerodynamic loadings and as a result, angular displacements in the flap and the lead–lag hinges happen. To simulate this phase of motion, first, the rigid body code is run and the flap and lead–lag solutions are calculated by solving Eqs. (7.99) and (7.102). Then, recalling that for a rigid blade with flap and lag degrees of freedom the angular velocity of the blade is a function of these degrees of freedom as well as the rotor shaft angular velocity,

$$\vec{\omega} = (\Omega\sin\beta\cos\xi)\hat{i} + (\Omega\sin\beta\sin\xi - \dot{\beta})\hat{j} + (\Omega\cos\beta - \dot{\xi})\hat{k} \tag{7.70}$$

the linear and angular velocity components at the root of the elastic blade are calculated. Considering Fig. 7.3, for a lead–lag hinge located at an offset distance eR from the rotation axis (R is the rotor radius), the root boundary conditions for linear and angular velocity components at the steady-state angular velocity Ω_{ss} would be

$$V = \begin{Bmatrix} 0 \\ eR\Omega_{\mathrm{ss}} \\ 0 \end{Bmatrix}, \quad \Omega = \begin{Bmatrix} \Omega_{\mathrm{ss}}\sin\beta\cos\xi \\ \Omega_{\mathrm{ss}}\sin\beta\sin\xi - \dot{\beta} \\ \Omega_{\mathrm{ss}}\cos\beta - \dot{\xi} \end{Bmatrix} \tag{7.108}$$

Having obtained these unknowns and referring to Fig. 2.5, one may apply the solution method discussed in Chap. 5 by using

$$q_1^+ = M_{N-1}^{\mathrm{tot}} \cdot q_N^+ + T_{N-1}^{\mathrm{tot}} \tag{5.21}$$

Substituting the zero force and the zero moment boundary conditions at the tip, i.e., at node, N, into Eq. (5.21) result in

$$\left\{\begin{matrix} F^{+} \\ M^{+} \\ \left\{\begin{matrix} 0 \\ eR\Omega_{\text{ss}} \\ 0 \end{matrix}\right\} \\ \left\{\begin{matrix} \Omega_{\text{ss}}\sin\beta\cos\xi \\ \Omega_{\text{ss}}\sin\beta\sin\xi-\dot{\beta} \\ \Omega_{\text{ss}}\cos\beta-\dot{\xi} \end{matrix}\right\} \\ \left\{\begin{matrix} 0 \\ \mu eR\Omega_{\text{ss}} \\ 0 \end{matrix}\right\} \\ \left\{\begin{matrix} (i_2+i_3)\Omega_{\text{ss}}\sin\beta\cos\xi \\ i_2(\Omega_{\text{ss}}\sin\beta\sin\xi-\dot{\beta}) \\ i_3(\Omega_{\text{ss}}\cos\beta-\dot{\xi}) \end{matrix}\right\} \\ \gamma^{+} \\ \kappa^{+} \end{matrix}\right\}_1 = M_{N-1}^{\text{tot}}\left\{\begin{matrix} 0 \\ 0 \\ V^{+} \\ \Omega^{+} \\ P^{+} \\ H^{+} \\ 0 \\ 0 \end{matrix}\right\}_N + T_{N-1}^{\text{tot}} \tag{7.109}$$

Equation (7.109) should now be solved for the sub-vectors of q_1 and q_N, which include the remaining unknowns at these two nodes. The solution method has been explained in Chap. 5 and is reminded by the following equations:

$$\underbrace{\left\{\begin{matrix} V^{+} \\ \Omega^{+} \\ P^{+} \\ H^{+} \end{matrix}\right\}_1}_{\text{all known}} = M_{N-1}^{\text{tot}}(7:18,7:18)\cdot\underbrace{\left\{\begin{matrix} V^{+} \\ \Omega^{+} \\ P^{+} \\ H^{+} \end{matrix}\right\}_N}_{\text{all unknown}} + T_{N-1}^{\text{tot}}(7:18) \tag{5.28}$$

or

$$\left\{\begin{matrix} V^{+} \\ \Omega^{+} \\ P^{+} \\ H^{+} \end{matrix}\right\}_N = \left[M_{N-1}^{tot}(7:18,7:18)\right]^{-1}.\left(\left\{\begin{matrix} V^{+} \\ \Omega^{+} \\ P^{+} \\ H^{+} \end{matrix}\right\}_1 - T_{N-1}^{\text{tot}}(7:18)\right) \tag{5.29}$$

By solving Eq. (5.29) all of the unknown variables at node N are obtained. Substituting Eq. (5.29) into (7.109) results in the remaining unknown variables at node 1. Having calculated all of the unknown variables at nodes 1 and N, one may use

$$A_i q_i^{+} + B_i q_{i+1}^{+} = J_i; \quad i = 1,\ldots,N-1 \tag{5.19}$$

in order to calculate the unknown variables at all interior nodes, by starting either from node 1 or node N.

7.10.1 Notes on Hinged and Hingeless Boundary Conditions

In determining the boundary conditions, the following notes should be utilized (Hodges (2008)):

1. The boundary conditions at the two ends are independent of each other and do not need to be complements in order to prevent rigid body motions.
2. At either end, one may not specify same components of both Ω and M, or both V and F. So, one cannot apply $M_3 = 0$ because of the hinge and at the same time apply Ω_3 at the root as input.
3. If one sets M_3 (lead–lag) equal to zero at the center of rotation, a zero stiffness condition will be introduced which results in a singular Jacobian. Such a singularity happens even when Ω_1 and Ω_2 at the root were set equal to zero.
4. One should not have M_3 equal to zero at the center of rotation. To this end, one may either introduce a hinge offset for the lead–lag or impose a constraint on it with something like a spring at the center of rotation.

In this section, the foregoing points are going to be discussed in more detail. In the cantilever case, the boundary conditions at the root and at the tip of the blade are complements (constrained Ω and V at the root versus constrained M and F at the tip). In articulated blades, however, the boundary conditions at the root and at the tip are not necessarily complements and there are variables that are not known at either end of the rotor blade. One example of the application of various boundary conditions is Rosen et al. (1991) in which the general case of an isotropic blade with orthogonal flap, lead–lag, and pitch hinges at its root has been discussed. It is assumed that no coupling between the motions about the hinges exists, the three hinges are located at the axis of rotation and the hinge offset values are zero.

In general, at either end of the blade, one may not specify same components of both Ω and M, or both V and F. So, if Ω_3 at the root has been given as an input, one cannot simultaneously apply $M_3 = 0$ at the root due to the lead–lag hinge. A formulation where both of these quantities are given is not valid.

Quantities such as V_3 and M_1 for a blade without pitching should be zero (for en vacuo dynamics where natural frequencies and mode shapes of the blade are studied). This solution is the steady-state solution, and therefore, it is limited to hover. In forward flight, the time-dependent Ω_1 at the root due to cyclic pitch cannot be ignored.

In the case of a lead–lag hinge, $M_3 = 0$ is applicable, but if the hinge has been placed at the axis of rotation (i.e., hinge offset is zero) it corresponds to zero stiffness at the root and a zero lead–lag natural frequency. Such a hinge placement results in a singular Jacobian matrix, an ill-conditioned problem, and an unbounded response. So, a blade pinned in lead–lag at the axis of rotation is an inherently ill-conditioned problem and the lead–lag hinge should not be put at the center of rotation. That is why real blades almost always have a nonzero offset lead–lag hinge. To prevent this problem, one may either give the lead–lag hinge an offset or put a torsional spring at the root to ensure nonzero stiffness.

For a flap hinge (with $M_2 = 0$ boundary condition), always the stiffening effect of rotor shaft rotation on the flapping motion exists; so the flap hinge may be even located at the center of rotation of the blade and it does not require a spring to prevent zero stiffness and ill-conditioning problems (neither hinge offset nor hinge spring is required).

The solution for the elastic blade can be verified by analyzing the resulting moments at the hinge location when the same aerodynamic load and the same hinge motion as the rigid blade are applied on the elastic blade. If the flap and lead–lag motions calculated at the hinge using the rigid body motion code is suitable for the elastic blade too, the moments at the hinge location obtained from the elastic model should be practically zero. Otherwise, application of the flap and lead–lag motions from the rigid body model in the elastic model is not justifiable.

7.11 Case Study: Damped Elastic Articulated Blade in Hover

The isotropic rectangular solid model introduced in Sect. 3.3 is considered here again, but it is modeled as an articulated rotating blade with flap damping. The blade is assumed to have a hinge offset ratio of $e = 0.04$ and a steady-state rotor shaft angular velocity of 100 rad/s. The accelerating part of the motion lasts for 0. 5 s, during which the blade accelerates to full speed.

The second part of the motion lasts for 0.1 s in which the blade continues to rotate at its full speed. Finally, in the last 0.5 s of the motion, while the blade is still rotating at full speed, it is subjected to two moment pulses in flap and lead–lag directions and as a result, angular displacements in the flap and the lead–lag hinges happen. One of the applied moments corresponds to the application of a collective pitch and the second one originates from the drag force in the lead–lag direction. The corresponding equations of motion for the rigid body motion of the blade in flap and lead–lag originate from Eqs. (7.99) and (7.102) and are, respectively,

$$\ddot{\beta} + 89.6\dot{\beta} + (100)^2(1 + 0.0621)\beta - 100(2\dot{\xi}\beta + \dot{\beta}\xi) = 0.0845 \tag{7.110}$$

$$\ddot{\xi} + 0.0617 \times (100)^2\xi + 200\beta\dot{\beta} = 0.0839 \tag{7.111}$$

Here, the flap motion has aerodynamic damping but the lead–lag motion has no mechanical damper. The solution of Eqs. (7.110) and (7.111) has been used in the algorithm discussed in Sect. 7.10 and the complete elasto-dynamic solution of the elastic articulated blade has been obtained and illustrated in Figs. 7.15, 7.16, 7.17, 7.18, 7.19, 7.20, 7.21, 7.22, and 7.23.

The time history variation of the induced bending moment M_3 along the blade is plotted in Fig. 7.15. Figure 7.16 illustrates the flap and lead–lag motions. It is observed that even though these motions are coupled, imposing damping only on the flap motion has negligible effect on the lead–lag motion. The reason is that the coupling happens only by small nonlinear terms.

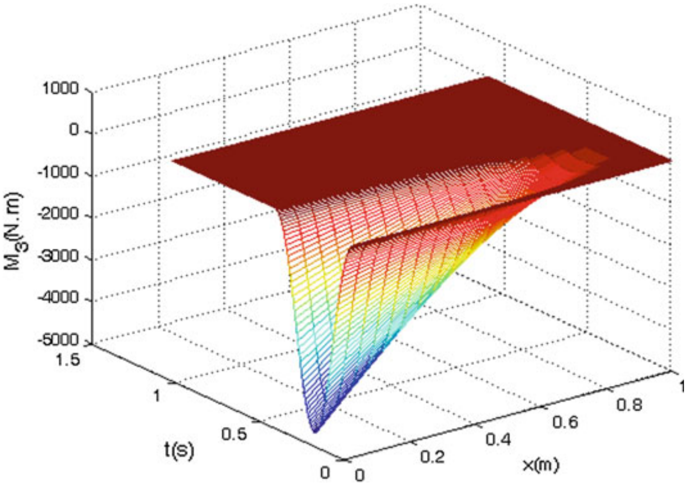

Fig. 7.15 Time history variation of the induced bending moment M_3 along the blade

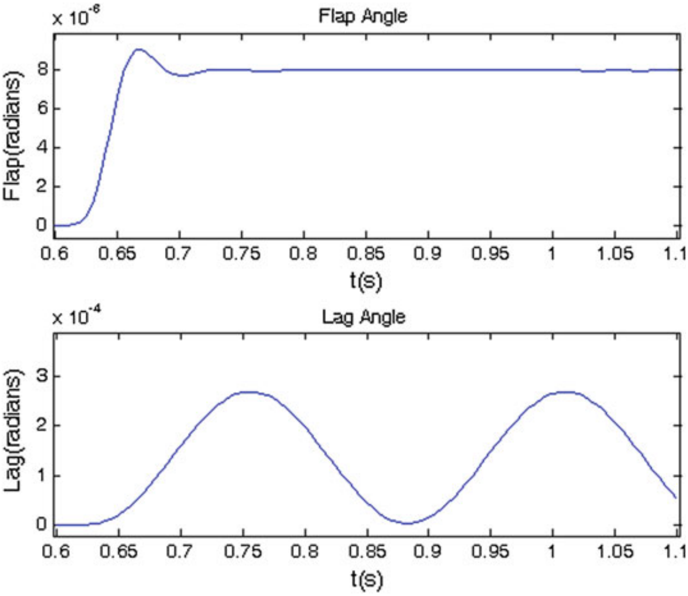

Fig. 7.16 Time history diagrams of lead–lag and flap motions

Variations of the root angular velocity and the resulting root moment are illustrated in Fig. 7.17. As expected, the maximum dynamic moment happens when the angular acceleration of the beam is the greatest. The moment diagrams in Fig. 7.18 illustrate the induced moments at the root of the blade before and after the

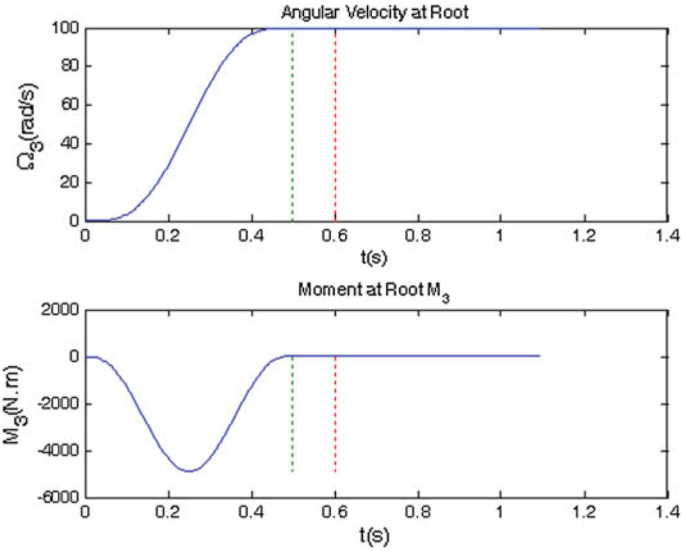

Fig. 7.17 Time history diagrams of the blade angular velocity, Ω_3, and the bending moment induced in the blade, M_3, at the root

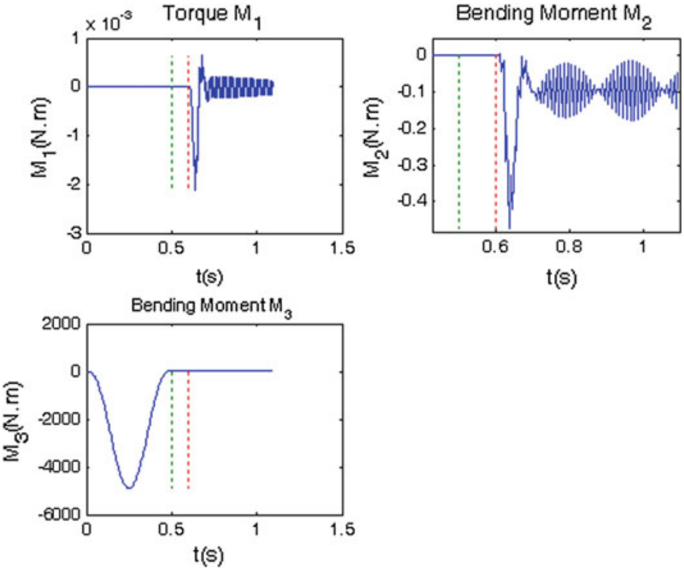

Fig. 7.18 Time history diagrams of the internal moment components of the blade at its root

hinges come into play in the third step of solution. The moment values at the end of the third step are seen to be small and always oscillating around zero as it is expected from a hinge.

The time history diagrams of the induced internal forces at the root of the blade are plotted in Fig. 7.19. It can be observed that the obtained result for F_1 (solid line) is very close to that of the approximate solution given in Eq. (5.35), which is plotted in dashed lines. In Fig. 7.20, the time history diagrams of various components of angular velocity have been illustrated. The convergence of Ω_2 to zero corresponds to the convergence of the flap angle to the constant coning angle in hover. One may compare Figs. 7.16 and 7.20 to see that the flap angle first has a positive slope and then a negative one, but Ω_2 first decreases and then increases. Therefore, their directions of variation are opposite. This observation makes sense because the positive sign conventions for the flap angle and its angular velocity are opposite to that of Ω_2.

The variations of the internal forces, induced moments, and angular velocities along the span of the blade at $t = 0.85$ s (during the third step of solution) are illustrated in Figs. 7.21, 7.22, and 7.23, respectively. In Figs. 7.21 and 7.22, the free boundary conditions at the tip of the beam are observed to have been satisfied, as expected.

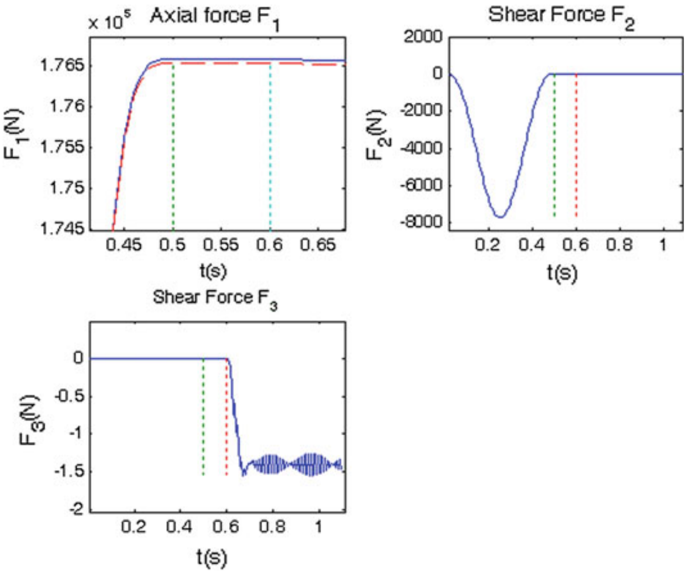

Fig. 7.19 Time history diagrams of internal force components at the root of the blade; present solution (*solid line*), Eq. (5.35) (*dashed line*)

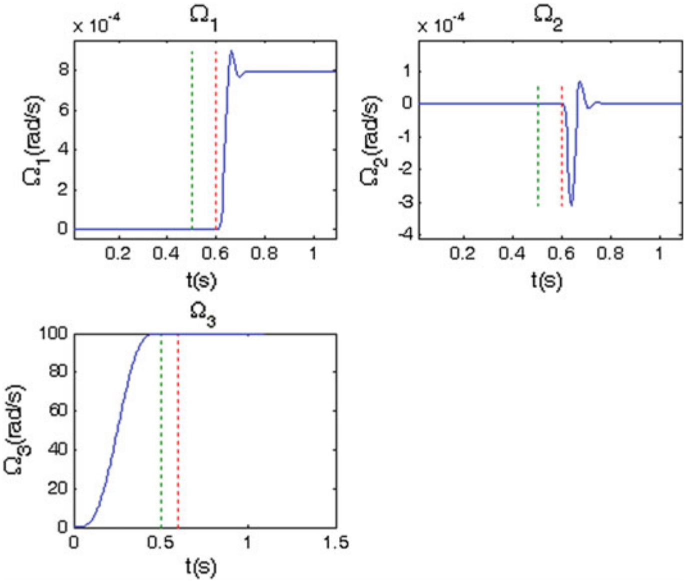

Fig. 7.20 Time history diagrams of angular velocity components of the blade at the root

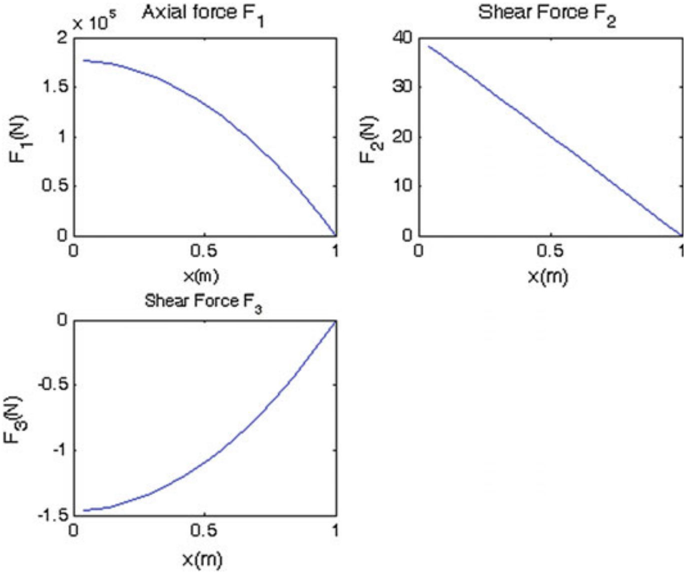

Fig. 7.21 Variation of the internal force components of the blade along its span at $t = 0.85$ s

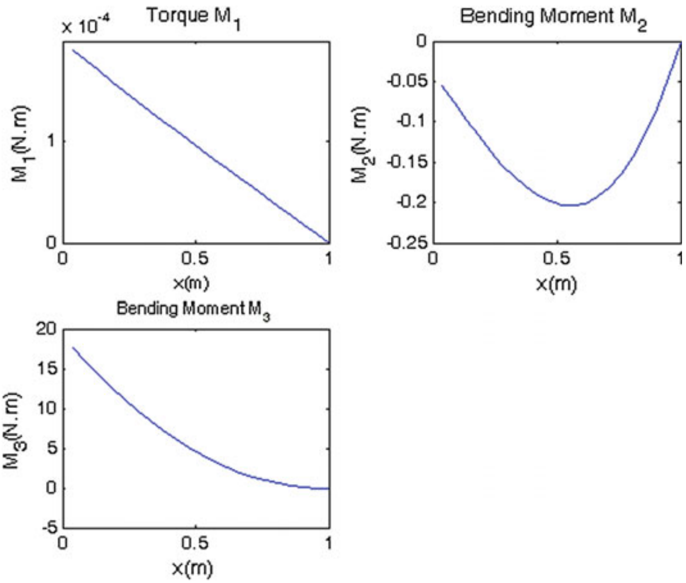

Fig. 7.22 Variation of internal moment components of the blade along its span at $t = 0.85$ s

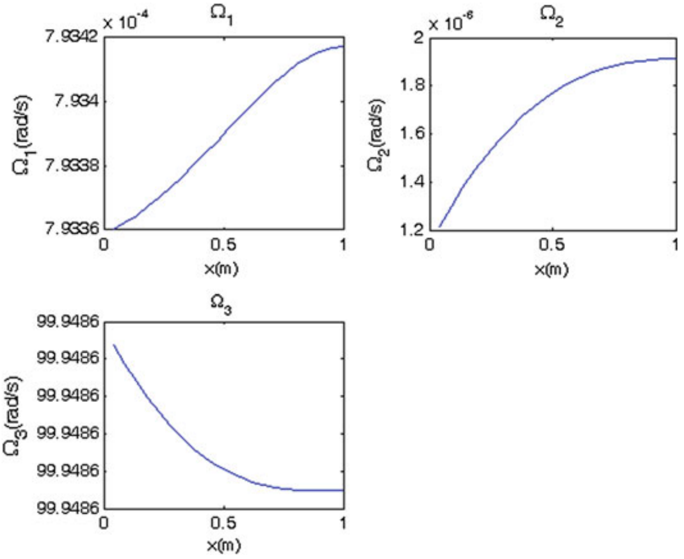

Fig. 7.23 Variation of angular velocity components of the blade along its span at $t = 0.85$ s

7.12 Case Study: Damped Elastic Composite Airfoil

Consider the case of a composite airfoil similar to what is discussed in Cesnik et al. (2003). The UM/VABS input file for this case is among the examples that is provided with the software. The airfoil is NACA 4415, which is a representative cross-sectional shape for high-altitude wings, and of similar basic geometry of rotor blades. It has double cells and a spar located at 38.6 % chord from the leading edge, as it is shown in Fig. 7.24. The centroid is located at $y = 0.3084$ m and $z = 0.06210$ m.

Figure 7.25 illustrates the ply layup definitions and the orientation angles on the section. A passive 0° ply is used to enclose the cross section. The inner layers consist of 90°, +45°, −45° and 0° active plies. So, the stacking order is, [0, +90, +45, −45, 0]. The angles are measured with respect to the longitudinal axis along

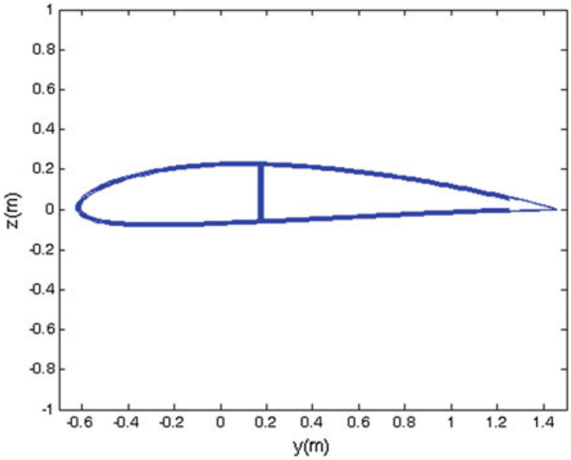

Fig. 7.24 Cross section of the airfoil

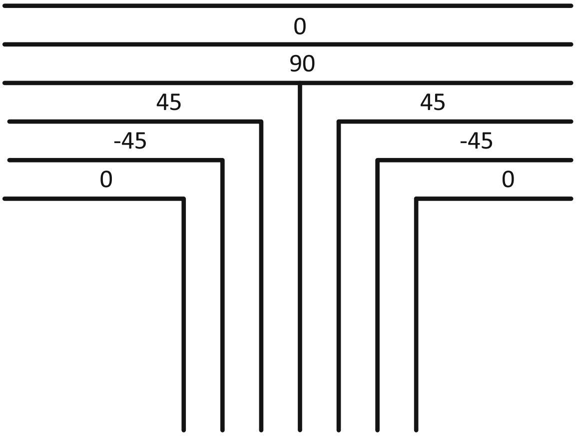

Fig. 7.25 Ply layup and orientation angles of the airfoil cross section

the wingspan. Therefore, the 0° and 90° plies are spanwise and chordwise, respectively. Here, no actuation is imposed. The case of active blades is discussed in Chap. 8.

The properties of the applied passive and active materials are shown in Table 8.4. Using that data and UM/VABS, the stiffness matrix of the cross section has been calculated as

$$S = \begin{bmatrix} 1.12577\times10^{9} & 3.615437\times10^{3} & -1.28217\times10^{4} & -1.64732\times10^{5} & -2.168324\times10^{5} & -5.681057\times10^{6} \\ 3.615437\times10^{3} & 3.15555\times10^{8} & -4.04582\times10^{5} & -1.0509\times10^{7} & 7.05125\times10^{4} & 4.33983\times10^{3} \\ -1.28217\times10^{4} & -4.04582\times10^{5} & 2.79485\times10^{7} & -1.06215\times10^{7} & 5.81197\times10^{2} & 1.08681\times10^{4} \\ -1.64732\times10^{5} & -1.0509\times10^{7} & -1.06215\times10^{7} & 1.75149\times10^{7} & -2.4470\times10^{3} & 2.00316\times10^{3} \\ -2.168324\times10^{5} & 7.05125\times10^{4} & 5.81197\times10^{2} & -2.4470\times10^{3} & 1.39200\times10^{7} & 1.16753\times10^{5} \\ -5.681057\times10^{6} & 4.33983\times10^{3} & 1.08681\times10^{4} & 2.00316\times10^{3} & 1.16753\times10^{5} & 3.3672\times10^{8} \end{bmatrix} \tag{7.112}$$

Other parameters are the full-speed angular velocity of 30 rad/s, a 4 % hinge offset ratio, unit moments applied in the transversal 2 and 3 directions and the cross-sectional inertia matrix,

$$I = \begin{bmatrix} 77.255 & 0 & 0 \\ 0 & 3.1362 & -0.20052 \\ 0 & -0.20052 & 74.119 \end{bmatrix} \times 10^{-2} \tag{7.113}$$

Figures 7.26, 7.27, 7.28, 7.29, 7.30, and 7.31 illustrate the solution for this case and result in conclusions that are similar to those of Sect. 7.11. Time history diagrams of induced moments, internal forces, and angular velocities are illustrated in Figs. 7.28, 7.29, and 7.30, respectively. In Fig. 7.31, the free boundary conditions for internal forces at the tip of the blade are observed to have been satisfied, as expected.

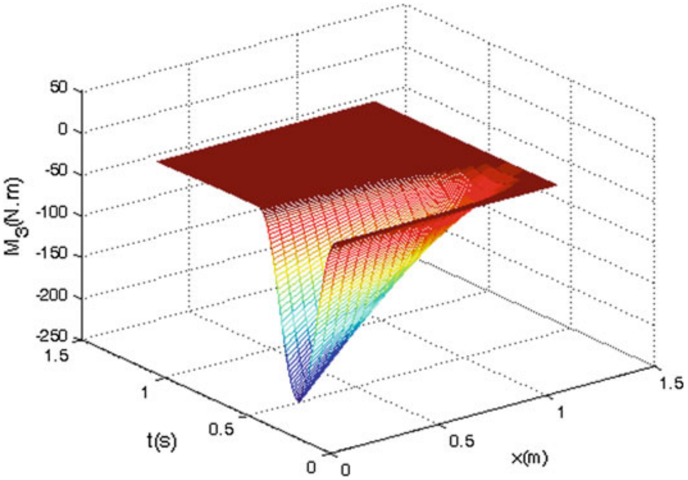

Fig. 7.26 Time history variation of the induced bending moment M_3 along the blade

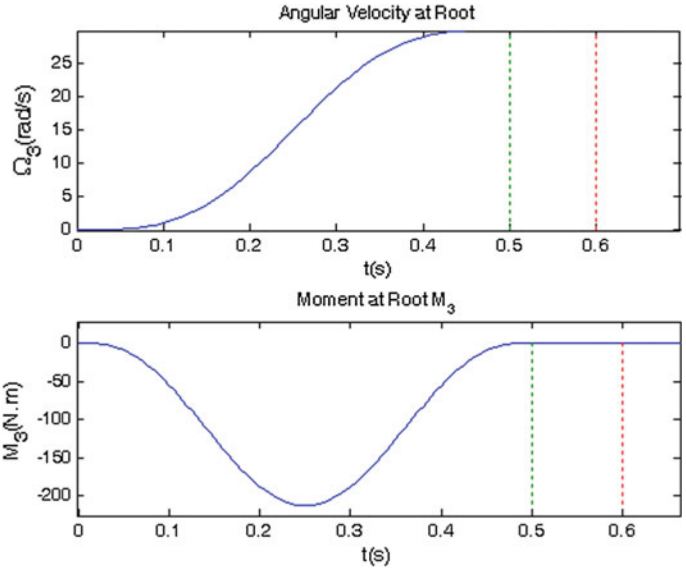

Fig. 7.27 Time history diagrams of the blade angular velocity, Ω_3, and the bending moment induced in the blade, M_3, at the root

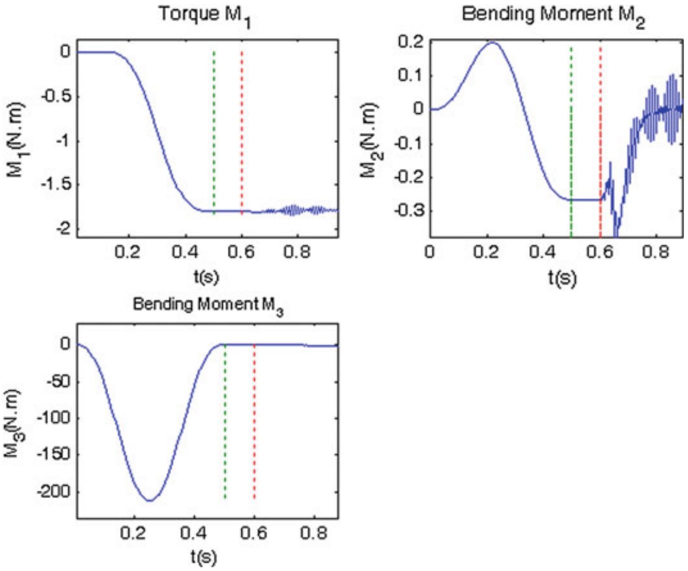

Fig. 7.28 Time history diagrams of the internal moment components of the blade at its root

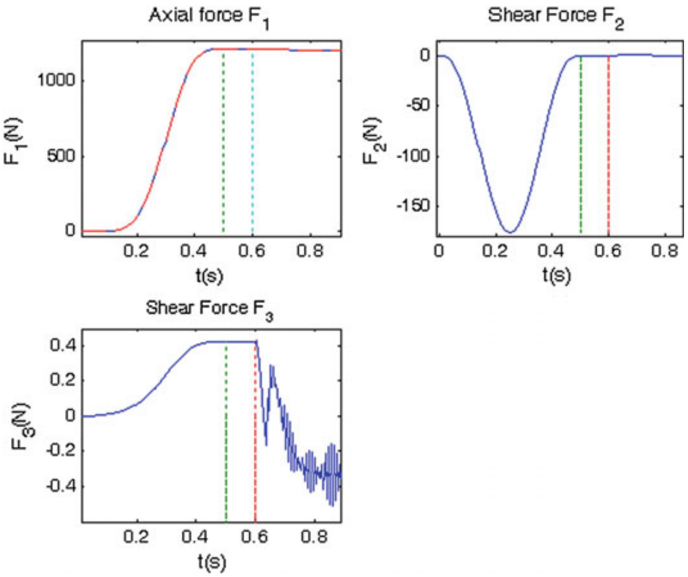

Fig. 7.29 Time history diagrams of internal force components at the root of the blade; present solution (*solid line*), Eq. (5.35) (*dashed line*)

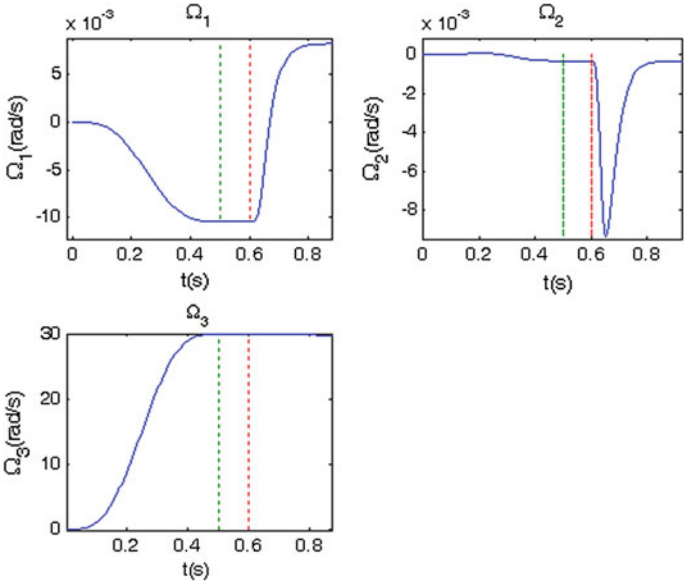

Fig. 7.30 Time history diagrams of angular velocity components of the blade at the root

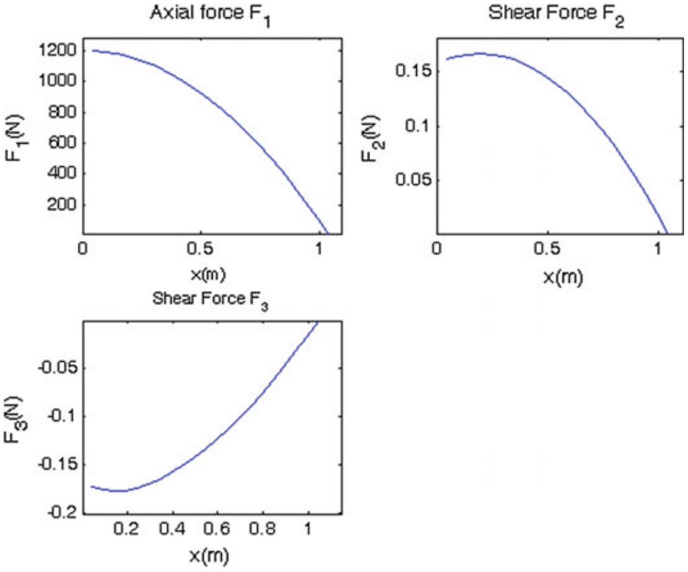

Fig. 7.31 Variation of the internal force components of the blade along its span at $t = 0.85$ s

References

Bramwell, A. R. S., Done, G., & Balmford, D. (2001). *Bramwell's helicopter dynamics* (2nd ed.). New York: AIAA.

Cesnik, C. E. S., Park, R. S., & Palacios, R. (2003). Effective cross-section distribution of anisotropic piezocomposite actuators for wing twist. *Proceedings of SPIE, 5056*, 21–32.

Ghorashi, M. (2009). *Dynamics of elastic nonlinear rotating composite beams with embedded actuators*, Ph.D. Thesis, Mechanical and Aerospace Engineering Department, Carleton University.

Ghorashi, M. (2012). Nonlinear analysis of the dynamics of articulated composite rotor blades. *Nonlinear Dynamics, 67*, 227–249.

Hodges, D. H. (2008). *Personal communications*.

Leishman, J. G. (2006). *Principles of helicopter aerodynamics* (2nd ed.). New York: Cambridge University Press.

Meriam, J. L., & Kraige, L. G. (2003). *Engineering mechanics, dynamics* (5th ed.). New York: John Wiley & Sons, Inc.

Rosen, A., Loewy, R. G., & Mathew, M. B. (1991). Unified treatment for dealing with auxiliary conditions in blade dynamics. *AIAA Journal, 29*(6), 968–976.

Chapter 8
Static and Dynamic Analysis of Beams and Rotor Blades with Embedded Piezocomposite Actuators

8.1 Introduction

A promising method for controlling the response of a rotor blade is by embedding piezocomposite actuators in it. Such actuators are basically composites made of piezoelectric fibers in an epoxy matrix. In this chapter, after a brief introduction of piezoelectric sensors and actuators, the mathematical modeling of such elements is presented and expressed in compressed matrix notation. Then, the intrinsic equations of motion of a beam with embedded piezoelectric elements are presented and solved using VABS for performing the cross-sectional analysis. The solution is applied to the static loading of an active composite box model and an airfoil-shaped beam. The chapter concludes by presenting the steady-state response of an active composite rotor blade with airfoil cross section. Both articulated and hingeless boundary conditions have been considered. In this way, the impact of inclusion of embedded piezocomposite actuators in a beam structure is analyzed. The presented method calculates the response of adaptive rotor blades that embedded actuators can control their geometry in order to achieve an intended performance. The contents of this chapter are mostly based on Ghorashi (2009) and Ghorashi and Nitzsche (2009).

8.2 Conceptual Introduction to Piezoelectric Sensors and Actuators

An intelligent structure includes sensors that monitor and actuators that change its state. Such sensors and actuators can be networked through feedback control to provide robust control of structures. Piezoelectric elements are frequently used to provide the mentioned sensing and actuating capability. A piezoelectric material changes its polarization under stress. Therefore, piezoelectricity is a coupling

M. Ghorashi, *Statics and Rotational Dynamics of Composite Beams*,
DOI 10.1007/978-3-319-14959-2_8

between electrical and mechanical systems. Imposing a mechanical force on a piezoelectric element results in the generation of an electrical field (direct piezoelectric effect also called the generator or the sensor mode). Conversely, application of an electrical field on such an element deforms it (inverse piezoelectric effect, motor, or actuator mode).

Perhaps, the best-known piezoelectric material is lead zirconate titanate (PZT) whose properties vary significantly due to small alterations in the constituent materials. The term PZT, however, is commonly used to refer to piezoelectric materials in general, including those of other compositions (Srinivasan and McFarland 2001).

In its original state, a piezoelectric material (usually a polycrystalline ceramic) has electric dipoles arranged in random directions so there is no net polarization and the ceramic is isotropic. This random orientation can be transformed into a preferred orientation through poling. Poling aligns the dipole domains and gives the piezoelectric material a net polarization. A piezoelectric material has a characteristic Curie temperature, T_c. During poling, the material is heated above its Curie temperature and a strong electric field (1–3 kV/mm) is applied to the part for sometime. As a result, the external field reorients the dipoles in the solid phase material so that a distinct poling direction is developed that is aligned with the applied field. The material is then cooled below its Curie temperature, while the poling field is maintained, with the result that the alignment of the dipoles is permanently fixed and the ceramic retains the polarization after the field is removed. As a result, the polycrystalline material behaves like a single crystalline one, with permanently fixed dipole directions. The piezoelectric material is then said to be poled and it becomes anisotropic.

The response of a poled PZT to an applied electric field is mechanical deformations. In this case, the piezoelectric element behaves as an actuator. The nature of this deformation (whether it is a tensile, compressive, or a shear deformation) depends on the orientation of the applied electric field E with respect to the existing poling direction P of the material. If these two directions are parallel, the PZT will expand or contract but does not distort. If these two directions are not parallel, the PZT would expand and distort at the same time. So both normal and shear strain will be developed. In the case these directions are perpendicular, the PZT will only distort, without expansion or contraction.

Figure 8.1 illustrates the PZT deformations in various cases. Applied electric field E that is parallel and is acting in the same direction as the existing poling direction P results in the increase in thickness in the poling direction (usually shown by z or 3) and contraction in a transversal direction (x or 1) due to the Poisson's effect. Conversely, if P and E are parallel but they have opposite directions, the PZT contracts in the z or 3 direction and it expands in the transversal direction x or 1.

Through the thickness induced strain, that was just mentioned, is used in stack actuators to create displacement in the direction of the stack. These linear actuators have several layers of piezoelectric material that are connected in series mechanically and in parallel electrically. They are characterized by small deflections and high forces. The very small deformations at high electrical voltages (1–10 kV) are disadvantageous for this kind of actuators (Ballas 2007).

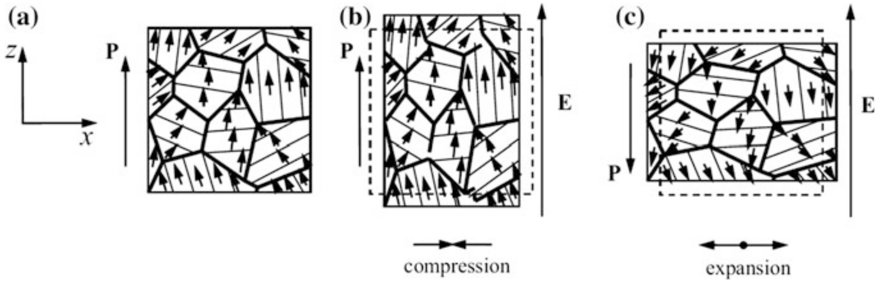

Fig. 8.1 PZT ceramics. **a** Polarized state. **b** Electric field *E* aligned parallel with *P*. **c** Electric field *E* aligned antiparallely with *P*, *dotted lines* illustrate the original geometry of the PZT (Ballas 2007, page 27 © Springer, reprinted with permission)

In unimorph and bimorph PZT benders, deformations along directions transversal to the poling and thickness direction are utilized (the transverse PZT effect). A unimorph bender has an active PZT and a passive elastic layer. In order to increase the deflection of a beam in a bimorph bender, as shown in Fig. 8.2, two active PZT layers are attached on opposite sides of the beam and act in opposite directions. The parallel bimorph shown in Fig. 8.2a has two layers that are electrically connected in parallel and have the same *P* directions. The serial bimorph actuator shown in Fig. 8.2b has two layers that are electrically connected in series and have opposite *P* directions.

In Fig. 8.2a, in the top layer, imposing the electric field *E* opposite to the poling direction *P* reduces the thickness of that layer (in the *z* direction). So the PZT will expand in the transversal direction *x* (i.e., the axial direction of the beam) due to Poisson's effect. The reverse happens in the bottom layer and the PZT will contract in the *x* direction. Since the two layers are constrained by the bond between them, the unimorph will bend. The resulting bending deflection of the beam in the *z* direction is much larger than the induced transversal PZT deformation along the *x* direction, and it can happen at relatively low voltages (24–200 V) (Ballas 2007).

Fig. 8.2 Bimorph piezoceramic actuator subjected to an electric voltage. **a** Parallel bimorph. **b** Serial bimorph (Ballas 2007, page 28 © Springer, reprinted with permission)

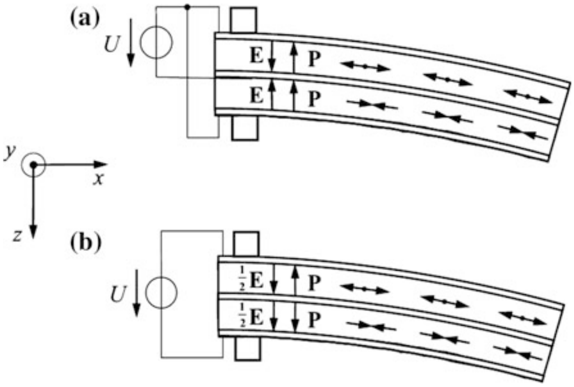

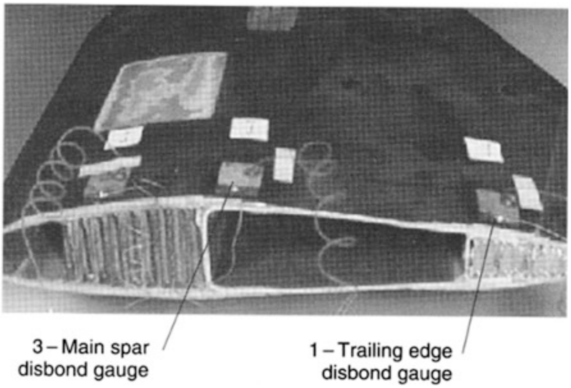

Fig. 8.3 Electromechanical impedance sensors were placed on a rear rotor blade section in critical areas to detect delamination between the adhesively bonded structural elements (Giurgiutiu 2008, page 406 © Academic Press, reprinted with permission)

Furthermore, since free induced strain is analogous to free thermal strain, the way a bimorph acts would be comparable to a bimetallic thermostat. In both cases, a normal strain causes a moment that bends the beam.

In the sensor mode of operation, forces and deformations generate electric charge that appears on the electrodes of PZT. If the electrodes are not short-circuited, a voltage is developed between the surfaces that is used to measure the applied deformation. In the actuator mode, the PZT elements have the ability to impose shape control. An example is a smart wing, which is capable of changing its geometry under certain flight conditions. In order to maximize a PZT's effectiveness for a particular mode, the center location of the PZT should be placed on an antinode for that mode.

Another application of PZT elements is in Structural Health Monitoring (SHM). Figure 8.3 illustrates the use of piezoelectric-wafer active sensors (PWAS) in Apache 64H helicopter rotor blades. These blades have a built-up construction consisting of preformed sheet metal members adhesively bonded with high-performance structural adhesive. In-service experience with these blades has shown disbands between the structural elements appearing because of in-flight vibrations.

An impedance analyzer is used to measure the electromechanical impedance of PWAS transducers. The variations of the real part of the impedance spectrum versus frequency are recorded at the sensors. Changes in the frequency response are indicators of structural changes like delamination.

8.3 Mathematical Modeling of Piezoelectric Sensors and Actuators

In the linear range of operation of piezoelectric materials, their constitutive equations can be described by the following tensorial equations (Giurgiutiu 2008),

$$S_{ij} = s^E_{ijkl} T_{kl} + d_{kij} E_k + \delta_{ij} \alpha^E \theta \quad i,j,k,l = 1,2,3 \tag{8.1}$$

$$D_i = d_{ikl} T_{kl} + \varepsilon^T_{ik} E_k + \widetilde{D}_i \theta \quad i,k,l = 1,2,3 \tag{8.2}$$

where the Einstein summation convention for repeated tensor indices is used (Knowles 1997). In Eqs. (8.1) and (8.2), S_{ij} and T_{kl} are the strain and stress (N/m^2), respectively. Variables E_k and D_i are the electric field intensity (V/m) and electric displacement (charge per unit area, C/m^2), and θ is the temperature (°C). The coefficient s_{ijkl} is a compliance (strain per unit stress, m^2/N). The piezoelectric coefficients d_{ikl} and d_{kij} (in C/N or m/V) represent the coupling between the electrical and the mechanical variables, i.e., the charge per unit stress (PZT charge coefficient) and the strain per unit electric field, respectively. The term δ_{ij} is the Kronecker delta, ($\delta_{ij} = 1$ if $i = j$; zero otherwise). The coefficient α is the coefficient of thermal expansion, (°C^{-1}), ε_{ik} is the permittivity (measured in F/m), and $\tilde{D}_i$ is the electric displacement temperature coefficient (°C^{-1}m^{-2}C).

Equation (8.1) is the actuation equation and it is used to predict how much strain is induced at a given stress, electric field, and temperature. Equations (8.1) and (8.2) can be replaced by the following equivalent set of equations to demonstrate piezoelectric sensor design and to predict how much electric field intensity will be generated by a given state of stress, electric displacement, and temperature (Giurgiutiu 2008).

$$S_{ij} = s^D_{ijkl} T_{kl} + g_{kij} D_k + \delta_{ij} \alpha^D \theta \tag{8.3}$$

$$E_i = g_{ikl} T_{kl} + \beta^T_{ik} D_k + \tilde{E}_i \theta \tag{8.4}$$

Equation (8.4) predicts how much electric field intensity is generated by squeezing the piezoelectric material (direct piezoelectric effect). The coefficient g_{ikl} is the piezoelectric voltage coefficient, and it represents how much electric field is induced per unit stress. The coefficient $\tilde{E}_i$ is the pyroelectric voltage coefficient, and it represents how much electric field intensity is induced per unit temperature change (Giurgiutiu 2008).

In Eqs. (8.1)–(8.4), the superscripts T, D, and E are used to show that the quantities are measured at zero stress ($T = 0$), zero electric displacement ($D = 0$), or zero electric field ($E = 0$), respectively. In practice, the zero electric displacement condition corresponds to open circuit (zero current across electrodes), whereas the zero electric field corresponds to closed circuit (zero voltage across electrodes).

As a convention, the orthogonal Cartesian axes 1, 2, and 3 (analogous to x, y, and z) are usually assigned to a piezoelectric element with the 3 or z direction being the thickness and the poling direction. Often, the polarization vector is shown on the manufacturer's data sheets.

8.4 Piezoelectric Equations in Compressed Matrix Notations

In a 2-D problem involving an elastic isotropic material, the compliance matrix can be used to relate stress and strain components to each other,

$$\begin{Bmatrix} \varepsilon_x \\ \varepsilon_y \\ \gamma_{xy} \end{Bmatrix} = \begin{bmatrix} \frac{1}{E} & -\frac{\nu}{E} & 0 \\ -\frac{\nu}{E} & \frac{1}{E} & 0 \\ 0 & 0 & \frac{1}{G} \end{bmatrix} \begin{Bmatrix} \sigma_x \\ \sigma_y \\ \tau_{xy} \end{Bmatrix} \tag{8.5}$$

where $G = \dfrac{E}{2(1+\nu)}$. If the material is orthotropic and it is loaded along its principal material directions 1 and 2, the stress–strain relation can be expressed as follows:

$$\begin{Bmatrix} \varepsilon_1 \\ \varepsilon_2 \\ \gamma_{12} \end{Bmatrix} = \begin{bmatrix} \frac{1}{E_1} & -\frac{\nu_{21}}{E_2} & 0 \\ -\frac{\nu_{12}}{E_1} & \frac{1}{E_2} & 0 \\ 0 & 0 & \frac{1}{G_{12}} \end{bmatrix} \begin{Bmatrix} \sigma_1 \\ \sigma_2 \\ \tau_{12} \end{Bmatrix} \tag{8.6}$$

where due to the symmetry of the compliance matrix,

$$\frac{\nu_{12}}{E_1} = \frac{\nu_{21}}{E_2} \tag{8.7}$$

In the case of a 3-D orthotropic material loaded along its principal material directions 1, 2, and 3, the stress–strain relation can be expressed as follows:

$$\begin{Bmatrix} \varepsilon_1 \\ \varepsilon_2 \\ \varepsilon_3 \\ \gamma_{23} \\ \gamma_{13} \\ \gamma_{12} \end{Bmatrix} = \begin{bmatrix} \frac{1}{E_1} & -\frac{\nu_{21}}{E_2} & -\frac{\nu_{31}}{E_3} & 0 & 0 & 0 \\ -\frac{\nu_{12}}{E_1} & \frac{1}{E_2} & -\frac{\nu_{32}}{E_3} & 0 & 0 & 0 \\ -\frac{\nu_{13}}{E_1} & -\frac{\nu_{23}}{E_2} & \frac{1}{E_3} & 0 & 0 & 0 \\ 0 & 0 & 0 & \frac{1}{G_{23}} & 0 & 0 \\ 0 & 0 & 0 & 0 & \frac{1}{G_{13}} & 0 \\ 0 & 0 & 0 & 0 & 0 & \frac{1}{G_{12}} \end{bmatrix} \begin{Bmatrix} \sigma_1 \\ \sigma_2 \\ \sigma_3 \\ \tau_{23} \\ \tau_{13} \\ \tau_{12} \end{Bmatrix} \tag{8.8}$$

The symmetry of the compliance matrix results in

$$\frac{\nu_{21}}{E_2} = \frac{\nu_{12}}{E_1}, \quad \frac{\nu_{31}}{E_3} = \frac{\nu_{13}}{E_1}, \quad \frac{\nu_{32}}{E_3} = \frac{\nu_{23}}{E_2} \tag{8.9}$$

Table 8.1 Conversion of indices from tensor to compressed matrix (Voigt) notation

Tensor (*ij* or *kl*)	Compressed matrix (*p* or *q*)
11	1
22	2
33	3
23 or 32	4
31 or 13	5
12 or 21	6

In Eq. (8.8), the 3 × 3 second-order stress and strain tensors T_{ij} and S_{ij} are replaced by 6-element-long column vectors. One may express these vectors as T_p and S_p, $p = 1, 2, 3, 4, 5, 6$. The 3 × 3 × 3 × 3 fourth-order compliance tensor s^E_{ijkl} is replaced by the 6 × 6 compliance matrix, s^E_{pq}. In general, using this alternative representation, the tensor notation is replaced by the compressed matrix (Voigt) notation. This compressed notation consists of replacing *ij* or *kl* by *p* or *q* where, $i, j, k, l = 1, 2, 3$ and $p, q = 1, 2, 3, 4, 5, 6$ according to Table 8.1.

In the compressed matrix notation, subscripts 1, 2, and 3 indicate the principal axes and 4, 5, and 6 denote shear around axes 1, 2, and 3, respectively. Similar transformations can be done on piezoelectric Eqs. (8.1) and (8.2). In these equations, piezoelectric coefficients d_{ikl} and d_{kij} are used to express the constitutive equations in tensorial form. In the compressed matrix notation, the 3 × 3 × 3 third-order piezoelectric tensor d_{ijk} is replaced by the 3 × 6 piezoelectric matrix of elements, d_{ip}.

The piezoelectric matrix elements have a clear physical meaning. For actuators and for given indices *i* and *j*, the piezoelectric modulus d_{ij} is defined as the ratio of normal strain in the *j* direction to the applied electric field intensity in the *i* direction (perpendicular to the electrodes). So,

$$S_3 = d_{33}E_3, \quad S_1 = S_2 = d_{31}E_3, \quad S_5 = d_{35}E_3, \quad E_3 = \frac{V}{t} \tag{8.10}$$

where V is the applied voltage and t is the thickness of the specimen, both in the 3 directions.

While stack actuators rely on the d_{33} or out of plane induced strain, benders like unimorphs and bimorphs rely on the d_{31} or the in-plane induced strain. Due to the Poisson's effect, clearly if $d_{33} > 0$, then $d_{31} < 0$. For shear strain, d_{35} indicates that the electrodes are perpendicular to the 3 axis and that the PZT-induced strain is shear around the 2 directions (i.e., on the 1-3 plane).

For sensor applications, the piezoelectric moduli d_{ij} can be defined as the ratio of the short circuit charge density over applied stress. In both actuator and sensor applications, materials with large *d* constants are desirable. This constant is the best single measurement of the strength of piezoelectric effect. The relationships between the tensorial and the compressed matrix forms of representations are as follows (Giurgiutiu 2008).

1. For the second-order tensors of stress and strain,

$$
\begin{aligned}
&T_{\mathrm{p}} = T_{\mathrm{ij}} \quad p = 1,2,3,4,5,6 \quad \text{whereas } i,j = 1,2,3\\
&S_p = S_{ij} \quad i = j, p = 1,2,3 \quad \text{whereas } i,j = 1,2,3\\
&S_p = 2S_{ij} \quad i \neq j, p = 4,5,6 \quad \text{whereas } i,j = 1,2,3
\end{aligned}
$$

So,

$$
\left\{\begin{matrix} S_1 \\ S_2 \\ S_3 \\ \frac{1}{2}S_4 \\ \frac{1}{2}S_5 \\ \frac{1}{2}S_6 \end{matrix}\right\} = \left\{\begin{matrix} S_{11} \\ S_{22} \\ S_{33} \\ S_{23} \\ S_{31} \\ S_{12} \end{matrix}\right\}, \quad \left\{\begin{matrix} T_1 \\ T_2 \\ T_3 \\ T_4 \\ T_5 \\ T_6 \end{matrix}\right\} = \left\{\begin{matrix} T_{11} \\ T_{22} \\ T_{33} \\ T_{23} \\ T_{31} \\ T_{12} \end{matrix}\right\} \tag{8.11}
$$

The factor of two in the strain equation relates to a factor of two in the definition of shear strains in the tensor and matrix formulation.

2. For third-order tensor of charge coefficient, d_{ijk},

$$d_{iq} = d_{ikl} \quad k = l,\ q = 1,2,3 \quad \text{whereas } i,k,l = 1,2,3 \tag{8.12}$$

$$d_{iq} = 2d_{ikl} \quad k \neq l,\ q = 4,5,6 \quad \text{whereas } i,k,l = 1,2,3 \tag{8.13}$$

3. For the fourth-order tensor of compliance, s_{ijkl},

$$s^E_{pq} = s^E_{ijkl} \quad i = j,\ k = l,\ p,q = 1,2,3 \quad \text{whereas } i,j,k,l = 1,2,3 \tag{8.14}$$

$$s^E_{pq} = 2s^E_{ijkl} \quad i = j,\ k \neq l,\ p = 1,2,3,\ q = 4,5,6 \quad \text{whereas } i,j,k,l = 1,2,3 \tag{8.15}$$

$$s^E_{pq} = 4s^E_{ijkl} \quad i \neq j,\ k \neq l,\ p,q = 4,5,6 \quad \text{whereas } i,j,k,l = 1,2,3 \tag{8.16}$$

The compressed matrix notations have the advantage of brevity, and they are commonly used in engineering applications. The values of the elastic and piezoelectric constants given by the active material manufacturers in their product specifications are given in compressed matrix notations. Using compressed matrix notation, the PZT tensor Eqs. (8.1) and (8.2) can be rewritten in the following matrix form,

$$S_p = s^E_{pq}T_q + d_{kp}E_k + \delta_{pk}\alpha^E_k\theta \quad p,q = 1,2,3,4,5,6; \quad k = 1,2,3 \tag{8.17}$$

$$D_i = d_{iq}T_q + \varepsilon^T_{ik}E_k + \tilde{D}_i\theta \quad q = 1,2,3,4,5,6; \quad i,k = 1,2,3 \tag{8.18}$$

which can be expanded as follows:

$$\begin{Bmatrix} S_1 \\ S_2 \\ S_3 \\ S_4 \\ S_5 \\ S_6 \end{Bmatrix} = \begin{bmatrix} s_{11} & s_{12} & s_{13} & 0 & 0 & 0 \\ s_{21} & s_{22} & s_{23} & 0 & 0 & 0 \\ s_{31} & s_{32} & s_{33} & 0 & 0 & 0 \\ 0 & 0 & 0 & s_{44} & 0 & 0 \\ 0 & 0 & 0 & 0 & s_{55} & 0 \\ 0 & 0 & 0 & 0 & 0 & s_{66} \end{bmatrix} \begin{Bmatrix} T_1 \\ T_2 \\ T_3 \\ T_4 \\ T_5 \\ T_6 \end{Bmatrix} + \begin{bmatrix} d_{11} & d_{21} & d_{31} \\ d_{12} & d_{22} & d_{32} \\ d_{13} & d_{23} & d_{33} \\ d_{14} & d_{24} & d_{34} \\ d_{15} & d_{25} & d_{35} \\ d_{16} & d_{26} & d_{36} \end{bmatrix} \begin{Bmatrix} E_1 \\ E_2 \\ E_3 \end{Bmatrix} + \begin{Bmatrix} \alpha_1 \\ \alpha_2 \\ \alpha_3 \\ 0 \\ 0 \\ 0 \end{Bmatrix} \theta \tag{8.19}$$

$$\begin{Bmatrix} D_1 \\ D_2 \\ D_3 \end{Bmatrix} = \begin{bmatrix} d_{11} & d_{12} & d_{13} & d_{14} & d_{15} & d_{16} \\ d_{21} & d_{22} & d_{23} & d_{24} & d_{25} & d_{26} \\ d_{31} & d_{32} & d_{33} & d_{34} & d_{35} & d_{36} \end{bmatrix} \begin{Bmatrix} T_1 \\ T_2 \\ T_3 \\ T_4 \\ T_5 \\ T_6 \end{Bmatrix} + \begin{bmatrix} \varepsilon_{11} & \varepsilon_{12} & \varepsilon_{13} \\ \varepsilon_{21} & \varepsilon_{22} & \varepsilon_{23} \\ \varepsilon_{31} & \varepsilon_{32} & \varepsilon_{33} \end{bmatrix} \begin{Bmatrix} E_1 \\ E_2 \\ E_3 \end{Bmatrix} + \begin{Bmatrix} \tilde{D}_1 \\ \tilde{D}_2 \\ \tilde{D}_3 \end{Bmatrix} \theta \tag{8.20}$$

As it has been seen so far, because of the anisotropic nature of piezoelectric materials, their properties are dependent on direction. Showing the poling direction by the 3 axes, if the piezoelectric material has transverse isotropy, material properties along the 1 and 2 axes would be identical. Thus, for simplicity, usually only the 3 and the 1 directions are mentioned and it is understood that 1 also implies 2. As a result, $d_{24} = d_{15}$ and $d_{31} = d_{32}$. Hence, Eqs. (8.19) and (8.20), for piezoelectric materials with transverse isotropy and pole axis 3, become,

$$\begin{Bmatrix} S_1 \\ S_2 \\ S_3 \\ S_4 \\ S_5 \\ S_6 \end{Bmatrix} = \begin{bmatrix} s_{11} & s_{12} & s_{13} & 0 & 0 & 0 \\ s_{12} & s_{22} & s_{23} & 0 & 0 & 0 \\ s_{13} & s_{23} & s_{33} & 0 & 0 & 0 \\ 0 & 0 & 0 & s_{44} & 0 & 0 \\ 0 & 0 & 0 & 0 & s_{55} & 0 \\ 0 & 0 & 0 & 0 & 0 & s_{66} \end{bmatrix} \begin{Bmatrix} T_1 \\ T_2 \\ T_3 \\ T_4 \\ T_5 \\ T_6 \end{Bmatrix} + \begin{bmatrix} 0 & 0 & d_{31} \\ 0 & 0 & d_{31} \\ 0 & 0 & d_{33} \\ 0 & d_{15} & 0 \\ d_{15} & 0 & 0 \\ 0 & 0 & 0 \end{bmatrix} \begin{Bmatrix} E_1 \\ E_2 \\ E_3 \end{Bmatrix} + \begin{Bmatrix} \alpha_1 \\ \alpha_2 \\ \alpha_3 \\ 0 \\ 0 \\ 0 \end{Bmatrix} \theta \tag{8.21}$$

$$\begin{Bmatrix} D_1 \\ D_2 \\ D_3 \end{Bmatrix} = \begin{bmatrix} 0 & 0 & 0 & 0 & d_{15} & 0 \\ 0 & 0 & 0 & d_{15} & 0 & 0 \\ d_{31} & d_{31} & d_{33} & 0 & 0 & 0 \end{bmatrix} \begin{Bmatrix} T_1 \\ T_2 \\ T_3 \\ T_4 \\ T_5 \\ T_6 \end{Bmatrix} + \begin{bmatrix} \varepsilon_{11} & 0 & 0 \\ 0 & \varepsilon_{22} & 0 \\ 0 & 0 & \varepsilon_{33} \end{bmatrix} \begin{Bmatrix} E_1 \\ E_2 \\ E_3 \end{Bmatrix} + \begin{Bmatrix} \tilde{D}_1 \\ \tilde{D}_2 \\ \tilde{D}_3 \end{Bmatrix} \theta \tag{8.22}$$

or in short,

$$\{S\} = [s]\{T\} + [d]^t\{E\} + \{\alpha\}\theta \tag{8.23}$$

$$\{D\} = [d]\{T\} + [\varepsilon]\{E\} + \{\tilde{D}\}\theta \tag{8.24}$$

Equations similar to (8.23) and (8.24) have been presented in Giurgiutiu (2008), for other constitutive equations as well.

8.5 The 1-D Beam Formulation with Embedded Piezoelectric Element

With actuators embedded in the structure, the whole applied force and moment vectors per unit length on the structure, at every location and every time, can be written as the summation of a mechanically applied load and a load that is imposed by the actuators. So,

$$\begin{Bmatrix} f \\ m \end{Bmatrix} = \begin{Bmatrix} f_M \\ m_M \end{Bmatrix} + \begin{Bmatrix} f_A \\ m_A \end{Bmatrix} \tag{8.25}$$

For a certain actuation scenario, UM/VABS can be used to provide the unit vectors of actuator forces and moments for each active material used in Eqs. (8.25). Then, the whole actuator forces and moments are obtained by multiplying each of the unit forces and moments by the corresponding electric field intensity and then adding up all of these terms together. Substitution of Eq. (8.25) into Eqs. (2.26) and (2.27) gives

$$F' + \tilde{K}F + (f_M + f_A) = \dot{P} + \tilde{\Omega}P \tag{8.26}$$

$$M' + \tilde{K}M + (\tilde{e}_1 + \tilde{\gamma})F + (m_M + m_A) = \dot{H} + \tilde{\Omega}H + \tilde{V}P \tag{8.27}$$

The following linear static equilibrium equations can be obtained from Eqs. (8.26) and (8.27) by ignoring initial curvature and assuming that all nonlinear terms are negligible.

$$F' + (f_M + f_A) = 0 \tag{8.28}$$

$$M' + \tilde{e}_1 F + (m_M + m_A) = 0 \tag{8.29}$$

by using,

$$\tilde{e}_1 = \begin{bmatrix} 0 & 0 & 0 \\ 0 & 0 & -1 \\ 0 & 1 & 0 \end{bmatrix} \tag{8.30}$$

Equations (8.28) and (8.29) can be expanded as follows:

$$F_1' + f_{M1} + f_{A1} = 0 \tag{8.31}$$

$$F_2' + f_{M2} + f_{A2} = 0 \tag{8.32}$$

$$F_3' + f_{M3} + f_{A3} = 0 \tag{8.33}$$

$$M_1' + m_{M1} + m_{A1} = 0 \tag{8.34}$$

$$M_2' - F_3 + m_{M2} + m_{A2} = 0 \tag{8.35}$$

$$M_3' + F_2 + m_{M3} + m_{A3} = 0 \tag{8.36}$$

8.6 Case Study: Static Active Composite Box Model

Consider the composite box model discussed in Sect. 3.4, but having a length of L = 0.5 m. This time active plies of the box are activated and two cases are considered. The first one is bending deformation obtained by imposing the left-hand side of the box to −2 kV and its right-hand side to +2 kV. In this case, the expansion of one side and contraction of the other result in a bending deformation. The second one is when both active sides are subjected to +2 kV that twists the box.

The actuation forces for the bending and twist actuations were calculated by UM/VABS and are listed in Tables 8.2 and 8.3, respectively. The results have also been compared with the ones presented in Cesnik and Palacios (2003) which are also based on using UM/VABS. As expected, the two sets of results are close.

The last step is to calculate the amount of deflections at the tip of the beam due to an actuation. For the case of twist actuation, using Eqs. (8.31) and (8.34), as well as Table 8.3, one obtaines

$$F_1' + 16.860 = 0 \tag{8.37}$$

$$M_1' + 3.518 = 0 \tag{8.38}$$

Table 8.2 Actuation force and moment in bending actuation

	UM/VABS	Cesnik and Palacios (2003)
f_3 (N/m)	227.98	232.67
m_3 (N.m/m)	−1.231	−1.283

Table 8.3 Actuation force and moment in twist actuation

	UM/VABS	Cesnik and Palacios (2003)
f_1 (N/m)	16.860	17.219
m_1 (N.m/m)	3.518	3.666

Integration results in,

$$F_1 = -16.86x_1 + C_1 \tag{8.39}$$

$$M_1 = -3.518x_1 + C_2 \tag{8.40}$$

To satisfy the free boundary conditions at $x_1 = 0.5$ m, i.e., at the free end of the beam, the integration constants should be

$$C_1 = 8.43, C_2 = 1.759 \tag{8.41}$$

Substituting these constants into Eqs. (8.39) and (8.40), the force and moment distributions are obtained as follows

$$F_1 = -16.86x_1 + 8.43 \tag{8.42}$$

$$M_1 = -3.518x_1 + 1.759 \tag{8.43}$$

Using Eqs. (8.42) and (8.43), at the clamped end, i.e., at $x_1 = 0$, one obtains the following reactions as a result of activating the actuators,

$$\begin{aligned} F_{1A} &= 8.43\text{N} \\ M_{1A} &= 1.759\text{N.m} \end{aligned} \tag{8.44}$$

Therefore, the maximum tensile force and twisting moment happen at the clamped end, and they decrease to zero at the free end of the beam. In order to calculate the total twist angle at the free end, one may apply the constitutive equation (2.56) together with the stiffness matrix (3.51) and the actuator induced force and moment values in Eq. (8.44) to get $\kappa_1 = 0.042$ rad/m. Using this outcome in Eq. (3.14) with zero undeformed (initial) curvature and twist, k, results in,

$$\theta_1 = 0.042x \tag{8.45}$$

Consequently, the twist angle at the free end, using $L = 0.5$ m, would be 1.209°. This value is close to 1.195° that is given in Cesnik and Palacios (2003).

8.7 Case Study: Static Active Composite Airfoil

Consider the composite airfoil discussed in Cesnik et al. (2003) and in Sect. 7.12, but this time the activation of the piezocomposite actuators embedded in it is going to be investigated. The properties of the passive and active materials used in the airfoil are shown in Table 8.4.

Table 8.4 Material properties of active composite airfoil (Cesnik et al. 2003)

	E_{11} GPa	E_{22} GPa	E_{33} GPa	G_{12} GPa	G_{13} GPa	G_{23} GPa	ν_{12}	ν_{13}	ν_{23}	ρ kg/m^3	d_{11} pm/V	d_{12} pm/V	d_{13} pm/V
Passive	19.3	9.8	9.8	5.5	5.5	4.4	0.35	0.35	0.496	1716	–	–	–
Active										4060	310	−130	−130

Table 8.5 Actuation forces and moments generated by active plies at various directions

	0° ply actuation	90° ply actuation	±45° plies actuation	All together
Extension (N/m)	71,042	−21,653	49,705	99,095
Shear f_2 (N/m)	0.603	5.089	2.658	8.349
Shear f_3 (N/m)	1.095	19.705	−16.799	4.002
Twist (N.m/m)	−0.288	15.67	−238.13	−222.746
Bending m_2 (N.m/m)	−41.44	15.19	−33.03	−59.28
Bending m_3 (N.m/m)	454.29	−409.01	575.276	620.557

Glass/epoxy is chosen as the passive material, and a hypothetical anisotropic piezocomposite material is selected with the same passive properties as the glass/epoxy, except for the different mass density and piezoelectric constants. The spar has no active layers, and each material layer has a thickness of 3429 μm. A constant electric potential of +1 kV between the two electrodes at a distance of 1100 μm is applied to the piezoelectric actuators.

Using UM/VABS, forces, moments, and stress components generated as a result of activating the plies at various directions are calculated and the results are listed in Table 8.5. A review of these results confirms that, as expected, the activation of the 0° spanwise ply and the ±45° plies generate maximum longitudinal force, F_1, and twisting, respectively. Furthermore, activation of the chordwise 90° ply results in negative extension due to Poisson's effect. It can also be observed that actuators aligned with the chord or span directions can generate twisting deformation through extension–twist and shear–twist couplings, as indicated by the existence of off-diagonal elements in the stiffness matrix.

In the forthcoming figures, in order to show the details of stress distributions more clearly, the original cross section shown in Fig. 7.24 has been stretched as it is illustrated in Fig. 8.4. Figures 8.5, 8.6, 8.7, 8.8, 8.9, and 8.10 illustrate the distribution of various stress components across the cross section when only the 90° plies are activated by the +1 kV excitation. The figures show high stresses in the 90° plies due to their actuation. They also illustrate the existence of stress concentration where the spar is connected to the rest of the airfoil or wherever sudden changes in geometry happen. The distributions of various stress components due to the actuation of all plies by +1 kV are depicted in Figs. 8.11, 8.12, 8.13, 8.14, 8.15, and 8.16.

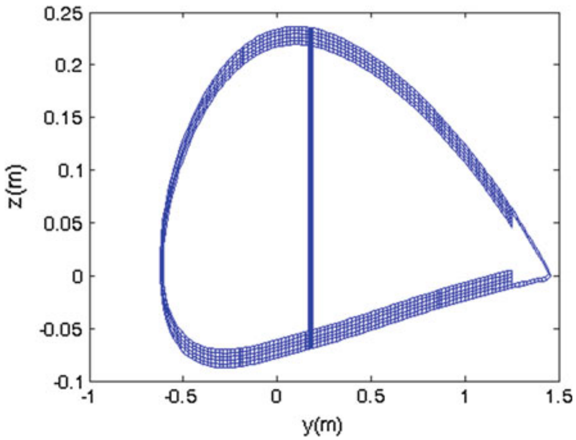

Fig. 8.4 The stretched image of the airfoil for enhancing clarity

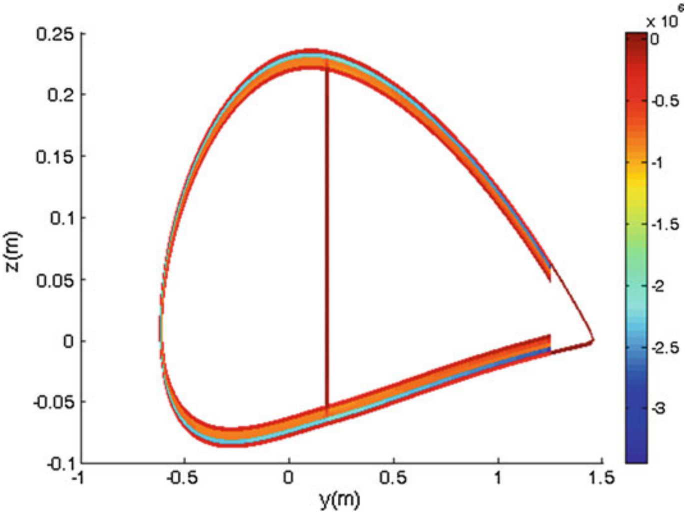

Fig. 8.5 Distribution of the T_{11} stress component due to 1 kV actuation of the 90° plies

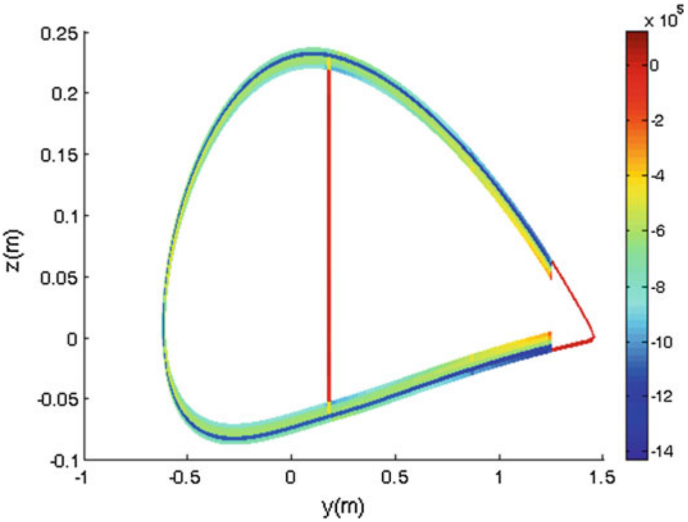

Fig. 8.6 Distribution of the T_{22} stress component due to 1 kV actuation of the 90˚ plies

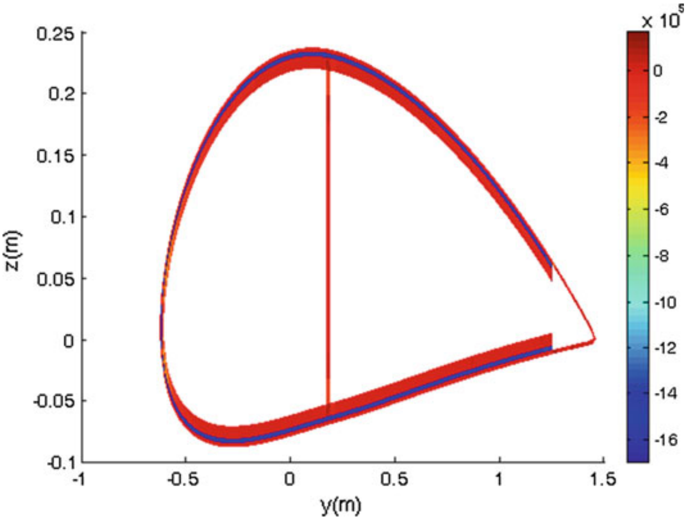

Fig. 8.7 Distribution of the T_{33} stress component due to 1 kV actuation of the 90° plies

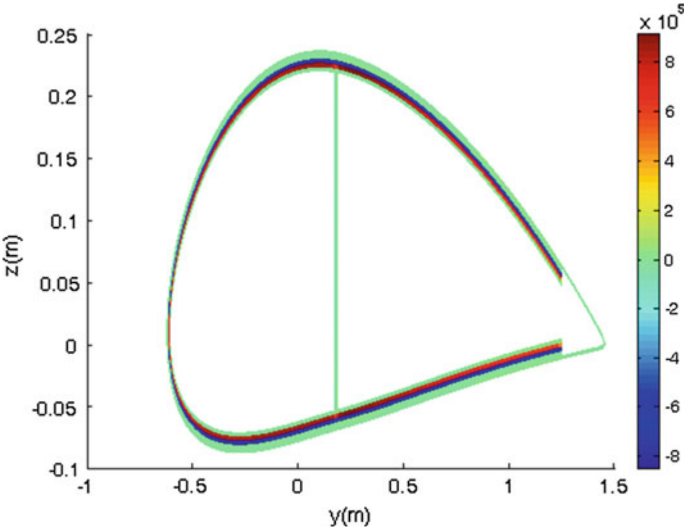

Fig. 8.8 Distribution of the T_{12} stress component due to 1 kV actuation of the 90° plies

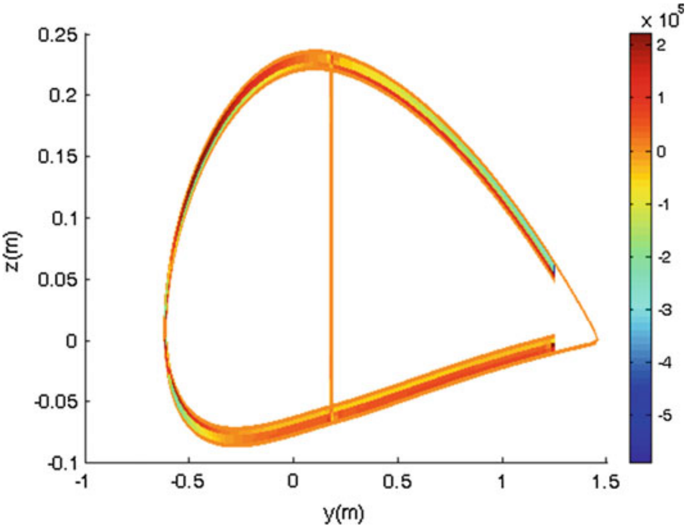

Fig. 8.9 Distribution of the T_{13} stress component due to 1 kV actuation of the 90° plies

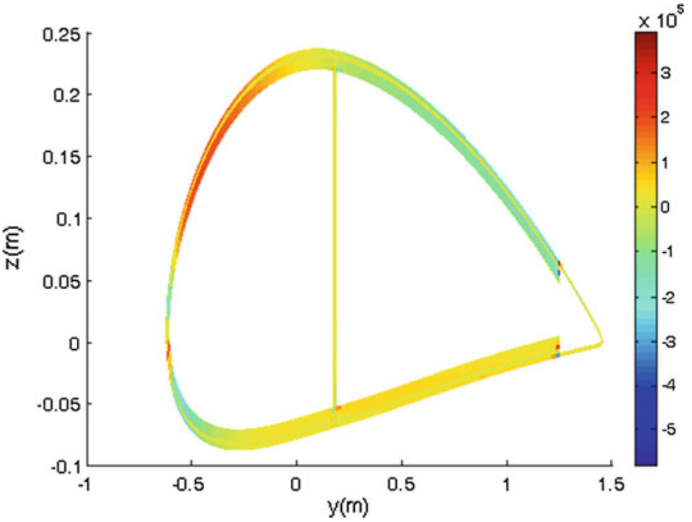

Fig. 8.10 Distribution of the T_{23} stress component due to 1 kV actuation of the 90° plies

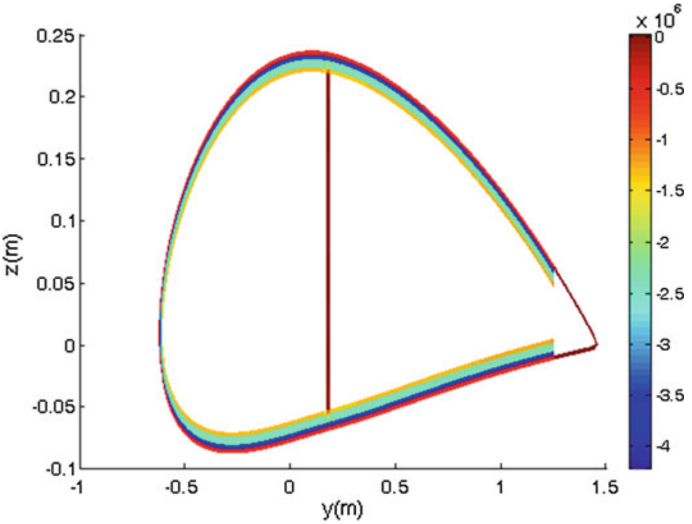

Fig. 8.11 Distribution of the T_{11} stress component in material coordinates due to 1 kV actuation of all active plies

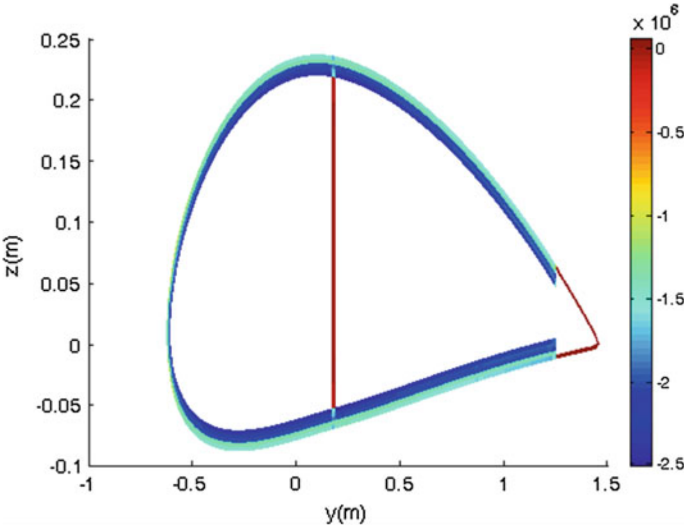

Fig. 8.12 Distribution of the T_{22} stress component in material coordinates due to 1 kV actuation of all active plies

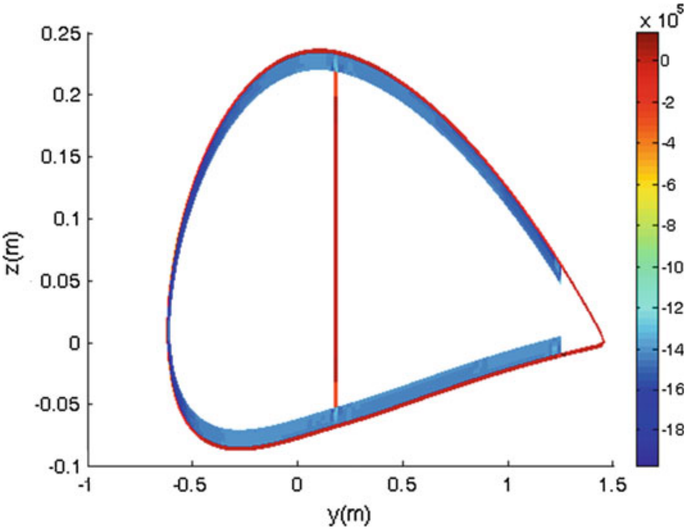

Fig. 8.13 Distribution of the T_{33} stress component in material coordinates due to 1 kV actuation of all active plies

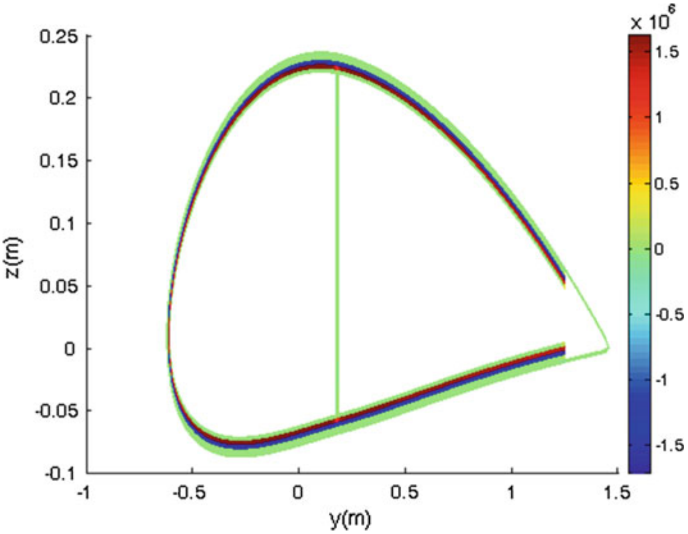

Fig. 8.14 Distribution of the T_{12} stress component in material coordinates due to 1 kV actuation of all active plies

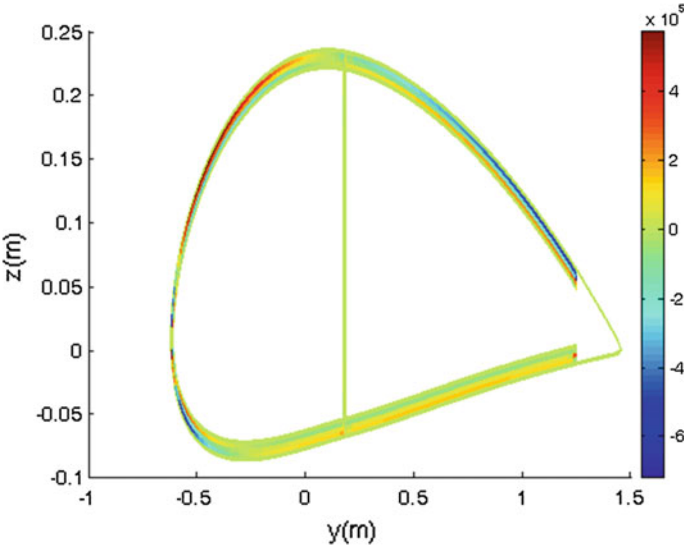

Fig. 8.15 Distribution of the T_{13} stress component in material coordinates due to 1 kV actuation of all active plies

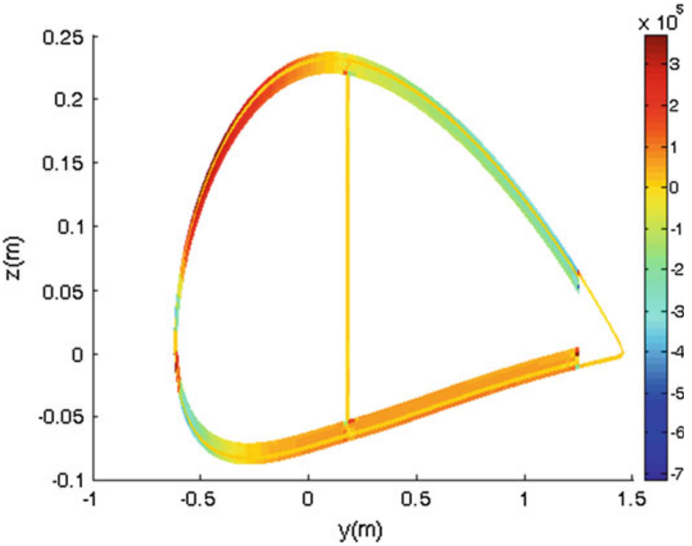

Fig. 8.16 Distribution of the T_{23} stress component in material coordinates due to 1 kV actuation of all active plies

8.8 Case Study: Steady-State Response of Rotating Active Airfoil

Consider the case of actuation of piezocomposite actuators embedded in the composite airfoil discussed in Sect. 8.7. However, this time the 3-m blade is rotating at an angular velocity of 100 rad/s and its steady-state response under different actuation scenarios is of interest. To this end, and using $\mu = 248.35$ kg/m, the method discussed in Chap. 6 is utilized to obtain the steady-state response.

First, no activation is applied and in order to analyze the effect of elastic coupling, two cases are considered. In one case, all of the terms in the stiffness and mass matrices are included in the analysis. Then, in the second case, the off-diagonal terms are ignored. The difference between these two sets of results provides an overall estimation of the impact of elastic coupling in the solution. The corresponding results are plotted in Figs. 8.17, 8.18, 8.19, and 8.20.

Next, active plies are activated one by one by applying a +1 kV potential to each one at a time, and the corresponding steady-state solutions are obtained. Finally, all of the active plies are activated simultaneously. The corresponding results are plotted in Figs. 8.21, 8.22, 8.23, and 8.24. Such diagrams can be used for controlling the response of the blade and the load distribution along it. It is observed that the actuators have significant controllability on M_3, but little control on F_1.

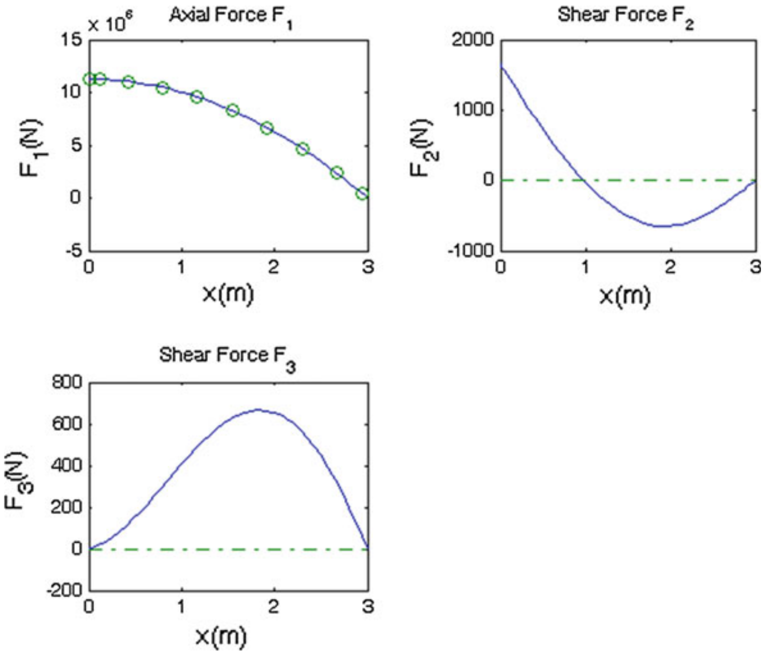

Fig. 8.17 The variation of internal force components along the blade; coupled solution (*solid line*) and uncoupled solution (*dashed* or *circles*)

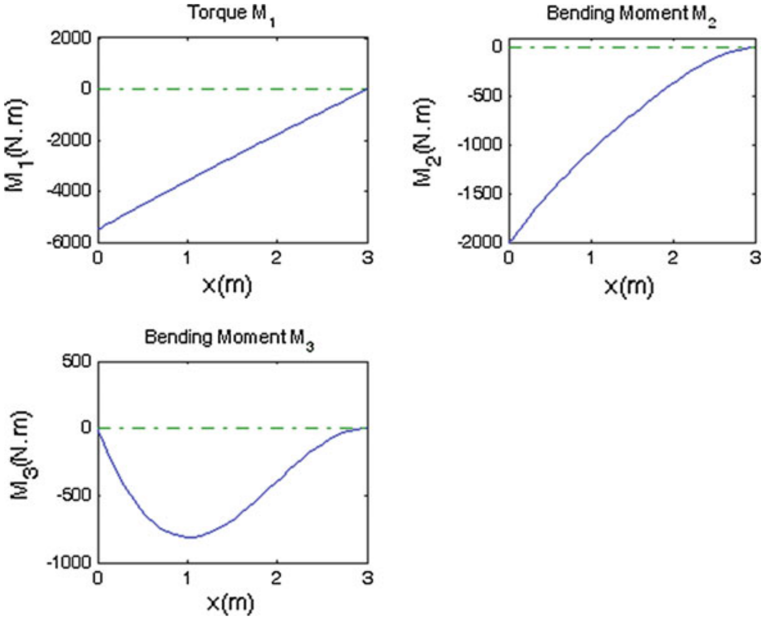

Fig. 8.18 The variation of internal moment components along the blade; coupled solution (*solid line*) and uncoupled solution (*dashed*)

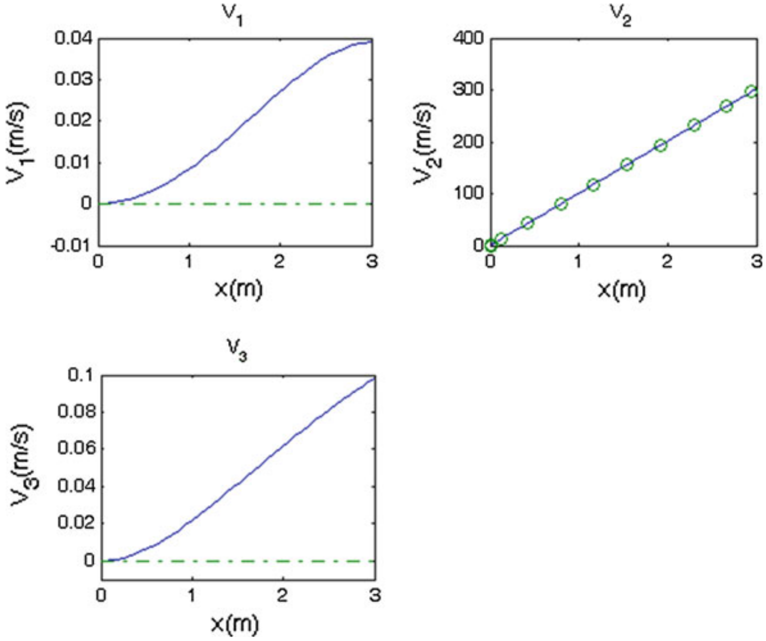

Fig. 8.19 The variation of velocity components along the blade; coupled solution (*solid line*) and uncoupled solution (*dashed* or *circles*)

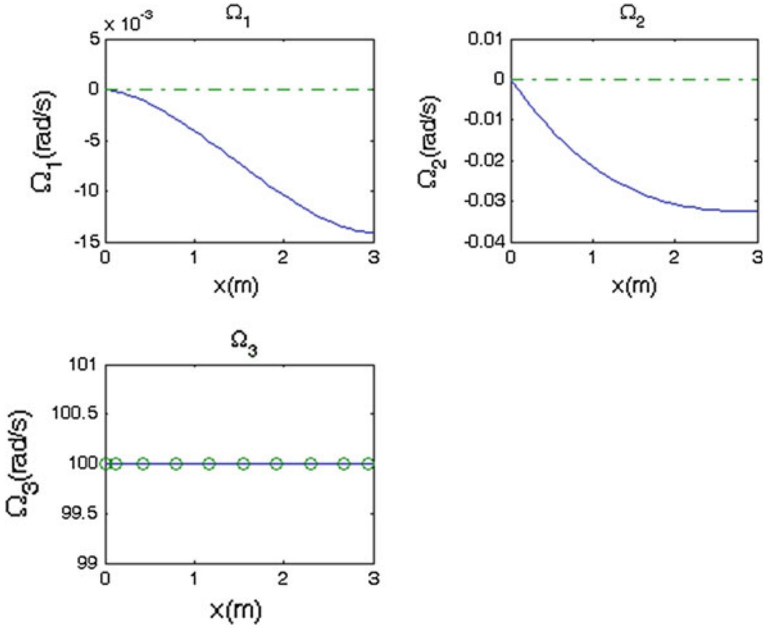

Fig. 8.20 The variation of angular velocity components along the blade; coupled solution (*solid line*) and uncoupled solution (*dashed* or *circles*)

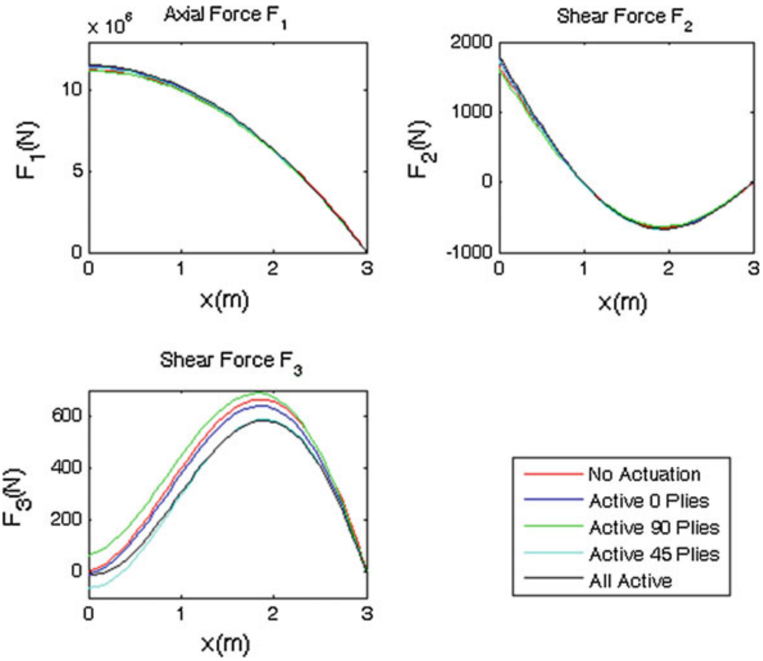

Fig. 8.21 The steady-state variation of internal force components along the beam due to various modes of activation of piezocomposite actuators

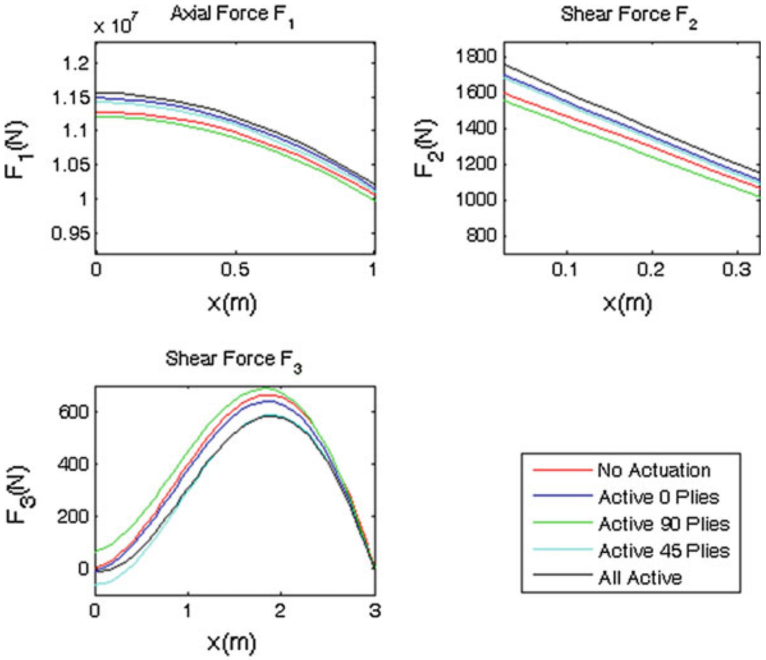

Fig. 8.22 The steady-state variation of internal force components along the beam due to various modes of activation of piezocomposite actuators (zoomed-in)

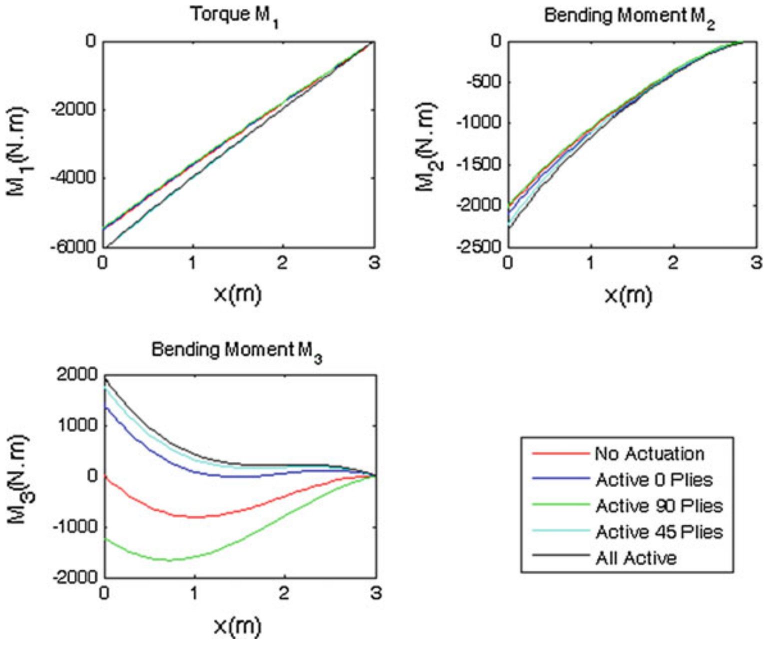

Fig. 8.23 The steady-state variation of internal moment components along the beam due to various modes of activation of piezocomposite actuators

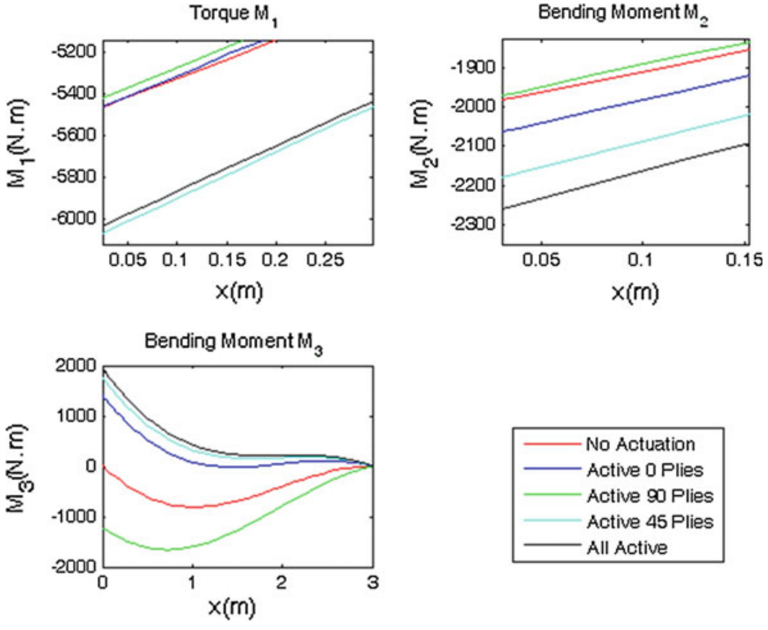

Fig. 8.24 The steady-state variation of internal moment components along the beam due to various modes of activation of piezocomposite actuators (zoomed-in)

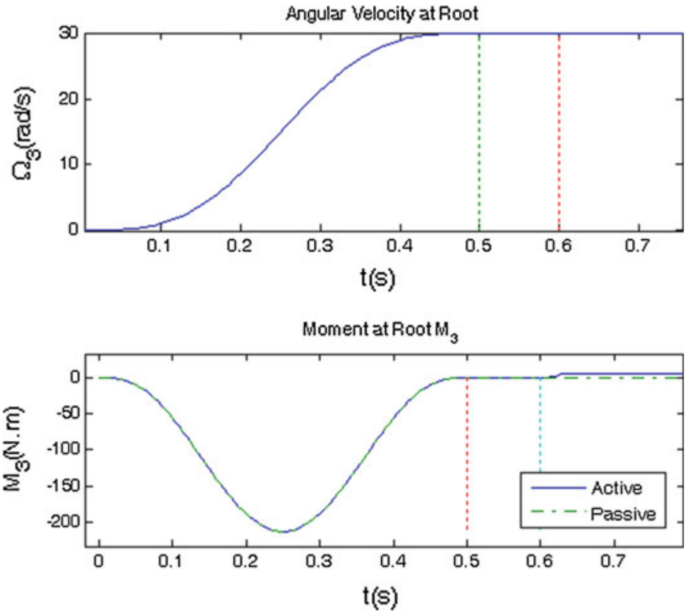

Fig. 8.25 Time history diagrams of shaft angular velocity and the M_3 bending moment induced in the blade at its root

8.9 Case Study: Rotating Articulated Active Composite Airfoil

Consider the case of actuation of the piezocomposite actuators embedded in the composite airfoil discussed in Sect. 8.7. Using 1 % of the full actuation forces and moments shown in Table 8.5, and a full speed angular velocity of 30 rad/s, distributions of forces with and without actuation are calculated and plotted in Figs. 8.25, 8.26, and 8.27. It is observed, in Figs. 8.26 and 8.27, that for this low inertia case with zero M_3 at the root, actuation (which happens at t = 0.6 s) has maximum influence on the axial force F_1.

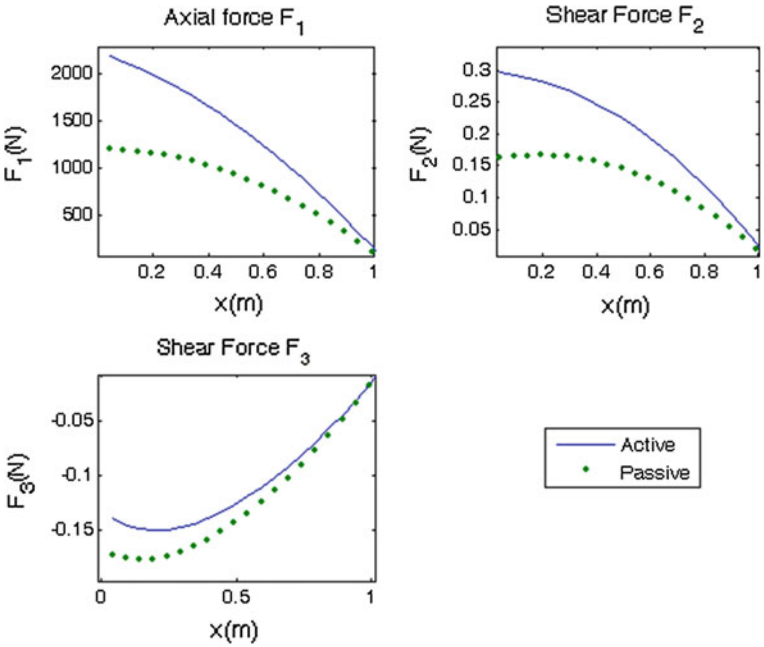

Fig. 8.26 Variation of the blade internal force components along its span at t = 0.85 s after actuation

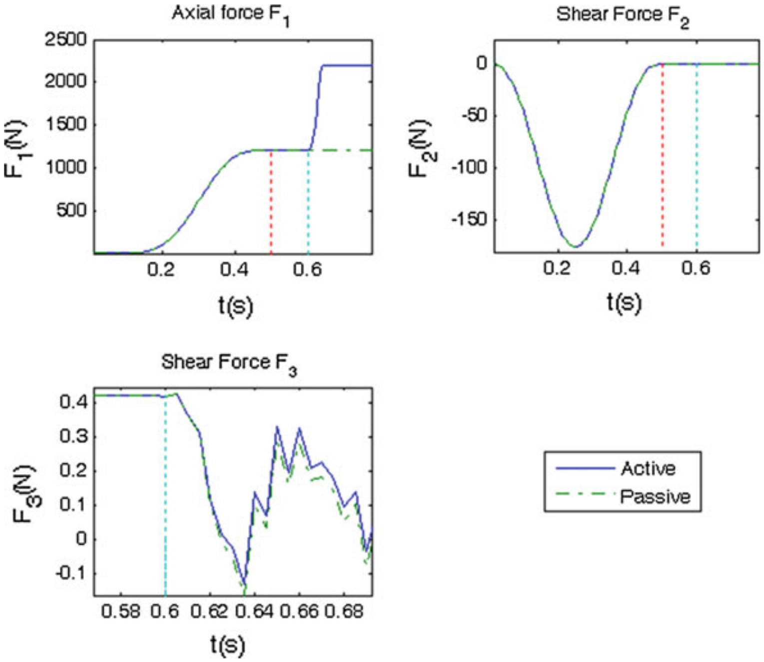

Fig. 8.27 Time history diagrams of the blade internal force components at the root

References

Ballas, R. G. (2007). *Piezoelectric multilayer beam bending actuators*. Springer.

Cesnik, C. E. S., & Palacios, R. (2003). Modeling piezocomposite actuators embedded in slender structures. In *Proceedings of the 44th AIAA/ASME/ASCE/AHS Structures, Structural Dynamics, and Materials Conference*, April 7–10, 2003, Norfolk, Virginia. Paper No.: AIAA 2003-1803.

Cesnik, C. E. S., Park, R. S., & Palacios, R. (2003). Effective cross-section distribution of anisotropic piezocomposite actuators for wing twist. *Proceedings of SPIE, 5056*, 21–32.

Ghorashi, M. (2009). *Dynamics of elastic nonlinear rotating composite beams with embedded actuators*. Ph.D. Thesis, Mechanical and Aerospace Engineering Department, Carleton University.

Ghorashi, M., & Nitzsche, F. (2009). Nonlinear dynamic response of an accelerating composite rotor blade using perturbations. *Journal of Mechanics of Materials and Structures, 4*, 693–718.

Giurgiutiu, V. (2008). *Structural health monitoring with piezoelectric wafer active sensors*. Academic Press.

Knowles, J. K. (1997). *Linear vector spaces and Cartesian tensors*. Oxford University Press.

Srinivasan, A. V., & McFarland, D. M. (2001). *Smart structures, analysis and design*. Cambridge University Press.

Appendix
Matrices A, B and J in Chap. 5

$$\begin{aligned}
J_i(1) = {} & \frac{1}{2\Delta x}\left(F_{1,i} - F_{1,i+1}\right) + \frac{1}{16}\left(\kappa_{3,i+1}F_{2,i+1} + \kappa_{3,i+1}F_{2,i} + \kappa_{3,i}F_{2,i+1} - 3\kappa_{3,i}F_{2,i}\right) \\
& - \frac{1}{16}\left(\kappa_{2,i+1}F_{3,i+1} + \kappa_{2,i+1}F_{3,i} + \kappa_{2,i}F_{3,i+1} - 3\kappa_{2,i}F_{3,i}\right) - \frac{1}{4}\left(f_{1,i+1} + f_{1,i} + f^{+}_{1,i+1} + f^{+}_{1,i}\right) \\
& - \frac{1}{2\Delta t}\left(P_{1,i} + P_{1,i+1}\right) - \frac{1}{16}\left(\Omega_{3,i+1}P_{2,i+1} + \Omega_{3,i+1}P_{2,i} + \Omega_{3,i}P_{2,i+1} - 3\Omega_{3,i}P_{2,i}\right) \\
& + \frac{1}{16}\left(\Omega_{2,i+1}P_{3,i+1} + \Omega_{2,i+1}P_{3,i} + \Omega_{2,i}P_{3,i+1} - 3\Omega_{2,i}P_{3,i}\right)
\end{aligned} \tag{A.1}$$

$$\begin{aligned}
J_i(2) = {} & \frac{1}{2\Delta x}\left(F_{2,i} - F_{2,i+1}\right) + \frac{1}{16}\left(\kappa_{1,i+1}F_{3,i+1} + \kappa_{1,i+1}F_{3,i} + \kappa_{1,i}F_{3,i+1} - 3\kappa_{1,i}F_{3,i}\right) \\
& - \frac{1}{16}\left(\kappa_{3,i+1}F_{1,i+1} + \kappa_{3,i+1}F_{1,i} + \kappa_{3,i}F_{1,i+1} - 3\kappa_{3,i}F_{1,i}\right) - \frac{1}{4}\left(f_{2,i+1} + f_{2,i} + f^{+}_{2,i+1} + f^{+}_{2,i}\right) \\
& - \frac{1}{2\Delta t}\left(P_{2,i} + P_{2,i+1}\right) - \frac{1}{16}\left(\Omega_{1,i+1}P_{3,i+1} + \Omega_{1,i+1}P_{3,i} + \Omega_{1,i}P_{3,i+1} - 3\Omega_{1,i}P_{3,i}\right) \\
& + \frac{1}{16}\left(\Omega_{3,i+1}P_{1,i+1} + \Omega_{3,i+1}P_{1,i} + \Omega_{3,i}P_{1,i+1} - 3\Omega_{3,i}P_{1,i}\right)
\end{aligned} \tag{A.2}$$

$$\begin{aligned}
J_i(3) = {} & \frac{1}{2\Delta x}\left(F_{3,i} - F_{3,i+1}\right) + \frac{1}{16}\left(\kappa_{2,i+1}F_{1,i+1} + \kappa_{2,i+1}F_{1,i} + \kappa_{2,i}F_{1,i+1} - 3\kappa_{2,i}F_{1,i}\right) \\
& - \frac{1}{16}\left(\kappa_{1,i+1}F_{2,i+1} + \kappa_{1,i+1}F_{2,i} + \kappa_{1,i}F_{2,i+1} - 3\kappa_{1,i}F_{2,i}\right) - \frac{1}{4}\left(f_{3,i+1} + f_{3,i} + f^{+}_{3,i+1} + f^{+}_{3,i}\right) \\
& - \frac{1}{2\Delta t}\left(P_{3,i} + P_{3,i+1}\right) - \frac{1}{16}\left(\Omega_{2,i+1}P_{1,i+1} + \Omega_{2,i+1}P_{1,i} + \Omega_{2,i}P_{1,i+1} - 3\Omega_{2,i}P_{1,i}\right) \\
& + \frac{1}{16}\left(\Omega_{1,i+1}P_{2,i+1} + \Omega_{1,i+1}P_{2,i} + \Omega_{1,i}P_{2,i+1} - 3\Omega_{1,i}P_{2,i}\right)
\end{aligned} \tag{A.3}$$

$$\begin{aligned}
J_i(4) = {} & \frac{1}{2\Delta x}\left(M_{1,i} - M_{1,i+1}\right) + \frac{1}{16}\left(\kappa_{3,i+1}M_{2,i+1} + \kappa_{3,i+1}M_{2,i} + \kappa_{3,i}M_{2,i+1} - 3\kappa_{3,i}M_{2,i}\right) \\
& - \frac{1}{16}\left(\kappa_{2,i+1}M_{3,i+1} + \kappa_{2,i+1}M_{3,i} + \kappa_{2,i}M_{3,i+1} - 3\kappa_{2,i}M_{3,i}\right) - \frac{1}{4}\left(m_{1,i+1} + m_{1,i} + m^{+}_{1,i+1} + m^{+}_{1,i}\right) \\
& - \frac{1}{2\Delta t}\left(H_{1,i} + H_{1,i+1}\right) - \frac{1}{16}\left(\Omega_{3,i+1}H_{2,i+1} + \Omega_{3,i+1}H_{2,i} + \Omega_{3,i}H_{2,i+1} - 3\Omega_{3,i}H_{2,i}\right) \\
& + \frac{1}{16}\left(\Omega_{2,i+1}H_{3,i+1} + \Omega_{2,i+1}H_{3,i} + \Omega_{2,i}H_{3,i+1} - 3\Omega_{2,i}H_{3,i}\right) \\
& + \frac{1}{8}\left(\gamma_{13,i+1}F_{2,i+1} + \gamma_{13,i+1}F_{2,i} + \gamma_{13,i}F_{2,i+1} - 3\gamma_{13,i}F_{2,i}\right) \\
& - \frac{1}{8}\left(\gamma_{12,i+1}F_{3,i+1} + \gamma_{12,i+1}F_{3,i} + \gamma_{12,i}F_{3,i+1} - 3\gamma_{12,i}F_{3,i}\right) \\
& - \frac{1}{16}\left(V_{3,i+1}P_{2,i+1} + V_{3,i+1}P_{2,i} + V_{3,i}P_{2,i+1} - 3V_{3,i}P_{2,i}\right) \\
& + \frac{1}{16}\left(V_{2,i+1}P_{3,i+1} + V_{2,i+1}P_{3,i} + V_{2,i}P_{3,i+1} - 3V_{2,i}P_{3,i}\right)
\end{aligned} \tag{A.4}$$

M. Ghorashi, *Statics and Rotational Dynamics of Composite Beams*,
DOI 10.1007/978-3-319-14959-2

$$\begin{aligned}
J_i(5) = {} & \frac{1}{2\Delta x}\left(M_{2,i} - M_{2,i+1}\right) + \frac{1}{16}\left(\kappa_{1,i+1}M_{3,i+1} + \kappa_{1,i+1}M_{3,i} + \kappa_{1,i}M_{3,i+1} - 3\kappa_{1,i}M_{3,i}\right) \\
& - \frac{1}{16}\left(\kappa_{3,i+1}M_{1,i+1} + \kappa_{3,i+1}M_{1,i} + \kappa_{3,i}M_{1,i+1} - 3\kappa_{3,i}M_{1,i}\right) - \frac{1}{4}\left(m_{2,i+1} + m_{2,i} + m^{+}_{2,i+1} + m^{+}_{2,i}\right) \\
& - \frac{1}{2\Delta t}\left(H_{2,i} + H_{2,i+1}\right) - \frac{1}{16}\left(\Omega_{1,i+1}H_{3,i+1} + \Omega_{1,i+1}H_{3,i} + \Omega_{1,i}H_{3,i+1} - 3\Omega_{1,i}H_{3,i}\right) \\
& + \frac{1}{16}\left(\Omega_{3,i+1}H_{1,i+1} + \Omega_{3,i+1}H_{1,i} + \Omega_{3,i}H_{1,i+1} - 3\Omega_{3,i}H_{1,i}\right) + \frac{1}{4}\left(F_{3,i} + F_{3,i+1}\right) \\
& + \frac{1}{16}\left(\gamma_{11,i+1}F_{3,i+1} + \gamma_{11,i+1}F_{3,i} + \gamma_{11,i}F_{3,i+1} - 3\gamma_{11,i}F_{3,i}\right) \\
& - \frac{1}{8}\left(\gamma_{13,i+1}F_{1,i+1} + \gamma_{13,i+1}F_{1,i} + \gamma_{13,i}F_{1,i+1} - 3\gamma_{13,i}F_{1,i}\right) \\
& - \frac{1}{16}\left(V_{1,i+1}P_{3,i+1} + V_{1,i+1}P_{3,i} + V_{1,i}P_{3,i+1} - 3V_{1,i}P_{3,i}\right) \\
& + \frac{1}{16}\left(V_{3,i+1}P_{1,i+1} + V_{3,i+1}P_{1,i} + V_{3,i}P_{1,i+1} - 3V_{3,i}P_{1,i}\right)
\end{aligned} \tag{A.5}$$

$$\begin{aligned}
J_i(6) = {} & \frac{1}{2\Delta x}\left(M_{3,i} - M_{3,i+1}\right) + \frac{1}{16}\left(\kappa_{2,i+1}M_{1,i+1} + \kappa_{2,i+1}M_{1,i} + \kappa_{2,i}M_{1,i+1} - 3\kappa_{2,i}M_{1,i}\right) \\
& - \frac{1}{16}\left(\kappa_{1,i+1}M_{2,i+1} + \kappa_{1,i+1}M_{2,i} + \kappa_{1,i}M_{2,i+1} - 3\kappa_{1,i}M_{2,i}\right) - \frac{1}{4}\left(m_{3,i+1} + m_{3,i} + m^{+}_{3,i+1} + m^{+}_{3,i}\right) \\
& - \frac{1}{2\Delta t}\left(H_{3,i} + H_{3,i+1}\right) - \frac{1}{16}\left(\Omega_{2,i+1}H_{1,i+1} + \Omega_{2,i+1}H_{1,i} + \Omega_{2,i}H_{1,i+1} - 3\Omega_{2,i}H_{1,i}\right) \\
& + \frac{1}{16}\left(\Omega_{1,i+1}H_{2,i+1} + \Omega_{1,i+1}H_{2,i} + \Omega_{1,i}H_{2,i+1} - 3\Omega_{1,i}H_{2,i}\right) - \frac{1}{4}\left(F_{2,i} + F_{2,i+1}\right) \\
& + \frac{1}{16}\left(\gamma_{11,i+1}F_{2,i+1} + \gamma_{11,i+1}F_{2,i} + \gamma_{11,i}F_{2,i+1} - 3\gamma_{11,i}F_{2,i}\right) \\
& + \frac{1}{8}\left(\gamma_{12,i+1}F_{1,i+1} + \gamma_{12,i+1}F_{1,i} + \gamma_{12,i}F_{1,i+1} - 3\gamma_{12,i}F_{1,i}\right) \\
& - \frac{1}{16}\left(V_{2,i+1}P_{1,i+1} + V_{2,i+1}P_{1,i} + V_{2,i}P_{1,i+1} - 3V_{2,i}P_{1,i}\right) \\
& + \frac{1}{16}\left(V_{1,i+1}P_{2,i+1} + V_{1,i+1}P_{2,i} + V_{1,i}P_{2,i+1} - 3V_{1,i}P_{2,i}\right)
\end{aligned} \tag{A.6}$$

$$\begin{aligned}
J_i(7) = {} & \frac{1}{2\Delta x}\left(V_{1,i} - V_{1,i+1}\right) + \frac{1}{16}\left(\kappa_{3,i+1}V_{2,i+1} + \kappa_{3,i+1}V_{2,i} + \kappa_{3,i}V_{2,i+1} - 3\kappa_{3,i}V_{2,i}\right) \\
& - \frac{1}{16}\left(\kappa_{2,i+1}V_{3,i+1} + \kappa_{2,i+1}V_{3,i} + \kappa_{2,i}V_{3,i+1} - 3\kappa_{2,i}V_{3,i}\right) \\
& + \frac{1}{8}\left(\gamma_{13,i+1}\Omega_{2,i+1} + \gamma_{13,i+1}\Omega_{2,i} + \gamma_{13,i}\Omega_{2,i+1} - 3\gamma_{13,i}\Omega_{2,i}\right) \\
& - \frac{1}{8}\left(\gamma_{12,i+1}\Omega_{3,i+1} + \gamma_{12,i+1}\Omega_{3,i} + \gamma_{12,i}\Omega_{3,i+1} - 3\gamma_{12,i}\Omega_{3,i}\right) - \frac{1}{2\Delta t}\left(\gamma_{11,i} + \gamma_{11,i+1}\right)
\end{aligned} \tag{A.7}$$

$$\begin{aligned}
J_i(8) = {} & \frac{1}{2\Delta x}\left(V_{2,i} - V_{2,i+1}\right) + \frac{1}{16}\left(\kappa_{1,i+1}V_{3,i+1} + \kappa_{1,i+1}V_{3,i} + \kappa_{1,i}V_{3,i+1} - 3\kappa_{1,i}V_{3,i}\right) \\
& - \frac{1}{16}\left(\kappa_{3,i+1}V_{1,i+1} + \kappa_{3,i+1}V_{1,i} + \kappa_{3,i}V_{1,i+1} - 3\kappa_{3,i}V_{1,i}\right) + \frac{1}{4}\left(\Omega_{3,i} + \Omega_{3,i+1}\right) \\
& + \frac{1}{16}\left(\gamma_{11,i+1}\Omega_{3,i+1} + \gamma_{11,i+1}\Omega_{3,i} + \gamma_{11,i}\Omega_{3,i+1} - 3\gamma_{11,i}\Omega_{3,i}\right) \\
& - \frac{1}{8}\left(\gamma_{13,i+1}\Omega_{1,i+1} + \gamma_{13,i+1}\Omega_{1,i} + \gamma_{13,i}\Omega_{1,i+1} - 3\gamma_{13,i}\Omega_{1,i}\right) - \frac{1}{\Delta t}\left(\gamma_{12,i} + \gamma_{12,i+1}\right)
\end{aligned} \tag{A.8}$$

$$\begin{aligned}
J_i(9) = {} & \frac{1}{2\Delta x}\left(V_{3,i} - V_{3,i+1}\right) + \frac{1}{16}\left(\kappa_{2,i+1}V_{1,i+1} + \kappa_{2,i+1}V_{1,i} + \kappa_{2,i}V_{1,i+1} - 3\kappa_{2,i}V_{1,i}\right) \\
& - \frac{1}{16}\left(\kappa_{1,i+1}V_{2,i+1} + \kappa_{1,i+1}V_{2,i} + \kappa_{1,i}V_{2,i+1} - 3\kappa_{1,i}V_{2,i}\right) - \frac{1}{4}\left(\Omega_{2,i} + \Omega_{2,i+1}\right) \\
& - \frac{1}{16}\left(\gamma_{11,i+1}\Omega_{2,i+1} + \gamma_{11,i+1}\Omega_{2,i} + \gamma_{11,i}\Omega_{2,i+1} - 3\gamma_{11,i}\Omega_{2,i}\right) \\
& + \frac{1}{8}\left(\gamma_{12,i+1}\Omega_{1,i+1} + \gamma_{12,i+1}\Omega_{1,i} + \gamma_{12,i}\Omega_{1,i+1} - 3\gamma_{12,i}\Omega_{1,i}\right) - \frac{1}{\Delta t}\left(\gamma_{13,i} + \gamma_{13,i+1}\right)
\end{aligned} \tag{A.9}$$

$$\begin{aligned}J_i(10) ={}& \frac{1}{2\Delta x}\left(\Omega_{1,i} - \Omega_{1,i+1}\right) + \frac{1}{16}\left(\kappa_{3,i+1}\Omega_{2,i+1} + \kappa_{3,i+1}\Omega_{2,i} + \kappa_{3,i}\Omega_{2,i+1} - 3\kappa_{3,i}\Omega_{2,i}\right)\\ &- \frac{1}{16}\left(\kappa_{2,i+1}\Omega_{3,i+1} + \kappa_{2,i+1}\Omega_{3,i} + \kappa_{2,i}\Omega_{3,i+1} - 3\kappa_{2,i}\Omega_{3,i}\right) - \frac{1}{2\Delta t}\left(\kappa_{1,i} + \kappa_{1,i+1}\right)\end{aligned}\tag{A.10}$$

$$\begin{aligned}J_i(11) ={}& \frac{1}{2\Delta x}\left(\Omega_{2,i} - \Omega_{2,i+1}\right) + \frac{1}{16}\left(\kappa_{1,i+1}\Omega_{3,i+1} + \kappa_{1,i+1}\Omega_{3,i} + \kappa_{1,i}\Omega_{3,i+1} - 3\kappa_{1,i}\Omega_{3,i}\right)\\ &- \frac{1}{16}\left(\kappa_{3,i+1}\Omega_{1,i+1} + \kappa_{3,i+1}\Omega_{1,i} + \kappa_{3,i}\Omega_{1,i+1} - 3\kappa_{3,i}\Omega_{1,i}\right) - \frac{1}{2\Delta t}\left(\kappa_{2,i} + \kappa_{2,i+1}\right)\end{aligned}\tag{A.11}$$

$$\begin{aligned}J_i(12) ={}& \frac{1}{2\Delta x}\left(\Omega_{3,i} - \Omega_{3,i+1}\right) + \frac{1}{16}\left(\kappa_{2,i+1}\Omega_{1,i+1} + \kappa_{2,i+1}\Omega_{1,i} + \kappa_{2,i}\Omega_{1,i+1} - 3\kappa_{2,i}\Omega_{1,i}\right)\\ &- \frac{1}{16}\left(\kappa_{1,i+1}\Omega_{2,i+1} + \kappa_{1,i+1}\Omega_{2,i} + \kappa_{1,i}\Omega_{2,i+1} - 3\kappa_{1,i}\Omega_{2,i}\right) - \frac{1}{2\Delta t}\left(\kappa_{3,i} + \kappa_{3,i+1}\right)\end{aligned}\tag{A.12}$$

$$\begin{aligned}J_i(13) ={}& -\frac{1}{4}\left(P_{1,i} + P_{1,i+1}\right) + \frac{\mu}{4}\left(V_{1,i} + V_{1,i+1}\right) + \frac{\mu}{4}\bar{x}_3\left(\Omega_{2,i} + \Omega_{2,i+1}\right)\\ &- \frac{\mu}{4}\bar{x}_2\left(\Omega_{3,i} + \Omega_{3,i+1}\right)\end{aligned}\tag{A.13}$$

$$J_i(14) = -\frac{1}{4}\left(P_{2,i} + P_{2,i+1}\right) + \frac{\mu}{4}\left(V_{2,i} + V_{2,i+1}\right) - \frac{\mu}{4}\bar{x}_3\left(\Omega_{1,i} + \Omega_{1,i+1}\right)\tag{A.14}$$

$$J_i(15) = -\frac{1}{4}\left(P_{3,i} + P_{3,i+1}\right) + \frac{\mu}{4}\left(V_{3,i} + V_{3,i+1}\right) + \frac{\mu}{4}\bar{x}_2\left(\Omega_{1,i} + \Omega_{1,i+1}\right)\tag{A.15}$$

$$\begin{aligned}J_i(16) ={}& -\frac{1}{4}\left(H_{1,i} + H_{1,i+1}\right) - \frac{\mu}{4}\bar{x}_3\left(V_{2,i} + V_{2,i+1}\right) + \frac{\mu}{4}\bar{x}_2\left(V_{3,i} + V_{3,i+1}\right)\\ &+ \frac{1}{4}i(1,1)\left(\Omega_{1,i} + \Omega_{1,i+1}\right) + \frac{1}{4}i(1,2)\left(\Omega_{2,i} + \Omega_{2,i+1}\right) + \frac{1}{4}i(1,3)\left(\Omega_{3,i} + \Omega_{3,i+1}\right)\end{aligned}\tag{A.16}$$

$$\begin{aligned}J_i(17) ={}& -\frac{1}{4}\left(H_{2,i} + H_{2,i+1}\right) + \frac{\mu}{4}\bar{x}_3\left(V_{1,i} + V_{1,i+1}\right)\\ &+ \frac{1}{4}i(2,1)\left(\Omega_{1,i} + \Omega_{1,i+1}\right) + \frac{1}{4}i(2,2)\left(\Omega_{2,i} + \Omega_{2,i+1}\right) + \frac{1}{4}i(2,3)\left(\Omega_{3,i} + \Omega_{3,i+1}\right)\end{aligned}\tag{A.17}$$

$$\begin{aligned}J_i(18) ={}& -\frac{1}{4}\left(H_{3,i} + H_{3,i+1}\right) - \frac{\mu}{4}\bar{x}_2\left(V_{1,i} + V_{1,i+1}\right)\\ &+ \frac{1}{4}i(3,1)\left(\Omega_{1,i} + \Omega_{1,i+1}\right) + \frac{1}{4}i(3,2)\left(\Omega_{2,i} + \Omega_{2,i+1}\right) + \frac{1}{4}i(3,3)\left(\Omega_{3,i} + \Omega_{3,i+1}\right)\end{aligned}\tag{A.18}$$

$$\begin{aligned}J_i(19) ={}& -\frac{1}{4}\left(\gamma_{11,i} + \gamma_{11,i+1}\right) + \frac{1}{4}R(1,1)\left(F_{1,i} + F_{1,i+1}\right) + \frac{1}{4}R(1,2)\left(F_{2,i} + F_{2,i+1}\right)\\ &+ \frac{1}{4}R(1,3)\left(F_{3,i} + F_{3,i+1}\right) + \frac{1}{4}Z(1,1)\left(M_{1,i} + M_{1,i+1}\right) + \frac{1}{4}Z(1,2)\left(M_{2,i} + M_{2,i+1}\right)\\ &+ \frac{1}{4}Z(1,3)\left(M_{3,i} + M_{3,i+1}\right)\end{aligned}\tag{A.19}$$

$$\begin{aligned}J_i(20) ={}& -\frac{1}{2}\left(\gamma_{12,i} + \gamma_{12,i+1}\right) + \frac{1}{4}R(2,1)\left(F_{1,i} + F_{1,i+1}\right) + \frac{1}{4}R(2,2)\left(F_{2,i} + F_{2,i+1}\right)\\ &+ \frac{1}{4}R(2,3)\left(F_{3,i} + F_{3,i+1}\right) + \frac{1}{4}Z(2,1)\left(M_{1,i} + M_{1,i+1}\right) + \frac{1}{4}Z(2,2)\left(M_{2,i} + M_{2,i+1}\right)\\ &+ \frac{1}{4}Z(2,3)\left(M_{3,i} + M_{3,i+1}\right)\end{aligned}\tag{A.20}$$

$$
\begin{aligned}
J_i(21) = &-\frac{1}{2}\left(\gamma_{13,i}+\gamma_{13,i+1}\right)+\frac{1}{4}R(3,1)\left(F_{1,i}+F_{1,i+1}\right)+\frac{1}{4}R(3,2)\left(F_{2,i}+F_{2,i+1}\right)\\
&+\frac{1}{4}R(3,3)\left(F_{3,i}+F_{3,i+1}\right)+\frac{1}{4}Z(3,1)\left(M_{1,i}+M_{1,i+1}\right)+\frac{1}{4}Z(3,2)\left(M_{2,i}+M_{2,i+1}\right)\\
&+\frac{1}{4}Z(3,3)\left(M_{3,i}+M_{3,i+1}\right)
\end{aligned}
\tag{A.21}
$$

$$
\begin{aligned}
J_i(22) = &-\frac{1}{4}\left(\kappa_{1,i}+\kappa_{1,i+1}\right)+\frac{1}{4}Z(1,1)\left(F_{1,i}+F_{1,i+1}\right)+\frac{1}{4}Z(2,1)\left(F_{2,i}+F_{2,i+1}\right)\\
&+\frac{1}{4}Z(3,1)\left(F_{3,i}+F_{3,i+1}\right)+\frac{1}{4}T(1,1)\left(M_{1,i}+M_{1,i+1}\right)+\frac{1}{4}T(1,2)\left(M_{2,i}+M_{2,i+1}\right)\\
&+\frac{1}{4}T(1,3)\left(M_{3,i}+M_{3,i+1}\right)
\end{aligned}
\tag{A.22}
$$

$$
\begin{aligned}
J_i(23) = &-\frac{1}{4}\left(\kappa_{2,i}+\kappa_{2,i+1}\right)+\frac{1}{4}Z(1,2)\left(F_{1,i}+F_{1,i+1}\right)+\frac{1}{4}Z(2,2)\left(F_{2,i}+F_{2,i+1}\right)\\
&+\frac{1}{4}Z(3,2)\left(F_{3,i}+F_{3,i+1}\right)+\frac{1}{4}T(2,1)\left(M_{1,i}+M_{1,i+1}\right)+\frac{1}{4}T(2,2)\left(M_{2,i}+M_{2,i+1}\right)\\
&+\frac{1}{4}T(2,3)\left(M_{3,i}+M_{3,i+1}\right)
\end{aligned}
\tag{A.23}
$$

$$
\begin{aligned}
J_i(24) = &-\frac{1}{4}\left(\kappa_{3,i}+\kappa_{3,i+1}\right)+\frac{1}{4}Z(1,3)\left(F_{1,i}+F_{1,i+1}\right)+\frac{1}{4}Z(2,3)\left(F_{2,i}+F_{2,i+1}\right)\\
&+\frac{1}{4}Z(3,3)\left(F_{3,i}+F_{3,i+1}\right)+\frac{1}{4}T(3,1)\left(M_{1,i}+M_{1,i+1}\right)+\frac{1}{4}T(3,2)\left(M_{2,i}+M_{2,i+1}\right)\\
&+\frac{1}{4}T(3,3)\left(M_{3,i}+M_{3,i+1}\right)
\end{aligned}
\tag{A.24}
$$

$$
A_i(1:24,1:3)=\begin{bmatrix}
\frac{-1}{2\Delta x} & \frac{-1}{16}\left(\kappa_{3,i+1}+3\kappa_{3,i}\right) & \frac{1}{16}\left(\kappa_{2,i+1}+3\kappa_{2,i}\right)\\
\frac{1}{16}\left(\kappa_{3,i+1}+3\kappa_{3,i}\right) & \frac{-1}{2\Delta x} & \frac{-1}{16}\left(\kappa_{1,i+1}+3\kappa_{1,i}\right)\\
\frac{-1}{16}\left(\kappa_{2,i+1}+3\kappa_{2,i}\right) & \frac{1}{16}\left(\kappa_{1,i+1}+3\kappa_{1,i}\right) & \frac{-1}{2\Delta x}\\
0 & \frac{-1}{8}\left(\gamma_{13,i+1}+3\gamma_{13,i}\right) & \frac{1}{8}\left(\gamma_{12,i+1}+3\gamma_{12,i}\right)\\
\frac{1}{8}\left(\gamma_{13,i+1}+3\gamma_{13,i}\right) & 0 & \frac{-1}{4}-\frac{1}{16}\left(\gamma_{11,i+1}+3\gamma_{11,i}\right)\\
\frac{-1}{8}\left(\gamma_{12,i+1}+3\gamma_{12,i}\right) & \frac{1}{4}+\frac{1}{16}\left(\gamma_{11,i+1}+3\gamma_{11,i}\right) & 0\\
0 & 0 & 0\\
0 & 0 & 0\\
0 & 0 & 0\\
0 & 0 & 0\\
0 & 0 & 0\\
0 & 0 & 0\\
0 & 0 & 0\\
0 & 0 & 0\\
0 & 0 & 0\\
0 & 0 & 0\\
0 & 0 & 0\\
0 & 0 & 0\\
\frac{-1}{4}R(1,1) & \frac{-1}{4}R(1,2) & \frac{-1}{4}R(1,3)\\
\frac{-1}{4}R(2,1) & \frac{-1}{4}R(2,2) & \frac{-1}{4}R(2,3)\\
\frac{-1}{4}R(3,1) & \frac{-1}{4}R(3,2) & \frac{-1}{4}R(3,3)\\
\frac{-1}{4}Z(1,1) & \frac{-1}{4}Z(2,1) & \frac{-1}{4}Z(3,1)\\
\frac{-1}{4}Z(1,2) & \frac{-1}{4}Z(2,2) & \frac{-1}{4}Z(3,2)\\
\frac{-1}{4}Z(1,3) & \frac{-1}{4}Z(2,3) & \frac{-1}{4}Z(3,3)
\end{bmatrix}
\tag{A.25}
$$

$$A_i(1:24,4:6)=\begin{bmatrix}
0 & 0 & 0\\
0 & 0 & 0\\
0 & 0 & 0\\
\frac{-1}{2\Delta x} & \frac{-1}{16}\left(\kappa_{3,i+1}+3\kappa_{3,i}\right) & \frac{1}{16}\left(\kappa_{2,i+1}+3\kappa_{2,i}\right)\\
\frac{1}{16}\left(\kappa_{3,i+1}+3\kappa_{3,i}\right) & \frac{-1}{2\Delta x} & \frac{-1}{16}\left(\kappa_{1,i+1}+3\kappa_{1,i}\right)\\
\frac{-1}{16}\left(\kappa_{2,i+1}+3\kappa_{2,i}\right) & \frac{1}{16}\left(\kappa_{1,i+1}+3\kappa_{1,i}\right) & \frac{-1}{2\Delta x}\\
0 & 0 & 0\\
0 & 0 & 0\\
0 & 0 & 0\\
0 & 0 & 0\\
0 & 0 & 0\\
0 & 0 & 0\\
0 & 0 & 0\\
0 & 0 & 0\\
0 & 0 & 0\\
0 & 0 & 0\\
0 & 0 & 0\\
0 & 0 & 0\\
\frac{-1}{4}Z(1,1) & \frac{-1}{4}Z(1,2) & \frac{-1}{4}Z(1,3)\\
\frac{-1}{4}Z(2,1) & \frac{-1}{4}Z(2,2) & \frac{-1}{4}Z(2,3)\\
\frac{-1}{4}Z(3,1) & \frac{-1}{4}Z(3,2) & \frac{-1}{4}Z(3,3)\\
\frac{-1}{4}T(1,1) & \frac{-1}{4}T(1,2) & \frac{-1}{4}T(1,3)\\
\frac{-1}{4}T(2,1) & \frac{-1}{4}T(2,2) & \frac{-1}{4}T(2,3)\\
\frac{-1}{4}T(3,1) & \frac{-1}{4}T(3,2) & \frac{-1}{4}T(3,3)
\end{bmatrix} \tag{A.26}$$

$$A_i(1:24,7:9)=\begin{bmatrix}
0 & 0 & 0\\
0 & 0 & 0\\
0 & 0 & 0\\
0 & \frac{-1}{16}\left(P_{3,i+1}+3P_{3,i}\right) & \frac{1}{16}\left(P_{2,i+1}+3P_{2,i}\right)\\
\frac{1}{16}\left(P_{3,i+1}+3P_{3,i}\right) & 0 & \frac{-1}{16}\left(P_{1,i+1}+3P_{1,i}\right)\\
\frac{-1}{16}\left(P_{2,i+1}+3P_{2,i}\right) & \frac{1}{16}\left(P_{1,i+1}+3P_{1,i}\right) & 0\\
\frac{-1}{2\Delta x} & \frac{-1}{16}\left(\kappa_{3,i+1}+3\kappa_{3,i}\right) & \frac{1}{16}\left(\kappa_{2,i+1}+3\kappa_{2,i}\right)\\
\frac{1}{16}\left(\kappa_{3,i+1}+3\kappa_{3,i}\right) & \frac{-1}{2\Delta x} & \frac{-1}{16}\left(\kappa_{1,i+1}+3\kappa_{1,i}\right)\\
\frac{-1}{16}\left(\kappa_{2,i+1}+3\kappa_{2,i}\right) & \frac{1}{16}\left(\kappa_{1,i+1}+3\kappa_{1,i}\right) & \frac{-1}{2\Delta x}\\
0 & 0 & 0\\
0 & 0 & 0\\
0 & 0 & 0\\
\frac{-1}{4}\mu & 0 & 0\\
0 & \frac{-1}{4}\mu & 0\\
0 & 0 & \frac{-1}{4}\mu\\
0 & \frac{1}{4}\mu\bar{x}_3 & \frac{-1}{4}\mu\bar{x}_2\\
\frac{-1}{4}\mu\bar{x}_3 & 0 & 0\\
\frac{1}{4}\mu\bar{x}_2 & 0 & 0\\
0 & 0 & 0\\
0 & 0 & 0\\
0 & 0 & 0\\
0 & 0 & 0\\
0 & 0 & 0\\
0 & 0 & 0
\end{bmatrix} \tag{A.27}$$

$$A_i(1:24,10:12)=\begin{bmatrix} 0 & \frac{-1}{16}\left(P_{3,i+1}+3P_{3,i}\right) & \frac{1}{16}\left(P_{2,i+1}+3P_{2,i}\right) \\ \frac{1}{16}\left(P_{3,i+1}+3P_{3,i}\right) & 0 & \frac{-1}{16}\left(P_{1,i+1}+3P_{1,i}\right) \\ \frac{-1}{16}\left(P_{2,i+1}+3P_{2,i}\right) & \frac{1}{16}\left(P_{1,i+1}+3P_{1,i}\right) & 0 \\ 0 & \frac{-1}{16}\left(H_{3,i+1}+3H_{3,i}\right) & \frac{1}{16}\left(H_{2,i+1}+3H_{2,i}\right) \\ \frac{1}{16}\left(H_{3,i+1}+3H_{3,i}\right) & 0 & \frac{-1}{16}\left(H_{1,i+1}+3H_{1,i}\right) \\ \frac{-1}{16}\left(H_{2,i+1}+3H_{2,i}\right) & \frac{1}{16}\left(H_{1,i+1}+3H_{1,i}\right) & 0 \\ 0 & \frac{-1}{8}\left(\gamma_{13,i+1}+3\gamma_{13,i}\right) & \frac{1}{8}\left(\gamma_{12,i+1}+3\gamma_{12,i}\right) \\ \frac{1}{8}\left(\gamma_{13,i+1}+3\gamma_{13,i}\right) & 0 & \frac{-1}{4}-\frac{1}{16}\left(\gamma_{11,i+1}+3\gamma_{11,i}\right) \\ \frac{-1}{8}\left(\gamma_{12,i+1}+3\gamma_{12,i}\right) & \frac{1}{4}+\frac{1}{16}\left(\gamma_{11,i+1}+3\gamma_{11,i}\right) & 0 \\ \frac{-1}{2\Delta x} & \frac{-1}{16}\left(\kappa_{3,i+1}+3\kappa_{3,i}\right) & \frac{1}{16}\left(\kappa_{2,i+1}+3\kappa_{2,i}\right) \\ \frac{1}{16}\left(\kappa_{3,i+1}+3\kappa_{3,i}\right) & \frac{-1}{2\Delta x} & \frac{-1}{16}\left(\kappa_{1,i+1}+3\kappa_{1,i}\right) \\ \frac{-1}{16}\left(\kappa_{2,i+1}+3\kappa_{2,i}\right) & \frac{1}{16}\left(\kappa_{1,i+1}+3\kappa_{1,i}\right) & \frac{-1}{2\Delta x} \\ 0 & \frac{-1}{4}\mu\bar{x}_3 & \frac{1}{4}\mu\bar{x}_2 \\ \frac{1}{4}\mu\bar{x}_3 & 0 & 0 \\ \frac{-1}{4}\mu\bar{x}_2 & 0 & 0 \\ \frac{-1}{4}i(1,1) & \frac{-1}{4}i(1,2) & \frac{-1}{4}i(1,3) \\ \frac{-1}{4}i(2,1) & \frac{-1}{4}i(2,2) & \frac{-1}{4}i(2,3) \\ \frac{-1}{4}i(3,1) & \frac{-1}{4}i(3,2) & \frac{-1}{4}i(3,3) \\ 0 & 0 & 0 \\ 0 & 0 & 0 \\ 0 & 0 & 0 \\ 0 & 0 & 0 \\ 0 & 0 & 0 \\ 0 & 0 & 0 \end{bmatrix} \tag{A.28}$$

$$A_i(1:24,13:15)=\begin{bmatrix} \frac{-1}{2\Delta t} & \frac{1}{16}\left(\Omega_{3,i+1}+3\Omega_{3,i}\right) & \frac{-1}{16}\left(\Omega_{2,i+1}+3\Omega_{2,i}\right) \\ \frac{-1}{16}\left(\Omega_{3,i+1}+3\Omega_{3,i}\right) & \frac{-1}{2\Delta t} & \frac{1}{16}\left(\Omega_{1,i+1}+3\Omega_{1,i}\right) \\ \frac{1}{16}\left(\Omega_{2,i+1}+3\Omega_{2,i}\right) & \frac{-1}{16}\left(\Omega_{1,i+1}+3\Omega_{1,i}\right) & \frac{-1}{2\Delta t} \\ 0 & \frac{1}{16}\left(V_{3,i+1}+3V_{3,i}\right) & \frac{-1}{16}\left(V_{2,i+1}+3V_{2,i}\right) \\ \frac{-1}{16}\left(V_{3,i+1}+3V_{3,i}\right) & 0 & \frac{1}{16}\left(V_{1,i+1}+3V_{1,i}\right) \\ \frac{1}{16}\left(V_{2,i+1}+3V_{2,i}\right) & \frac{-1}{16}\left(V_{1,i+1}+3V_{1,i}\right) & 0 \\ 0 & 0 & 0 \\ 0 & 0 & 0 \\ 0 & 0 & 0 \\ 0 & 0 & 0 \\ 0 & 0 & 0 \\ 0 & 0 & 0 \\ \frac{1}{4} & 0 & 0 \\ 0 & \frac{1}{4} & 0 \\ 0 & 0 & \frac{1}{4} \\ 0 & 0 & 0 \\ 0 & 0 & 0 \\ 0 & 0 & 0 \\ 0 & 0 & 0 \\ 0 & 0 & 0 \\ 0 & 0 & 0 \\ 0 & 0 & 0 \\ 0 & 0 & 0 \\ 0 & 0 & 0 \end{bmatrix} \tag{A.29}$$

$$A_i(1:24,16:18) = \begin{bmatrix} 0 & 0 & 0 \\ 0 & 0 & 0 \\ 0 & 0 & 0 \\ \frac{-1}{2\Delta t} & \frac{1}{16}\left(\Omega_{3,i+1}+3\Omega_{3,i}\right) & \frac{-1}{16}\left(\Omega_{2,i+1}+3\Omega_{2,i}\right) \\ \frac{-1}{16}\left(\Omega_{3,i+1}+3\Omega_{3,i}\right) & \frac{-1}{2\Delta t} & \frac{1}{16}\left(\Omega_{1,i+1}+3\Omega_{1,i}\right) \\ \frac{1}{16}\left(\Omega_{2,i+1}+3\Omega_{2,i}\right) & \frac{-1}{16}\left(\Omega_{1,i+1}+3\Omega_{1,i}\right) & \frac{-1}{2\Delta t} \\ 0 & 0 & 0 \\ 0 & 0 & 0 \\ 0 & 0 & 0 \\ 0 & 0 & 0 \\ 0 & 0 & 0 \\ 0 & 0 & 0 \\ 0 & 0 & 0 \\ 0 & 0 & 0 \\ 0 & 0 & 0 \\ \frac{1}{4} & 0 & 0 \\ 0 & \frac{1}{4} & 0 \\ 0 & 0 & \frac{1}{4} \\ 0 & 0 & 0 \\ 0 & 0 & 0 \\ 0 & 0 & 0 \\ 0 & 0 & 0 \\ 0 & 0 & 0 \\ 0 & 0 & 0 \end{bmatrix} \tag{A.30}$$

$$A_i(1:24,19:21) = \begin{bmatrix} 0 & 0 & 0 \\ 0 & 0 & 0 \\ 0 & 0 & 0 \\ 0 & \frac{1}{16}\left(F_{3,i+1}+3F_{3,i}\right) & \frac{-1}{16}\left(F_{2,i+1}+3F_{2,i}\right) \\ \frac{-1}{16}\left(F_{3,i+1}+3F_{3,i}\right) & 0 & \frac{1}{16}\left(F_{1,i+1}+3F_{1,i}\right) \\ \frac{1}{16}\left(F_{2,i+1}+3F_{2,i}\right) & \frac{-1}{16}\left(F_{1,i+1}+3F_{1,i}\right) & 0 \\ \frac{-1}{2\Delta t} & \frac{1}{16}\left(\Omega_{3,i+1}+3\Omega_{3,i}\right) & \frac{-1}{16}\left(\Omega_{2,i+1}+3\Omega_{2,i}\right) \\ \frac{-1}{16}\left(\Omega_{3,i+1}+3\Omega_{3,i}\right) & \frac{-1}{2\Delta t} & \frac{1}{16}\left(\Omega_{1,i+1}+3\Omega_{1,i}\right) \\ \frac{1}{16}\left(\Omega_{2,i+1}+3\Omega_{2,i}\right) & \frac{-1}{16}\left(\Omega_{1,i+1}+3\Omega_{1,i}\right) & \frac{-1}{2\Delta t} \\ 0 & 0 & 0 \\ 0 & 0 & 0 \\ 0 & 0 & 0 \\ 0 & 0 & 0 \\ 0 & 0 & 0 \\ 0 & 0 & 0 \\ 0 & 0 & 0 \\ 0 & 0 & 0 \\ 0 & 0 & 0 \\ \frac{1}{4} & 0 & 0 \\ 0 & \frac{1}{4} & 0 \\ 0 & 0 & \frac{1}{4} \\ 0 & 0 & 0 \\ 0 & 0 & 0 \\ 0 & 0 & 0 \end{bmatrix} \tag{A.31}$$

$$A_i(1:24,22:24)=\begin{bmatrix}
0 & \frac{1}{16}\left(F_{3,i+1}+3F_{3,i}\right) & \frac{-1}{16}\left(F_{2,i+1}+3F_{2,i}\right)\\
\frac{-1}{16}\left(F_{3,i+1}+3F_{3,i}\right) & 0 & \frac{1}{16}\left(F_{1,i+1}+3F_{1,i}\right)\\
\frac{1}{16}\left(F_{2,i+1}+3F_{2,i}\right) & \frac{-1}{16}\left(F_{1,i+1}+3F_{1,i}\right) & 0\\
0 & \frac{1}{16}\left(M_{3,i+1}+3M_{3,i}\right) & \frac{-1}{16}\left(M_{2,i+1}+3M_{2,i}\right)\\
\frac{-1}{16}\left(M_{3,i+1}+3M_{3,i}\right) & 0 & \frac{1}{16}\left(M_{1,i+1}+3M_{1,i}\right)\\
\frac{1}{16}\left(M_{2,i+1}+3M_{2,i}\right) & \frac{-1}{16}\left(M_{1,i+1}+3M_{1,i}\right) & 0\\
0 & \frac{1}{16}\left(V_{3,i+1}+3V_{3,i}\right) & \frac{-1}{16}\left(V_{2,i+1}+3V_{2,i}\right)\\
\frac{-1}{16}\left(V_{3,i+1}+3V_{3,i}\right) & 0 & \frac{1}{16}\left(V_{1,i+1}+3V_{1,i}\right)\\
\frac{1}{16}\left(V_{2,i+1}+3V_{2,i}\right) & \frac{-1}{16}\left(V_{1,i+1}+3V_{1,i}\right) & 0\\
\frac{-1}{2\Delta t} & \frac{1}{16}\left(\Omega_{3,i+1}+3\Omega_{3,i}\right) & \frac{-1}{16}\left(\Omega_{2,i+1}+3\Omega_{2,i}\right)\\
\frac{-1}{16}\left(\Omega_{3,i+1}+3\Omega_{3,i}\right) & \frac{-1}{2\Delta t} & \frac{1}{16}\left(\Omega_{1,i+1}+3\Omega_{1,i}\right)\\
\frac{1}{16}\left(\Omega_{2,i+1}+3\Omega_{2,i}\right) & \frac{-1}{16}\left(\Omega_{1,i+1}+3\Omega_{1,i}\right) & \frac{-1}{2\Delta t}\\
0 & 0 & 0\\
0 & 0 & 0\\
0 & 0 & 0\\
0 & 0 & 0\\
0 & 0 & 0\\
0 & 0 & 0\\
0 & 0 & 0\\
0 & 0 & 0\\
0 & 0 & 0\\
\frac{1}{4} & 0 & 0\\
0 & \frac{1}{4} & 0\\
0 & 0 & \frac{1}{4}
\end{bmatrix} \tag{A.32}$$

$$B_i(1:24,1:3)=\begin{bmatrix}
\frac{1}{2\Delta x} & \frac{-1}{16}\left(\kappa_{3,i+1}+3\kappa_{3,i}\right) & \frac{1}{16}\left(\kappa_{2,i+1}+3\kappa_{2,i}\right)\\
\frac{1}{16}\left(\kappa_{3,i+1}+3\kappa_{3,i}\right) & \frac{1}{2\Delta x} & \frac{-1}{16}\left(\kappa_{1,i+1}+3\kappa_{1,i}\right)\\
\frac{-1}{16}\left(\kappa_{2,i+1}+3\kappa_{2,i}\right) & \frac{1}{16}\left(\kappa_{1,i+1}+3\kappa_{1,i}\right) & \frac{1}{2\Delta x}\\
0 & \frac{-1}{8}\left(\gamma_{13,i+1}+3\gamma_{13,i}\right) & \frac{1}{8}\left(\gamma_{12,i+1}+3\gamma_{12,i}\right)\\
\frac{1}{8}\left(\gamma_{13,i+1}+3\gamma_{13,i}\right) & 0 & \frac{-1}{4}-\frac{1}{16}\left(\gamma_{11,i+1}+3\gamma_{11,i}\right)\\
\frac{-1}{8}\left(\gamma_{12,i+1}+3\gamma_{12,i}\right) & \frac{1}{4}+\frac{1}{16}\left(\gamma_{11,i+1}+3\gamma_{11,i}\right) & 0\\
0 & 0 & 0\\
0 & 0 & 0\\
0 & 0 & 0\\
0 & 0 & 0\\
0 & 0 & 0\\
0 & 0 & 0\\
0 & 0 & 0\\
0 & 0 & 0\\
0 & 0 & 0\\
0 & 0 & 0\\
0 & 0 & 0\\
0 & 0 & 0\\
\frac{-1}{4}R(1,1) & \frac{-1}{4}R(1,2) & \frac{-1}{4}R(1,3)\\
\frac{-1}{4}R(2,1) & \frac{-1}{4}R(2,2) & \frac{-1}{4}R(2,3)\\
\frac{-1}{4}R(3,1) & \frac{-1}{4}R(3,2) & \frac{-1}{4}R(3,3)\\
\frac{-1}{4}Z(1,1) & \frac{-1}{4}Z(2,1) & \frac{-1}{4}Z(3,1)\\
\frac{-1}{4}Z(1,2) & \frac{-1}{4}Z(2,2) & \frac{-1}{4}Z(3,2)\\
\frac{-1}{4}Z(1,3) & \frac{-1}{4}Z(2,3) & \frac{-1}{4}Z(3,3)
\end{bmatrix} \tag{A.33}$$

$$B_i(1:24,4:6)=\begin{bmatrix} 0 & 0 & 0\\ 0 & 0 & 0\\ 0 & 0 & 0\\ \frac{1}{2\Delta x} & \frac{-1}{16}\left(\kappa_{3,i+1}+3\kappa_{3,i}\right) & \frac{1}{16}\left(\kappa_{2,i+1}+3\kappa_{2,i}\right)\\ \frac{1}{16}\left(\kappa_{3,i+1}+3\kappa_{3,i}\right) & \frac{1}{2\Delta x} & \frac{-1}{16}\left(\kappa_{1,i+1}+3\kappa_{1,i}\right)\\ \frac{-1}{16}\left(\kappa_{2,i+1}+3\kappa_{2,i}\right) & \frac{1}{16}\left(\kappa_{1,i+1}+3\kappa_{1,i}\right) & \frac{1}{2\Delta x}\\ 0 & 0 & 0\\ 0 & 0 & 0\\ 0 & 0 & 0\\ 0 & 0 & 0\\ 0 & 0 & 0\\ 0 & 0 & 0\\ 0 & 0 & 0\\ 0 & 0 & 0\\ 0 & 0 & 0\\ 0 & 0 & 0\\ 0 & 0 & 0\\ 0 & 0 & 0\\ \frac{-1}{4}Z(1,1) & \frac{-1}{4}Z(1,2) & \frac{-1}{4}Z(1,3)\\ \frac{-1}{4}Z(2,1) & \frac{-1}{4}Z(2,2) & \frac{-1}{4}Z(2,3)\\ \frac{-1}{4}Z(3,1) & \frac{-1}{4}Z(3,2) & \frac{-1}{4}Z(3,3)\\ \frac{-1}{4}T(1,1) & \frac{-1}{4}T(1,2) & \frac{-1}{4}T(1,3)\\ \frac{-1}{4}T(2,1) & \frac{-1}{4}T(2,2) & \frac{-1}{4}T(2,3)\\ \frac{-1}{4}T(3,1) & \frac{-1}{4}T(3,2) & \frac{-1}{4}T(3,3) \end{bmatrix} \tag{A.34}$$

$$B_i(1:24,7:9)=\begin{bmatrix} 0 & 0 & 0\\ 0 & 0 & 0\\ 0 & 0 & 0\\ 0 & \frac{-1}{16}\left(P_{3,i+1}+3P_{3,i}\right) & \frac{1}{16}\left(P_{2,i+1}+3P_{2,i}\right)\\ \frac{1}{16}\left(P_{3,i+1}+3P_{3,i}\right) & 0 & \frac{-1}{16}\left(P_{1,i+1}+3P_{1,i}\right)\\ \frac{-1}{16}\left(P_{2,i+1}+3P_{2,i}\right) & \frac{1}{16}\left(P_{1,i+1}+3P_{1,i}\right) & 0\\ \frac{1}{2\Delta x} & \frac{-1}{16}\left(\kappa_{3,i+1}+3\kappa_{3,i}\right) & \frac{1}{16}\left(\kappa_{2,i+1}+3\kappa_{2,i}\right)\\ \frac{1}{16}\left(\kappa_{3,i+1}+3\kappa_{3,i}\right) & \frac{1}{2\Delta x} & \frac{-1}{16}\left(\kappa_{1,i+1}+3\kappa_{1,i}\right)\\ \frac{-1}{16}\left(\kappa_{2,i+1}+3\kappa_{2,i}\right) & \frac{1}{16}\left(\kappa_{1,i+1}+3\kappa_{1,i}\right) & \frac{1}{2\Delta x}\\ 0 & 0 & 0\\ 0 & 0 & 0\\ 0 & 0 & 0\\ \frac{-1}{4}\mu & 0 & 0\\ 0 & \frac{-1}{4}\mu & 0\\ 0 & 0 & \frac{-1}{4}\mu\\ 0 & \frac{1}{4}\mu\bar{x}_3 & \frac{-1}{4}\mu\bar{x}_2\\ \frac{-1}{4}\mu\bar{x}_3 & 0 & 0\\ \frac{1}{4}\mu\bar{x}_2 & 0 & 0\\ 0 & 0 & 0\\ 0 & 0 & 0\\ 0 & 0 & 0\\ 0 & 0 & 0\\ 0 & 0 & 0\\ 0 & 0 & 0 \end{bmatrix} \tag{A.35}$$

$$B_i(1:24,10:12)=\begin{bmatrix}
0 & \frac{-1}{16}\left(P_{3,i+1}+3P_{3,i}\right) & \frac{1}{16}\left(P_{2,i+1}+3P_{2,i}\right)\\
\frac{1}{16}\left(P_{3,i+1}+3P_{3,i}\right) & 0 & \frac{-1}{16}\left(P_{1,i+1}+3P_{1,i}\right)\\
\frac{-1}{16}\left(P_{2,i+1}+3P_{2,i}\right) & \frac{1}{16}\left(P_{1,i+1}+3P_{1,i}\right) & 0\\
0 & \frac{-1}{16}\left(H_{3,i+1}+3H_{3,i}\right) & \frac{1}{16}\left(H_{2,i+1}+3H_{2,i}\right)\\
\frac{1}{16}\left(H_{3,i+1}+3H_{3,i}\right) & 0 & \frac{-1}{16}\left(H_{1,i+1}+3H_{1,i}\right)\\
\frac{-1}{16}\left(H_{2,i+1}+3H_{2,i}\right) & \frac{1}{16}\left(H_{1,i+1}+3H_{1,i}\right) & 0\\
0 & \frac{-1}{8}\left(\gamma_{13,i+1}+3\gamma_{13,i}\right) & \frac{1}{8}\left(\gamma_{12,i+1}+3\gamma_{12,i}\right)\\
\frac{1}{8}\left(\gamma_{13,i+1}+3\gamma_{13,i}\right) & 0 & \frac{-1}{4}-\frac{1}{16}\left(\gamma_{11,i+1}+3\gamma_{11,i}\right)\\
\frac{-1}{8}\left(\gamma_{12,i+1}+3\gamma_{12,i}\right) & \frac{1}{4}+\frac{1}{16}\left(\gamma_{11,i+1}+3\gamma_{11,i}\right) & 0\\
\frac{1}{2\Delta x} & \frac{-1}{16}\left(\kappa_{3,i+1}+3\kappa_{3,i}\right) & \frac{1}{16}\left(\kappa_{2,i+1}+3\kappa_{2,i}\right)\\
\frac{1}{16}\left(\kappa_{3,i+1}+3\kappa_{3,i}\right) & \frac{1}{2\Delta x} & \frac{-1}{16}\left(\kappa_{1,i+1}+3\kappa_{1,i}\right)\\
\frac{-1}{16}\left(\kappa_{2,i+1}+3\kappa_{2,i}\right) & \frac{1}{16}\left(\kappa_{1,i+1}+3\kappa_{1,i}\right) & \frac{1}{2\Delta x}\\
0 & \frac{-1}{4}\mu\bar{x}_3 & \frac{1}{4}\mu\bar{x}_2\\
\frac{1}{4}\mu\bar{x}_3 & 0 & 0\\
\frac{-1}{4}\mu\bar{x}_2 & 0 & 0\\
\frac{-1}{4}i(1,1) & \frac{-1}{4}i(1,2) & \frac{-1}{4}i(1,3)\\
\frac{-1}{4}i(2,1) & \frac{-1}{4}i(2,2) & \frac{-1}{4}i(2,3)\\
\frac{-1}{4}i(3,1) & \frac{-1}{4}i(3,2) & \frac{-1}{4}i(3,3)\\
0 & 0 & 0\\
0 & 0 & 0\\
0 & 0 & 0\\
0 & 0 & 0\\
0 & 0 & 0\\
0 & 0 & 0
\end{bmatrix} \tag{A.36}$$

$$B_i(1:24,13:15)=\begin{bmatrix}
\frac{-1}{2\Delta t} & \frac{1}{16}\left(\Omega_{3,i+1}+3\Omega_{3,i}\right) & \frac{-1}{16}\left(\Omega_{2,i+1}+3\Omega_{2,i}\right)\\
\frac{-1}{16}\left(\Omega_{3,i+1}+3\Omega_{3,i}\right) & \frac{-1}{2\Delta t} & \frac{1}{16}\left(\Omega_{1,i+1}+3\Omega_{1,i}\right)\\
\frac{1}{16}\left(\Omega_{2,i+1}+3\Omega_{2,i}\right) & \frac{-1}{16}\left(\Omega_{1,i+1}+3\Omega_{1,i}\right) & \frac{-1}{2\Delta t}\\
0 & \frac{1}{16}\left(V_{3,i+1}+3V_{3,i}\right) & \frac{-1}{16}\left(V_{2,i+1}+3V_{2,i}\right)\\
\frac{-1}{16}\left(V_{3,i+1}+3V_{3,i}\right) & 0 & \frac{1}{16}\left(V_{1,i+1}+3V_{1,i}\right)\\
\frac{1}{16}\left(V_{2,i+1}+3V_{2,i}\right) & \frac{-1}{16}\left(V_{1,i+1}+3V_{1,i}\right) & 0\\
0 & 0 & 0\\
0 & 0 & 0\\
0 & 0 & 0\\
0 & 0 & 0\\
0 & 0 & 0\\
0 & 0 & 0\\
\frac{1}{4} & 0 & 0\\
0 & \frac{1}{4} & 0\\
0 & 0 & \frac{1}{4}\\
0 & 0 & 0\\
0 & 0 & 0\\
0 & 0 & 0\\
0 & 0 & 0\\
0 & 0 & 0\\
0 & 0 & 0\\
0 & 0 & 0\\
0 & 0 & 0\\
0 & 0 & 0
\end{bmatrix} \tag{A.37}$$

$$B_i(1:24,16:18)=\begin{bmatrix}
0 & 0 & 0\\
0 & 0 & 0\\
0 & 0 & 0\\
\frac{-1}{2\Delta t} & \frac{1}{16}\left(\Omega_{3,i+1}+3\Omega_{3,i}\right) & \frac{-1}{16}\left(\Omega_{2,i+1}+3\Omega_{2,i}\right)\\
\frac{-1}{16}\left(\Omega_{3,i+1}+3\Omega_{3,i}\right) & \frac{-1}{2\Delta t} & \frac{1}{16}\left(\Omega_{1,i+1}+3\Omega_{1,i}\right)\\
\frac{1}{16}\left(\Omega_{2,i+1}+3\Omega_{2,i}\right) & \frac{-1}{16}\left(\Omega_{1,i+1}+3\Omega_{1,i}\right) & \frac{-1}{2\Delta t}\\
0 & 0 & 0\\
0 & 0 & 0\\
0 & 0 & 0\\
0 & 0 & 0\\
0 & 0 & 0\\
0 & 0 & 0\\
0 & 0 & 0\\
0 & 0 & 0\\
0 & 0 & 0\\
\frac{1}{4} & 0 & 0\\
0 & \frac{1}{4} & 0\\
0 & 0 & \frac{1}{4}\\
0 & 0 & 0\\
0 & 0 & 0\\
0 & 0 & 0\\
0 & 0 & 0\\
0 & 0 & 0\\
0 & 0 & 0
\end{bmatrix} \tag{A.38}$$

$$B_i(1:24,19:21)=\begin{bmatrix}
0 & 0 & 0\\
0 & 0 & 0\\
0 & 0 & 0\\
0 & \frac{1}{16}\left(F_{3,i+1}+3F_{3,i}\right) & \frac{-1}{16}\left(F_{2,i+1}+3F_{2,i}\right)\\
\frac{-1}{16}\left(F_{3,i+1}+3F_{3,i}\right) & 0 & \frac{1}{16}\left(F_{1,i+1}+3F_{1,i}\right)\\
\frac{1}{16}\left(F_{2,i+1}+3F_{2,i}\right) & \frac{-1}{16}\left(F_{1,i+1}+3F_{1,i}\right) & 0\\
\frac{-1}{2\Delta t} & \frac{1}{16}\left(\Omega_{3,i+1}+3\Omega_{3,i}\right) & \frac{-1}{16}\left(\Omega_{2,i+1}+3\Omega_{2,i}\right)\\
\frac{-1}{16}\left(\Omega_{3,i+1}+3\Omega_{3,i}\right) & \frac{-1}{2\Delta t} & \frac{1}{16}\left(\Omega_{1,i+1}+3\Omega_{1,i}\right)\\
\frac{1}{16}\left(\Omega_{2,i+1}+3\Omega_{2,i}\right) & \frac{-1}{16}\left(\Omega_{1,i+1}+3\Omega_{1,i}\right) & \frac{-1}{2\Delta t}\\
0 & 0 & 0\\
0 & 0 & 0\\
0 & 0 & 0\\
0 & 0 & 0\\
0 & 0 & 0\\
0 & 0 & 0\\
0 & 0 & 0\\
0 & 0 & 0\\
0 & 0 & 0\\
\frac{1}{4} & 0 & 0\\
0 & \frac{1}{4} & 0\\
0 & 0 & \frac{1}{4}\\
0 & 0 & 0\\
0 & 0 & 0\\
0 & 0 & 0
\end{bmatrix} \tag{A.39}$$

$$B_i(1:24, 22:24) = \begin{bmatrix} 0 & \frac{1}{16}\left(F_{3,i+1} + 3F_{3,i}\right) & \frac{-1}{16}\left(F_{2,i+1} + 3F_{2,i}\right) \\ \frac{-1}{16}\left(F_{3,i+1} + 3F_{3,i}\right) & 0 & \frac{1}{16}\left(F_{1,i+1} + 3F_{1,i}\right) \\ \frac{1}{16}\left(F_{2,i+1} + 3F_{2,i}\right) & \frac{-1}{16}\left(F_{1,i+1} + 3F_{1,i}\right) & 0 \\ 0 & \frac{1}{16}\left(M_{3,i+1} + 3M_{3,i}\right) & \frac{-1}{16}\left(M_{2,i+1} + 3M_{2,i}\right) \\ \frac{-1}{16}\left(M_{3,i+1} + 3M_{3,i}\right) & 0 & \frac{1}{16}\left(M_{1,i+1} + 3M_{1,i}\right) \\ \frac{1}{16}\left(M_{2,i+1} + 3M_{2,i}\right) & \frac{-1}{16}\left(M_{1,i+1} + 3M_{1,i}\right) & 0 \\ 0 & \frac{1}{16}\left(V_{3,i+1} + 3V_{3,i}\right) & \frac{-1}{16}\left(V_{2,i+1} + 3V_{2,i}\right) \\ \frac{-1}{16}\left(V_{3,i+1} + 3V_{3,i}\right) & 0 & \frac{1}{16}\left(V_{1,i+1} + 3V_{1,i}\right) \\ \frac{1}{16}\left(V_{2,i+1} + 3V_{2,i}\right) & \frac{-1}{16}\left(V_{1,i+1} + 3V_{1,i}\right) & 0 \\ \frac{-1}{2\Delta t} & \frac{1}{16}\left(\Omega_{3,i+1} + 3\Omega_{3,i}\right) & \frac{-1}{16}\left(\Omega_{2,i+1} + 3\Omega_{2,i}\right) \\ \frac{-1}{16}\left(\Omega_{3,i+1} + 3\Omega_{3,i}\right) & \frac{-1}{2\Delta t} & \frac{1}{16}\left(\Omega_{1,i+1} + 3\Omega_{1,i}\right) \\ \frac{1}{16}\left(\Omega_{2,i+1} + 3\Omega_{2,i}\right) & \frac{-1}{16}\left(\Omega_{1,i+1} + 3\Omega_{1,i}\right) & \frac{-1}{2\Delta t} \\ 0 & 0 & 0 \\ 0 & 0 & 0 \\ 0 & 0 & 0 \\ 0 & 0 & 0 \\ 0 & 0 & 0 \\ 0 & 0 & 0 \\ 0 & 0 & 0 \\ 0 & 0 & 0 \\ 0 & 0 & 0 \\ \frac{1}{4} & 0 & 0 \\ 0 & \frac{1}{4} & 0 \\ 0 & 0 & \frac{1}{4} \end{bmatrix} \tag{A.40}$$

Index

M. Ghorashi, *Statics and Rotational Dynamics of Composite Beams*,
DOI 10.1007/978-3-319-14959-2